Universidade do Porto
Faculdade de Engenharia
FEUP



Telmo Reis Cunha

High Precision Navigation Integrating Satellite Information - GPS - and Inertial System Data

Porto, 2002

FACULTY OF ENGINEERING OF THE UNIVERSITY OF PORTO
PORTUGAL

Philosophiae Doctor Thesis
of
Telmo Reis Cunha

Title:

High Precision Navigation Integrating Satellite Information – GPS – and Inertial System Data



Universidade do Porto

Faculdade de Engenharia

FEUP

December of 2002

Departamento de Engenharia Electrotécnica e de Computadores

UNIVERSIDADE DO PORTO
Faculdade de Engenharia
BIBLIOTECA
N.º 65415
CDU
Data 2 / 4 / 2003

TABLE OF CONTENTS

TABLE OF CONTENTS i

TABLE OF ACRONYMS iii

PREFACE 1

1 INTRODUCTION 2

1.1 LAYOUT OF THE THESIS 5

2 SATELLITE BASED AND INERTIAL NAVIGATION SYSTEMS 7

2.1 GLOBAL POSITIONING SYSTEM (GPS) 8
2.1.1 Principle of Satellite Based Navigation 8
2.1.2 Brief Description of GPS 10
2.1.2.1 Space Segment 11
2.1.2.2 User Segment 14
2.1.2.3 Control Segment 15
2.1.3 Main Error Sources in GPS 15
2.2 OTHER GLOBAL NAVIGATION SATELLITE SYSTEMS 17
2.2.1 GLONASS 17
2.2.1.1 Space Segment 17
2.2.1.2 Control Segment 19
2.2.1.3 User Segment 19
2.2.2 GALILEO 21
2.2.2.1 GALILEO Services 22
2.2.2.2 GALILEO Components 24
2.3 INERTIAL NAVIGATION SYSTEMS 28
2.3.1 Principle of Inertial Navigation 28

3 THE NAVIGATION SYSTEM 33

3.1 AIRBORNE SURVEYS 34
3.2 IMPLEMENTATION OF AN AIRBORNE GPS/INS SYSTEM 37
3.3 APPLICATION OF THE GPS/IMU SYSTEM ON A LAND VEHICLE 45

4 GPS PROCESSING 47

4.1 GPS MEASUREMENTS 48
4.1.1 Raw Measurements 48
4.1.1.1 Pseudorange Measurement 48
4.1.1.2 Carrier Phase Measurement 50
4.1.1.3 Doppler Measurement 53
4.1.2 Measurement Error Sources 54
4.1.2.1 Clock Errors 54
4.1.2.2 Tropospheric Error 55
4.1.2.3 Ionospheric Error 57
4.1.2.4 Multipath Error 61
4.1.2.5 Orbit Errors 62
4.1.2.6 Other Error Sources 63
4.1.3 Measurement Combinations 63
4.1.3.1 Wide Lane Combination 64
4.1.3.2 Single Differences 65
4.1.3.3 Double Differences 66
4.2 POSITIONING WITH GPS 68
4.2.1 Formulation 68
4.2.2 Ambiguity Fixing Concept 72
4.2.3 Difficulties of Ambiguity Fixing 74
4.2.4 Ambiguity Fixing Methods 75
4.2.4.1 Ambiguity Function Search Technique 75
4.2.4.2 Least Squares Search Technique 76

5 ALGORITHMS FOR RTK GPS PROCESSING 82

5.1 PROPOSED POSITIONING ALGORITHMS 83
5.1.1 Cycle Slip Fixing Algorithm *83*
5.1.2 L1 Ambiguity Fixing Method *86*
5.1.2.1 Initial Position Estimate 87
5.1.2.2 Wide-Laning 90
5.1.2.3 L1 Ambiguity Fixing 94
5.1.2.4 Testing and Results 97
5.2 RELATIVE POSITIONING BETWEEN TWO CLOSE ANTENNAS 106
5.2.1 Formulation *106*
5.2.2 Method *107*

6 INS PROCESSING AND ITS INTEGRATION WITH GPS 112

6.1 REFERENCE FRAME DEFINITION 114
6.1.1 The Inertial Frame *114*
6.1.2 The Earth-Centered, Earth-Fixed Frame (ECEF) *115*
6.1.3 The Body Frame *116*
6.1.4 The Local Navigation Frame *117*
6.2 THE IMU HARDWARE 120
6.2.1 Accelerometer Technology *120*
6.2.1.1 Mechanical Accelerometers 123
6.2.1.2 Solid State Accelerometers 125
6.2.2 Gyroscope Technology *128*
6.2.2.1 Mechanical Gyroscopes 129
6.2.2.2 Optical Gyroscopes 132
6.2.3 The 3D IMU *135*
6.3 DYNAMIC EQUATIONS OF AN IMU 136
6.4 REPRESENTATIONS OF VEHICLE ATTITUDE 147
6.4.1 Direction Cosine Matrix *147*
6.4.2 Euler Angles *147*
6.4.3 Quaternions *147*
6.5 INTEGRATION OF IMU AND GPS DATA 149
6.5.1 IMU Processing Integrating GPS Data *149*
6.5.2 GPS Processing Integrating IMU Data *152*

7 IMPLEMENTATION, CAMPAIGNS AND RESULTS 157

7.1 SOFTWARE IMPLEMENTATION 158
7.2 CAMPAIGNS 166
7.2.1 Azores 1997 *166*
7.2.2 Sintra 1999 *176*

8 OTHER APPLICATION AREAS 191

8.1 TERRESTRIAL NAVIGATION 192
8.1.1 Mobile Mapping Application *194*
8.1.2 Coastal Erosion Monitoring Application *198*
8.1.3 Vehicle Tracking *200*
8.2 LOCAL AREA AUGMENTATION SYSTEMS (LAAS) 201

9 CONCLUSIONS AND FINAL REMARKS 203

9.1 CONCLUSIONS 203
9.2 FUTURE DEVELOPMENTS AND PERSPECTIVES 208

REFERENCES 210

TABLE OF ACRONYMS

AGMASCO	Airborne Geoid MApping System for Coastal Oceanography
AIRB	AIRcraft Back antenna
AIRF	AIRcraft Front antenna
AIRW	AIRcraft Wing antenna
AS	AntiSpoof
C/A Code	Clear (Coarse) Acquisition Code
CAD	Computer Aided Design
CDMA	Code Division Multiple Access
CIO	Conventional International Origin
CSIG	Coordination Scientific Information Center
CPU	Central Processing Unit
DART	Dual-Axis Rate Transducer
DGPS	Differential GPS
DLL	Dynamic Link Library
DoD	Department of Defence
ECEF	Earth-Centered Earth-Fixed frame
EGNOS	European Geostationary Navigation Overlay Service
ERS	ESA Remote sensing Satellite
FARA	Fast Ambiguity Resolution Approach
FDMA	Frequency Division Multiple Access
FOG	Fibre Optics Gyro
GALILEO	European GNSS
GLONASS	GLObal Navigation Satellite System
GNSS	Global Navigation Satellite Systems
GPS	Global Positioning System
GSM	Global System for Mobile communication
HP	High Precision
HSI	Horizontal Situation Indicator
ICAO	International Civil Aviation Organization
IMU	Inertial Measurement Unit
INS	Inertial Navigation System

ITS	Intelligent Transportation Systems
LAAS	Local Area Augmentation Systems
LAMBDA	Least-squares AMBiguity Decorrelation Adjustment
MEO	Medium Earth Orbit
NAGU	Notice Advisory to GLONASS Users
NAVSTAR	NAVigation Satellite Timing And Ranging
NED	North-East-Down frame
NGS	National Geodetic Survey
NOAA	National Oceanic and Atmospheric Administration
PC	Personal Computer
P Code	Precise Code
PDOP	Position Dilution Of Precision
PLL	Phase-Lock Loop
PPM	Parts Per Million
PPS	Precise Positioning Service
PRN	Pseudo-Random Number
PZ-90	*Parametry Zemli 1990* (Parameters of the Earth 1990)
RINEX	Receiver INdependent EXchange format
RLG	Ring Laser Gyro
RMS	Root Mean Square
RTK	Real-Time Kinematic
SA	Selective Availability
SARPs	Standards And Recommended Practices
SNAP	*Sistema de Navegação Aérea de Precisão e longo alcance* (long range high precision aerial navigation system)
SP	Standard Precision
SPS	Standard Positioning Service
TCAR	Triple CARrier technique
TCP/IP	Transmission Control Protocol / Internet Protocol
TEC	Total Electron Content
TTL	Transistor-Transistor Logic
UMTS	Universal Mobile Telecommunications System
USNO	United States National Observatory
UTC	Universal Time Coordinated

VGA	Video Graphics Array
VHF	Very High Frequency
WGS84	World Geodetic System 1984
Y Code	Encrypted version of the P code

RESUMO

A tese de Doutoramento intitulada "*High Precision Navigation Integrating Satellite Information – GPS – and Inertial System Data*" foca como ponto principal o desenvolvimento de algoritmos e metodologias de processamento das medidas recolhidas por receptores GPS (*Global Positioning System*) de modo a se obter, em tempo-real e em modo diferencial, uma elevada precisão nas posições absolutas daí provenientes, considerando apenas um conjunto de amostras de alguns segundos (tipicamente entre 3 a 10 segundos). Estes algoritmos centram-se na determinação dos valores inteiros ambíguos que estão associados às medidas de fase da portadora de L1 (denominados Ambiguidades de Fase de L1), sendo este um processo não trivial, principalmente quando se considera um curto conjunto de dados em que a variação da geometria dos satélites observados é imperceptível. A metodologia desenvolvida considera as observações da segunda portadora L2 para melhoria da eficiência do processamento. Nesta tese apresentam-se os princípios de funcionamento dos sistemas de navegação considerados (GPS e sensores inerciais) de modo a facilitar o acompanhamento da descrição dos algoritmos e procedimentos desenvolvidos.

Este trabalho fez parte do desenvolvimento e implementação de um sistema de navegação baseado em receptores GPS e num sensor inercial IMU (*Inertial Measurement Unit*) de baixo custo e composto por três pares acelerómetro-giroscópio dispostos em três eixos ortogonais. Este sistema de navegação GPS/IMU foi implementado numa aeronave da Força Aérea Portuguesa, tendo sido colocadas três antenas GPS na sua estrutura (uma por cima do *cockpit*, uma outra na parte traseira do corpo central da aeronave, e uma terceira na asa direita). O objectivo final deste sistema GPS/IMU era a determinação da posição absoluta de uma das antenas, e a determinação da atitude da aeronave (que consiste na estimação dos ângulos de rotação *roll*, *pitch* e *yaw*). Estas grandezas são essenciais para as aplicações de detecção remota aéreas, tais como gravimetria, altimetria, fotogrametria, entre outras. É necessário conhecer as posições e orientações destes sensores para se poder obter resultados úteis das suas medidas.

Atendendo ao comportamento complementar dos dois sistemas de navegação (GPS e IMU), foi desenvolvida uma metodologia de processamento integrado dos seus dados por forma a se obter resultados de elevada precisão em posicionamento

absoluto e em atitude, sendo estes resultados equiparáveis aos de sistemas de navegação substancialmente mais caros que utilizam sistemas inerciais INS (*Inertial Navigation Systems*) de elevado rigor, eventualmente com plataformas estabilizadoras. Sendo o IMU um sensor de *dead-reckoning*, os resultados da integração temporal das suas medidas apresentam desvios e derivas consideráveis que devem ser estimados da melhor forma. As posições absolutas determinadas por GPS, obtidas em modo diferencial pela metodologia acima mencionada, servem para estimar alguns desses parâmetros, mas outros são pouco sensíveis a essas grandezas, necessitando de outro processo para se proceder à sua estimação. Este é o caso de ângulos de atitude como o *yaw* que, principalmente numa aeronave, pouca relação têm com a posição absoluta ou com a variação desta (devido, principalmente, à acção do vento). Para a resolução deste problema, foram desenvolvidos, no âmbito deste doutoramento, algoritmos para a determinação com grande rigor do vector tridimensional entre duas antenas da aeronave. Este procedimento consiste novamente em técnicas de fixação das ambiguidades das medidas de fase da portadora L1, complementadas com as medidas da portadora L2, desenvolvidas especificamente para aplicações de tempo-real. Com a disposição apropriada das antenas, estes vectores traduzem uma estimativa não enviesada da atitude da aeronave. De referir que estes algoritmos não consideram a utilização dos dados de um receptor GPS estático de referência (localizado num ponto no solo). Este facto torna este procedimento independente do sistema de comunicações entre avião e estação terrestre, fornecendo sempre estimativas não enviesadas da atitude em cada instante de amostragem, mesmo quando não é possível estabelecer comunicação com a estação terrestre.

Uma outra análise considerada nesta tese é a possibilidade de utilização das medidas dadas pelo IMU para ajudar o processo de fixação de ambiguidades das observações GPS. Concluiu-se que, para o caso de IMUs com as características idênticas às do IMU utilizado, poucos seriam os benefícios práticos dessa abordagem. No entanto, em termos de aumento de robustez das soluções de navegação provenientes do processamento GPS, que é uma característica muito importante, conclui-se que a complementaridade dos dois sistemas (GPS e IMU) é muito útil uma vez que as variações suaves das medidas do IMU podem servir para detectar saltos esporádicos nas observações GPS.

Nesta tese são apresentados vários exemplos de aplicação deste sistema e das metodologias desenvolvidas. Salientam-se duas campanhas de teste do sistema GPS/IMU, utilizando uma aeronave da Força Aérea Portuguesa, efectuadas no arquipélago dos Açores e na zona da Estremadura. A primeira realizou-se integrada com uma campanha de gravimetria aérea (projecto europeu AGMASCO – *Airborne Geoid MApping System for Coastal Oceanography*), e a segunda contemplou um equipamento para fotografia aérea, sendo este utilizado como sistema independente para avaliação do rigor da solução de atitude obtida. Nesta última campanha, o sistema GPS/IMU foi utilizado em tempo-real, fornecendo aos pilotos, em cada instante, o percurso (pré-definido) a seguir, incluindo as fases de aproximação à pista e aterragem. Apresentam-se nesta tese resultados obtidos em ambas as campanhas que ilustram os bons resultados obtidos pelo sistema de navegação GPS/IMU desenvolvido.

Uma vez que as técnicas desenvolvidas neste trabalho não são restringidas por pormenores específicos do veículo em consideração, apresentam-se exemplos e resultados de aplicações destas metodologias ao caso de veículos terrestres. Assim, é referida uma implementação do sistema GPS/IMU num veículo todo-o-terreno para geo-referenciação de infra-estruturas urbanas e mapeamento de redes viárias (uma aplicação de *Mobile Mapping*). Apresenta-se, também, a aplicação dos métodos desenvolvidos para processamento das observações GPS ao estudo da erosão/sedimentação de zonas costeiras arenosas. A aplicabilidade destas metodologias a outros casos práticos é também focada, salientando-se a possibilidade de estas serem integradas em componentes de um sistema LAAS (*Local Area Augmentation System*).

PREFACE

In this thesis I present the work that I developed in the subjects of GPS (Global Positioning System) high precision positioning and the benefits of its integration with an IMU (Inertial Measurement Unit). The main focus of this thesis is on GPS processing algorithms for quasi-instantaneous carrier phase ambiguity resolution, for real-time high accuracy positioning of a kinematic mode GPS receiver. Also described are the developed algorithms for vehicle attitude determination based on the vector between two GPS antennas mounted on the vehicle. The implementation of this methodology on a GPS/IMU navigation system, and the obtained results, are also shown. An analysis of the benefits that GPS processing could gain from the integration of IMU data is also presented.

This work has been developed in the scope of the Portuguese project SNAP (*Sistema de Navegação Aérea de Precisão e Longo Alcance*). It consisted on the development of a GPS/IMU based navigation system and its actual implementation on a Portuguese Air Force aircraft. This developed system, oriented for real-time navigation, was mounted on a CASA212 and some flight tests were performed in order to evaluate the navigation system's performance. Most of the examples shown in this thesis are from real-time data retrieved from these tests.

I would like to thank the Portuguese Foundation for Science and Technology (*Fundação para a Ciência e a Tecnologia*) for having financed both the SNAP project (*ref: PRAXIS/3/3.1/CTAE/1933/95*) and the development of this thesis' subject (*ref: PRAXIS/4/4.1/BD/3475*).

This work was developed at the Astronomical Observatory of the Faculty of Science of the University of Porto (OAUP), being the Ph.D. degree conceded by the Faculty of Engineering of the University of Porto (FEUP). It was oriented by Professor Maria Luisa Cerqueira Bastos at the OAUP, and by Professor Jorge Leite Martins de Carvalho at the FEUP, to whom I thank for their dedication. I would like to thank the other SNAP team members (Sérgio Reis Cunha and Phillip Tomé) for their commitment and dedication to this project. I would like to present a special appreciation to Sérgio Cunha, my brother, for the several discussions we have had on the subjects of this thesis. I thank all those that supported me, with a special mention to my wife Teresa, my brothers and my parents, to whom I dedicate this thesis.

CHAPTER 1

INTRODUCTION

Over centuries, navigation and position determination have been areas of major concern for several civilisations, being these studied and researched world-wide, with direct reflections on society's daily life and progress. Along this process, several technical developments took place, from instruments as simple as a magnetic compass, passing through devices based on angular measurements of elevation angles of space objects (such as the Astrolabe used, for example, in open sea ship location), and reaching today's state-of-the-art technologies based on electronic devices, electromagnetic wave propagation and high-precision mechanics. As in the past, the developments in the navigation field make new applications feasible, and as more precise and accurate navigation systems become, more demanding applications appear and new limits can be drawn. For example, in the XV and beyond centuries, the navigation and timing instruments available allowed a raw determination of latitude and/or longitude, but this poor (as seen with today's eyes) estimation of position made possible for the Portuguese, and others, to navigate across the oceans, discovering new territories (and returning home), and establishing long commercial routes through the seas.

Current navigation systems allow position determination from a few meters down to some centimeters of accuracy, which makes possible not only precise navigation but also the existence of applications like photogrammetry, laser scanning and airborne gravimetry where high levels of precision are required for positioning diverse equipment mounted on an aircraft. With the introduction of the Global Navigation Satellite Systems (GNSS), availability of high precision all-weather positioning all around the globe became a fact, supporting a wide range of new applications like car navigation, fleet management, as well as precise point positioning (static surveys), precise timing applications, and many others.

Regarding current high precision navigation, two navigation systems are immediately recognised as potential instruments for that purpose – the Global Positioning System (or GPS, the most advanced and reliable GNSS at the moment this work was performed) and the Inertial Navigation System (or simply INS).

Due to the importance of these navigation systems and their achievable accuracy, several studies and techniques have been developed in the last two decades. One particular area that has called the attention of many research groups all over the world is GPS carrier phase processing. As shall be shown in this thesis, from the GPS observables, carrier phase measurement is the one that allows the most accurate position determination. But since this measurement does not have an initial reference, there is an unknown integer number of carrier cycles associated with it. This number is denominated Carrier Phase Ambiguity, and its determination (or Ambiguity Fixing) is not a trivial task and it is essential for the achievement of high accuracy positioning. Many ambiguity fixing algorithms have been presented but most of them rely on the variation of the satellite geometry, requiring a considerable amount of time. Others consider special constraints like keeping the GPS antenna at a static position during the ambiguity determination process.

In this thesis, a methodology for real-time L1 ambiguity fixing is presented, considering that the GPS antenna whose position is to be determined has no movement constraints. This method aims at general kinematic applications that require high accurate positions, and has the objective of making the ambiguity fixing process quasi-instantaneous.

In many applications, like airborne altimetry or photogrammetry, the knowledge of the sensors' positions is usually not enough. Their orientation, or attitude, is also required. For example, the measurements of an altimeter mounted on an aircraft are useless if only the positions of the altimeter are known – the direction of the beam is also required.

With this in mind, a navigation system consisting of three GPS receivers and an Inertial Measurement Unit (IMU) was developed. This integrated GPS/IMU system was developed for real-time high accuracy and robust absolute positioning and attitude determination. This system was implemented and installed onboard a Portuguese Air Force aircraft. The characteristics of both devices are somehow complementary, and their integration constitutes an improved and robust navigation system. The GPS results are the main source for absolute positioning, used to estimate the drifting of the IMU sensors. The algorithms developed in this work were implemented in the software component of this navigation system.

Regarding the attitude determination, the three GPS antennas, coherently placed in different spots of the aircraft, were used to provide an unbiased estimate of

the vehicle attitude. For this purpose, a methodology for processing the 3D vector between two vehicle antennas was developed and is presented in this thesis. Again, the determination of the ambiguity values is the central issue, being this achieved quasi-instantaneously. As will be shown, the presented algorithms are suited for real-time processing. One important aspect of this attitude determination method is that there is no need for a static ground reference station. The raw stand-alone absolute position (calculated by one of the onboard receivers) is enough for the determination of the vector between two antennas with a precision under 3 centimeters. In order to increase reliability and reduce the processing time of this method, the constant distance between antennas is used as a constraint, reducing the set of ambiguity vector candidates.

Another aspect that is analysed in this thesis is how the IMU measurements and solutions can be used in processing the GPS data. As will be shown, the benefits are basically in the robustness of the navigation solution, when considering an IMU with identical characteristics to the one that was used. The IMU data processing analysis considering the integration of GPS solutions was not considered in this work.

Throughout this thesis, the methods' descriptions are followed by results obtained from processing real data, most of it gathered in aircraft flights with the GPS/IMU system. The data collected in these flights was processed with the presented algorithms and relevant results are shown in this thesis, illustrating the behaviour and characteristics of the methods.

Also presented in this thesis is the analysis of the applicability of the developed algorithms in other areas than aerial navigation. Results obtained in different land applications are shown, and the main issues of these specific cases are discussed.

1.1 Layout of the Thesis

Following is a brief description of the contents of each of the following chapters.

In chapter 2, the general aspects of the concepts of global satellite navigation and inertial navigation are presented. With respect to the first item, a basic description of the currently existing Global Navigation Satellite Systems (GPS and GLONASS) is given. Also, the European GALILEO, which is still under development, is generally described. More emphasis is given to GPS since most of the work here presented is based on that system. The last section of this chapter presents the basic principles of inertial navigation though a simple 2D example.

A description of the implemented GPS/IMU navigation system is given in chapter 3. Since the developed algorithms use some particularities of the physically implemented system, it was thought to be important to firstly introduce the reader to the composition of this navigation system, its hardware and installation. Two system configurations were used – aircraft installation and land vehicle installation – and both implementations are described.

Chapter 4 presents a more detailed description of GPS, focusing on the GPS measurements, their properties, and the aspects that need to be taken into account for the positioning algorithms. It was intended for this chapter to contain the information required to clearly describe the problem of carrier phase ambiguity fixing. This chapter also provides the nomenclature for the formulations presented in the subsequent chapters. Some of the most well-known ambiguity fixing techniques are described in the last section of the chapter.

The proposed methodology for achieving quasi-instantaneous L1 ambiguity fixing is presented in chapter 5. The developed algorithms that constitute this methodology are described in detail. Different real tests and respective results are presented, together with an efficiency and reliability analysis. The chapter includes the description of the developed technique to precisely determine the vector between two close antennas (rigidly mounted on the same structure), using L1 ambiguity fixing, again requiring just a few seconds of data, and without the use of any ground reference station. The usefulness of this vector as an unbiased estimate of vehicle attitude is demonstrated.

Chapter 6 starts with a deeper analysis on 3D strapdown IMU navigation. It presents the navigation equations for a 3 accelerometer – 3 gyro instrument, together with its main error sources and their characteristics. In the second part of this chapter is presented an analysis of the benefits that GPS processing takes when IMU based data is combined with GPS data. This analysis is based on the characteristics of the installed IMU.

In chapter 7 are described two airborne campaigns where the developed navigation system was used. The first involved 17 test flights over the Portuguese region of the Azores archipelago, and the second campaign consisted of 3 flights in the Portuguese region of Estremadura. In the latter, positioning and attitude determination was performed in real-time. Most of the data used in this work was gathered in these campaigns, and results achieved with the developed algorithms are presented.

Chapter 8 focuses on other domains where the developed algorithms and methodologies were or can be used. Examples of applications performed in urban areas are shown, stressing the main differences to an airborne environment. In the last section, the application of the developed techniques to Local Area Augmentation Systems (LAAS) is discussed.

Concluding remarks are given in chapter 9, with suggestions for future developments of this work. A brief discussion on the near-future perspectives of satellite and inertial based navigation is also presented.

CHAPTER 2

SATELLITE BASED AND INERTIAL NAVIGATION SYSTEMS

In this chapter, a brief presentation of the working principles of the navigation systems that were considered in this thesis is given. These are the Global Navigation Satellite Systems (GNSS) and the Inertial Navigation System.

Regarding the GNSS, more focus will be given to the Global Positioning System (GPS), owned by the United States of America, since most of the work developed is based on this system. The general concept of satellite positioning are presented within the description of GPS.

At the time that the work supporting this thesis was developed, only two GNSS were available – GPS and the Russian GLONASS (GLObal NAvigation Satellite System), but the latter presented a lack of maintenance due to the Russian economical crisis, reducing the system's effectiveness. On the other hand, GPS presented a fully operational satellite constellation and it was the selected GNSS. Nevertheless, since the principles of operation of both systems are very similar (although they present some implementation differences), the developed methodologies and algorithms can be also used with GLONASS, with proper adaptations. The same holds for the European GALILEO, a satellite navigation system that, in the considered period, was still in its development stage. Due to the promising features foreseen for GALILEO, a brief description of this system is also given.

The final section of this chapter focuses on the Inertial Navigation System (INS). A general approach to the principles involved in inertial navigation is shown through an example in the two-dimensional space. The idea is to provide the reader with the aspects that are involved in the processing of inertial sensor measurements for the determination of a navigation solution. A more detailed description of a full three-dimensional Inertial Measurement Unit (IMU) is given in chapter 6.

2.1 Global Positioning System (GPS)

2.1.1 Principle of Satellite Based Navigation

In order to rapidly introduce the reader to the concept of satellite based navigation, a simple example is here presented.

Let us suppose that there is a satellite orbiting around the Earth containing a perfect clock oscillator and a radio transmitter through which it sends a message containing its current clock value. If there is a user located on the Earth's surface also equipped with a perfect clock, and a radio receiver able to decode that message, the time interval obtained by subtracting the satellite clock value, contained in the message, from the user clock value at message reception time, is the time that took the message to travel from the satellite antenna to the user antenna. If the propagation medium is considered to have the same propagation characteristics as vacuum, the distance from the user to the satellite is obtained by multiplying that time interval by the speed of light in vacuum. If the satellite position at the transmission instant is known (for example, if it is included in the satellite message), the user knows that his position lies on a spherical surface with known radius and known center coordinates. Figure 2.1 illustrates this concept, although restricting to the two-dimensional case.

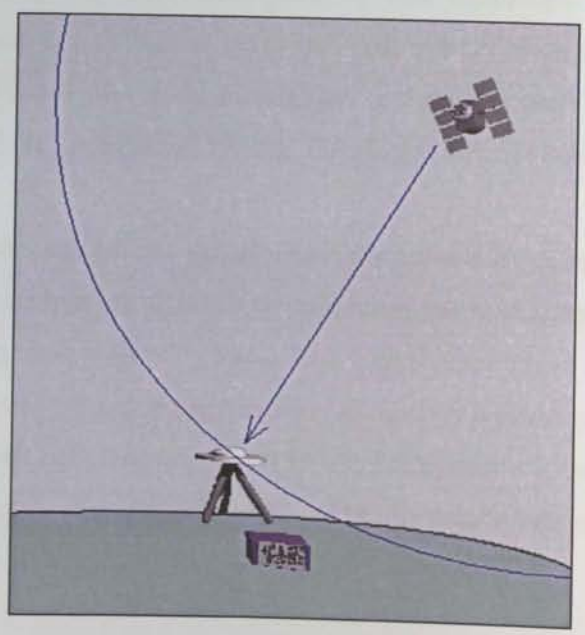


Figure 2.1 – The concept of satellite ranging.

If two more identical satellites are above the horizon, being the radio receiver able to simultaneously collect messages from all satellites, and logging them at the same time instant, then the user can determine his three-dimensional position by intersecting the three distinct spherical surfaces, as is depicted in figure 2.2.

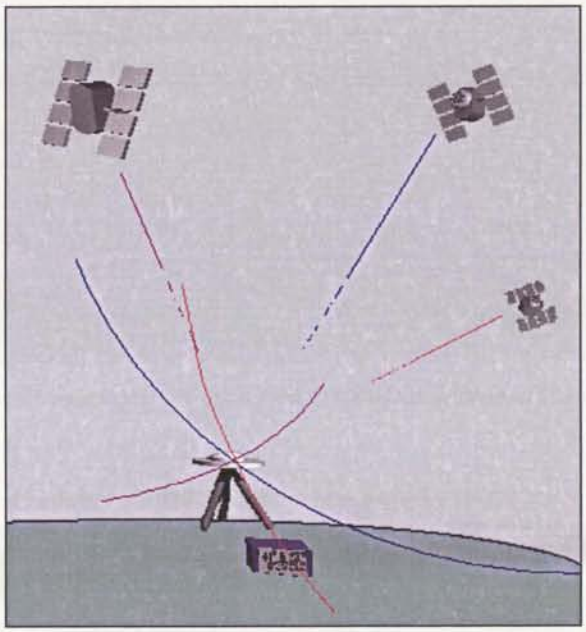


Figure 2.2 – Three-dimensional satellite based positioning.

In reality, the user clock should be far from being perfect since highly accurate clock oscillators are also highly expensive. So, a time bias should be considered in the user clock with respect to the real time. This clock bias is a new variable that must be determined together with the three-dimensional position of the user equipment. So the measurement of a fourth satellite is required in order to have a solvable system of four independent equations with four unknowns. Figure 2.3 provides an illustration of this satellite based positioning concept.

A similar clock bias appears in the satellite equipment but, since they have highly stable oscillators, their clock drift is very low. These biases are previously estimated and uploaded into the satellites. This way, each satellite sends in its messages, along with the transmission instant and its position, its current clock bias.

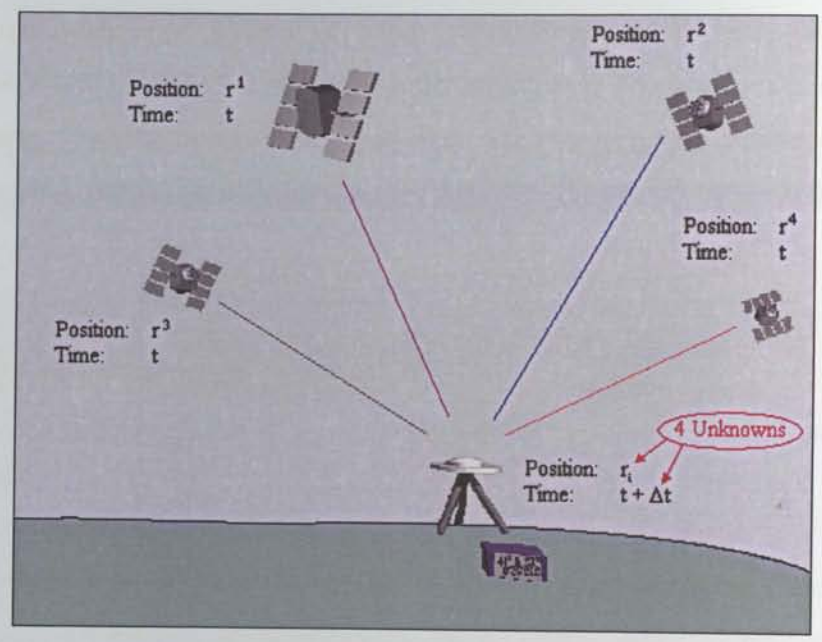


Figure 2.3 – Four satellite measurements are necessary to determine 3D position and time.

It should be pointed that some of the assumptions made in this description to simplify this positioning concept are not completely true. For example, the signal sent by the satellite does not always travel through a vacuum-like medium till it reaches the user equipment. It crosses several layers, like the ionosphere and the troposphere, which contain particles that slow down the signal travelling velocity, and are also responsible for refraction or bending of the signal path. These are errors of the above positioning model that must be considered in order to improve position and time accuracy.

Given the basic concept of satellite based positioning, the following section will describe a real implementation of this concept – the Global Positioning System, or simply GPS.

2.1.2 Brief Description of GPS

The Global Positioning System (GPS) is a satellite based navigation system developed in the 70s by a group of military and civilians, under the ceiling of the Department of Defence (DoD) of the United States of America (see, for example, [ARINC Research Corporation, 1991], [Parkinson and Spilker, 1996], [Hofmann-Wellenhof et al., 1998], [Leick, 1995] and [Seeber, 1993] for more detailed

information on the GPS system). Its main purpose was to provide the means to quickly, accurately and inexpensively determine the three-dimensional position of a point located anywhere in the world, at any time of the day [Hofmann-Wellenhof et al., 1998].

GPS is composed of three distinct segments – the space segment, the control segment, and the user segment.

The basic reference frame used by GPS is the World Geodetic System 1984 (or WGS84), which is an Earth fixed frame with center in the Earth center of mass, with the x axis passing through the intersection of the Zero Geodetic Meridian (formerly Greenwich) with the equator, the z axis pointing to the Conventional Terrestrial Pole (CIO), and the y axis yielding a right-handed system. GPS also uses the WGS84 ellipsoid as the Earth surface model. Its main parameters are given in table 2.1.

Table 2.1 – Parameters of the WGS84 ellipsoid.

Semimajor axis	a=6378137 m
Flattening	f=1/298.257223563
Earth angular velocity	we=7292115e-11 rad/s

GPS also uses its own time reference – GPS Time – which is maintained by a set of high accuracy cesium beam atomic clocks, at control and monitor stations. This time reference is kept within 1 μs of UTC – Universal Time Coordinated reference kept by the United States Naval Observatory (USNO) – modulo 1 second.

2.1.2.1 Space Segment

The space segment consists of a nominal constellation of 24 satellites entitled NAVSTAR (NAVigation Satellite Timing And Ranging), which are deployed on almost circular orbits of about 26561.75 km of semimajor axis and eccentricity generally below 0.02. These satellites are distributed in groups of four, through six equally spaced orbital planes with an inclination of 55° respecting the Earth equatorial plane. Each satellite orbit has a period of approximately 12 sidereal hours. Their spatial distribution was designed to guarantee that at least four satellites have elevations over 15° above the horizon at any location on Earth, at any time of the day [Hofmann-Wellenhof et al., 1998]. Figure 2.4 depicts the NAVSTAR constellation.

The geometry formed by the observed satellites at one site affects the positioning results for that site. The better that geometry is (satellites spread all around the visible sky), the better is the positioning quality, in principle. For that purpose, a factor denominated Position Dilution Of Precision (PDOP) is determined based on the positions of the visible satellites, and whose application indicates the estimated positioning error based on the error that the signals from the satellites are expected to have. Equation (2.1) presents this relation.

$$RMS\ Position\ Error = PDOP \cdot (RMS\ Ranging\ Error) \tag{2.1}$$

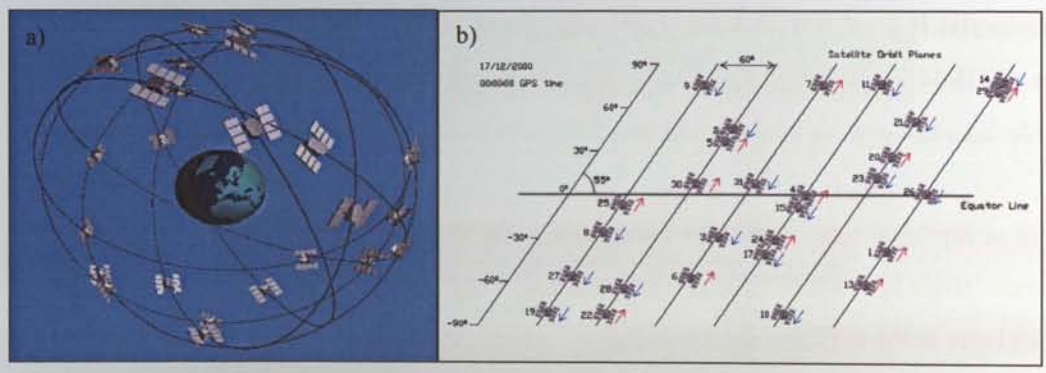


Figure 2.4 – a) GPS constellation. b) GPS satellite distribution in orbital planes (at 00:00 17/Dec/2000).

Each satellite basically contains atomic clocks (rubidium or cesium), a radio transceiver, computers, and auxiliary equipment. The atomic clocks, which reach a long term frequency stability of a few parts in 10^{-13} and 10^{-14} over one day, are used to produce the fundamental L-band frequency of 10.23 MHz from which are coherently derived two sinusoidal carrier waves denominated L1 and L2. L1 is generated by multiplying the fundamental frequency by 154, while L2 uses the factor 120, yielding:

L1 = 1575.42 MHz

L2 = 1227.60 MHz

On these two carrier waves, binary sequences are modulated and the resulting signals are transmitted by each satellite towards the Earth surface so that a GPS receiver can track and decode them. One issue that immediately arises from this exposition is the problem a receiver would have to track and isolate the signal from a specific satellite. Since every satellite is transmitting in the same frequency band, the

receiver would only see a messy sum of all signals sent by the visible satellites. This problem is solved in the GPS system by giving each satellite a particular binary sequence to be modulated in the carrier waves. In fact, each satellite has its own pair of binary sequences, which are called pseudo-random codes since those sequences look like a random set of zeros and ones, although being well determined. What makes it possible for all satellites to transmit in the same frequency band is that the pseudo-random codes of one satellite are very poorly correlated with the respective codes given to all other satellites. This technique is called Code Division Multiple Access (CDMA), in contrast with the Frequency Division Multiple Access (FDMA) technique that requires a larger frequency band [Parkinson and Spilker, 1996].

The two well known pseudo-random codes given to one satellite have distinct characteristics. These codes are known as:

- Clear (Coarse) Acquisition Code (C/A Code);
- Precise Code (P Code).

C/A Code is constituted by a sequence of 1023 binary chips, with a bit-rate of 1.023 MHz, being this sequence repeated every millisecond. This code is modulated on L1 only and it aims for accessibility to civil users, being always transmitted unencrypted. This code is the basis of the Standard Positioning Service (SPS), in contrast to the Precision Positioning Service (PPS) which provides higher precision through the use of the P Code.

P Code is a very long sequence of binary chips (it would repeat itself after slightly more than 38 weeks, but it is reset every week, starting from the beginning of the sequence every Saturday to Sunday transitions), and is transmitted with a bit-rate of 10.23 MHz. Having a higher bit-rate than C/A code, it naturally enables positioning with higher precision. P code is modulated on both L1 and L2 carrier waves, allowing a significant reduction of the ionospheric influence as will be shown later, but, at the moment this work was performed, it was encrypted before being transmitted so that only authorised users could access the Precise Position Service. This encryption is denominated Antispoof (AS) and, instead of being called P Code, this encrypted version is denominated Y Code.

In the following description of the User Segment, it will be shown how a GPS receiver can convert these codes into range measurements.

As explained in the introductory description of satellite based positioning, the satellite position and clock offset are supposedly known by the user receiver. To make

this possible, each satellite also modulates a third binary signal over the same carriers, which contains the information of the satellite orbit parameters, its clock correction, other satellites' positioning information, and other parameters. This message is usually denominated by navigation message. Its signal has a frequency much lower than the previous pseudo-random codes, being sent at a 50 bits per second rate.

A GPS satellite multiplexes the C/A code and P(Y) code in phase quadrature on the L1 carrier (L2 carrier only transmits P(Y) code or C/A code), after both being modulo-2 added to the 50 bps navigation message.

2.1.2.2 User Segment

The basis of the user segment is the GPS receiver whose general functional diagram is depicted in figure 2.5.

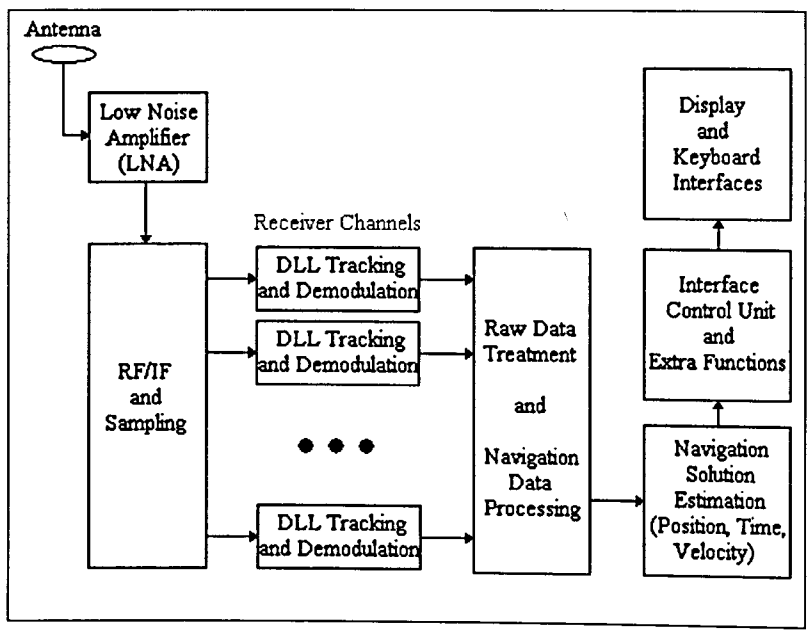


Figure 2.5 – Functional diagram of a general GPS receiver.

Like the GPS satellite, the GPS receiver also contains a clock oscillator, naturally less stable than those of the satellites, for economical reasons. After receiving through its omnidirectional antenna (or hemispherical antenna) the signals transmitted by the visible satellites, the GPS receiver treats them and then tries to isolate each satellite signal. This is performed through the use of different hardware channels working in parallel (in some old receivers some channels were multiplexed

instead of working in parallel). Each channel, at a certain instant, tries to isolate the signal from one specific satellite. This is achieved by generating in the channel the same PRN (pseudo-random number) sequence as the one used by the satellite, and then correlating it with the captured signals. A time-shifting strategy is used till the maximum correlation is obtained, and the satellite signal is then being tracked. This mechanism allows the isolation of one particular satellite signal among the set of simultaneously received signals because the cross-correlation of the PRN sequences of the different satellites is very low.

2.1.2.3 Control Segment

As the name indicates, the Control Segment is the set of equipment and people spread around the Globe that monitor, control and update the Space Segment so that the GPS system is working in proper conditions at all times.

The Control Segment consists of 5 monitor stations, 4 ground antenna upload stations and the Operational Control Center. It began operating in 1985 and it is responsible for:

- Maintaining each satellite in its orbit through small command maneuvers;
- Making adjustments to the satellite clocks and payload as needed;
- Tracking each satellite's data, and generating and uploading the satellite navigation data;
- Commanding major satellite relocations in the event of satellite failure.

2.1.3 Main Error Sources in GPS

In the previous description of the satellite based positioning concept, some simplifications were used. For example, the signal travelling mean was considered to have vacuum-like characteristics. In reality this is not true. The signals cross several layers, like the ionosphere and the troposphere, that contain particles that decrease signal propagation speed, and also deflect their paths. These and other effects are generally treated as error sources to the ideal system, that must be considered and determined in the calculations. The main error sources are:

- Ionospheric effects;

- Tropospheric effects;
- Multipath effects;
- Relativistic effects;
- Deliberately introduced error sources.

Ionospheric and tropospheric errors reflect the effects on signal propagation caused by the presence of particles in those two layers. Multipath is the error introduced by signal reflection on objects close to the receiver antenna, or even on surfaces of the body of the emitting satellite. Relativistic effects are those introduced by the magnitude of the velocity of the satellites with respect to the user equipment. These relativistic effects are minimised *a priori* by slightly shifting the satellite's oscillator frequency. The US DoD has the possibility of introducing some deliberate errors in order to degrade the obtainable accuracy of a SPS user. Selective Availability (or simply SA) is how these deliberate errors are denominated.

A technique, denominated Differential GPS (or just DGPS), is commonly used for elimination or minimisation of some of those errors. This technique considers a second GPS receiver placed (static) in a location whose coordinates are known (this is usually known as the Reference Receiver). The *a priori* knowledge of its coordinates allows the estimation of errors like SA and atmospheric delays. Unfortunately, it is not a trivial task to dissociate these errors. If the reference receiver is placed relatively near the receiver whose coordinates are to be determined (the Rover Receiver), the satellite signals cross the atmospheric layers through similar paths. In other words, if both receivers are relatively near, the atmospheric errors affecting one receiver are approximately identical to those affecting the other receiver. Taking the difference between the corresponding measurements of both receivers, those errors are eliminated (or, at least, minimised) and a more accurate position can be determined for the rover receiver. With this differentiating process, the position of the rover receiver is determined relatively to the position of the reference receiver, but since the coordinates of the latter are known, the absolute position of the former can be determined. The vector between reference and rover positions is called Baseline. It is worth noticing that the correlation between some of the errors on both receivers (like atmospheric and satellite ephemeris errors) is dependent on the baseline length. The longer the baseline is, the less correlated are the errors between receivers.

2.2 Other Global Navigation Satellite Systems

Together with GPS, two more Global Navigation Satellite Systems (GNSS) must be considered – GLONASS and GALILEO, being the former already deployed, and the latter still in its development stage. In this section, these two systems will be briefly described, and some results will be presented from an integration test of GPS and GLONASS data.

2.2.1 GLONASS

The Russian global navigation satellite system is denominated GLONASS (GLObal Navigation Satellite System) and is managed by the Russian Space Forces. This system's description is provided in the GLONASS Interface Control Document [Coordination Scientific Information Center, 1998]. GLONASS provides two types of navigation services – the standard precision (SP) and the high precision (HP) services. The SP service is available world-wide to all GLONASS users and is meant to provide horizontal position accuracy of 57 to 70 meters (with a probability of 99.7%) and vertical accuracy within 70 meters (99.7%). The HP service is only accessible to authorised users. When used in differential mode and when carrier phase measurements are processed, positioning accuracy can be substantially improved.

Like GPS, GLONASS can be divided into three distinct segments – the Space Segment, the Control Segment and the User Segment.

2.2.1.1 Space Segment

The fully deployed GLONASS constellation consists of 24 satellites in three orbital planes. The ascending nodes of the three planes are separated by 120 degrees angles. In each orbital plane 8 satellites are equally spaced with argument of latitude displacements of 45 degrees. The satellite orbits have a radius of about 25510 km and present an inclination angle of 64.8 degrees with respect to the Earth equatorial plane. Each satellite completes an orbit in approximately 11 hours and 15 minutes. The

disposition of the satellites in their orbits is such that at least 5 satellites should be visible from any point in the globe, at any time, and with an adequate geometry.

The GLONASS satellites are equipped with cesium clocks, with daily frequency stability below 5×10^{-13}. With clock corrections being uploaded twice a day, a synchronisation within 15 ns (1σ) for the satellite clocks is maintained.

As in GPS, each GLONASS satellite broadcasts spread-spectrum signals on two frequency bands (L1 around 1.6 GHz and L2 around 1.2 GHz). But, instead of using Code Division Multiple Access (CDMA) like GPS, GLONASS is based on Frequency Division Multiple Access (FDMA), that is, each satellite transmits on its own carrier frequency which is different from the frequencies used by the other satellites (except, in some cases, for satellites in antipodal slots). In GPS, a satellite is identified by the pseudorandom code it is sending modulated in the carrier; in GLONASS, it is the frequency of the transmitted carriers that identify the satellite. The set of frequencies used, in both L1 and L2 bands, by the GLONASS satellites is given through (2.2).

$$\begin{cases} f_1(k) = f_{o_1} + k \cdot \Delta f_1 \\ f_2(k) = f_{o_2} + k \cdot \Delta f_2 \\ f_{o_1} = 1602\ MHz \qquad \Delta f_1 = 562.5\ KHz \\ f_{o_2} = 1246\ MHz \qquad \Delta f_2 = 437.5\ KHz \\ k = -7,...,13 \end{cases} \tag{2.2}$$

Although k is supposed to vary between –7 and 13, due to interference problems the Russian Federation decided that between 1998 and 2005 only values from 0 to 13 would be used (frequencies from 1602.0 MHz to 1609.3125 MHz), and beyond 2005 k could have values from –7 to 6 (from 1598.0625 MHz to 1605.375 MHz).

A GLONASS satellite sends code signals modulated in its two carriers. One signal, accessible to any GLONASS user, provides the GLONASS SP service, having a chip rate of 511 kcps (kilo chips per second) and a code length of 511 chips. This code is repeated every millisecond. For the HP service another code signal is modulated being 10 times faster than the SP signal, but only authorised users can access it.

Providing information of satellite ephemeris and clock readings (together with other data such as the GLONASS almanaque), a navigation signal with low chip rate is also modulated in the carriers. The GLONASS ephemeris is composed of the satellite position at a certain instant, together with its first and second derivatives. The position of the satellite at the instant of interest (when processing GLONASS data) can be determined through, for example, the 4^{th} order Runge-Kutta method.

GLONASS positioning is always referred to the PZ-90 geocentric reference system. This is based on an Earth-Centered Earth-Fixed ellipsoid with semimajor axis of 6378136 meters and a flattening of 1/298.257839303. For example, the broadcast ephemeris of the GLONASS satellites are given in PZ-90 coordinates. Also, GLONASS has its own time system which is equal to the UTC time plus a constant offset of 3 hours. GLONASS time is incremented by 1 second jumps whenever UTC is incremented, so there is no leap second difference between both time systems.

2.2.1.2 Control Segment

The Control Segment is composed by the System Control Center and a network of Command and Tracking Stations spread through the Russian territory. Its function is to monitor the status of the GLONASS constellation, to correct clock and orbital parameters, and to upload information into the satellites such as the navigation message.

The Control Segment holds a high precision hydrogen atomic clock which establishes the reference for the GLONASS time system. Through laser ranging devices, the tracking stations periodically calibrate the GLONASS ranging data (laser reflectors were mounted on each satellite for this purpose).

2.2.1.3 User Segment

The User Segment is based on GLONASS receivers which are able to track and decode the signals sent by the satellites and, after processing the resulting data, they provide the user with position, velocity and timing information.

Unfortunately, and due to maintenance difficulties, during the period of the work here presented, the GLONASS constellation was very reduced in the number of effectively operating satellites. Since there was not the desired satellite maintenance, a significant percentage of this constellation became unusable, greatly reducing the usefulness of this global navigation system in that period. For example, the NAGU (Notice Advisory to GLONASS Users) published by the Coordination Scientific Information Center (CSIC) under the Russian Federation Ministry of Defence, in the 25th of June 2002, presents only seven satellites as fully operational.

Nevertheless, in the beginnings of 1999 and in the scope of this work, some static tests combining GLONASS data with GPS data were performed for the determination of double difference wide lane ambiguities on a long baseline (151 km). The algorithms used to process this data (from GPS and GLONASS) are presented in chapter 5. A comparison of the obtained positioning precision, using GPS only, GLONASS only and GPS/GLONASS combination, is presented in figure 2.6 where the difference to a raw estimate of the antenna's position is plotted.

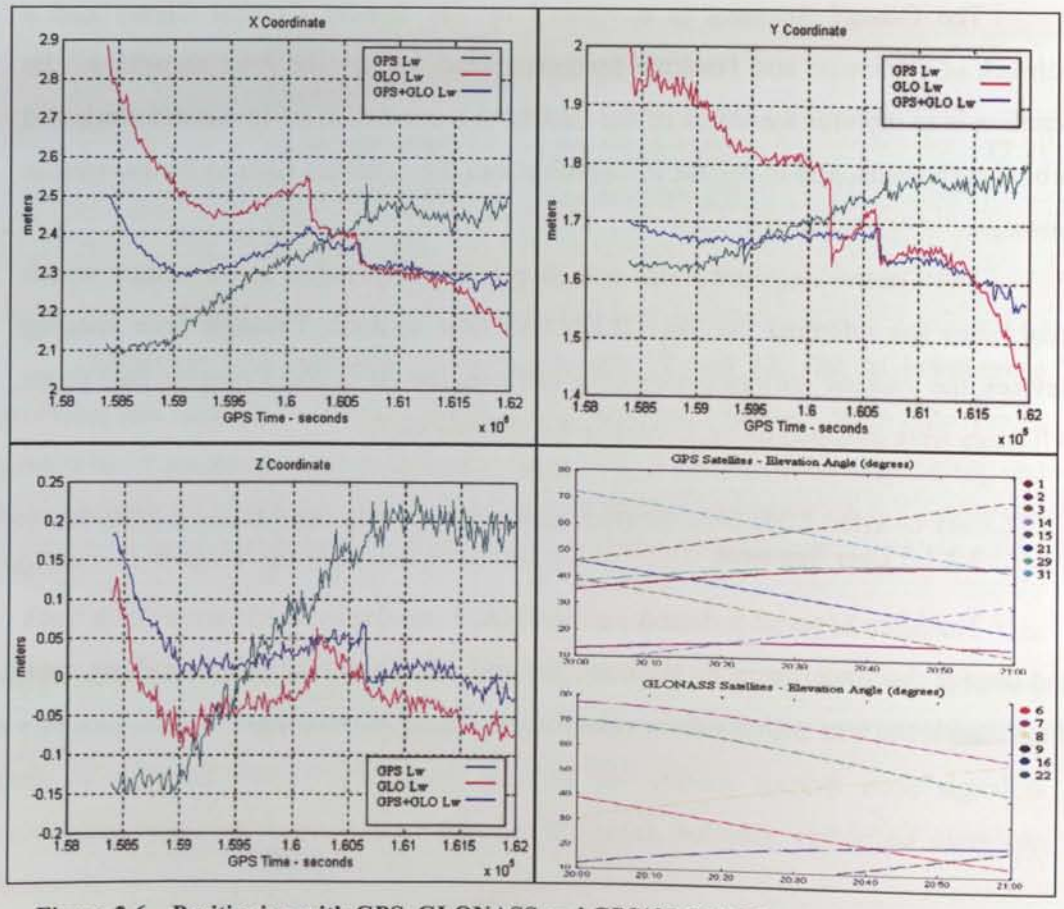


Figure 2.6 – Positioning with GPS, GLONASS and GPS/GLONASS data, in a long baseline.

For the example on figure 2.6, the determination of the double difference wide lane ambiguities was based on the phase minus code combination presented in equation (5.5), chapter 5. GLONASS data processing algorithms were developed taking into account the frequency difference between satellite signals.

2.2.2 GALILEO

GALILEO is the European state-of-the-art global navigation satellite system, which is still under development, and that will provide world-wide satellite navigation and timing services. It is meant to offer high quality positioning services with adequate reliability and high availability. It also aims to satisfy the requirements of mass-market, professional, safety-of-life and security related applications. Objectives such as independence from other navigation systems (but with the possibility to operate integrated with other systems like GPS) and navigation and timing services with global Earth coverage (and also near-Earth space coverage) were considered as development basis of GALILEO.

Europe has already given an important contribution to global satellite-based navigation with the EGNOS programme, part of the first generation of Global Navigation Satellite Systems (GNSS-1). The EGNOS programme consists of the augmentation of the GPS and GLONASS systems, mainly to improve transport applications (land, sea and air) in the European region and beyond. It is based on the transmission, from geostationary satellites, of ranging signals with GPS and GLONASS integrity data and differential corrections.

Since EGNOS is not a completely independent navigation system, which does not depend only on European control, the European Community Council decided to launch the development of GALILEO, an independent satellite-based system, being this the European contribution to the next generation of Global Navigation Satellite Systems (GNSS-2). Some details on the GALILEO system can be found in [Benedicto, 2001], [Benedicto and Ludwig, 2001], [Hein et al., 2001] and [Dellago et al., 2001], for example.

2.2.2.1 GALILEO Services

Being GALILEO a global navigation satellite system, it is being designed to provide world-wide positioning and timing services. But, besides those services, GALILEO will also provide other useful value added services. Different policies will be considered regarding the accessibility to these services, being some of them available anywhere and free of charge, and others being restricted to some users and with some costs associated.

The predicted GALILEO services are defined in the following text.

Open Service

The Open Service provides positioning, navigation and timing signals that can be freely accessed. This service is suitable for mass-market navigation applications such as fleet management and car navigation. The timing service (which is provided in UTC) is suitable to many applications requiring time synchronisation such as computer networks. Table 2.2 presents the expected main performance characteristics of this service.

Table 2.2 – Open Service characteristics.

Receiver Types	Single and Dual Frequency
Receiver Integrity Computation	No
Position Accuracy (95%)	Single Freq.: H - 15m V - 35m
	Dual Freq.: H - 4m V - 8m
Timing Accuracy	50 nsec for dual freq.
Certification and Liability	None
Availability	99% - 99.9%

Commercial Service

This service is basically the Open Service with added value. Through this service, encrypted signals that are sent from the satellites become accessible, allowing positioning up to the sub-meter accuracy in differential applications. A signal dedicated to the integration of GALILEO and wireless communication networks (GSM/UMTS) also becomes available.

Safety-Of-Life Service

The Safety-Of-Life service has identical characteristics to the Open Service for a dual frequency receiver, except that an integrity computation is now performed and its result available to users, making this an highly reliable service. The

performance of this service is compatible with the Approach with Vertical Guidance (APV-II) requirements defined by the ICAO SARPs (International Civil Aviation Organization – Standards And Recommended Practices). It is being studied the possibility to provide the Safety-Of-Life service through one single frequency, providing also a detailed model of the ionosphere, achieving with only one frequency a similar performance as the obtained in dual-frequency mode.

The integrity analysis for this service will take into account regional certification issues and liability constraints.

Public Regulated Service

This is a service which is provided on dedicated frequencies, and it aims public applications devoted to European and National Security, such as police, civil protection, law enforcement, emergency services, and others. Some vital sectors are also aimed by this service like some energy, transports and telecommunication applications. Economic and industrial activities of strategic interest for Europe are also to be considered by this service. This is to be a highly robust service, offering high resistance to interference and jamming.

The performance characteristics of the positioning and timing provided by this service are similar to the presented for the Safety-Of-Life service, being the former implemented with high signal robustness.

Navigation Services for Local Components

These are based on a local station providing differential corrections which would lead single frequency users to achieve sub-meter accuracy. Also, with receivers using the triple-carrier technique (TCAR – see, for example, [Vollath et al., 1998]), sub-decimeter accuracy could be met. Local integrity monitoring and warning mechanisms are also to be implemented.

Also conceived is the intention to easily integrate this local station with GSM/UMTS-assisted positioning, which could allow position determination in difficult environments (difficult when considering current satellite navigation signals), such as urban canyons and indoor applications.

Search and Rescue Service

The GALILEO satellites are equipped with a Search and Rescue transponder that supports the provision of an enhanced COSPAS-SARSAT search and rescue service (COSPAS-SARSAT is an international satellite system for search and rescue). A user equipped with a COSPAS-SARSAT beacon can activate this beacon sending a distress call to the satellites. The satellites down-link this distress call to a ground station which will route the message to a proper rescue center where it will be processed. After processing the message, the rescue center sends back to the GALILEO system an acknowledgement message which will be routed to the satellites and from there to the originator of the alarm.

The COSPAS-SARSAT parties are coordinating the implementation approach of this service.

Navigation-Related Communication Services

Although the basis of this implementation is the combination of GALILEO with existing communication networks (wireless, satellite-based, and others), it is being studied the possibility of implementing onboard communication devices in the GALILEO satellites. This service aims to applications requiring global, highly available and reliable position reporting. This communication is based on the transmission of short messages from the user to a service center and vice versa.

2.2.2.2 GALILEO Components

The GALILEO system can be divided into three distinct components – the Global, the Regional, and the Local components. These will now be briefly described.

The Global Component

As in the case of GPS and GLONASS, the global component is divided into three segments – the Space Segment, the User Segment, and the Control Segment.

The space segment is to be constituted of a constellation of up to 30 satellites in Medium Earth Orbit (MEO), providing adequate coverage all around the Earth globe, making widely available the services GALILEO is supposed to supply. Those satellites will be divided in three orbital planes, in orbits with an altitude of 23616 km, each plane containing 9 satellites (three satellites will be used as spares – one spare

per plane). The planes are supposed to have an inclination of 56 degrees over the Earth equatorial plane, and the satellites will complete $1+2/3$ revolutions per day.

Each satellite will broadcast five navigation signals. Each signal is composed of one or two ranging codes, and navigation data. Some signals will also include integrity, commercial and search-and-rescue data. The ranging codes and the data can be broadcasted in an encrypted format in order to limit the access to certain services. There are four frequency bands allocated to the GALILEO system, being the five signals modulated in four carriers, each one in its frequency band (the possibility of using only three carriers is also being studied). The frequency bands are the following:

- 1164 MHz – 1215 MHz (E5/L5): an open signal in this band will support the Open Service and, possibly, the Safety-Of-Life service will be also placed in this band;
- 1260 MHz – 1300 MHz (E6): this band will support the Public Regulated Service and the Open Service (commercial-encrypted) as well;
- 1559 MHz – 1563 MHz (E2): a signal for the Public Regulated Service is to be placed in this band;
- 1587 MHz – 1591 MHz (E1): this is dedicated to the Open and Safety-Of-Life Services.

The previewed chip rates for the signals are between 2-4 Mcps (mega chips per second) for the E1 and E2 carriers, 5-10 Mcps for the E6 carrier and 10-20 Mcps for the E5 carrier. The data rates are expected to be as high as 1000 bps (bits per second), which is high enough to transmit the navigation data together with the data inherent to the various services provided by the GALILEO system. It should be noticed that GPS uses a data rate of 50 bps. With the 1000 bps of GALILEO, the navigation message can be sent more frequently, reducing the time to first fix (and the reacquisition time) of the receivers, compared to GPS.

The User Segment is based on the GALILEO receivers which will be prepared to receive and decode the signals sent by the GALILEO satellites, according to the services they are supposed to access. Also, there will be receivers capable of directly receiving differential corrections from local stations. It is expectable to find receivers that will track signals from more than one global navigation satellite system. Like in the case of GPS+GLONASS receivers, it will be interesting to have, for example,

GALILEO+GPS receivers to which the satellite availability is supposed to be very high, permitting position determination in situations (such as urban canyons) where it would be hard or impossible with only one of the systems.

The Control Segment is constituted by several ground stations, spread world-wide, with the responsibility of controlling the satellite orbit and clock parameters. Also, some stations have as objective the determination of the system integrity, being this up-loaded into the satellites.

The Control Segment is responsible to maintain the GALILEO system at its best operational conditions, providing the various GALILEO services within the specified level.

The Regional Component

This is an augmentation to the global component where, through ground stations spread in a certain region, the integrity data to that particular region is computed. Preferring this integrity computation to the one provided by the global component, the former can be routed to a GALILEO ground station that will then send the produced data to the satellites.

The Local Component

For applications where, in a certain area, the performance of the global component is not enough (higher accuracy, integrity, better signal acquisition/reacquisition time), there is the possibility of installing local equipment that will locally improve the system performance. These extra services can be, for example:

- Differential positioning, leading to more accurate positions;
- Local integrity monitoring with very short time-to-alarm (within 1 second (for comparison, the time-to-alarm for the Safety-Of-Life service is estimated to be around 6 seconds));
- Extra data (corrections, maps, databases);
- Additional signals from pseudolites;
- Additional positioning information from the integration with GSM/UMTS positioning calculations;
- Local communication channels (from GSM/UMTS, for example).

The GALILEO signal design takes into consideration the possibility to support the operation with local components, allowing an easier and cheaper way of local augmentation of the global component, resulting on an improvement of the overall performance.

Being still the GALILEO system in its development stage, and being estimated that it will be working at its fullest in the year 2008, it is a very promising satellite-based navigation system, constituting a worthy alternative to the current GPS and GLONASS systems. More than that, huge improvements in this area are to be expected with the combined systems (GALILEO+GPS receivers, for example) where satellite availability will increase tremendously, allowing positioning in areas with plenty of obstacles, improving, for example, navigation in urban areas.

2.3 INERTIAL NAVIGATION SYSTEMS

Inertial navigation is the most common navigation solution for air and sea vehicles. It is based on an equipment denominated Inertial Navigation System (INS) which is able to measure and process the accelerations sensed by the vehicle. The accelerations can be integrated yielding the vehicle velocity, and with further integration its position is determined. The principle of inertial navigation is briefly presented hereafter.

2.3.1 PRINCIPLE OF INERTIAL NAVIGATION

Starting with a situation where only the horizontal one-dimensional displacement of a vehicle is considered, the vehicle's position can be determined at any instant if:

- the accelerations resulting from its movement (with respect to the referential of interest) can be measured;
- its initial position and velocity are known.

Simply by integrating the measured accelerations, from the initial time instant to the current time, the current velocity can be determined. If the accelerations are integrated twice, then the position is obtained.

The accelerometer is the device that measures acceleration but, unfortunately, it cannot distinguish the accelerations resulting only from the movement of the vehicle from other accelerations, such as gravitational attraction. Another aspect is that it can only measure acceleration with respect to the inertial reference frame. If the frame of interest is moving with respect to the inertial reference frame, extra accelerations will be sensed in the accelerometer. This fact led to two different types of implementations of inertial systems - Strapdown and Gimbaled Inertial Navigation Systems. On a strapdown inertial system, the sensors (accelerometers and others, as shown below) are rigidly coupled with the vehicle's structure. In gimbaled inertial systems, the sensors are placed on a gimbaled platform which is responsible for

maintaining constant (regarding the inertial reference frame) the directions of the sensors' sensitive axes. In this discussion, only strapdown systems will be considered.

The physical realisation of an accelerometer leads to measurements containing noise, biases, and a fixed sampling frequency. It is typical for the inertial navigation solutions to drift with time from the true value due to the integration of noise and biases. The fixed sampling frequency limits the dynamics of the vehicle for which this process is valid, and it has to be set regarding the applications where it is supposed to be used. On the following analysis, ideal accelerometers will be considered, that is, the measurements are accurate and continuous in time.

Considering now the example presented on figure 2.7, let us suppose that a vehicle is describing a trajectory near the surface of a perfect sphere, always with constant longitude, and, for simplicity, let us consider that the sphere has no movement (either of translation or rotation) relatively to the inertial reference frame.

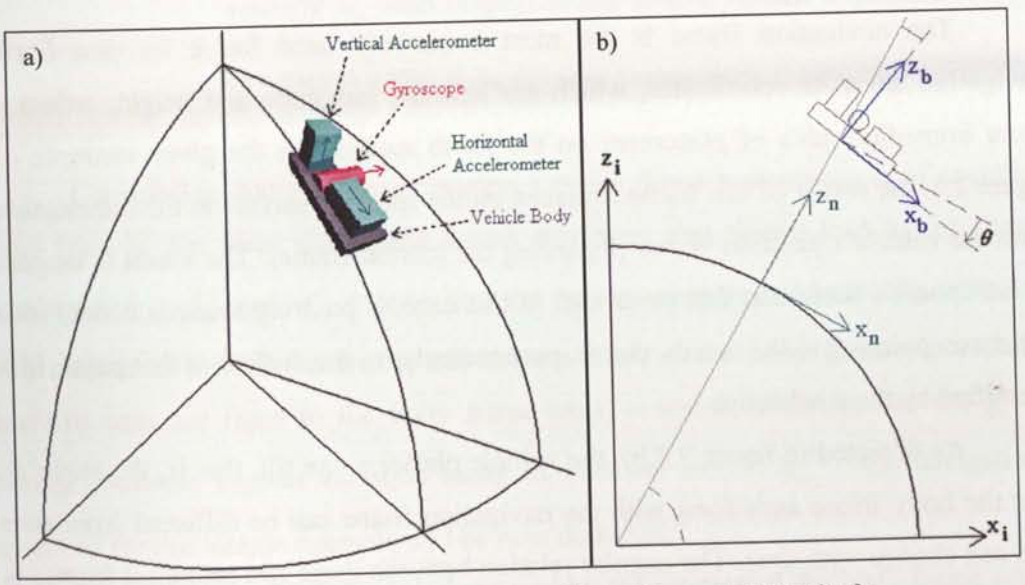


Figure 2.7 – Example of vehicle travelling with constant longitude.

This can be viewed as a two-dimensional problem since the vehicle draws a trajectory on a plane – the plane containing the meridian of constant longitude. Figure 2.7.b) represents this aspect. Since there are two orthogonal displacement components, two accelerometers must be used having their sensitive axes placed in orthogonal directions.

In inertial navigation, the choice and definition of reference frames is essential since accelerometer measurements, which are evaluated with respect to the inertial

frame, must be transformed to the frame of interest. For the example of figure 2.7, three reference frames will be considered - the inertial frame, the body frame and the navigation frame.

As the name says, the inertial frame is a set of three orthogonal axes that, for the specific application, has no absolute movement. For near-Earth applications it is usually considered that this is a frame whose axes are non-rotating with respect to the fixed stars. In the case of the current example, the inertial frame was selected to have its center at the center of the sphere, with the z axis through the North pole and the x axis intersecting the sphere's equator and the referred meridian. It is identified by the i subscript in figure 2.7.b).

The body frame consists of a set of orthogonal axes attached to the vehicle (and, subsequently, to the onboard sensors). The accelerometers' sensitive axes have their directions fixed regarding this body frame. In figure 2.7.b), the body frame is represented by the b subscript.

The navigation frame is the most commonly used frame for near-Earth navigation since its coordinates, which are latitude, longitude and height, reflect a more immediate idea of placement on the Earth surface. In the given example of figure 2.7, the center of this frame is placed on the sphere's surface at the intersection with the vehicle's position vector (regarding the inertial frame). The x axis is tangent to the sphere's surface at that point and, in this case, is pointing towards South, with the z axis pointing to the zenith, that is, perpendicular to the surface at that point. It is identified by the n subscript.

As depicted in figure 2.7.b), the vehicle platform can tilt, that is, the angle θ that the body frame axes form with the navigation frame can be different from zero and can change with time. The angular relation between these two reference frames is usually called the vehicle's attitude (which in the example is reduced to only one angle, but in a three-dimensional case consists of a set of three angles). It then becomes necessary to determine that angle θ for the accelerometer measurement integration to have any sense (the direction regarding the acceleration measurements must be known at every time instant). In order to measure this angle, a device called gyroscope (or, for simplicity, gyro) must be also installed. A gyroscope usually measures variation of angular displacement around an axis (its sensitive axis), also requiring integration (and knowledge of its initial conditions) for the determination of the absolute angular value. In the case shown in figure 2.7, the gyro is fixed in the

vehicle with its sensitive axis orthogonal to those of the accelerometers. Again, only an ideal gyro will be considered for now, disregarding noise and gyro drift (which is one of the predominant sources of error in most inertial navigation instruments). It should also be pointed that the gyro measurements refer to the inertial frame since any rotation regarding that frame is sensed by this device.

Let us now view the equations inherent to this example and how the measurements given by those three devices can be used to determine the navigation solution (position, velocity and attitude) of the vehicle, at any time instant.

The following nomenclature will be used for the quantities being presented in the subsequent equations:

X_a^b - where X is the quantity being expressed, the subscript a is the frame to which the term X is considered, and the superscript b is the frame where the term X is expressed (for example, the vehicle velocity v_x with respect to the sphere surface expressed in the navigation frame is $v_{xi}^{\ n}$).

Considering that the accelerometers provide direct measurements of specific force (that is, the force considered on an unit mass that would lead to the same acceleration) – f_{xi}^b and f_{zi}^b (notice that the accelerometers sense velocity changes with respect to the inertial frame, but express them in the body frame since their sensitive axes are fixed to the body frame axes) – and considering that the gyro directly measures angular variation along its sensitive axis – $\omega_{y_i}^{\ b}$ – the navigation equations for this simple example will be now deducted.

The variation of the θ angle is caused by the rotation of the body frame with respect to the inertial frame ($\omega_{y_i}^{\ b}$) and by the rotation of the navigation frame again with respect to the inertial frame. Equation (2.3) shows this relation where R is the radius of the sphere.

$$\dot{\theta} = \omega_{y_i}^{\ b} - \frac{v_{xi}^{\ n}}{R + z_n^n} \tag{2.3}$$

Regarding the θ angle, the decomposition of the specific force values from the body frame to the navigation frame, as equations (2.4) indicate, becomes trivial.

$$\begin{cases} f_{xi}^{n} = f_{xi}^{b}\cos(\theta) - f_{zi}^{b}\sin(\theta) \\ f_{zi}^{n} = f_{xi}^{b}\sin(\theta) + f_{zi}^{b}\cos(\theta) \end{cases} \tag{2.4}$$

The relation between the vehicle's acceleration and the specific force values is almost direct, but two points must be considered. Firstly, since the navigation frame is not a static frame (regarding the inertial frame, to which the measurements are sensed), Coriolis components appear. Secondly, the gravitational attraction force induced by the sphere's mass in the vehicle needs also to be considered. In this case, the gravitational force will only be considered as acting in the z axis direction of the navigation frame (the local vertical), since an ideal and homogeneous sphere is being used in this example. It is also supposed that a known model of the gravitational attraction force (g_z) exists with enough precision. Equations (2.5) show the relation between accelerations, specific forces, Coriolis components and gravitational force.

$$\begin{cases} \dot{v}_{xi}^{n} = f_{xi}^{n} + \dfrac{v_{xi}^{n} \cdot v_{zi}^{n}}{R + z_{n}^{n}} \\ \dot{v}_{zi}^{n} = f_{zi}^{n} + g_z - \dfrac{v_{xi}^{n^2}}{R + z_{n}^{n}} \end{cases} \tag{2.5}$$

Since there are till now 6 unknowns and 5 equations, one more equation must be considered for the system to be solvable. Equation (2.6) presents the obvious relation between the z axis coordinate and its variation, being this the remaining equation.

$$\dot{z}_{n}^{n} = v_{zi}^{n} \tag{2.6}$$

Equations (2.3) to (2.6) form the navigation equation system that describes the simple situation of figure 2.7. It can be seen that plenty of simplifications were taken, but they must be considered when studying the motion of a vehicle near the Earth surface. The Earth is not a perfect sphere, its mass is not homogeneously distributed, it has a rotation motion around its polar axis, the problem cannot be reduced to the two-dimensional space, and the measurements taken by the sensors have errors associated. In chapter 6, a deeper analysis of inertial sensors will be presented.

CHAPTER 3

THE NAVIGATION SYSTEM

As mentioned in the chapter 1, the developed work had direct insertion in some practical applications. One such application was the development and implementation of a navigation system integrating three GPS antennas/receivers and one IMU. This was the main focus of the Portuguese project SNAP (*Sistema de Navegação Aérea de Precisão e longo alcance,* meaning – long range high precision aerial navigation system), within which the work here presented was inserted. Its objective was to verify that, with the integration of GPS and a low cost IMU, a navigation system with a performance similar, or even better, to that of a highly expensive high grade INS could be achieved. This navigation system was installed onboard a Portuguese Air Force aircraft and several test flights were performed.

The implemented GPS/IMU system is suitable for many applications involving airborne sensor positioning and orientation determination. The developed methodologies presented in subsequent chapters will be better illustrated if the characteristics of this navigation system and the aspects behind these applications are firstly presented. Therefore, this chapter provides a general description of the requirements inherent to this sort of applications, focusing the details that are connected with the strategies used in the developed algorithms.

In chapter 7 a more detailed description of the performed flight campaigns will be presented, including the results obtained with the developed methodologies.

3.1 AIRBORNE SURVEYS

Nowadays, the use of aircrafts to quickly survey large areas, or areas not easily accessible by land, is becoming more and more common. Laser profiling/scanning, aerial imaging, photogrammetry and airborne gravimetry are examples of these applications. Each survey has its own objectives and characteristics, and depending on these, the nature of the instruments installed onboard the aircraft may be diverse. For example, the photogrammetric camera is the main equipment for photogrammetry surveys, as for gravimetry surveys the gravimeter (or a high quality INS) is the base instrument. It is usual in airborne surveys to have several other instruments such as altimeters and pressure sensors.

What is common to almost all airborne applications is the requirement of knowing the position and orientation of the employed instruments, at each epoch, so that their measurements can be correctly interpreted. Altimeter measurements (distance from the aircraft to a reflection point in the ground) make no sense if the aircraft attitude regarding the ground surface is not known. Also, the gravimeter position and orientation (and also the aircraft second order dynamics) must be known in order to map the Earth gravity values of the surveyed area.

It is then necessary to install a navigation system able to determine the three-dimensional position of the aircraft and its attitude. This is where GPS and INS play their role. The INS, with its accelerometers and gyroscopes, allows the determination of the angular displacements of the aircraft (and its sensors) with respect to the selected frame (usually the navigation frame). It can also determine position variations. Since the aircraft flies at relatively high velocities, the high sampling rate the INS systems usually have allows a high definition over ground. As an example, for a flying speed of 250 km/h, a GPS receiver sampling at 1Hz would generate positions about 70 meters apart. With an INS sampling at 100Hz, for instance, the distance between two consecutive positions would be about 70 centimeters. The use of GPS can lead to aircraft positioning with an absolute precision up to sub-decimeter level, limiting the drifting problems inherent to an INS system. Another measure to compensate gyroscope drifting is to equip the aircraft with more than one GPS antenna, placed along its structure, in order to generate an unbiased estimate of the aircraft attitude. For example, with two antennas placed in the main body (one in the

front and another in the back), the pitch and yaw angles can be estimated, and with a third antenna mounted on a wing the roll angle can be computed (although wing flexure and vibration can introduce errors in this estimation). Figure 3.1 presents the graphical definition of these three angles.

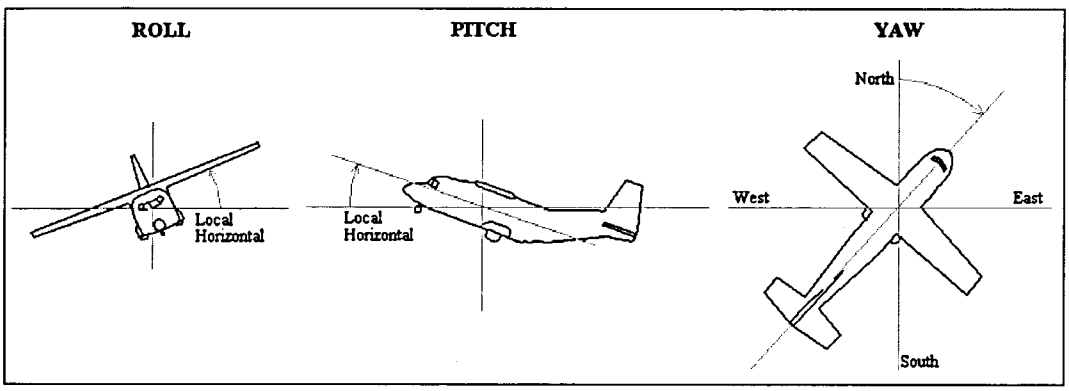


Figure 3.1 – Roll, pitch and yaw angles.

An important aspect to be considered in airborne surveying is efficiency. Since flight costs have a significant weight on the budget, it is required that the survey objectives are fulfilled using the minimum possible flight time. Therefore, in many applications, it is important to know the aircraft navigation solution during the flight, instantaneously. This way, it becomes possible, for example, to flight with high accuracy (up to the pilots, or aircraft instruments, capabilities) previously defined profiles, to detect locations of interest (through the sensor measurements) on the spot and immediately re-survey them, or to repeat the same profile on several occasions. In order to make this possible, real-time data processing must be performed. The data collecting algorithms and the processing algorithms must be designed to provide navigation solutions as soon as data is available.

As mentioned in chapter 2, to achieve high precision with GPS measurements it is necessary to have the data from a stationary GPS receiver (the reference receiver) located at a known location and not too far away from the rover receiver. This processing method is generally called Differential GPS (DGPS). To enable high accuracy real-time processing, the data from that reference receiver must be sent to the aircraft through a communication link between the reference station and the aircraft. The performance of this radio link is a key issue to achieve higher accuracy

in real-time applications since the GPS solution gets rapidly degraded in the absence of the data from the reference receiver.

The growth of airborne applications and the need to position and orient the onboard sensors motivated the development of a GPS/INS navigation system, on which the work presented in this thesis was included. This navigation system was implemented on a Portuguese Air Force aircraft and test flights were performed. The following section describes the navigation equipment used and its installation.

3.2 Implementation of an Airborne GPS/INS System

A GPS/INS navigation system was developed and installed on a Portuguese Air Force aircraft, a CASA 212. The system main components were:

- an Inertial Measurement Unit (IMU), a LN200 from Litton;
- three dual frequency GPS receivers, two Trimble 4000 SSi and one Ashtech Z-12;
- an industrial PC, Pentium MMX 200MHz, from BSI, with Microsoft Windows NT4.0 installed;
- a communication radio, the DGR-115HWW from Freewave Technologies.

Figure 3.2 shows the CASA 212 aircraft, and figure 3.3 presents the equipment placement on the aircraft.



Figure 3.2 – The CASA 212 aircraft used to test the GPS/INS system.

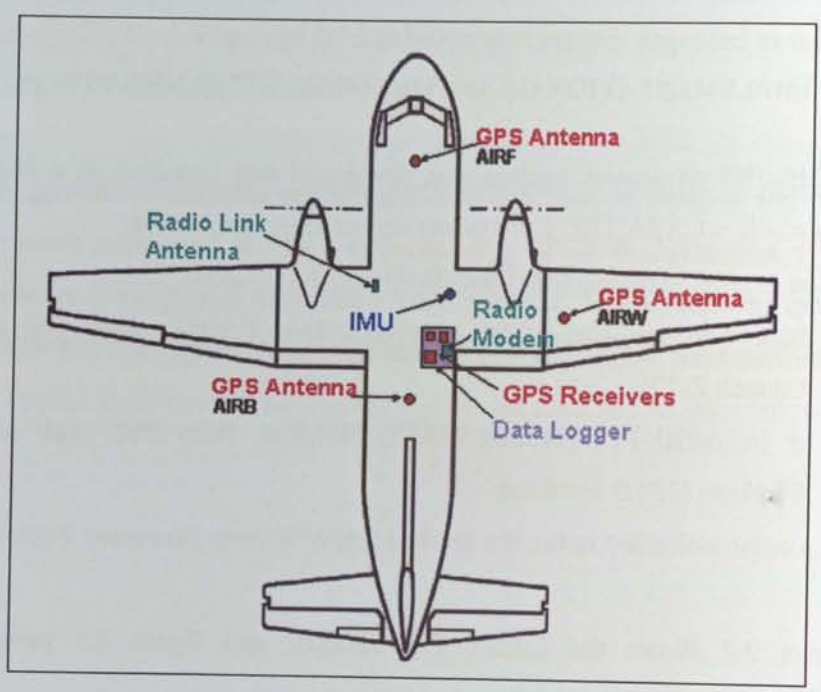


Figure 3.3 – Equipment distribution in the aircraft.

The inertial sensor, the LN200 IMU, is composed of three silicon accelerometers and three fibre optics gyros (FOG), all disposed in three orthogonal axes. It provides, through a RS485 connection, the raw measurements from its sensors (3 specific force measurements and 3 variations of angular velocity), its inner temperature (since accelerometers are very sensitive to temperature, its variation must be compensated), and a time tag generated by the IMU for those measurements. The chosen output rate for these measurements was 100Hz. As can be immediately observed, proper time tagging of this data is essential to a correct determination of the navigation solution. The position and attitude of the aircraft must refer to the instant the data was sampled. Also, considering a combined processing of IMU and GPS data, the time system to which the IMU data is tagged must have a known relation with GPS time. Since the GPS receivers used had the 1PPS (one pulse per second) capability, that is, they generate a TTL 1Hz pulse synchronised with the GPS time (with an error of about 0.5 μs), a computer card was included to capture that pulse and generate an hardware interrupt in the microprocessor. Also, a Microsoft Windows NT device driver was developed to register the PC clock offset and drift at the interruption instant. This way, the software responsible for time tagging the IMU data could register the PC clock and apply the correction to GPS time. It was necessary to perform this operation at device driver level and not at application level because, in

the latter, the operating system does not immediately pass CPU control to the application capturing the interrupt, and an ambiguous delay would affect IMU data recording. (Later, this solution was replaced by the use of a PC card containing a real-time clock that could be slaved by hardware to an external reference - in this case, the 1PPS signal was used. For a more detailed description refer to [Tomé, 2002].)

Figure 3.4 shows a picture of the Litton LN200, and table 3.1 presents its main characteristics (some of which will be later explained in chapter 6).



Figure 3.4 – The Litton LN200 Inertial Measurement Unit.

Table 3.1 – Litton LN200 main characteristics.

Physical	
Weight	700 g
Size	8.9 cm by 8.5 cm
Power	10 W
Fiber Optic Gyros	
Bias Repeatability	1 °/hr to 10 °/hr, 1σ
Random Walk	0.04 to 0.1 °/√hr
Scale Factor Stability	100 ppm, 1σ
Bias Variation	0.35 °/hr 1σ, with 100 sec correlation time
Silicon Accelerometers	
Bias Repeatability	200 μg to 1 mg, 1σ
White Noise	50 μg/√Hz
Scale Factor Stability	300 ppm, 1σ
Bias Variation	50 μg 1σ, with 60 sec correlation time
Operating Range	
Angular Rate	± 1000 °/sec
Acceleration	± 40 g

The Trimble 4000 SSi is a dual frequency receivers with 9 channels for each L1 and L2 carriers. In order to reduce the influence in the aircraft aerodynamics, proper kinematic aeronautical antennas were installed. Both Trimble antennas were mounted on the main body of the aircraft, one in the back and the other in the front, separated from each other by 5.224 meters. Through the rest of this thesis and to

simplify the description, these antennas/receivers will be designated by AirBack (or simply AIRB) and AirFront (AIRF).

The Ashtech Z-12 is a 12 channel, dual frequency receiver. Again, an aeronautical antenna was used and it was placed on the right wing of the aircraft (distanced from AIRB by 4.798 meters, and by 5.510 meters from AIRF). This antenna/receiver will be addressed as AirWing (or AIRW).

Figure 3.5 shows the pictures of the GPS receivers, and in tables 3.2 and 3.3 are their main characteristics.

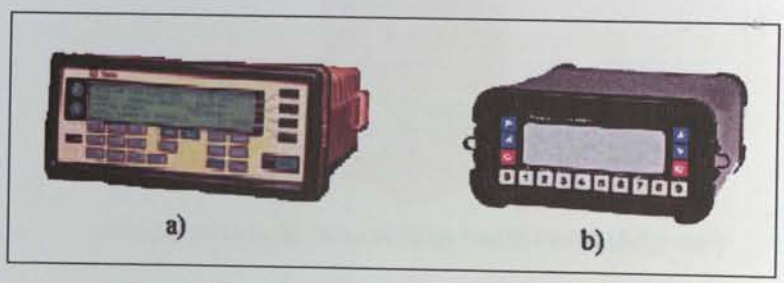


Figure 3.5 – a) Trimble 4000 SSi. b) Ashtech Z-12.

Table 3.2 – Trimble 4000 SSi main characteristics.

Number of Channels	9 (L1 and L2)
Carrier Phase Tracking	Full wavelength carrier on L1 and L2
Tracking Technology	Super-Track(TM)
Cold Start	< 2 minutes
Power Consumption	10.5 watt
Internal Data Storage	Yes
Interfacing	RS232

Table 3.3 – Ashtech Z-12 main characteristics.

Number of Channels	12 (L1 and L2)
Carrier Phase Tracking	Full wavelength carrier on L1 and L2
Tracking Technology	Z-Tracking(TM)
Cold Start	< 2 minutes
Power Consumption	18 watt
Internal Data Storage	Yes
Interfacing	RS232

The industrial PC logs the GPS data through serial ports. The sampling rate of the GPS receivers was set to 1Hz. Time tagging the GPS data was not a problem since the data sent every epoch contained the respective GPS time.

The IMU was rigidly attached to the aircraft structure (in the floor of the aircraft there were metallic bars that were fixed to the aircraft structure) by means of a specially designed support. This support, shown in figure 3.6, allows levelling and alignment of the IMU. This functionality was required to align the IMU axes with the aircraft axes, that is, imagining the aircraft frame with center in the aircraft mass center, x axis pointing to the nose of the aircraft, y axis through the right wing and z axis pointing down, it makes sense to try to set the IMU axes as collinear as possible with those of the aircraft. To analyse the aircraft attitude, a relation between the aircraft axes and the IMU axes must be known, so it seems reasonable to try to align them. To do so, the aircraft was supported by three jacks that were used to level its floor. Pictures of this procedure are presented in figure 3.7. To place the aircraft floor on an horizontal position an optical high precision levelling instrument was used. After that, the same optical instrument was used to place the IMU base on a horizontal position, by adjusting only the IMU support. The IMU xy plane was set parallel to the aircraft xy plane, that is, both z axes were set to be collinear. To align the x and y axes, the IMU base was rotated (around its z axes) till their direction matched the aircraft axes. In laboratory, some marks were placed in the IMU base indicating the IMU x and y axes directions. These marks were visually aligned with the aircraft axes. Since this process obviously includes angular offsets, two total stations were used to measure distances and angles to several points in the aircraft floor and in the IMU base and, with these values, an estimate of the angular offset between frames was estimated.

In order to integrate GPS data with IMU data, the position of the GPS antennas with respect to the IMU frame must be known. Again, with total stations, the distances and angles to the GPS antennas were measured, together with points in the IMU base. Since total station angular measurements lead to more precise positions than distance measurements, two total stations were used so that the point positioning could be determined only through angles (and the distance measurements between both total stations).



Figure 3.6 – Picture of the IMU support.

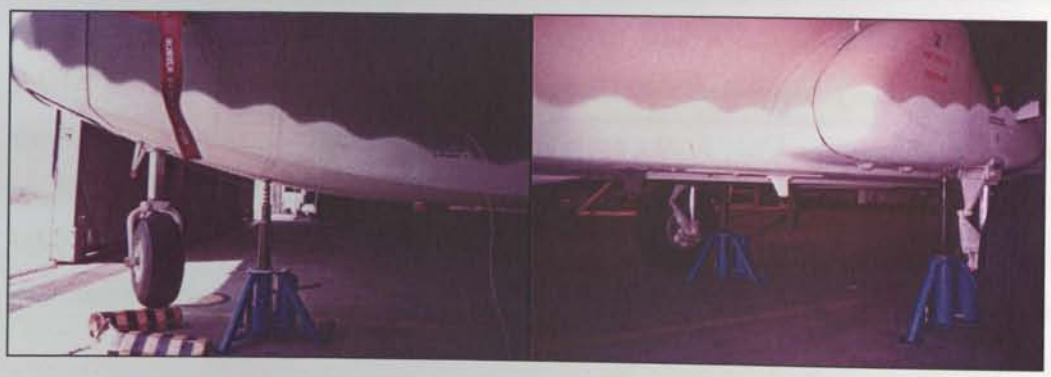


Figure 3.7 – Supporting the aircraft in three jacks to level its floor.

The communication system used to send the reference station data to the aircraft was based on a set of transceivers working in the 902 - 928 MHz range, and using spread spectrum technology. When properly configured, this system behaves like a null-modem serial cable. Table 3.4 shows some characteristics of these communication transceivers.

Table 3.4 –Characteristics of the Freewave Technologies DGR-115HWW transceiver.

Model	DGR-115HWW
Frequency Range	902 - 928 MHz
Technology	GFSK (Gaussian Frequency Shift Keying)
Inter-tranceiver Max Range	20 miles with direct line of sight

Attending to its characteristics and the objective of its application, this was the chosen system between some others possibly available (and tested). It allows fast enough communication, achieving the transmission of a considerable volume of data, but requires line-of-sight between consecutive transceivers. The system also allows the transceivers to be organised as a network of three or more units, keeping the protocol completely transparent to the communicating computers. This way, some transceivers can be spread though the area being surveyed (usually located in high places to cover as much area as possible). Five transceivers were available and, with a nominal line-of-sight distance of 20 miles between units, an area of about 40 by 100 miles could be covered, in ideal conditions.

Figure 3.8 presents a picture of the installation of this navigation system on the referred aircraft.



Figure 3.8 – The navigation system installation.

The reference station was equipped with a dual frequency GPS receiver connected to a computer, which was responsible for storing the raw data from the receiver (for backup purposes, since the receiver itself was able to store it), to compress the required data and to send it to the aircraft, through the radio link. The GPS receiver was collecting data at a 1Hz rate, and every epoch the compressed data was being sent to the aircraft. Specific compression algorithms were developed, benefiting from the characteristics of the GPS data being handled. It is very important for the reference GPS receiver to be located on a place with very good visibility, that is, without obstacles blocking the signals sent by any visible satellite, and without any source of interference such as near by antennas of other systems. The reference GPS antenna must be absolutely static, and its position must be known. Since there are various sources of perturbation in this navigation system, it is important to try to minimise those that can be, in some way, controlled. So, the location of the reference GPS antenna must be carefully chosen.

3.3 Application of the GPS/IMU System on a Land Vehicle

In terms of GPS navigation, a completely different scenario from the one presented above is met when the rover is a land vehicle. While in the air there are no obstacles blocking the GPS satellite signals (except for the aircraft body when maneuvering), in land these obstacles are very common. Specially in urban environments, the most significant problems encountered in GPS navigation are the frequent signal obstruction and the signal reflection on buildings that induce wrong measurements on the GPS receiver (as mentioned in chapter 2, this phenomena is commonly denominated by multipath). Foliage is also a common obstruction to GPS satellite signals.

One positive aspect regarding land navigation is that its dynamics are much lower than that of air navigation. Velocities are usually much lower and the wind effects are not influent as in an aircraft, so the heading of a land vehicle is usually collinear with the path direction. Figure 3.9 illustrates this aspect. Considering this, two GPS receivers (or even one) are sufficient for the land GPS/INS navigation system.

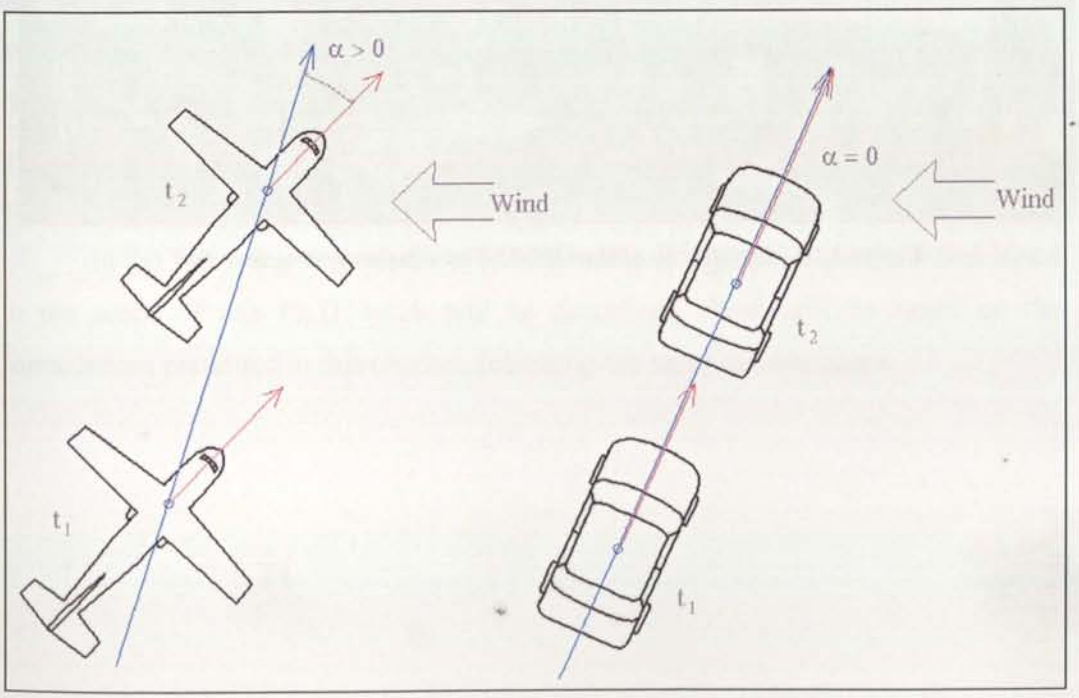


Figure 3.9 – Wind effect in air and land navigation.

Since there are lots of visual references in land navigation, the reasons mentioned earlier for the need of real-time navigation are usually not valid for land navigation. It is in applications such as fleet management that real-time (or almost real-time) navigation is required but, in this case, the position precision does not need to be in the sub-decimeter level. In this case, the communication system must be adequate to an environment full of obstacles. The transceivers mentioned above would not perform as desirable in such environment since they require line-of-sight between two units. For example, mobile GSM modems would be more suitable.

There are other applications, such as operations related with the construction business (streets, buildings, bridges, and so on), where there are direct benefits of using real-time sub-decimeter positioning (both in static and kinematic modes).

Figure 3.10 shows this navigation system installed on a car. Like in the aircraft, the positions of the GPS antennas (and other points in the car), relatively to the IMU frame, were measured with two total stations.

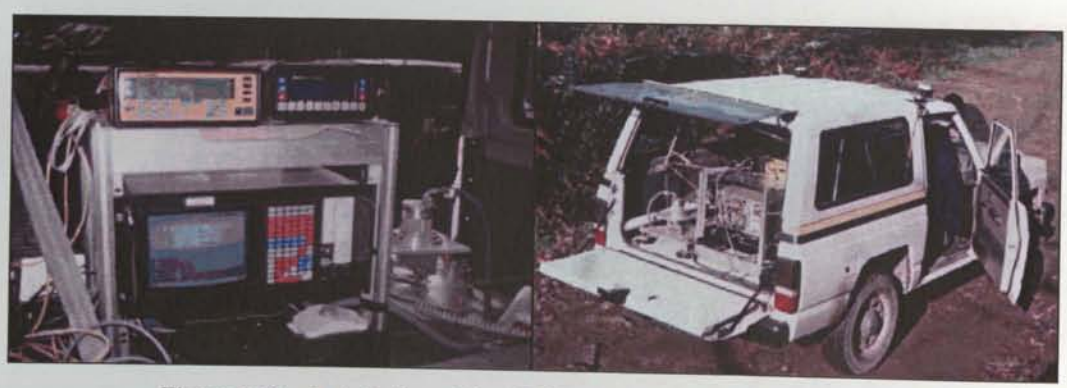


Figure 3.10 – Installation of the GPS/INS navigation system on a car.

CHAPTER 4

GPS PROCESSING

After presenting, in chapter 2, the basic concepts of satellite-based navigation, and describing the basics of GPS, the methods and algorithms to process GPS measurements will be the following issue. The hardware aspects around the capture of GPS measurements will not be taken much into account. It will be just considered that a certain GPS receiver will sample the data from all tracked satellites at the same time instant, and every time instant corresponding to a data sample is denominated by epoch. Each epoch data is time tagged with the receiver clock value at sampling instant (usually, an integer number of seconds, in GPS time) and contains the raw measurements from the satellite data that were available at that instant. This description will mainly focus on GPS receivers capable of tracking both carriers (L1 and L2), usually called dual-frequency receivers.

This chapter will begin with a description of these raw measurements, their behaviour and error factors. Different data combinations will be discussed, showing ways to isolate some of the physical quantities merged in the data. Following, some known methods and algorithms that lead to high precision positioning will be reviewed, stressing their performance and characteristics. The determination of the integer number of cycles associated with the carrier phase measurement (carrier phase ambiguities) is the central aspect of those algorithms.

In the following chapter, the proposed methodology and algorithms developed in the scope of this Ph.D. work will be described. These will be based on the formulations presented in this chapter, following the same nomenclature.

4.1 GPS MEASUREMENTS

4.1.1 RAW MEASUREMENTS

4.1.1.1 Pseudorange Measurement

As mentioned in chapter 2, a GPS receiver can retrieve from the L1 carrier the pseudorange measurement through correlation with the pseudorandom C/A code. (With a receiver capable of decoding the encrypted Y-code it would also be possible to measure the pseudorange from P-code which is more precise, but since this feature is reserved to U.S. military or authorised users and not to civil receivers, only access to C/A code will be considered.) This pseudorange is a raw estimate of the distance from the satellite antenna, at time of emission, to the antenna of the GPS receiver, at time of reception. Equation 4.1 defines this pseudorange concept.

$$P_i^k(t) = \left(t_i(t) - t^k(t - \tau_i^k)\right) \cdot c \tag{4.1}$$

with:

$P_i^k(t)$ - Pseudorange measurement determined by the receiver i at instant t, to satellite k, in meters.

$t_i(t)$ - Time presented by the receiver i clock at sampling instant t, in accumulated seconds. This is the signal reception time seen by receiver i.

$t^k(t - \tau_i^k)$ - Time of signal emission, derived from the pseudorandom code received in the signal from satellite k, that was captured at sampling instant t.

τ_i^k - True signal travelling time, from the antenna of satellite k, to the antenna of receiver i, in seconds. Note that this is an unknown.

t - True time at sampling instant, in accumulated seconds in the GPS time system.

c - Speed of light in vacuum (299792458.0 m/s).

As explained earlier, the receiver clock has naturally an offset (dt_i) to the true GPS time. Likewise, the satellite clock also presents an offset (dt^k). It should be noticed that dt_i, dt^k and also τ_i^k are time dependent, but this dependency will not be presented in the formulas in order to keep these simple.

Again, the signal travelling path is not always through a vacuum-like medium, crossing layers with particles that delay signal propagation and also bend its trajectory. This effect can be simply modelled by adding a delay in the signal travelling time. To this delay, two of the layers provide a far more significant contribution – the ionosphere and the troposphere. Due to the different nature of their components, it makes sense to separate the delays caused by these layers. As will be explained below with more detail, the ionosphere is a dispersive medium, that is, the delay caused in the propagation of an electromagnetic signal depends on the signal frequency. (This characteristic led to the implementation of a second carrier – L2 – with a different frequency than that of L1, so that the effect of the ionosphere could be reduced by comparing the resulting delays on both carriers.) The troposphere is not a dispersive medium in the frequency band used in the GPS system. Considering the exposed, the pseudorange equation can now be written as:

$$\begin{aligned} P_i^k(t) &= \left[(t_R + dt_i) - (t^E + dt^k)\right] \cdot c + I_i^k + T_i^k \\ &= (t_R - t^E) \cdot c + (dt_i - dt^k) \cdot c + I_i^k + T_i^k \\ &= \rho_i^k(t, t - \tau_i^k) + (dt_i - dt^k) \cdot c + I_i^k + T_i^k \end{aligned} \tag{4.2}$$

where:

t_R - True time of signal reception (in seconds).

t^E - True time of emission (in seconds).

I_i^k - Ionospheric delay from satellite k to receiver i (in meters, that is, the time delay was multiplied by the speed of light). Notice that, although not represented, this value varies with time.

T_i^k - Tropospheric delay from satellite k to receiver i (in meters). Again, this quantity is time dependent.

$\rho_i^k(t, t - \tau_i^k)$ - True distance from the satellite k antenna at instant t^E to the receiver i antenna at instant t_R (in meters).

It should be noticed that the time the signal travels from the satellite hardware to the satellite antenna (d^k), and the time taken from the receiver antenna to the its correlators (d_i), should be considered as part of the pseudorange measurement.

Still not considered, but evidently present, is the random noise ε_i^k that is introduced by the receiver measuring process and also by the propagation medium.

With these final considerations, and neglecting other error sources, equation (4.3) presents the final approximation to the pseudorange measurement.

$$P_i^k(t) = \rho_i^k(t, t-\tau_i^k) + (dt_i - dt^k)\cdot c + I_i^k + T_i^k + (d_i + d^k)\cdot c + \varepsilon_i^k \qquad (4.3)$$

Equation (4.3) does not include some error sources like multipath or relativistic effects. In the rest of this thesis, these errors will not be considered unless they are a central issue. This is to simplify the presented analysis since, for example, multipath is an error whose effect is not easily treatable in kinematic environments. Again, regarding the application to aircraft navigation, heavy multipath effects are not likely to appear since the possible reflecting objects are parts of the aircraft body or parts of the satellite structure, although reflections on the sea surface (or other ground surfaces) can actually cause significant multipath effects under certain conditions (when the aircraft flies at low altitude). In this measurement, the multipath error is typically below 1 code chip (1 code chip which is equivalent to about 300 meters). As explained in chapter 2, due to the intentional offset introduced in the satellite oscillators, the relativistic effects will be neglected hereafter.

The random noise ε_i^k, with gaussian characteristics, affecting this measurement can reach significant levels. For example, in the case of the C/A pseudorange, the noise standard deviation can vary from 10 up to 300 centimeters (for a typical receiver, the noise standard deviation is about one cent of the code chip length).

4.1.1.2 Carrier Phase Measurement

When tracking the signal from a satellite, the receiver Phase-Lock-Loop (PLL) continuously follows the restored sinusoidal carrier wave. Due to the relative motion between satellite and receiver antennas, the transmitted carrier wave suffers from variations on its frequency, according to the Doppler principle. By monitoring these changes and comparing them to the nominal carrier wave (which is generated in the receiver), the relative motion between receiver and satellite can be estimated. Accumulating the measured carrier cycles between epochs (and comparing that value

to the accumulated number of cycles of the nominal carrier wave in that period) provides a means of determination of receiver motion from one epoch to the other.

When the receiver begins to track the transmitted carrier phase from one satellite, the receiver is not able to determine the accumulated carrier cycles that correspond to the initial distance between satellite and receiver. Each carrier cycle has no time reference that may distinguish it from any other carrier cycles, and what the receivers usually do in that case is to start accumulating from zero, at that instant. Due to initial synchronisation mechanisms in the receiver, that number of unknown initial cycles is made to have an integer nature. This unknown number of integer cycles is called Phase Ambiguity. With knowledge of the phase ambiguities, it is possible to determine the receiver absolute position based only on phase measurements, but without it, only relative positioning (to an initial position) is possible. As shall be seen later in this chapter, the essence of GPS high precision positioning is based on the determination of this set of integer numbers, being this a non-trivial task.

Equation (4.4) provides an initial mathematical model to this phase measurement. It should be mentioned that, in literature, different terms are used to refer to this measurement, such as "accumulated delta range", "integrated Doppler" or "carrier beat phase". In this thesis, the term "phase measurement" will be used.

$$\phi_i^k(t) = \phi_i(t) - \phi^k(t - \tau_i^k) + N_i^k \tag{4.4}$$

where:

$\phi_i^k(t)$ - Phase measurement provided by the receiver at instant t (in number of carrier cycles).

$\phi_i(t)$ - Quantity of accumulated cycles of the receiver generated nominal carrier wave, at instant t (in carrier cycles).

$\phi^k(t - \tau_i^k)$ - Quantity of accumulated cycles of the satellite generated carrier wave measured by the receiver hardware (in carrier cycles).

N_i^k - Integer number of unknown initial cycles – Phase Ambiguity, (in carrier cycles). It should be noticed that, as long as the carrier is continuously tracked without interruption, this value is constant over time.

The accumulated cycles on both carriers can be written by (4.5) and (4.6).

$$\phi_i(t) = f_o \cdot (t + dt_i) + \phi_i(t_o) \tag{4.5}$$

$$\phi^k(t - \tau_i^k) = f_o \cdot (t - \tau_i^k + dt^k) + \phi^k(t_o) \tag{4.6}$$

where:

f_o - Nominal carrier frequency (in Hz).

dt_i - Offset of the receiver time with respect to true GPS time (in seconds).

$\phi_i(t_o)$ - Initial fraction of a cycle of the receiver generated carrier wave (in cycles).

dt^k - Offset of the satellite time with respect to true GPS time (in seconds).

$\phi^k(t_o)$ - Initial fraction of a cycle of the satellite generated carrier wave (in cycles).

Replacing (4.5) and (4.6) in (4.4), (4.7) is obtained.

$$\phi_i^k(t) = f_o \cdot \left(\tau_i^k + dt_i - dt^k\right) + \left(\phi_i(t_o) - \phi^k(t_o)\right) + N_i^k \tag{4.7}$$

To transform accumulated cycles into distances, it is necessary to multiply the given values by the corresponding wavelength of the carrier. The wavelength of a determined carrier is given by equation (4.8). It is the distance between two consecutive carrier cycles of a wave travelling at the speed of light in vacuum. Table 4.1 presents the wavelength values for both L1 and L2 carriers.

$$\lambda = \frac{c}{f_o} \tag{4.8}$$

Table 4.1 – L1 and L2 wavelengths.

	fo (MHz)	λ (m)
L1	1575,42	0,19029
L2	1227,60	0,24421

It can be seen in equation (4.7) that τ_i^k represents the true time interval the signal took to travel from the satellite hardware to the receiver tracking loops. As described in the pseudorange measurement, the ionosphere and troposphere also affect

the phase measurement. The time elapsed from the satellite hardware to the satellite antenna (δ^k), and the time taken from the receiver antenna to the receiver tracking loops (δ_i), must also be considered. Considering these effects together with the random noise that is present in the measuring process and in the wave propagation medium (ε_i^k), equation (4.9) presents the mathematical model to be used for phase measurements, in units of distance.

$$\begin{aligned}\Phi_i^k(t) = \lambda\phi_i^k(t) = \rho_i^k(t, t-\tau_i^k) + (dt_i - dt^k)\cdot c - \\ -I_i^k + T_i^k + (\delta_i + \delta^k)\cdot c + \lambda\cdot(\phi_i(t_o) - \phi^k(t_o)) + \\ +\lambda\cdot N_i^k + \varepsilon_i^k\end{aligned} \tag{4.9}$$

The ionospheric contribution to the phase measurement is equal in value to its contribution to the pseudorange measurement, but opposite in sign. The explanation of this phenomenon will be given below when presenting the ionosphere effect with more detail.

Again, for simplicity, other error sources such as multipath are not considered in the mathematical model, although they must be in mind when processing is to take place. The error caused by multipath in the phase measurement is below 0.25λ, but high multipath can lead to loss of phase lock.

The random noise ε_i^k associated with the carrier phase measurement (usually with gaussian properties) is much lower than the noise affecting the pseudorange measurement, being below the 5 mm level.

When the carrier ambiguities are well fixed, the phase measurements act as high precision pseudorange measurements.

4.1.1.3 Doppler Measurement

Another measurement that GPS receivers usually provide is the instantaneous Doppler shift that the frequency of the emitted carrier wave suffers, with respect to its nominal frequency. This measurement is provided by the receiver at every epoch instant, and it can be mathematically interpreted as the first order derivative of the phase measurement equation. That is, this is a measurement of the first order

derivative of the phase measurement, at each sampling instant. Equation (4.10) presents the formulation of the Doppler measurement.

$$\lambda D_i^k(t) = \dot{\rho}_i^k(t, t-\tau_i^k) + (\dot{dt}_i - \dot{dt}^k)\cdot c - \dot{I}_i^k + \dot{T}_i^k + \dot{\varepsilon}_i^k \qquad (4.10)$$

where:

$D_i^k(t)$ - Doppler measurement given by the receiver at instant t (in Hz).

$\dot{\rho}_i^k(t, t-\tau_i^k)$ - Instantaneous variation of the distance from the satellite at transmission instant and the receiver at reception instant (in meters per second).

$\dot{dt}_i$ - Receiver clock drift (sec/sec).

$\dot{dt}^k$ - Satellite clock drift (sec/sec).

$\dot{I}_i^k$ - Ionospheric variation (m/s).

$\dot{T}_i^k$ - Tropospheric variation (m/s).

$\dot{\varepsilon}_i^k$ - Process noise (m/s).

The ionospheric and tropospheric effects have relatively slow variation with time, being their effects on Doppler measurements usually not very significant. Receiver clock drift is usually the predominant source of error in this measurement. Satellite clock drift is usually very low due to the high stability of their oscillators.

4.1.2 Measurement Error Sources

Some considerations about the main error sources contained in these raw measurements will be now presented. Their influence and procedures to treat them are also given.

4.1.2.1 Clock Errors

Both receiver and satellite clocks present offsets and drifts with respect to the true GPS time. Since the clock stability of the satellite oscillators is very good, their clock offset can be, up to a point, predictable. But the same is usually not true for the receiver clock since it is much less stable than those of the satellites. It must be noticed that if a precision of, for example, 10 cm (rms error) is required for the absolute three-dimensional position, a rms error of about 3.3 cm would be necessary

for the range measurement, with a PDOP value of 3. This would require that the clock errors would not exceed 3.3 cm (disregarding the other error sources), that is, the clock offset would have to be known with a resolution up to 0.11 ns.

The satellite clock behaviour is sent in the navigation message by means of a four parameter model (it is a second order polinomium), as can be seen in [ARINC, 1991]. These model parameters are determined by the control segment and are frequently uploaded into the satellites. Besides the possible errors this model can introduce (and, as time passes from the last upload, the errors tend to increase), when Selective Availability (SA) is active there is a possibility that this model would contain a deliberate random error that can reach several meters.

Two procedures are usually adopted to deal with the clock errors. One is to consider these offsets as unknowns, together with the three position coordinates, reformulating the equation system. Another technique, to which will be given preference throughout this thesis, is to combine the measurements from two different receivers and two different satellites. Considering the measurements from two GPS receivers tracking the same satellite, if the difference of the measurements (phase or pseudorange) from both receivers is taken (referring to that same satellite), the satellite clock error is cancelled out. This will be explained in more detail in the next section where several data combinations will be presented. To eliminate the receiver clock offset, the difference between measurements of two satellites, on the same receiver, is taken. It is usual to consider a reference satellite, usually the one with highest elevation, to which all other tracked satellites have their measurements subtracted, eliminating the receiver clock error from the equation system.

4.1.2.2 Tropospheric Error

The troposphere is the lower layer of the Earth's atmosphere, extending to an height of about 9 km over the poles and about 16 km over the equator [Lutgens and Tarbuck, 1989]. Mainly containing neutral atoms and molecules, the troposphere effect on propagation of electromagnetic signals is to delay it and bend its path, that is, the signals are refracted while crossing it. In the frequency band of the GPS signals, the troposphere behaves as a non-dispersive medium, i.e., the refractive index of the troposphere is not dependent on the signal's frequency.

Several studies have been made to analyse the refractive index of the troposphere and the tropospheric effects on GPS, for example, [de Munck and Spoelstra, 1992], [Brunner, 1988], [Brunner and Welsch, 1993], [Yunck, 1993], [Smith and Weintraub, 1953], [Thayer, 1974], [Saastamoinen, 1973], [Hopfield, 1969], [Boon, 1997], and others. Basically, the refractivity N of a volume of air can be modelled by equation (4.11).

$$N = K_1\left(\frac{P_d}{T}\right)Z_d^{-1} + \left[K_2\left(\frac{e}{T}\right) + K_3\left(\frac{e}{T^2}\right)\right]Z_W^{-1} \tag{4.11}$$

Here, N is a function of temperature (T) and the partial pressures of the dry gases (P_d) and the water vapour (e). K_1, K_2 and K_3 are empirically determined constants (cf. [Smith and Weintraub, 1953] and [Thayer, 1974]), Z_d is the compressibility factor for dry air, and Z_W is the compressibility factor for water vapour.

From equation (4.11) it can be deducted that the troposphere effect can be divided into two parts – the effect caused by the dry part of the troposphere, and the one caused by the wet part of the troposphere. These parts are usually referred has "dry" and "wet" components of refractivity.

Tropospheric delay in GPS is usually processed using a mathematical model that, from some measurements of pressure and temperature, and also an altitude estimate, can determine with some precision the "dry" and "wet" delay components. The "dry" component roughly accounts for 90% of the total tropospheric delay and, based on some assumptions such as hydrostatic equilibrium of the atmosphere, can be estimated by the models to sufficient precision. On the other hand, the "wet" component is more unstable, being highly variable both in space and time. This reason makes its prediction more difficult.

Several models were developed to estimate the tropospheric delay. Some of the most used are the Saastamoinen (cf. [Saastamoinen, 1973]), the Hopfield (cf. [Hopfield, 1969]) and the Modified Hopfield (cf. [Goad and Goodman, 1974], [Black, 1978] and [Hofmann-Wellenhof et al., 1998]). The usual procedure of these models is to estimate the total zenith delay and then apply a Mapping Function that takes into

account the satellite elevation angle. Several authors have studied these Mapping Functions (see, for example, [Black, 1978], [Black and Eisner, 1984], [Davis et al., 1985], [Goad and Goodman, 1974], [Herring, 1992], [Hopfield, 1969], and [Saastamoinen, 1973]).

One problem that is usually encountered on GPS surveys is to measure the meteorological data required for these models. Sometimes it is just not possible to have it. In these cases, some typical values are entered in the models and an approximate value of the tropospheric delay is obtained, with an higher error. Another aspect is that there usually appears a residual delay after using the models, in the form of a bias. This bias has to be dealt with, by using large sets of data or by stochastic estimation methods such as Kalman filtering.

In order to further reduce the tropospheric error, the difference between measurements of two GPS receivers is usually taken. This is called Differential GPS (DGPS). When two GPS receivers are relatively close to each other, the signals' path from the satellites to the receivers cross more or less the same tropospheric region, being affected by similar delays. Taking the difference of the measurements of both receivers, most of the tropospheric delay cancels out. But some care must be taken because tropospheric delay is highly dependent on the altitude of the antenna. For example, on a DGPS aircraft survey, one of the antennas is placed on a fix point in the ground (the reference antenna) and the other is in the aircraft (the rover antenna). During the flight, even though the aircraft can be passing in the same area of the reference antenna, due to the altitude difference, the tropospheric delay is different for both receivers and tropospheric modelling should take place.

4.1.2.3 Ionospheric Error

The ionosphere is the layer where the emissions of ionising radiation (such as ultraviolet and X-ray emissions) lead to the presence of free electrons which cause perturbations to the electromagnetic propagation. This layer extends from about 50 km up to 1000 km or more.

For the GPS frequency band, the ionosphere behaves as a dispersive medium – its refraction index is dependent of the frequency of the electromagnetic wave. It has

been studied (cf. [Bradley, 1989], for example) that in the conditions of the ionosphere, the refractive index can be approximated by equation (4.12).

$$n \cong 1 - \frac{N_e e^2}{\varepsilon_o m_o \omega^2} = 1 - \alpha \frac{N_e}{f^2} \tag{4.12}$$

where:

n - Medium refractive index.

N_e - Electron density.

e - Electron charge.

m_o - Electron mass.

ε_o - Permitivity of free space.

ω - Angular frequency of the electromagnetic wave ($\omega=2\pi f$).

The dependence of the refractive index on the inverse of the squared frequency is evident from equation (4.12).

The integration of the refraction index along the wave travelling path yields the electromagnetic path length which, when compared to the path length it would have in vacuum, provides the delay quantity introduced by the travelling medium.

Since the carrier phase observation only involves the sinusoidal carrier wave, on which other signals are modulated, its respective refractive index is equal to the one presented in equation (4.12). Equation (4.13) then presents the effect of the ionosphere on the phase measurement.

$$\rho_\phi = \int_{path} n_\phi ds = \int_{path} \left(1 - \alpha N_e / f^2\right) ds = \rho - I \tag{4.13}$$

where ρ is the corresponding travelled path on vacuum and I is the difference to ρ caused by the ionosphere. As can be seen, instead of being affected by a delay, the phase measurement suffers an advance due to the presence of the ionosphere.

The conclusion taken from equation (4.13) is not valid for the pseudorange measurement. The pseudorange measurement is derived from the signals modulated in the carrier phase. This modulated signals can be considered as signals whose frequency are around the carrier wave frequency, and since the medium is dispersive,

they will suffer a different effect from that of the carrier wave. Studies on the propagation of these modulated signals led to the formulation of their refractive index, called group refractive index, and equation (4.14) presents this relation.

$$n_g = n + f\frac{\partial n}{\partial f} \tag{4.14}$$

Applying equation (4.14) to equation (4.12) yields the refractive index regarding the pseudorange measurements, presented in equation (4.15).

$$n_P = 1 + \alpha\frac{N_e}{f^2} \tag{4.15}$$

Proceeding to the integration of this index along the travelled path, as can be seen in equation (4.16), the effect of the ionosphere in the pseudorange measurement is traduced not on an advance as in the phase measurement, but as a delay. This delay has the same absolute value as the advance induced on the carrier phase measurement.

$$\rho_P = \int_{path} n_P ds = \int_{path} \left(1 + \alpha N_e / f^2\right) ds = \rho + I \tag{4.16}$$

These equations reflect that the main influence of the ionosphere on GPS signals is the number of electrons along the path, that is, the integrated electron density along the signal path, which is usually called the Total Electron Content (TEC). Equation (4.17) expresses the dependence of the ionospheric effect on the TEC.

$$I = \alpha\frac{TEC}{f^2} \tag{4.17}$$

The TEC has been studied by many researchers, also with the help of GPS signals. It is sensitive to solar activity, presenting higher values in daytime (typically in the order of $10^{18}m^{-2}$ at mid-latitude locations) than in night-time ($10^{17}m^{-2}$). The range effect of the ionosphere (I) can reach 30 meters or more in the zenith direction.

Several models for the ionospheric influence have been developed ([Klobuchar, 1986], [Fees and Stephens, 1986], [Georgiadou and Kleusberg, 1988], [Wild et al., 1989] and [Webster and Kleusberg, 1992]), but these are only able to remove about 50% to 60% rms of the effect. The usual method to reduce the ionospheric influence on GPS measurements is to use Differential GPS (DGPS) where difference of the measurements of two close GPS receivers is used. With this method, only a residual effect remains due to the slight difference of the signal paths to both receivers. But there is a constraint on the distance between the two GPS receivers (usually called Baseline) because the more distant they are, the less correlated are the ionospheric effects on both receivers. It could be said that the ionosphere is the main restricting factor to baseline length since it becomes the main error source as the baseline reaches a certain distance. For example, considering sub-decimeter rapid positioning, baselines of 100 km are usually very problematic to solve, and that limit can go down to 20 km during periods of high solar activity.

Dual frequency receivers have the advantage to measure the ionospheric influence in two carrier waves with different frequencies. Knowing the frequency values, combination of the measurements of both carriers can be used to estimate the ionospheric effect (see, for instance, [Brunner and Gu, 1991] and [Klobuchar, 1991]). Equation (4.18) provides an estimator for ionospheric influence on L1 but, since it is based on pseudorange measurements, its noise level is far beyond the desirable precision. (In the following equations, the subscript $_1$ refers to the measurements on the L1 carrier, and the subscript $_2$ to the L2 carrier.) A similar estimate based not on pseudoranges but on phase measurements could also be used but, for the determination of its absolute value, it would be required also to know the phase ambiguities for both carriers. Estimation techniques based on these two combinations can be implemented. In figure 4.1, the estimated L1 ionospheric delay affecting code and phase measurements for one satellite is depicted, resulting from a Kalman filter using both code pseudorange and carrier phase measurements. It is worth noticing the natural dependence of the delay with the satellite elevation angle. The lower the elevation angle is, the longer is the path the signal has to cross through the ionosphere.

$$I_1 = \frac{\lambda_1^2}{\lambda_1^2 - \lambda_2^2}(P_1 - P_2) \tag{4.18}$$

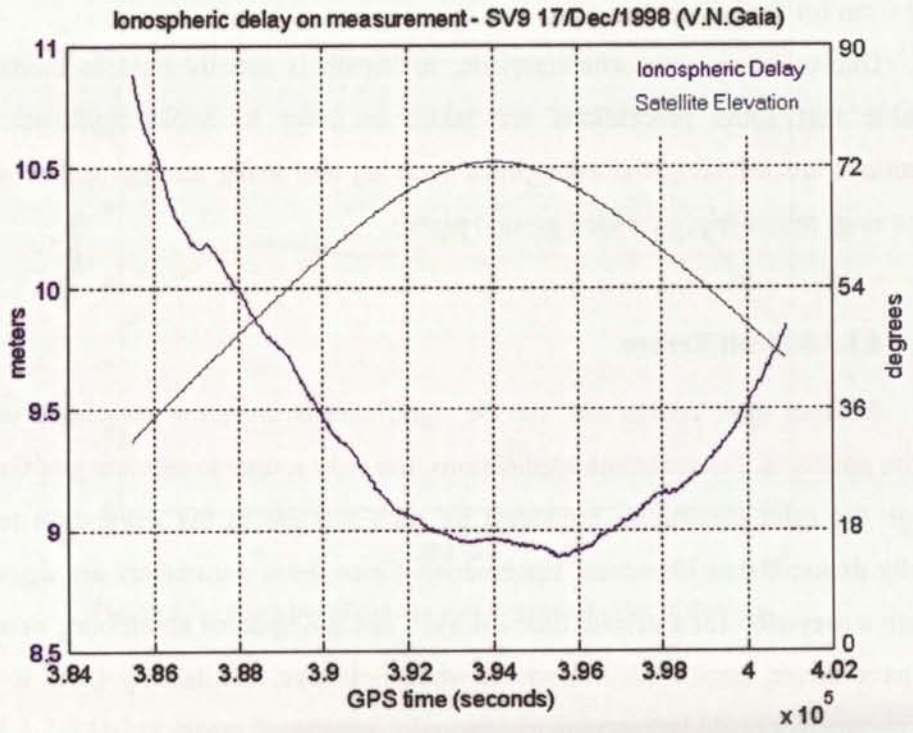


Figure 4.1 – Example of the L1 ionospheric delay.

Sudden changes on the electron density along the signal path, due to, for example, an unusual number of particles released from solar flares, cause a rapid variation on the carrier phase that the carrier tracking loops of some GPS receivers may not follow, loosing lock of the carrier phase measurement. This phenomenon is usually called Ionospheric Scintillation. This can cause an interruption of the carrier phase measurement, or a Cycle Slip.

4.1.2.4 Multipath Error

Multipath results from signal reflection on objects in the antenna surrounding environment (and also on the satellite structure). The reflected signal is added to the direct signal when being received by the GPS antenna, causing the receiver to consider a different measured distance to the satellite. Studies on this subject (cf. [Bishop et al., 1985], [Evans and Hermann, 1990], [Martin, 1978], and [Seeber, 1993], for example) indicate that a theoretical maximum multipath error of 15 meters could affect the P-Code pseudorange, and a maximum of 150 meters for the C/A pseudorange. Carrier phase measurements are more insensitive to multipath,

considering a maximum possible effect of 5 cm for the L1 phase measurement and about 6 cm for the L2 carrier.

Due to its spurious characteristic, multipath is usually hard to model. It is desirable that some precautions are taken in order to avoid multipath. Main precautions are selecting the appropriate location and using an appropriate antenna (choke ring, microstrip, extended ground plane).

4.1.2.5 Orbit Errors

Another error source that can be significant is the error associated with the satellite positions. For real-time applications, the only source to satellite positioning is through the orbit parameters broadcast by each satellite in the navigation message (usually denominated Broadcast Ephemeris). Since these parameters are determined through a prevision for a certain time interval, and are updated about once every day, they have errors associated. Moreover, when Selective Availability (SA) is active, these parameters could be carrying intentionally introduced errors.

Some organisations provide *a posteriori* files containing precise satellite positions (and precise values of their clock offsets). Those files were based on GPS data observations for some large periods, aiming for a high precision orbit determination. These organisations make possible the access to these files through the internet (ftp), allowing the elimination of such errors when post-processing GPS data all over the world.

Figure 4.2 shows the satellite position difference between precise and broadcast orbits for satellite PRN9, over a period of approximately 5.6 hours.

When it is not possible to use a precise orbit file, the errors introduced by broadcast orbits can be significantly reduced using the DGPS technique. When two GPS receivers are relatively close, the geometry likelihood involving them and the satellite makes similar to both receivers the effect of the orbit error. So, when taking the difference between their measurements, those errors cancel out. But it should be noticed that, again, when the baseline length increases, that error correlation decreases.

See, for example, [Colombo, 1986] for more information on ephemeris errors.

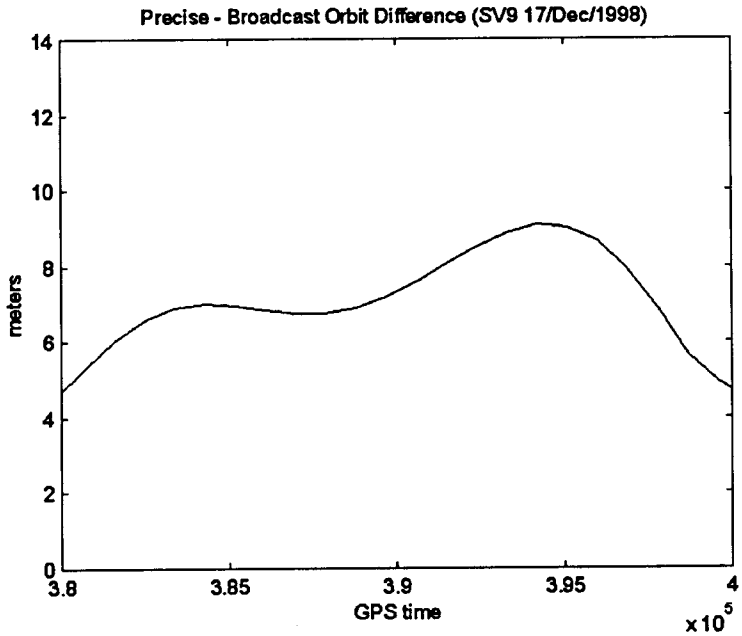


Figure 4.2 – Example of precise and broadcast orbit difference.

4.1.2.6 Other Error Sources

As described in the presentation of the various measurements, random noise is always accompanying the observations. With a considerably high value for C/A pseudorange, and with a much lower value for phase measurements, random noise has to be taken into account, usually by some sort of stochastic process.

Relativistic effects, as mentioned in chapter 2, will be negligible considering the small frequency offset introduced in each satellite oscillator, to compensate them.

It should also be noticed that the constants affecting the individual measurements, such as hardware to antenna delays and carrier phase value at initial instant, are cancelled by taking the difference between measurements of two receivers, or measurements of two satellites. Since the presented processing techniques will be based on such differences, no particular concern with these quantities will be stressed throughout this thesis.

4.1.3 Measurement Combinations

As can be seen from the mathematical models presented above, some terms are common to different measurements. Since some of the terms respect the

environment surrounding the receiver, it should be expected that these would be very similar to another receiver placed in the neighbourhood of the first. This fact leads to the use of combined measurements in order to minimise or isolate the effects caused by some error sources. Although several data combinations can be found in literature, only those considered relevant for this work will be shown.

4.1.3.1 Wide Lane Combination

For a dual frequency receiver, one of the most used combinations is the Wide Lane Combination, which results from subtracting the L2 phase measurement from the L1 phase measurement, in cycles. Equation (4.19) presents this combination.

$$\begin{aligned}\phi_{i,w}^k(t) &= \phi_{i,1}^k(t) - \phi_{i,2}^k(t) = K \cdot \rho_i^k(t, t-\tau_i^k) + c \cdot K \cdot (dt_i - dt^k) - \\ &-\left(\frac{1}{\lambda_1} I_{i,1}^k - \frac{1}{\lambda_2} I_{i,2}^k\right) + K \cdot T_i^k + N_{i,1}^k - N_{i,2}^k + \\ &+\frac{c}{\lambda_1}(\delta_{i,1} + \delta_1^k) - \frac{c}{\lambda_2}(\delta_{i,2} + \delta_2^k) + \\ &+\left(\phi_{i,1}(t_o) - \phi_1^k(t_o)\right) - \left(\phi_{i,2}(t_o) - \phi_2^k(t_o)\right) + \varepsilon_{i,w}^k\end{aligned} \tag{4.19}$$

with

$$K = \frac{1}{\lambda_1} - \frac{1}{\lambda_2} = \frac{1}{\frac{\lambda_1\lambda_2}{\lambda_2 - \lambda_1}} = \frac{1}{\lambda_w} \qquad \lambda_w = \frac{\lambda_1\lambda_2}{\lambda_2 - \lambda_1} \cong 0.86 \ m \tag{4.20}$$

Using the approximation shown in equation (4.17), the relation between L1 and L2 ionospheric influence can be reached, as presented in equation (4.21).

$$\alpha \cdot TEC = f_1^2 I_1 = f_2^2 I_2 \Leftrightarrow I_2 = \frac{f_1^2}{f_2^2} I_1 \tag{4.21}$$

Replacing (4.20) and (4.21) in (4.19), and multiplying the result by λ_w, equation (4.22) is obtained.

$$\begin{aligned}\lambda_w\phi_{i,w}^k(t) &= \rho_i^k(t,t-\tau_i^k)+c\cdot(dt_i-dt^k)+\\ &+\frac{\lambda_2}{\lambda_1}I_{i,1}^k+T_i^k+\lambda_w N_{i,w}^k+\\ &+\lambda_w\frac{c}{\lambda_1}(\delta_{i,1}+\delta_1^k)-\lambda_w\frac{c}{\lambda_2}(\delta_{i,2}+\delta_2^k)+\\ &+\lambda_w\left(\phi_{i,1}(t_o)-\phi_1^k(t_o)\right)-\lambda_w\left(\phi_{i,2}(t_o)-\phi_2^k(t_o)\right)+\varepsilon_{i,w}^k\end{aligned} \tag{4.22}$$

From equation (4.22) it can be inferred that the wide-lane combination can be treated as an hypothetical carrier wave (Lw) of wavelength λ_w. Since λ_w is larger than λ_1 or λ_2 (λ_w = 0.86 m), the determination of the wide-lane ambiguities (N_w) is theoretically easier than those of L1 or L2 because the density of ambiguity candidates on the same three-dimensional region is much smaller. In other words, the grid formed by the possible positions corresponding to the possible ambiguity candidates has a much larger spacing for Lw than for L1 or L2. The drawback is that the wide-lane carrier measurement has an higher noise component than L1 or L2 phase measurements. Considering that ϕ_1 and ϕ_2 have associated white gaussian noise with the same standard deviation σ, the ϕ_w measurement noise has a standard deviation of about $6.7\cdot\sigma$. Also, the ionospheric influence in ϕ_w is about 1.3 the amplitude of the corresponding effect in ϕ_1. Despite these facts, the wide-lane measurement is very useful especially as a step to reach to L1 ambiguities, reducing the N_1 search space considerably. One of the main problems of ambiguity fixing is the processing time required to examine all the possible ambiguity candidates. Reducing the search space is, therefore, desirable and essential to improve efficiency.

4.1.3.2 Single Differences

As mentioned above, it is common practice to take the difference between the measurements of two GPS receivers to eliminate satellite and atmospheric related errors. This combination is usually called Single Difference. Equation (4.23) introduces the notation used for single differences between receivers *i* and *j*, for the carrier phase measurement. As can be seen, the satellite clock offset is eliminated and, if the receivers are close enough, the ionospheric and tropospheric errors are attenuated.

$$\begin{aligned}
&\lambda\phi_{ij}^{k}(t,\Delta t) = \lambda\phi_{i}^{k}(t) - \lambda\phi_{j}^{k}(t+\Delta t) = \\
&= \rho_{i}^{k}(t, t-\tau_{i}^{k}) - \rho_{j}^{k}(t+\Delta t, t+\Delta t-\tau_{j}^{k}) + \\
&+c(dt_{i} - dt_{j}) - I_{ij}^{k} + T_{ij}^{k} + \lambda N_{ij}^{k} + \\
&+c\delta_{ij} + \lambda\phi_{ij}(t_{o}) + \varepsilon_{ij}^{k}
\end{aligned} \tag{4.23}$$

In this representation, a quantity X with subscript $_{ij}$ means $X_{ij} = X_i - X_j$, with the exception of the noise term which only represents the associated noise of this combination (not a subtraction).

The term Δt exists because both receivers are not sampling at the very same instant due to their clock offsets. Figure 4.3 illustrates this difference. Although most receivers try to keep their clock offset within a small interval around the true epoch instant (the intervals [-1ms, 0] and [-1ms, +1ms] are typical), a small difference between sampling instants introduces considerable differences in the measurements.

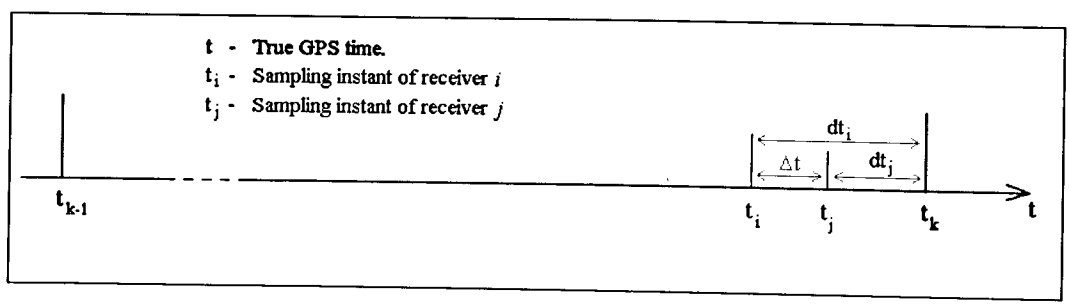


Figure 4.3 – Timing diagram for the sampling instants of two GPS receivers.

4.1.3.3 Double Differences

Taking the difference between the measurements of two satellites eliminates the errors that respect the GPS receiver (clock offset and other biases). If the subtraction of two single difference combinations is taken, between two satellites, both satellite and receiver relative errors are eliminated, and the atmospheric errors are attenuated if the receivers are relatively close. This combination is called Double Difference and the work here presented will be based mostly on this combination. Equation (4.24) shows the notation used for double differences.

$$\begin{aligned}\lambda\phi_{ij}^{kl}(t,\Delta t) &= \lambda\phi_{ij}^{k}(t,\Delta t) - \lambda\phi_{ij}^{l}(t,\Delta t) = \\ &= \rho_i^k(t,t-\tau_i^k) - \rho_j^k(t+\Delta t,t+\Delta t-\tau_j^k) - \\ &-\rho_i^l(t,t-\tau_i^l) + \rho_j^l(t+\Delta t,t+\Delta t-\tau_j^l) - \\ &-I_{ij}^{kl} + T_{ij}^{kl} + \lambda N_{ij}^{kl} + \varepsilon_{ij}^{kl}\end{aligned} \tag{4.24}$$

The superscript ^{kl} means that $X^{kl} = X^k - X^l$.

For double differences, besides a reference GPS receiver, a reference satellite must also be selected. It is to that reference satellite that the measurements of all other satellites are differenced. It should be noticed that it is not necessary to take the differences to one only reference satellite. Other combinations could be considered (such as differencing the measurements of two consecutive satellites) as long as *m-1* independent equations would be formed with *m* satellites being tracked. In the notation used in this text, the superscript ^{k} refers to the reference satellite and the superscript ^{l} to another tracked satellite. Also, the subscript $_j$ identifies the reference GPS receiver and the subscript $_i$ the receiver whose position is to be determined (rover receiver).

With double differences, the order of the equation system is reduced by one, that is, if *m* satellites are tracked simultaneously by both receivers, only *m-1* double difference equations can be formed. But also an unknown has disappeared – the receiver clock offset; and only the position (and ambiguity vector, for phase measurements) needs to be determined.

The selection of the reference satellite should consider some aspects. For example, since the reference satellite measurement is present in all system equations, it should introduce the minimum possible noise. This and other considerations lead to the rule of choice of the satellite with highest elevation for reference satellite.

The fact that a common measurement is present in all system equations leads to a non-zero correlation between the equations, that is, the variance-covariance matrix associated with the system has non-diagonal terms different than zero. A diagonal matrix could be considered for the single differences system.

As can be noted from equation (4.24), the initial phase biases and the delays from the equipment hardware to the respective antennas were cancelled. For simplicity, throughout the rest of this thesis, these terms will not be explicitly written except when their presence is significant.

4.2 POSITIONING WITH GPS

The formulation of the GPS positioning problem will now be presented. Also, some implementation details and some state-of-the-art ambiguity fixing techniques will be introduced. Although most of the formulation will be based on phase measurements, a similar approach can be used for pseudorange measurements.

4.2.1 FORMULATION

When m satellites are being tracked by both rover and reference receivers, a system of m-1 equations as in (4.24) can be formed. It should be noticed that this is not a linear system because the distances from satellites to receivers are non-linear on the position variables (which are the variables of interest). It is common to consider approximate values of the variables and then linearize the system around those values. With this process, the algorithms only have to deal with small magnitude values instead of treating directly with the full position vector and the large values of the ambiguities. Besides benefiting the computation procedure, it also allows some simplifications through linearization, has will be shown below, turning this initially quadratic system into a linear problem.

Before going through this linearization process, an intuitive perspective of this problem could be to decompose the distance between receiver and satellite in the product of the difference of the two position vectors (of the satellite and the receiver) with the unit vector of the direction defined by both positions. Equation (4.25) presents this decomposition.

$$\rho_i^k(t, t-\tau_i^k) = u_i^{k^T} \cdot \left(r^k(t-\tau_i^k) - r_i(t) \right) \tag{4.25}$$

where:

$r^k(t-\tau_i^k)$ - position vector of satellite k at instant $t-\tau_i^k$.

$r_i(t)$ - position vector of antenna of GPS receiver i, at time instant t.

u_i^k - unit vector from $r_i(t)$ to $r^k(t-\tau_i^k)$.

The problem with equation (4.25) is that the satellite and rover positions must be known with sufficient precision so that the introduced error is small enough to be discarded. Regarding the satellite-receiver geometry, the satellite position errors will have similar effects in (4.25) for both receivers if they are not too far apart from each other. The same is not true for the receiver position errors since the satellites are not usually close to each other. Figure 4.4 shows the error introduced in (4.25) against the satellite elevation angle, considering that the rover position has a horizontal offset of 5 meters.

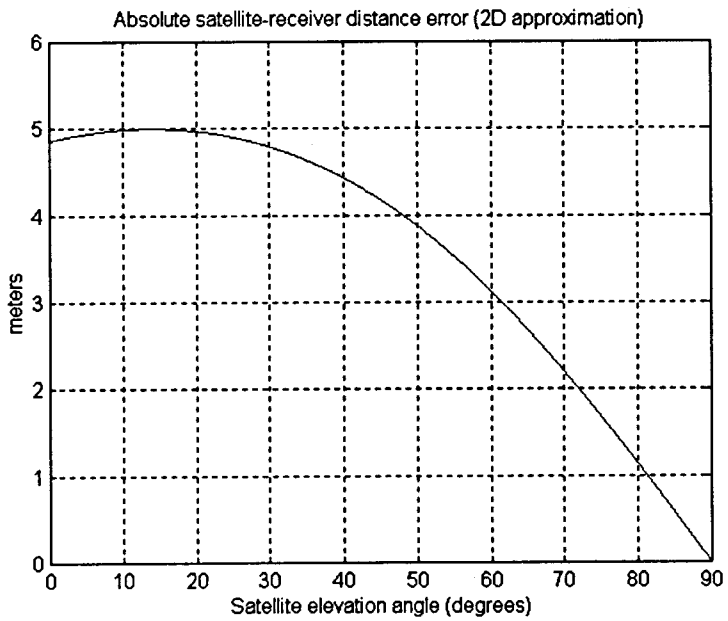


Figure 4.4 – Error introduced in (4.25) due to a 5 meter horizontal offset on the rover position.

Equation (4.25) can be used, for example, with the pseudorange measurements only to determine a raw estimate of the rover position. The determined position could be improved by iteratively replacing the new position into (4.25). For higher precision positioning, this problem must be eliminated. This is done through linearizing of the receiver to satellite distance terms around an estimated value. Knowing a raw estimate for the rover position, $\hat{r}_i$, an estimate of the rover to satellite distance can be computed, $\rho_i^k(\hat{r}_i)$, together with its associated error, $\Delta\rho_i^k$. Using a Taylor series decomposition (4.26), the first order linear approximation of the true rover to satellite distance, around the estimated distance, can be represented by (4.28), considering the determination of its gradient given in (4.27).

$$f(x)=\sum_{i=0}^{\infty}\frac{1}{i!}\cdot\frac{\partial^{(i)}f(x_o)}{\partial x^i}(x-x_o)^i \tag{4.26}$$

$$\begin{cases}\rho_i^k(r_i)=\sqrt{(r^k-r_i)^T(r^k-r_i)} & (true)\\ \rho_i^k(\hat{r}_i)=\sqrt{(r^k-\hat{r}_i)^T(r^k-\hat{r}_i)} & (estimated)\\ \dfrac{\partial\rho_i^k(r_i)}{\partial r_i}=-\dfrac{(r^k-r_i)^T}{\sqrt{(r^k-r_i)^T(r^k-r_i)}}=-u_i^{k^T}\end{cases} \tag{4.27}$$

$$\rho_i^k(r_i)\cong\rho_i^k(\hat{r}_i)-\hat{u}_i^{k^T}\cdot(r_i-\hat{r}_i) \tag{4.28}$$

In (4.28), the true unit vector from receiver to satellite was replaced by the estimated unit vector since the true rover position is not available. But this approximation does not introduce significant errors since the unit vector is only multiplied by the small difference between true and estimated rover position.

The same procedure can be applied to the other terms in the double difference equation (4.24). An estimate for the double difference ionospheric delay can be introduced, together with the tropospheric delay, and the ambiguity value. Equations (4.29) show these approximations and in (4.30) the linearized double difference equation is displayed.

$$\begin{cases}I_{ij}^{kl}=\widehat{I_{ij}^{kl}}+\Delta I_{ij}^{kl}\\ T_{ij}^{kl}=\widehat{T_{ij}^{kl}}+\Delta T_{ij}^{kl}\\ N_{ij}^{kl}=\widehat{N_{ij}^{kl}}+\Delta N_{ij}^{kl}\\ r_i(t)=\hat{r}_i(t)+\Delta r_i(t)\end{cases} \tag{4.29}$$

In these equations, the ^ symbol over some terms refers to estimated values, while its absence refers to the true values. The Δ symbol represents the offset from the estimated value to the real value.

$$\begin{vmatrix} \lambda\phi_{ij}^{kl}(t,\Delta t) - \widehat{\rho_{ij}^{kl}}(t,\Delta t) + \widehat{I_{ij}^{kl}}(t) - \widehat{T_{ij}^{kl}}(t) - \lambda\widehat{N_{ij}^{kl}} = \\ = \lambda\Delta\phi_{ij}^{kl}(t,\Delta t) \cong \left(\widehat{u_i^l}(t,t-\tau_i^l) - \widehat{u_i^k}(t,t-\tau_i^k)\right)^T \cdot \Delta r_i(t) - \\ - \Delta I_{ij}^{kl}(t) + \Delta T_{ij}^{kl}(t) + \lambda\Delta N_{ij}^{kl} + \varepsilon_{ij}^{kl}(t) \end{vmatrix} \quad (4.30)$$

In equation (4.30), the reference station position was considered to be known with enough precision.

Equation (4.30) presents the base formulation that is to be used throughout this thesis.

Considering that the ionospheric and tropospheric residuals are sufficiently small to be discarded (that is, their estimated values are precise enough), the double difference equation can be written in a more compact way.

$$\begin{vmatrix} y_{ij}^{kl}(t,\Delta t) = \lambda\Delta\phi_{ij}^{kl}(t,\Delta t) \\ b_i^{kl}(t) = \widehat{u_i^l}(t,t-\tau_i^k) - \widehat{u_i^k}(t,t-\tau_i^l) \end{vmatrix} \quad (4.31)$$

$$y_{ij}^{kl}(t,\Delta t) = b_i^{kl}(t)^T \cdot \Delta r_i(t) + \lambda N_{ij}^{kl} + \varepsilon_{ij}^{kl}(t) \quad (4.32)$$

For m tracked satellites, the equation system (4.33), of dimension m-1, can be formed (considering the satellite k as the reference satellite).

$$\begin{vmatrix} y_{ij}^{k1}(t,\Delta t) = b_i^{k1}(t)^T \cdot \Delta r_i(t) + \lambda\Delta N_{ij}^{k1} + \varepsilon_{ij}^{k1}(t) \\ y_{ij}^{k2}(t,\Delta t) = b_i^{k2}(t)^T \cdot \Delta r_i(t) + \lambda\Delta N_{ij}^{k2} + \varepsilon_{ij}^{k2}(t) \\ \cdots \\ y_{ij}^{k(k-1)}(t,\Delta t) = b_i^{k(k-1)}(t)^T \cdot \Delta r_i(t) + \lambda\Delta N_{ij}^{k(k-1)} + \varepsilon_{ij}^{k(k-1)}(t) \\ y_{ij}^{k(k+1)}(t,\Delta t) = b_i^{k(k+1)}(t)^T \cdot \Delta r_i(t) + \lambda\Delta N_{ij}^{k(k+1)} + \varepsilon_{ij}^{k(k+1)}(t) \\ \cdots \\ y_{ij}^{km}(t,\Delta t) = b_i^{km}(t)^T \cdot \Delta r_i(t) + \lambda\Delta N_{ij}^{km} + \varepsilon_{ij}^{km}(t) \end{vmatrix} \quad (4.33)$$

Writing (4.33) in matrix notation yields (4.34).

$$Y_{ij}^{k\cdot}(t,\Delta t) = B_i^{k\cdot}(t)^T \cdot \Delta r_i(t) + \lambda \Delta N_{ij}^{k\cdot} + \varepsilon_{ij}^{k\cdot}(t) \tag{4.34}$$

Notice that matrix B is dependent only on the satellite geometry (with respect to the rover receiver position).

An equivalent set of equations can be derived for the pseudorange measurements, reaching the same formulation as in (4.34) but without the ambiguity vector.

4.2.2 Ambiguity Fixing Concept

As previously mentioned, the phase measurements become a high precision pseudorange measurement if the ambiguity vector is known. Unfortunately, the determination of this term is not trivial, as equation (4.34) can illustrate. For each tracked satellite (except for the reference satellite), an integer ambiguity must be determined. This means that, when tracking m satellites, m-1 unknown ambiguity values must be determined. Also, the coordinates of the rover receiver are not known. This leads to $m+2$ unknowns for m-1 equations, leaving (4.34) with a rank deficiency of 3.

Knowing that the ambiguity vector is constant with time (if no loss of carrier lock occurs in the receiver tracking loops) gathering the measurements taken at two different time instants yields $2(m-1)$ equations for $m+5$ unknowns. At least 7 satellites would have to be continuously tracked by both receivers to eliminate the rank deficiency of this new system. But this would still not be enough because satellite geometry changes slowly with time and for two time instants relatively close (t and t_o), the matrices $B(t)$ and $B(t_o)$ would be very similar, making the system nearly undetermined and resulting on a poor estimation of the unknowns. Figure 4.5 presents the condition number of matrix A (the concatenation of both matrices $B(t)$ and $B(t_o)$), for several values of t, using a data set of 7 satellites.

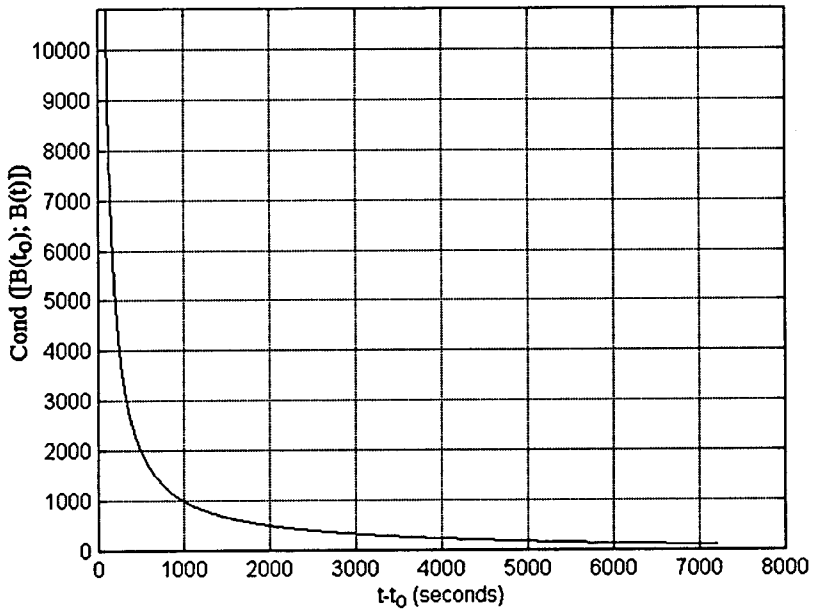


Figure 4.5 – Condition number of matrix $A=[B(t_o);B(t)]$.

Another aspect of the determination of the ambiguity vector is related with its integer nature. The use of the traditional least squares (or weighted least squares) technique results in real values for those ambiguities (usually denominated Float Ambiguity Solution) which are naturally not the true solution simply because they are not integers. Many ambiguity fixing strategies start by determining, through least squares, the float ambiguities.

It should be pointed out the importance of fixing the ambiguities to integer values. It is clear that, through the real-valued least squares adjustment, the obtained sum of squared residuals is smaller than that obtained with the true integer ambiguities. This happens because both the ambiguities and the position vector are the system real-valued unknowns. Considering the integer nature of ambiguities is entering with an extra condition that will cause the ambiguities to differ from the initially determined ones (causing the increment in the sum of squared residuals) but, on the other hand, it will cause the position vector to be more accurate than that determined with float ambiguities. The real-valued least squares process reflects on the position vector the non consideration of those integer constraints, adding an error in position.

4.2.3 Difficulties of Ambiguity Fixing

Besides the few points mentioned above about the difficulties of determining the true integer ambiguity vector, some considerations re-enforcing this matter will be now presented.

If the equations given in (4.33) were not correlated, once the float ambiguity solution was encountered (using a few epochs of data), a simple process of approximating the float values to the closest integer would have a good success rate as an ambiguity fixing method. Unfortunately, as will be shown below when describing some least squares search techniques, those equations are highly correlated and the variation of one ambiguity value cannot be considered as an isolated act since it could significantly affect the residuals of other equations in that system (4.33).

Another aspect is that of the slowly changing geometry of the satellite constellation with time. As has been mentioned, the design matrix of the equation system (4.34) is basically the same for two epochs of data close to each other in time. In order to obtain a significant variation of such matrix, it would be required to have data over a considerable period of time. For real-time high accuracy positioning, and specially when the ambiguity fixing is meant to happen as soon as possible (a few seconds) as in the case of the work being presented, it is most undesirable to wait for such a time period.

These remarks and requirements led to the development of other alternative strategies that, escaping from the traditional resolution of a full rank linear system, use particular characteristics and combinations of the data to fix the integer ambiguity vector in a very reduced time interval. But, before describing those methods, some traditional ambiguity search techniques will be presented to the reader.

Another aspect that should also be mentioned is that of the validation of the determined ambiguity vector. One thing is selecting the best ambiguity candidate according to a certain rule, another thing is validating that candidate as the correct ambiguity vector. This usually goes through some statistical treatments such as the "τ test method" or the Fisher test, and also through some more or less empirical tests. One of such tests is the determination of the ratio between the residuals of the second best candidate and the residuals of the best candidate, being fixed a threshold over which the best solution is to be validated or not. Another consideration is that, when

just a few epochs of data are to be analysed to achieve ambiguity fixing, the statistics generated by such a small set of data are naturally weaker than those achieved over a large data set. Naturally, any test based on such statistics becomes less reliable than one considering a wider set of data. This aspect will be taken into consideration when analysing the performance of the proposed methods, where larger time periods will be used, together with other testing details, to determine the reliability of the presented algorithms.

4.2.4 AMBIGUITY FIXING METHODS

Basically, two different ambiguity search approaches have been developed throughout these recent years. One performing the search on the physical 3D space, and the other searching on the ambiguity *m*-dimensional space (where *m* is the number of ambiguity values to be determined). A brief description of some of the methods that have been developed will now be presented. Although many ambiguity fixing algorithms have been created, only a few of them will be mentioned.

4.2.4.1 Ambiguity Function Search Technique

The Ambiguity Function, which can be found in more detail in [Counselman and Gourevitch, 1981], [Remondi, 1984], [Remondi, 1986], [Mader, 1990] and [Remondi, 1991], performs its search technique in the physical 3D space. Based on an initial raw position and its uncertainty (up to a certain level of confidence), it consists on forming a grid on the produced search volume and, for every grid position (x,y,z) the calculated GPS measurements from that point to the satellites are compared with the actually received GPS measurements. This comparison is based on equation (4.35) which will present a high value when there is a good agreement between the position and the measurements.

$$A(x,y,z) = \sum_k \left\| \sum_j e^{i2\pi\left[\phi_{obs}^{kj} - \phi_{calc}^{kj}(x,y,z)\right]} \right\| \tag{4.35}$$

The problem with algorithms based on searching through the physical space is that the grid must be sufficiently thin in order to obtain the desired accuracy. Also, the initial raw position has usually a significant uncertainty associated, leading to a large search volume with a small grid spacing, producing a huge number of possible candidates. This situation is not well suited for real-time processing since the determination of the initial ambiguities would take plenty of processing time. One positive aspect of the Ambiguity Function method is that it is immune to cycle-slips.

4.2.4.2 Least Squares Search Technique

The alternative to searching in the physical space is to consider the possible intervals for each ambiguity value and to check each combination of ambiguities against the collected measurements. With this method, instead of searching in the 3D physical space, the search is performed in the m-dimensional ambiguity space (being m the number of ambiguity values to be determined). The Least Squares Search Technique starts with defining the range for each ambiguity, and every combination of those ambiguities is replaced on the measurement equations, leaving some residuals. The best candidate is the one that presents the smallest sum of squared residuals (or weighted residuals), according to a certain metric.

Compared with physical space search methods, although the grid spacing (with the size of one wavelength) is now higher than the used in the former method, the number of variables increases (usually, m is higher than 3). The set of ambiguity combinations is therefore considerable and ambiguity fixing is still computationally demanding.

Several authors have published algorithms based on this strategy. Only a few will now be referred. In [Hatch 1990], a reduction of the ambiguity search space is performed by dividing the ambiguity values in two sets – one of the independent ambiguities (the primary set), and other with the dependent ambiguities (the secondary set). As can be easily seen, considering double differences ambiguities, only three ambiguity values are independent since only three measurement equations are needed to determine the 3D position of the rover antenna. The inclusion of the other m-3 ambiguities will only add redundancy. Based on this fact, this method performs the search on the primary set (using only a small number of ambiguity

combinations since only three values are used), and uses the residuals of the secondary set of equations to select the best combination.

In terms of computational effort, this method shows good characteristics for real-time implementation. But, due to errors intrinsic to the measurement equations, it is possible that one or more combination of m ambiguities, not included in the set of combinations provided only by the primary set, would lead also to a small sum of squared residuals. In fact, combinations leading to a sum of squared residuals under a certain threshold should be considered as possible candidates (using, afterwards, a validation heuristic for the best possible candidate, such as the ratio between the sum of squared residuals of the second best and best combinations, which should be higher than a certain value). With this method, the true combination could be left out of the tried combinations simply because no variation is considered for the secondary set of ambiguities, these are calculated based on the primary set.

Least squares full-dimensional search methods have also been developed (see, for example, [Euler and Landau, 1992] and [Wübbena, 1991]). In this case, the whole set of m ambiguities is allowed to vary, but instead of examining every possibly generated combination, branch-and-bound algorithms are used to reject as soon as possible some sub-sets of combinations, saving a lot of computational time.

Searching in the m-dimensional integer ambiguity space is usually preceded with the least squares determination of the float ambiguity vector, together with its variance-covariance matrix. Since it is often to exist a high correlation between double difference ambiguity values (their float estimates), the determined variance-covariance matrix is not diagonal and the sub-space around the float ambiguity vector, where the probability of finding the true integer ambiguity vector is below a certain threshold, becomes an hyper-ellipsoid instead of a hyper-sphere. Figure 4.6 shows the desired and actual search spaces for the illustrative two-dimensional case.

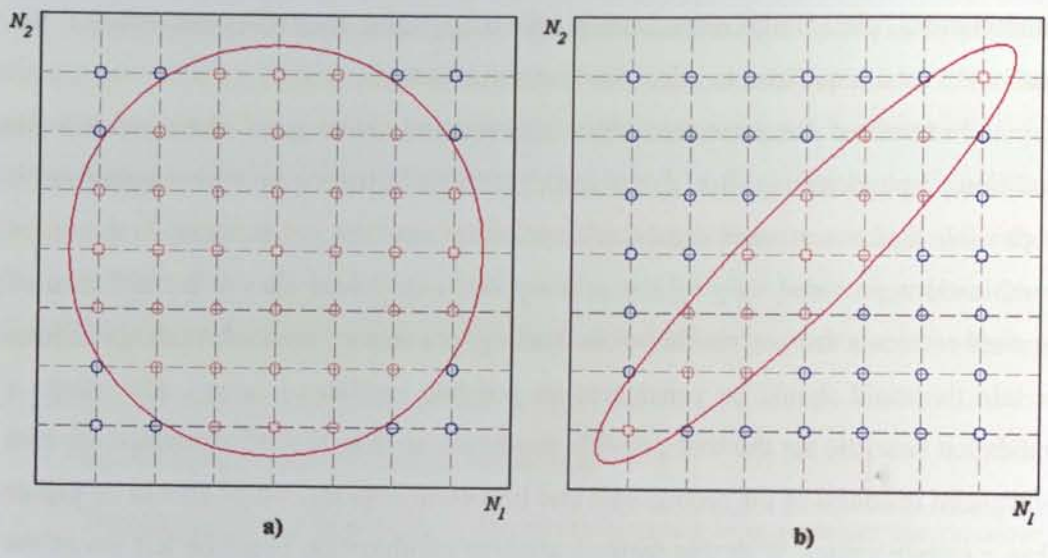


Figure 4.6 – a) Ideal hyper-spherical search space. b) Real hyper-ellipsoidal search space.

The hyper-ellipsoidal search space is given by (4.36), where C_N is the float ambiguity vector variance-covariance matrix, N_f is the determined float ambiguity vector, and $\chi^2_{m,1-\alpha}$ is the chi-squares percentile for m degrees of freedom and confidence level $1-\alpha$.

$$\left\{N \in \mathbb{R}^m : (N-N_f)^T C_N^{-1} (N-N_f) \leq \chi^2_{m,1-\alpha}\right\} \tag{4.36}$$

In terms of implementation on a software algorithm, the easiest way to form the search space is to consider it to be a hyper-cube. In the case of figure 4.6.a), the overload of extra ambiguity combinations caused by this approximation is not considerable. But in the real case of figure 4.6.b), it can be seen that too many unnecessary ambiguity combinations will be examined, causing a loss of efficiency in the algorithm. Figure 4.7 illustrates the effect of this approximation on both cases.

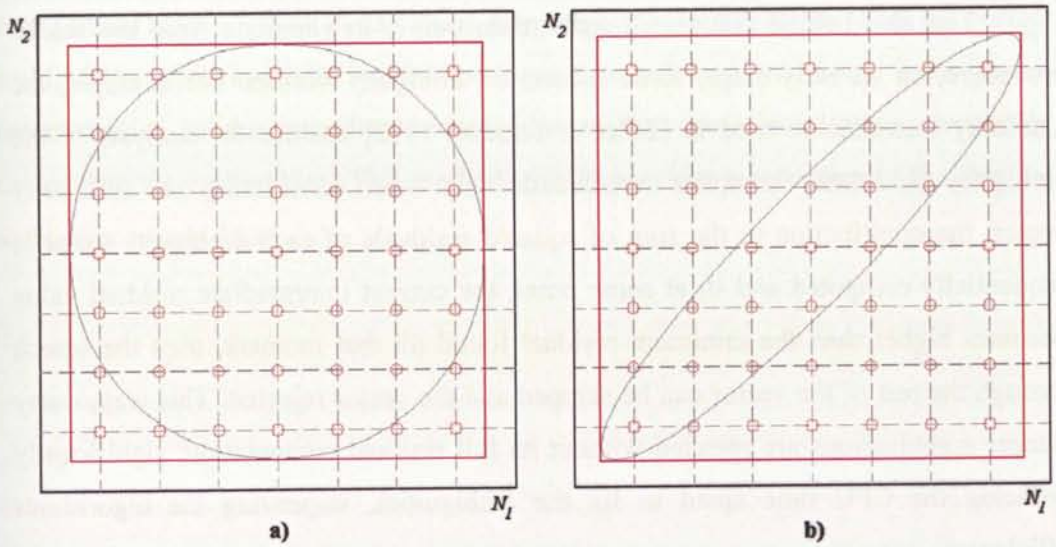


Figure 4.7 – Approximation of the ideal and real search spaces by an hyper-cube.

Many full-dimensional search strategies aim to the search space reduction, saving lots of processing time. A Cholesky-factorisation of the variance-covariance matrix is often performed in order to further limit the search space. [Ober, 1993], presenting the basis reduction method, and [Euler & Landau, 1992] are examples of this methodology. Figure 4.8 shows the considerable reduction of possible candidates achieved with these methods. Important processing time is saved with the application of these strategies.

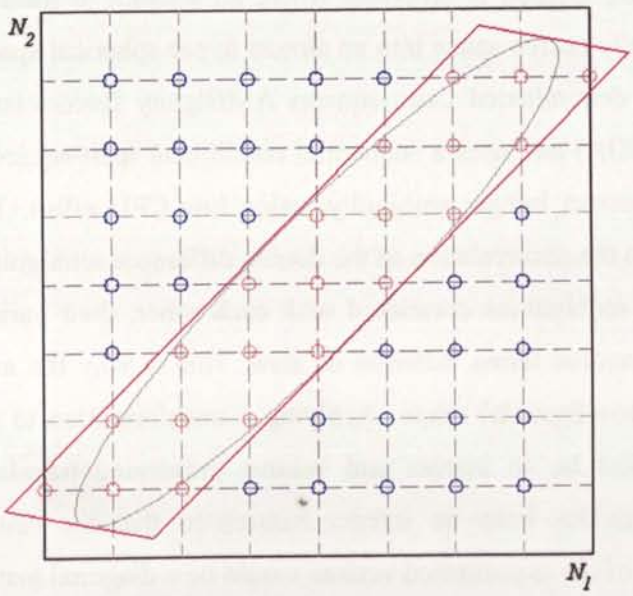


Figure 4.8 – Search space reduction with Cholesky-factorisation based method.

The idea behind this search space reduction is to eliminate from the search procedure, on an early stage, some subsets of ambiguity vectors. For example, the Cholesky factorisation used in [Euler & Landau, 1992] enables the analysis of the ambiguity candidates through a certain order that, when considering one ambiguity vector, the contribution to the sum of squared residuals of each ambiguity value is sequentially computed and if, at some point, the current intermediate residual value becomes higher than the minimum residual found till that moment, then the search through the rest of the vector can be skipped and the vector rejected. This way, many integer combinations are rejected without its full residual computation, significantly reducing the CPU time spent to fix the ambiguities, improving the algorithm's efficiency.

The Fast Ambiguity Resolution Approach (or simply FARA), presented by [Frei and Beutler, 1990] uses statistic criteria to determine the ambiguity search space, also based on the initial float ambiguity solution and its characteristics. Initially, an individual range for each integer ambiguity value is determined and then the candidate vectors are formed and organised in a specific order. A statistical criterion is then used analysing the difference between two ambiguity values. When one of such differences does not satisfy the statistic criterion, the whole set of ambiguity vectors containing those two ambiguity values is skipped and rejected.

In [Teunissen, 1993], [Teunissen, 1994] and [Teunissen and Tiberius, 1994], an ambiguity fixing method is proposed where an attempt to transform the hyper-ellipsoidal ambiguity search space into an almost hyper-spherical space is performed. This method was denominated Least-squares AMBiguity Decorrelation Adjustment (or simply LAMBDA) and uses a sequential conditional least-squares adjustment in order to fix the correct integer ambiguity, using low CPU effort. The idea of this method is based on the decorrelation of the double difference ambiguities. Being these double difference ambiguities correlated with each other, their variance-covariance matrix has non-diagonal terms different of zero. This is why the ambiguity search space has an hyper-ellipsoidal shape. Applying a transformation to these ambiguity vectors (which must be an integer and volume preserving transformation so the transformed ambiguities keep an integer nature) so that the resulting variance-covariance matrix of the transformed vectors would be a diagonal matrix would mean that these new ambiguities would be uncorrelated (the new search space would have an hyper-spherical shape) meaning that, in principle, a simple rounding of the

transformed float solution to its closest integer vector would suffice to fix the correct ambiguities (applying, afterwards, the inverse transformation). Some cautions are recommended in this rounding process due to the usual inability to completely decorrelate the ambiguities. This method usually provides a reduction of the original ambiguity search space.

CHAPTER 5

ALGORITHMS FOR RTK GPS PROCESSING

After having described the mathematical models associated with the GPS measurements, the presentation of the GPS processing algorithms that were developed within this work will now be given. These algorithms are especially dedicated to the situation where the rover receiver may be moving, with no specific indication of its initial position or of its dynamics, and for which a highly accurate positioning is required in a matter of a few seconds. This situation is usually referred has Real-Time Kinematic GPS positioning (RTK). There are some particularities that are expected to occur though, such as a considerably high data sampling rate, for example. These requirements will be presented through the algorithm presentation but, as will be noticeable, these are natural characteristics of kinematic GPS surveys.

Some illustrative results will be shown, together with robustness analysis under certain conditions. Also, the sensitive points of the presented methods will be mentioned. One of which is the growing influence of the ionospheric effect as the baseline length increases. A possible solution to go around that problem is to model the ionospheric effect by means of a reference station network. This subject is proposed and verified through the presentation of a simple example with two reference stations.

The chapter will end with the description of a method to determine the 3D vector between two very close antennas which keep a constant distance between them. As will be seen, these vectors are very useful as an unbiased estimate of vehicle attitude, eliminating the drift from the navigation solution when considering the integration with an IMU sensor.

5.1 Proposed Positioning Algorithms

Since this thesis focuses on real-time kinematic applications, some characteristics of this type of survey were considered in the development of specific algorithms. One such consideration is that the time interval between two consecutive epochs is relatively short (one second or less, for example). In this subsection, the methodologies developed throughout this work will be presented, together with some results and reliability tests.

5.1.1 Cycle Slip Fixing Algorithm

One of the first steps when dealing with carrier phase measurement is to check its validity. For several reasons, the carrier tracking loops of the receiver can sometimes skip some carrier cycles causing a discontinuity on the phase measurement. Every time this occurs, the respective integer ambiguity value has to be recalculated in order to account for the cycle slip. Since the determination of the integer ambiguity values is not trivial, advantages are obtained if the cycle slip detection and correction is performed in order to constantly supply the positioning algorithms with good phase measurements. Many researchers have studied this cycle-slip detection/fixing problem (see, for instance, [Goad, 1986] and [Bastos and Landau, 1988]). In the following, an algorithm to detect and correct cycle slips is presented, together with performance test results.

Since the difference between L1 and L2 phase measurements reflects only a scaled value of the ionospheric delay together with the ambiguity difference on both carriers, for short time intervals the variation of that difference can be used to detect cycle slips. Equation (5.1) presents this relation. Knowing that the ionospheric delay presents a relatively slow variation, on the occurrence of a cycle slip this quantity will show an abnormal jump which can be detected. Equation (5.2) shows this cycle slip detection condition.

$$\begin{aligned}\lambda_1\phi_1(t)-\lambda_2\phi_2(t) &= -I_1\left(1-\frac{f_1^2}{f_2^2}\right)+\lambda_1N_1-\lambda_2N_2+\varepsilon_{12}\\ &\simeq 0.647\cdot I_1+\lambda_1N_1-\lambda_2N_2+\varepsilon_{12}\end{aligned} \tag{5.1}$$

$$\left|\frac{(\lambda_1\phi_1(t)-\lambda_2\phi_2(t))-(\lambda_1\phi_1(t-\Delta t)-\lambda_2\phi_2(t-\Delta t))}{\Delta t}\right| > K_{cs} \tag{5.2}$$

K_{cs} is a constant determined empirically, dependent on the time interval Δt.

This cycle slip detection scheme has some drawbacks. First of all, it does not tell if the cycle slip occurred only on L1, or on L2, or even on both carriers. Another aspect is that some combinations of cycle slips are undetectable. For example, a jump of 77 cycles on ϕ_1 and one of 60 cycles on ϕ_2 will not be sensed by this model.

For these reasons, a complementary test model has to be used. Following the analysis of [Lu et al., 1995], equation (5.3) presents the quantity to test whether or not a cycle slip occurred on L1.

$$\left|\phi_1(t)-\left(\phi_1(t-\Delta t)+\frac{(D(t)+D(t-\Delta t))\cdot\Delta t}{2}\right)\right| > 3\sigma_{cs} \tag{5.3}$$

σ_{cs} is the standard deviation based on a sliding window of the past values obtained from the first member of equation (5.3). $D(t)$ is the doppler measurement in Hertz, at instant t.

Being equation (5.3) based on a linear approximation, it is a noisier detection model than that of (5.2), but it reflects jumps on only one carrier phase measurement.

These models are only used to detect cycle slips. The next step is to validate and correct the detected jumps. Validation is required because noise is always present in the data and false cycle slips can be detected.

When a possible cycle slip is detected, a set of reasonable L1 and L2 variations is generated, considering the standard deviation determined by the sliding window procedure associated with (5.3). From this set of L1 and L2 possible jumps, the pairs that do not verify condition (5.2) are excluded. The parameter K_{cs} in (5.2) has to be well tuned in order to allow that only one candidate verifies that condition.

The standard deviation produced by the sliding window has also its influence because it is desirable to have the least possible candidates, and the wider the search interval gets, the larger is the number of possible cycle-slip candidates. Figure 5.1 clarifies this strategy. The set of candidates is depicted through the red dots and the two lines represent the validation condition (5.2). Due to the inclination of these lines (which is λ_1/λ_2), valid candidate pairs are not in the vicinity of each other, making this method able to detect the true candidate if the initial set is narrow enough. In situations where two much noise is accompanying the data, cycle-slip fixing through this method can fail.

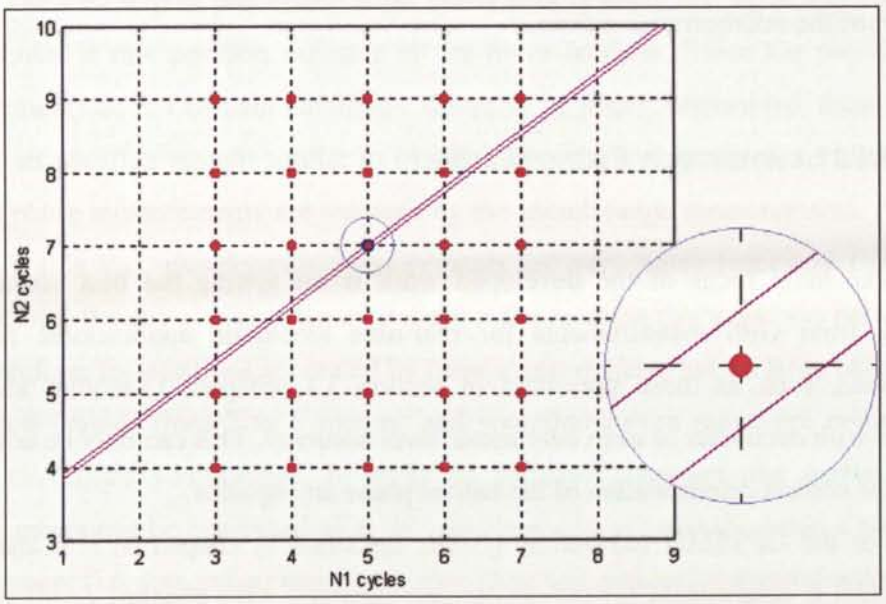


Figure 5.1 – Graphical representation of the cycle-slip fixing method.

Several tests over long data sets were performed in order to check the efficiency of this method, either with real cycle-slips and with simulated cycle-slips (jumps that were deliberately introduced in the data). Table 5.1 shows the overall performance obtained from these tests.

Table 5.1 – Cycle-slip fixing method performance.

	L1	L2
Correction Success Rate	95.8%	97.2%

It should be again noticed that some assumptions were taken in the development of this method. The main assumption was that the data sampling rate

would be sufficiently high in order to consider that the ionosphere effects change slowly from epoch to epoch and also that the phase linearization through the doppler measurement would be valid. These conditions are often inherent to kinematic applications. One advantage of this method is that it enables detection and fixing of cycle-slips individually for each receiver, without requiring any combination between data from different satellites or different receivers. This allows fixing cycle-slips on an early stage of the GPS processing software (right after data acquisition and initial filtering), removing from the following algorithms the burden of handling that problem.

This method is easily implemented on a real-time algorithm, consuming a very small cut of the microprocessor time.

5.1.2 L1 Ambiguity Fixing Method

The main focus of the developed work is on getting the best positioning accuracy from GPS measurements for real-time kinematic applications. Several applications, such as those presented in section 3.1, chapter 3, require absolute positions with decimeter or even centimeter level accuracy. This can only be achieved though the correct determination of the carrier phase ambiguities.

For the GPS/IMU navigation system described in chapter 3, it is the GPS solution that is determinant for the positioning accuracy. This absolute positioning is of great importance for the final navigation solution since it is fed into the Kalman filter that combines the IMU data with the GPS results. The IMU is a dead-reckoning equipment, therefore its stand alone absolute precision suffers rapidly from drifts caused by integration of its measurements through time. In this navigation system, GPS is the base provider of absolute positions.

In order to achieve the highest positioning accuracy with GPS, L1 carrier phase ambiguities have to be solved first so that the carrier phase measurements can behave as highly accurate pseudoranges. It should be mentioned that, when integrating with the IMU measurements, instead of feeding the final DGPS positions into the Kalman filter, the double difference equations for each satellite can be used [Tomé, 2002], but also in this case the carrier phase ambiguities have to be known.

This section describes the method developed and implemented to determine the L1 carrier phase ambiguities for applications with the characteristics earlier described. It assumes that dual-frequency receivers are available in the reference and rover stations. One of the method's objectives is to determine those ambiguities almost instantaneously and without any movement restriction for that purpose. This is to minimise initialisation time, or recovery time after some signal tracking loss that may happen, for example, while an aircraft turns with high banking.

5.1.2.1 Initial Position Estimate

The first step in processing, after initial data filtering and cycle slip fixing, is to determine a raw position estimate of the rover receiver. Since the pseudorange measurements do not contain ambiguity values to be priory determined, these can be used in an equation system similar to (4.33), where the ambiguity vector disappears and the phase measurements are replaced by the pseudorange measurements. As seen before in this text, pseudorange measurements are very noisy (specially C/A code pseudorange, the one available for civil users at the moment this work was performed) and, therefore, the positions generated by these measurements have a large uncertainty associated (values from 2 to 5 meters, and sometimes even more, are common in DGPS C/A code positioning). In order to increase precision, the carrier phase measurements can be combined with the pseudoranges in order to obtain a smoother measurement (i.e. less noisy) that is still free from any ambiguity determination. This process is usually called *code smoothing*. The implemented smoothing algorithm will now be presented, together with some results from which the obtained accuracy can be retrieved.

Basically, the carrier phase measurement has the same behaviour as the pseudorange measurement except that:

- it has an initial number of unknown cycles (ambiguity), and the pseudorange has not;
- it has a much lower noise level than the pseudorange;
- the ionospheric effect is symmetric on both measurements.

Given the pseudorange and carrier phase measurements for a sequence of epochs, from both L1 and L2 carriers, the ionospheric effect variation (with respect to the L1 carrier) can be determined from equation (5.1), relatively to the first epoch of

the sequence. Since the ambiguity terms of that equation do not change with time, subtracting the value of (5.1) for the first epoch to the values for the following epochs (and dividing by ~0.647) yields the variation of the ionospheric effect on L1. Adding the calculated ionospheric variation to the sequence of carrier phase measurements, and subtracting it from the pseudorange sequence, results on two sets of measurement where the noise level difference still exists but, besides that, only an initial offset between them makes the difference (corresponding to the ambiguity value plus a float value of the ionospheric difference for the first epoch). With these two sequences of data (modified pseudorange and modified carrier phase measurements), it is possible to estimate that offset between them in the sense of least squares (the offset is determined with the current and past (up to a point) epochs). The resulting measurement comes from adding that determined constant to the modified carrier phase sequence. Figure 5.2 shows the improvement that smoothing introduces in the code measurement.

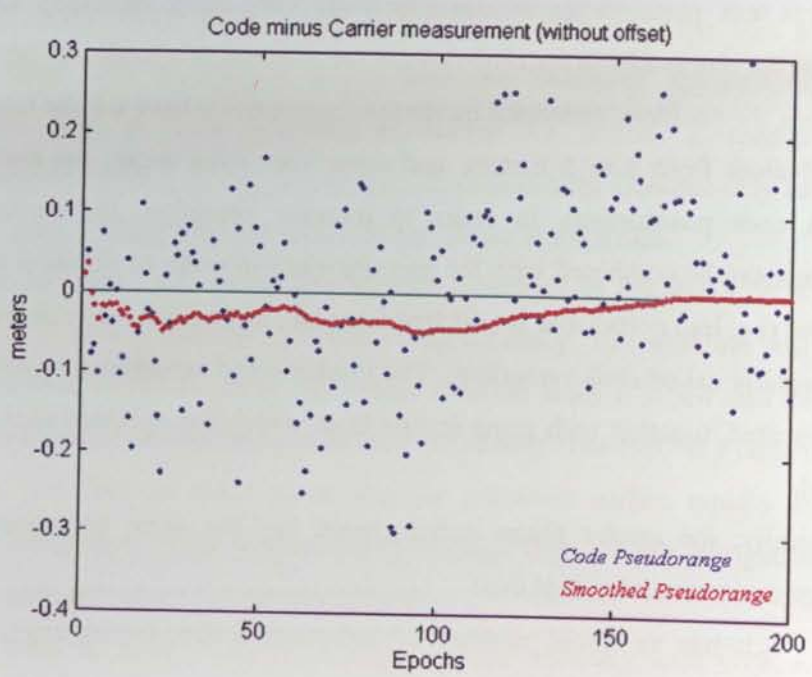


Figure 5.2 – Code pseudorange smoothing process.

With the resulting measurement, a single difference (between receivers) equation system is formed (shown in (5.4)) and the position estimate of the rover antenna is determined, together with the clock offset between both receivers. In order

to improve precision, the initial offsets associated with these modified measurements are tuned following a residual minimisation.

$$\begin{cases} y_{ij}^1(t,\Delta t) = b_i^1(t)^T \cdot \Delta r_i(t) + \Delta_{\Delta t} + \varepsilon_{ij}^1(t) \\ y_{ij}^2(t,\Delta t) = b_i^2(t)^T \cdot \Delta r_i(t) + \Delta_{\Delta t} + \varepsilon_{ij}^2(t) \\ \cdots \\ y_{ij}^m(t,\Delta t) = b_i^m(t)^T \cdot \Delta r_i(t) + \Delta_{\Delta t} + \varepsilon_{ij}^m(t) \end{cases} \quad (5.4)$$

In equation (5.4), the first member values are determined from subtracting the estimated terms in single difference mode from the resulting measurements. The initial position estimate entering this equation can be, for example, the position given by the receiver in stand-alone mode. $\Delta_{\Delta t}$ is the error associated to the estimation of Δt, the difference between the clock offset of the rover receiver with the clock offset of the reference receiver.

Several tests were performed in order to assess this method's accuracy. For example, figure 5.3 shows the horizontal position error determined with this method for a static receiver over 2 hours, at 1Hz.

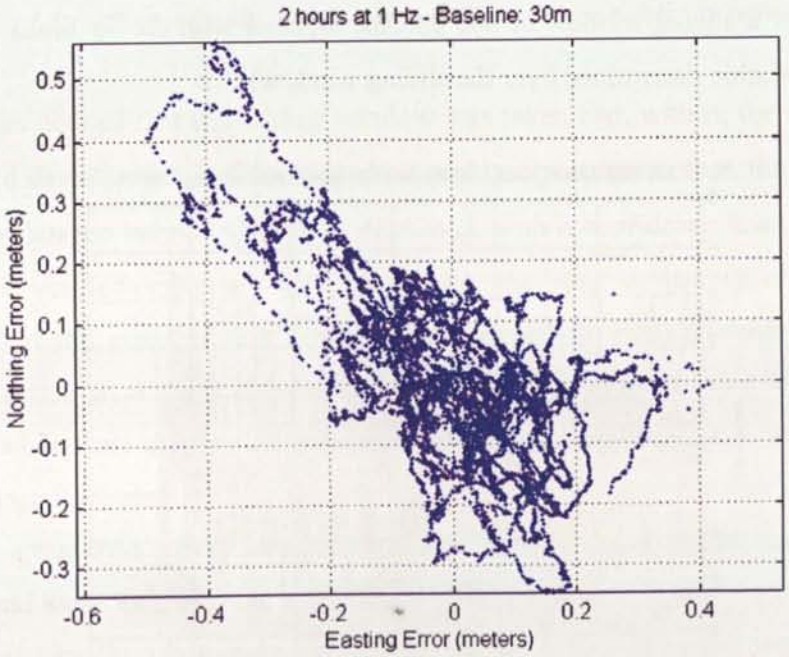


Figure 5.3 – Smoothed DGPS horizontal position error, an example.

5.1.2.2 Wide-Laning

After determining the raw position of the rover receiver, a step forward in precision is taken with the determination of the wide-lane ambiguities. Fixing these ambiguities is simpler than fixing directly L1 ambiguities due to the magnitude of the wide-lane wave length. As shall be shown below, the knowledge of the wide-lane integer ambiguities enables an easier determination of the L1 carrier phase integer ambiguities.

Considering that both pseudorange and carrier phase measurements are available on both frequencies L1 and L2, the combination presented by equation (5.5) provides a noisy estimate of those wide-lane double difference ambiguities.

$$\phi_{1,ij}^{kl}(t,\Delta t)-\phi_{2,ij}^{kl}(t,\Delta t)-\frac{P_{1,ij}^{kl}(t,\Delta t)+P_{2,ij}^{kl}(t,\Delta t)}{2\lambda_w}\cong N_{w,ij}^{kl}+\varepsilon_{w,ij}^{kl}(t) \qquad (5.5)$$

In this combination, the geometry and tropospheric delay terms are completely cancelled, and the ionospheric double difference delay is attenuated up to 4.7% of the total L1 double difference ionospheric delay. The problem is that its noise level is considerable, as shown in figure 5.4. Also shown is the average of the resulting quantity over a sliding window of 800 epochs, together with the 3σ limits (being the standard deviation determined over the sliding window).

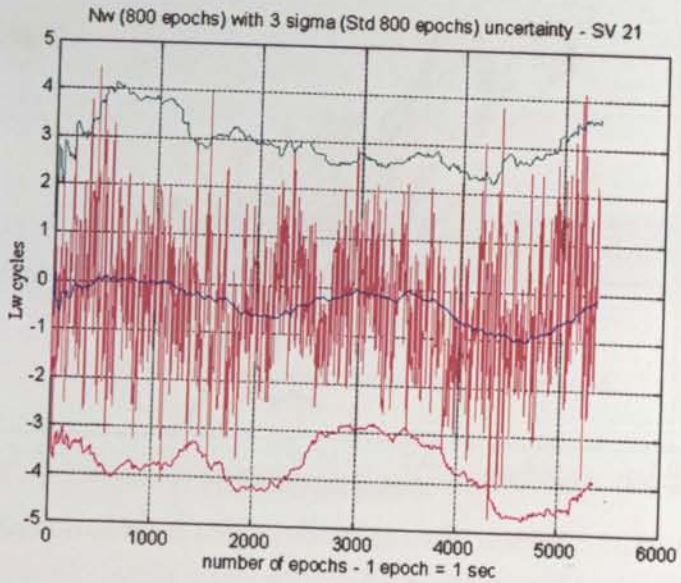


Figure 5.4 – Wide-lane ambiguity instantaneous estimate through equation (5.5).

Since the noise associated with this estimate appears to have white noise characteristics with zero mean, averaging that estimate throughout a time interval leads to a better estimate of the ambiguities. But sometimes that estimate does not behave as expected and instead of a zero mean process, an offset appears, and also some drifting patterns were found. Several tests were performed in order to identify the nature of this phenomenon, processing with different GPS receivers and with different baseline lengths and even with a zero baseline (using an antenna splitter to connect the same antenna to two different receivers), but it did not became clear what was causing this. Figure 5.5 shows two situations where this occurred.

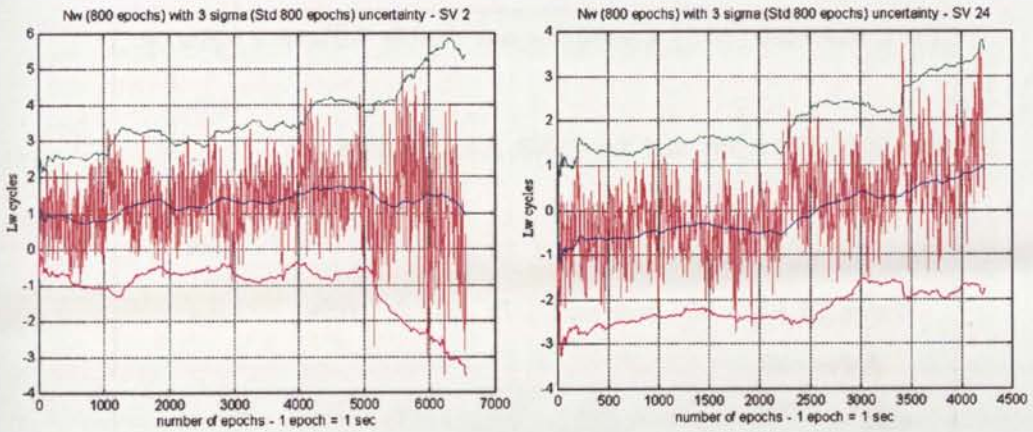


Figure 5.5 – Offset and drifting phenomena in the wide-lane ambiguity estimate.

It was noticed that if a sliding window was taken and, with it, the mean (N_w) and standard deviation (σ_w) of the wide-lane ambiguity estimate, then the true value would be within the interval [N_w-3σ_w , N_w+3σ_w], with a confidence level of 99.9%. This fact was verified empirically after extensively analysing several sets of data.

One of the goals of this system's implementation was to generate an high accurate position in a short time period. This is an important issue in real-time navigation since there can be situations where the cost of waiting some minutes for a precise navigation solution can be high. For example, considering that an aircraft, performing a real-time survey of some kind over a certain area, would make an high bank turn and loose lock of some satellites, it would be unpractical to wait much time for new positions (in one minute, an aircraft flying at 70 meters per second would travel 4.2 km which would be left uncovered if that would be the time to regain high precision navigation solutions). Aiming for ambiguity fixing with only a few seconds

of data (10 or less), a problem regarding reliability of the calculated statistics comes into consideration. Determining the standard deviation of the wide-lane ambiguity estimate with only a few seconds of data can lead to an inaccurate interval for that estimate. To go around this problem, some heuristics are also considered in the model, working in parallel with the statistics, so that a more robust algorithm is generated. After analysing several set of data, one proposed heuristic for the range of each wide-lane ambiguity (around the mean value) is simply to apply fixed ranges according to the elevation angles of the satellites and the signal-to-noise ratios of the measurements. Figure 5.6 presents one such heuristic.

For 2 satellites, i and j, composing one double difference equation:

```
if min(El_i,El_j) > 60° and min(SNR_i,SNR_j) > 50%
  ΔNw = ±1
else
  if min(El_i,El_j) < 35° and min(SNR_i,SNR_j) < 30%
    ΔNw = ±3
  else
    ΔNw = ±2
```

El - satellite elevation angle.
SNR - measurement Signal-to-Noise Ratio.
ΔNw - wide-lane ambiguity interval around mean.

Figure 5.6 – Heuristic proposed to fix the double difference wide-lane ambiguity ranges.

This method was implemented in order to determine a set of candidates for the wide-lane double difference integer ambiguities. To reduce this set of candidates, some of them are eliminated considering the distance between the position they would generate and the one determined previously through the code smoothed algorithm (and the assumed accuracy of the latter). Those candidates positioning the antenna outside the valid region are ignored. Figure 5.7 shows the number of candidates the heuristic given in figure 5.6 would generate for a set of data of 1.8 hours (an aircraft test flight), each second, tracking 6 satellites. Figure 5.8 shows the fitting of the wide-

lane ambiguity range given by the heuristic, against the instantaneous real-valued ambiguity determined by (5.5), for one satellite. Considering the raw position determined each second and its expected accuracy, figure 5.9 presents the number of candidates fitting the position valid area. Since the wide-lane combination is equivalent to a carrier phase measurement with wave length of 86 cm, the reduction of candidates is very significant, increasing the algorithm performance.

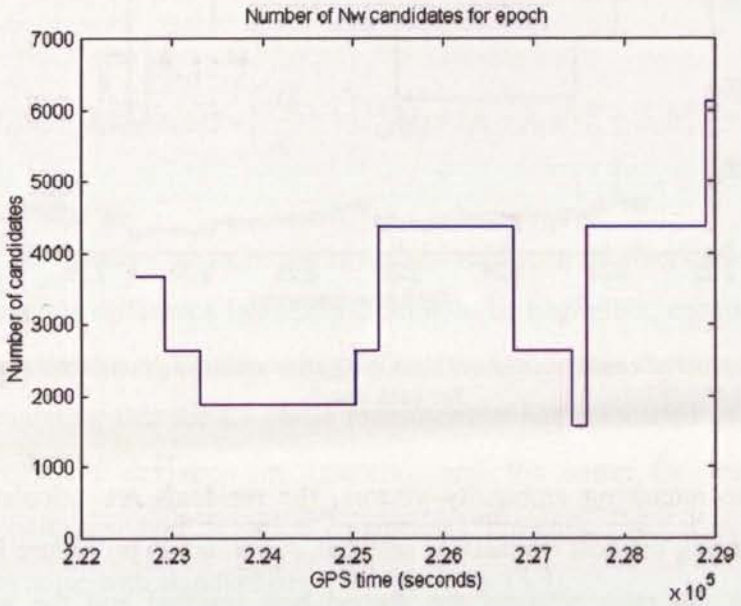


Figure 5.7 – Number of candidate vectors generated by the presented heuristic, for each epoch.

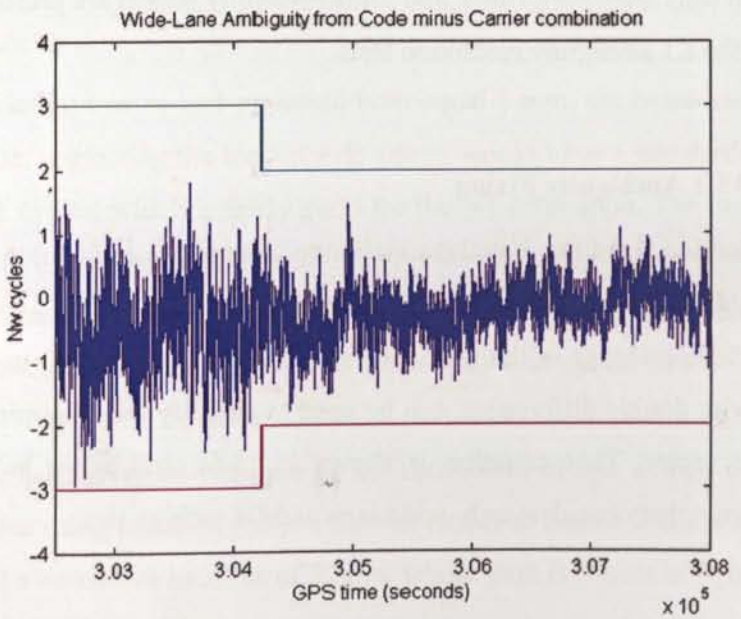


Figure 5.8 – Fitting of the ambiguity range determined by the heuristic, for one satellite.

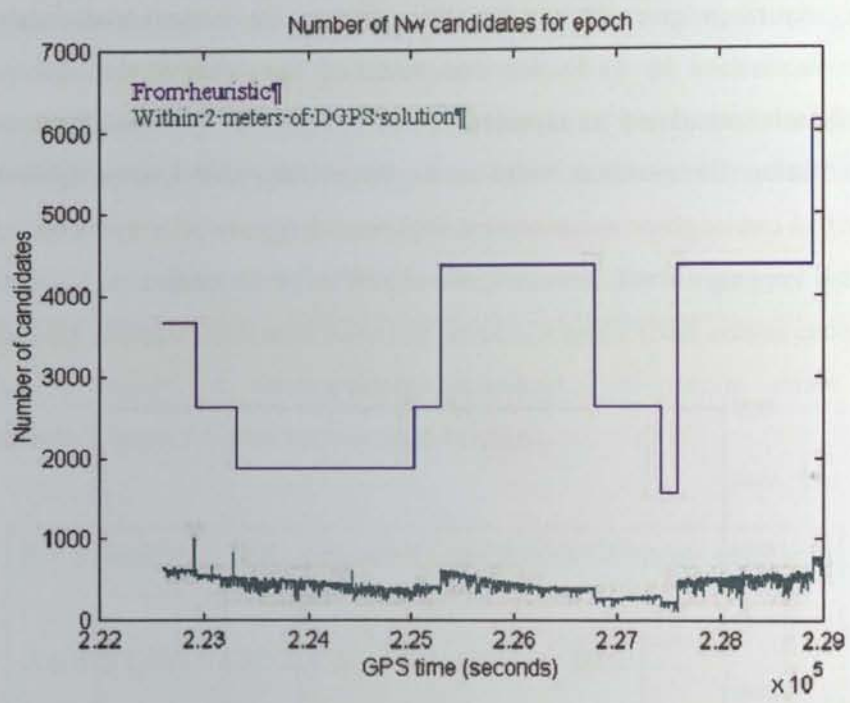


Figure 5.9 – Number of candidate vectors remaining after validating their determined positions, for each epoch.

For the remaining ambiguity vectors, the residuals are calculated and the solution presenting the best residuals is selected. A validation procedure is performed by calculating the ratio between the second best residual and the selected best residual, considering the selection valid if that ratio is higher than 2.

Several tests were performed, and some reliability results are presented below together with the L1 ambiguity resolution tests.

5.1.2.3 L1 Ambiguity Fixing

After having fixed the wide-lane ambiguity vector, the calculation of the more precise L1 ambiguity vector comes into consideration.

With the knowledge of the wide-lane ambiguities, an equation similar to (5.1), but working with double differences, can be used to simplify the determination of the L1 ambiguity vector. That equation is shown in (5.6), and again in (5.8) in an equivalent format that considers only wide-lane and L1 ambiguities.

$$\lambda_1\phi_{1,ij}^{kl}(t,\Delta t)-\lambda_2\phi_{2,ij}^{kl}(t,\Delta t)=\left(\frac{\lambda_2^2}{\lambda_1^2}-1\right)I_{1,ij}^{kl}(t)+\lambda_1 N_{1,ij}^{kl}-\lambda_2 N_{2,ij}^{kl}+\varepsilon_{12,ij}^{kl}(t) \quad (5.6)$$

Knowing the relation between L1, L2 and Lw ambiguities given in (5.7), the pretended equation (5.8) is formed.

$$N_{w,ij}^{kl}=N_{1,ij}^{kl}-N_{2,ij}^{kl} \quad (5.7)$$

$$\lambda_1\phi_{1,ij}^{kl}(t,\Delta t)-\lambda_2\phi_{2,ij}^{kl}(t,\Delta t)=\left(\frac{\lambda_2^2}{\lambda_1^2}-1\right)I_{1,ij}^{kl}(t)+(\lambda_1-\lambda_2)N_{1,ij}^{kl}+\lambda_2 N_{w,ij}^{kl}+\varepsilon_{12,ij}^{kl}(t) \quad (5.8)$$

When the baseline between the rover and reference receivers is not too long, allowing the double difference ionospheric delay to be negligible, equation (5.8) can be used as an estimator of the L1 ambiguity vector. Once again there is the presence of noise. Considering that the L1 phase measurement has associated gaussian white noise with standard deviation σ_1 (meters), and the same for the L2 phase measurement, with standard deviation σ_2 (meters), the noise present in (5.8) is still white gaussian noise with standard deviation given by (5.9).

$$\sigma_{\varepsilon_{12,ij}^{kl}}=2\sqrt{\sigma_1^2+\sigma_2^2} \quad (5.9)$$

Considering that σ_1 and σ_2 would both equal 1 mm, the noise associated with the N_1 estimate, neglecting the ionospheric effect, would have a standard deviation of about 0.05 L1 cycles, which is fairly good for the N1 estimation. The problem is that there is a factor of 12 relating the double difference ionospheric effect (in meters) and the double difference L1 ambiguity (in L1 cycles). An error of 2 cm in the ionospheric double differentiated delay would lead to an error of 0.24 cycles in the L1 ambiguity estimate.

Figure 5.10 gives an example of the estimation of one double difference L1 ambiguity value using equation (5.8). This was retrieved from a 2 hours aircraft flight data, reaching a maximum baseline of 37 km, whose path is shown in figure 5.10.b).

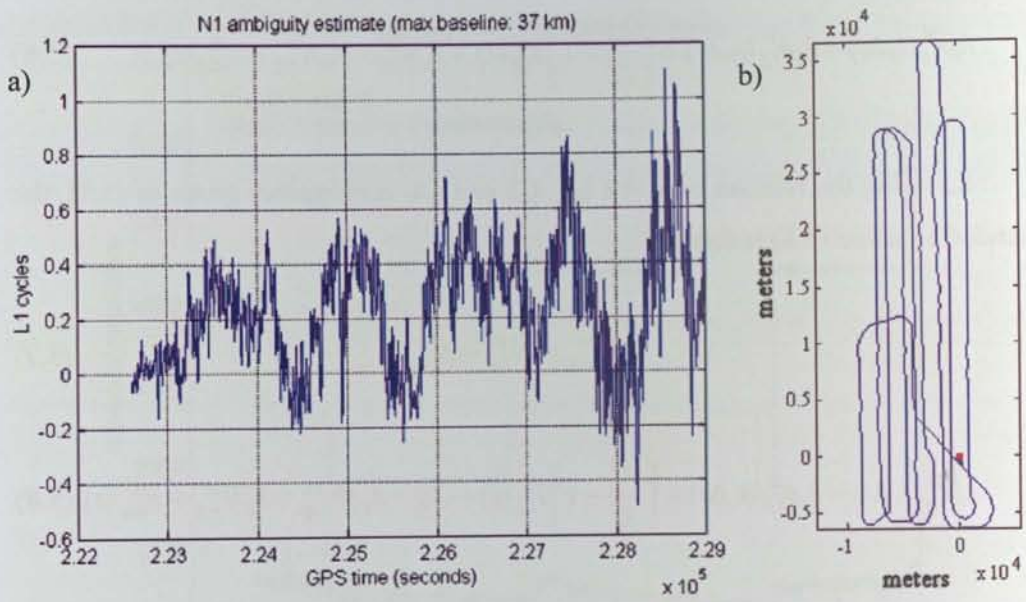


Figure 5.10 – a) L1 ambiguity value estimation. b) Respective flight path.

Based on this estimate, a similar heuristic to the one presented in figure 5.6 is applied to determine the range for each L1 ambiguity value. The resulting search space is further reduced eliminating those vectors that lead to a L1 position outside the region of the wide-lane position.

With the resulting L1 search space, the fixing criterion to determine the best ambiguity candidate is the weighted function given by equation (5.10).

$$\min_{N_1} \quad \alpha_1 R_{1,ij}^{kl} + \alpha_2 R_{2,ij}^{kl} + \alpha_d D_{1,2} \tag{5.10}$$

The α terms are weighting factors, and the R_1 and R_2 terms are the residuals resulting from the L1 and L2 double difference equations. The L2 equations are also considered because, once the wide-lane ambiguities are determined, the L2 ambiguities are just a function of the L1 ambiguities, as is shown in equation (5.7).

The term $D_{1,2}$ is the position distance between the L1 and the L2 solutions, for each N_1 ambiguity vector. To show that this position difference varies with the N_1 vector, equations (5.11) are deduced. The first two equations show the L1 and L2 measurement equations, respectively, where the residual (with respect to an initial

estimate) position vectors (Δr_1 and Δr_2) and the residual ambiguity vectors (ΔN_1 and ΔN_w, where the latter is null) are isolated. The third equation presents the dependency of the L1 to L2 position difference with the ΔN_1 ambiguity vector (the second term in the second member).

$$\begin{cases} \Delta y_1 = B \cdot \Delta r_1 + \lambda_1 \Delta N_1 \\ \Delta y_2 = B \cdot \Delta r_2 + \lambda_2 (\Delta N_1 - \Delta N_W) \\ \\ \Delta r_1 - \Delta r_2 = A \cdot (\Delta y_1 - \Delta y_2 - \lambda_2 \Delta N_W) + A \cdot (\lambda_2 - \lambda_1) \Delta N_1 \end{cases} \tag{5.11}$$

5.1.2.4 Testing and Results

Several data sets were used to test the performance and robustness of this method. In this section, some of those tests will be described, together with the respective results.

The first test consisted of a 2 hour data collected at 1 Hz from two GPS receivers placed on well known static positions, with a baseline of about 30 meters. Since what was being evaluated was the ability to correctly fix the L1 ambiguity, and the amount of time spent on that operation, the source code of the software application was modified in order to generate a reset of the ambiguity fixing status every 60 seconds. This way, regardless of having the ambiguities fixed or not, every minute the algorithm would restart looking for the correct ambiguities as if it was starting to process at that instant. The time to fix the Lw and the L1 ambiguity were registered, being this presented in figure 5.11.

It should be noticed that the program itself imposed the necessity of having at least 3 epochs of data before trying to fix the L1 ambiguities, and two epochs for the Lw ambiguities.

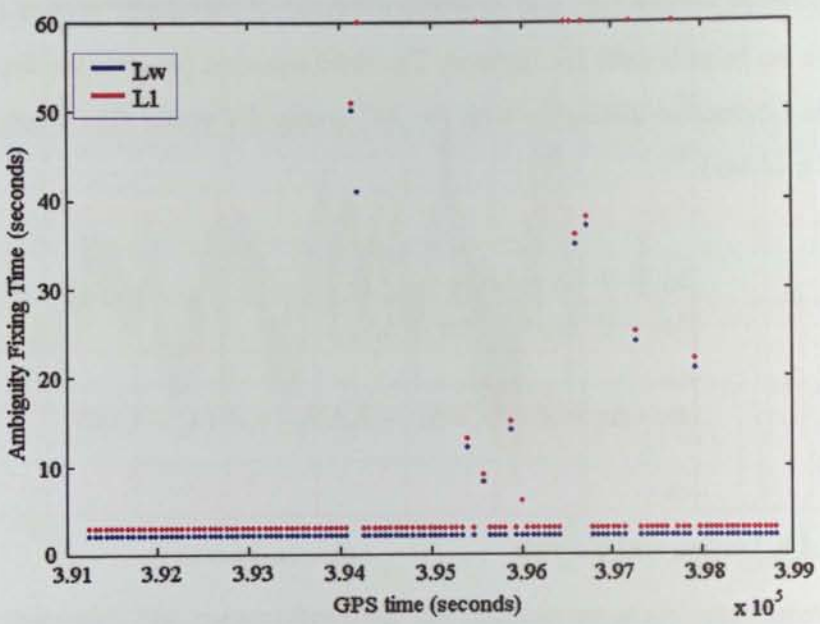


Figure 5.11 – Time to fix Lw and L1 ambiguities.

As can be seen from the graphic, most of the fixings were achieved after only 3 seconds. Some of the statistics taken from this experiment are shown in table 5.2.

Table 5.2 – Some statistical results of the short-baseline static test.

Fixing Time	Percentage
< 10 sec	89%
< 20 sec	91%
> 60 sec	5%

In order to test if the correct ambiguities were being computed, their values were stored together with their determined positions. Comparing the determined ambiguities with the ones computed using the whole data set (also verified by a third party software), and also checking with the cycle-slip occurrences in that period, no wrong fixing was detected. Also, since the coordinates of the antennas were known, the error of the determined positions were observed, as can be seen in figure 5.12, and no significant discrepancy was detected, sustaining the fact that the determined ambiguities were the correct ones.

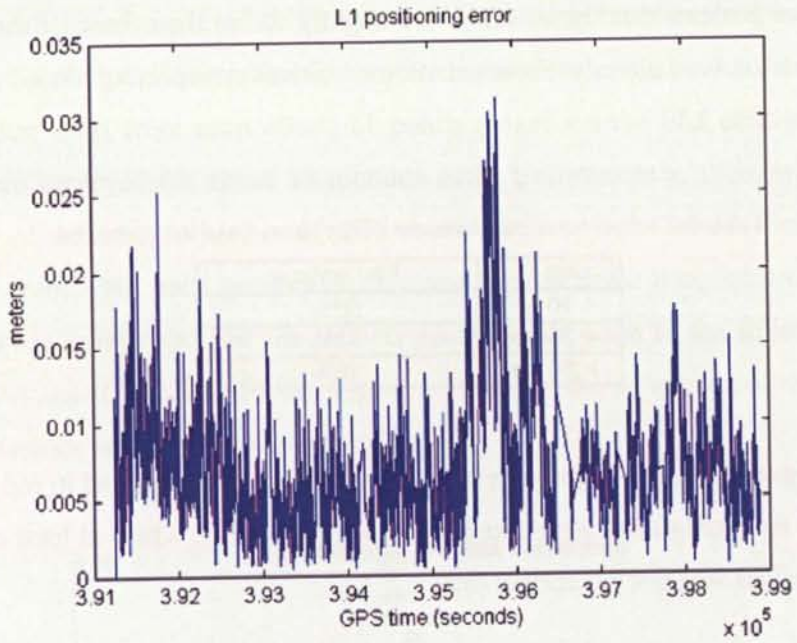


Figure 5.12 – Absolute L1 position error.

Another data set that was examined was that of an aircraft flight in the Portuguese area of Estremadura that lasted for about 2 hours. Again, the algorithm was changed in order to force the ambiguity search every minute. The time to fix the ambiguities was registered and it is depicted in figure 5.13.

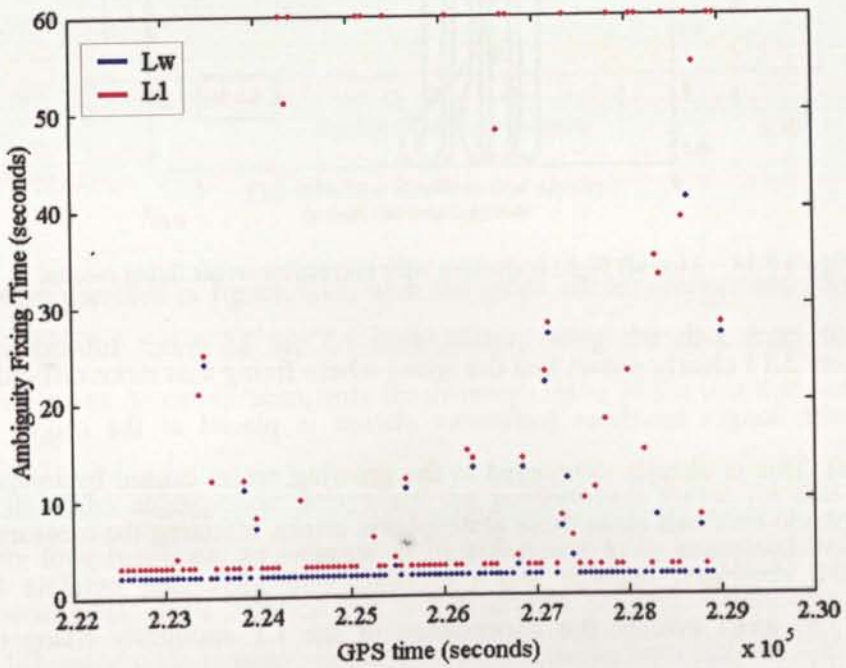


Figure 5.13 – Time to fix Lw and L1 ambiguities.

It can be seen that these results are slightly worse than those of the previous example, which was already expected. Some statistics respecting those values are presented in table 5.3.

Table 5.3 – Some statistical results of the short-baseline static test.

Fixing Time	Percentage
< 10 sec	56%
< 20 sec	73%
> 60 sec	15%

In figure 5.14, the flight path is drawn where the areas plotted in red represent parts where the ambiguities were fixed but to wrong vectors, where at least one of the ambiguity values was not the correct one.

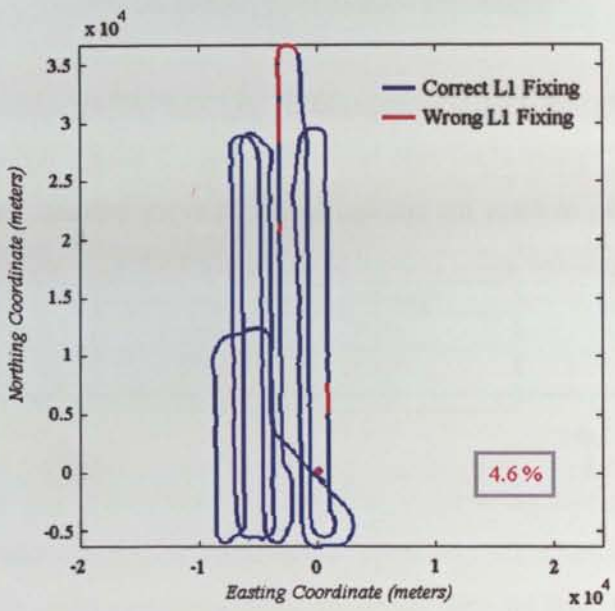


Figure 5.14 – Aircraft flight trajectory with correct/incorrect fixing results.

Figure 5.14 clearly shows that the zones where fixing was more difficult were the ones with longer baselines (reference station is placed at the origin of the coordinates). This is directly connected to the growing errors caused by ionospheric and tropospheric residuals since these atmospheric errors, affecting the measurements of both GPS receivers, become less correlated with increasing baseline length. Equation (5.8) turns evident the dependence of the L1 ambiguity fixing on the influence of the ionospheric residuals.

To test the response of this method to increasing baseline length, a simple survey was conducted. Having two GPS reference stations placed at known locations about 100 km apart from each other, 11 points placed on the line connecting both stations were surveyed for about 10 minutes each. Unfortunately, there was not the availability of an enough number of GPS receivers in order to obtain simultaneous data in all points. So, each point was surveyed at difference time instants, but the period between points was just the time to go from one point to the following. The points are distanced by about 10 km. Figure 5.15 shows the surveyed points, together with the reference station locations (in red).

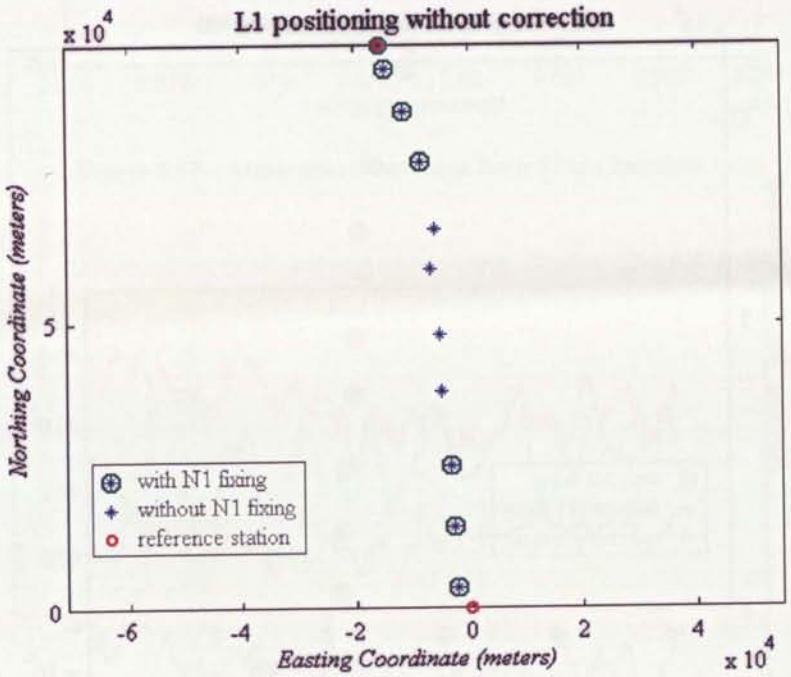


Figure 5.15 – Baseline test survey.

Also depicted in figure 5.15, with the green circles around, are points which had a successful fixing of the L1 ambiguities, using the data from the nearest reference station. As can be seen, only for distances up to 30 km was that possible.

Since the atmospheric delays are the predominant factor for this method's failure for long baselines, an estimate of its effect was to be examined based on the atmospheric effect seen between the two reference stations. Considering that the double difference wide-lane ambiguity is known between both stations – it should be

BIBLIOTECA F.E. PORTO

noticed that in equation (5.5) the ionosphere influence is very reduced – and their positions evidently known, an estimate of those atmospheric residuals can be observed using the wide-lane equations. With the residuals between reference stations, some inference based on a simple model was used to estimate the magnitude of those residuals for every surveyed point in the line, according to some parameters like the baseline length. This way, a correction was made to the measurements of each point and the method was again applied. For this test, after the introduction of this correction, every surveyed point was successfully positioned with L1 ambiguity fixing using the method here presented, as depicted in figure 5.16.

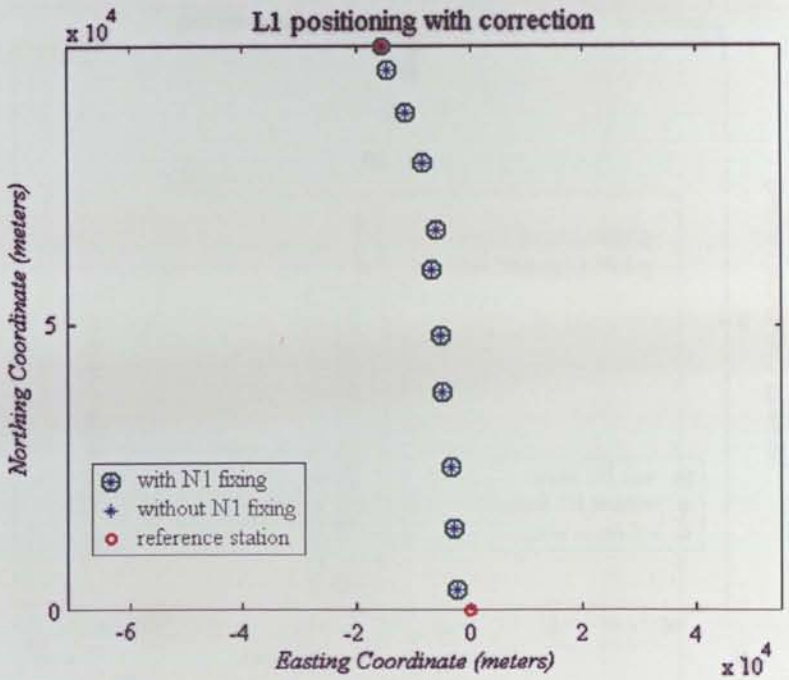


Figure 5.16 – Position fixing after atmospheric correction.

Figures 5.17 to 5.20 present the obtained residuals for some of the points, respectively for baselines of 97 km, 52 km, 13 km, and 30 meters. The decreasing magnitude of these values with baseline length in evident.

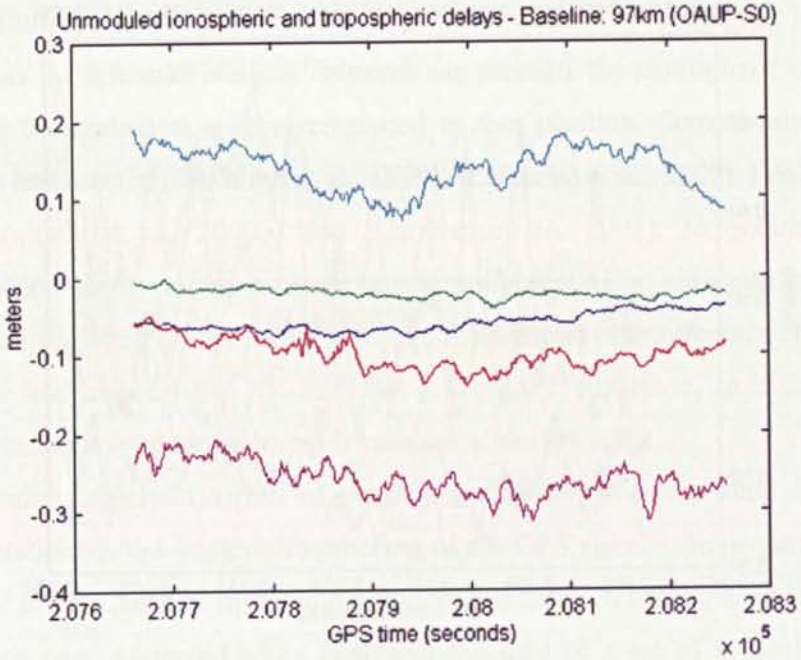


Figure 5.17 – Atmospheric residuals for a 97 km baseline.

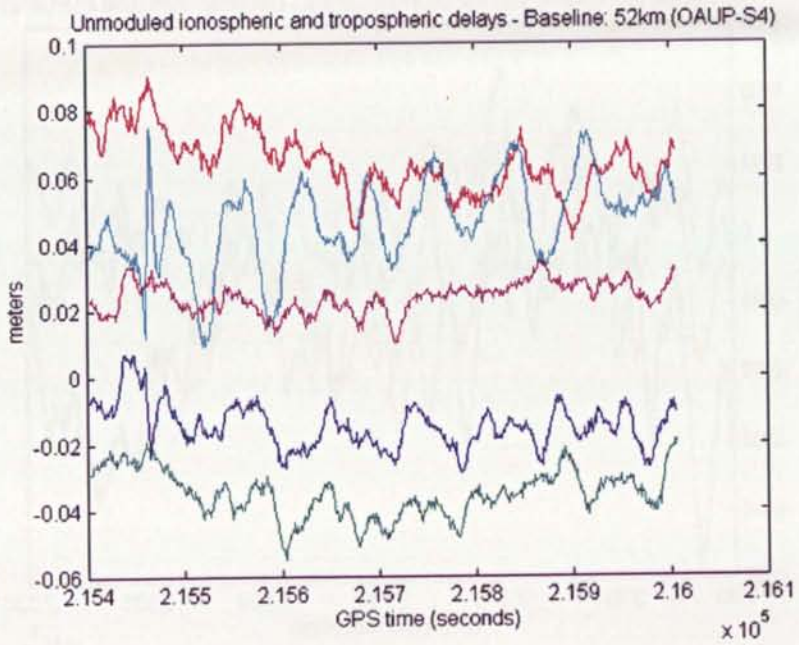


Figure 5.18 – Atmospheric residuals for a 52 km baseline.

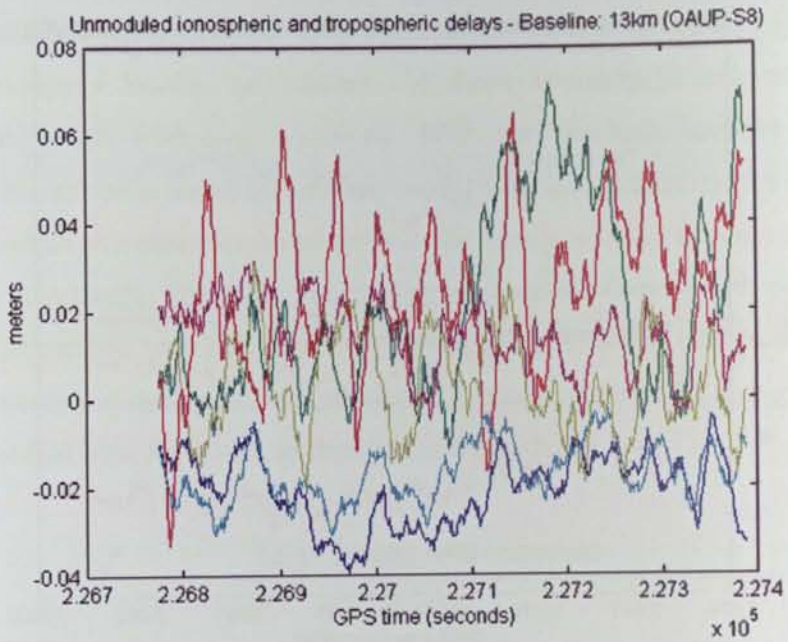


Figure 5.19 – Atmospheric residuals for a 13 km baseline.

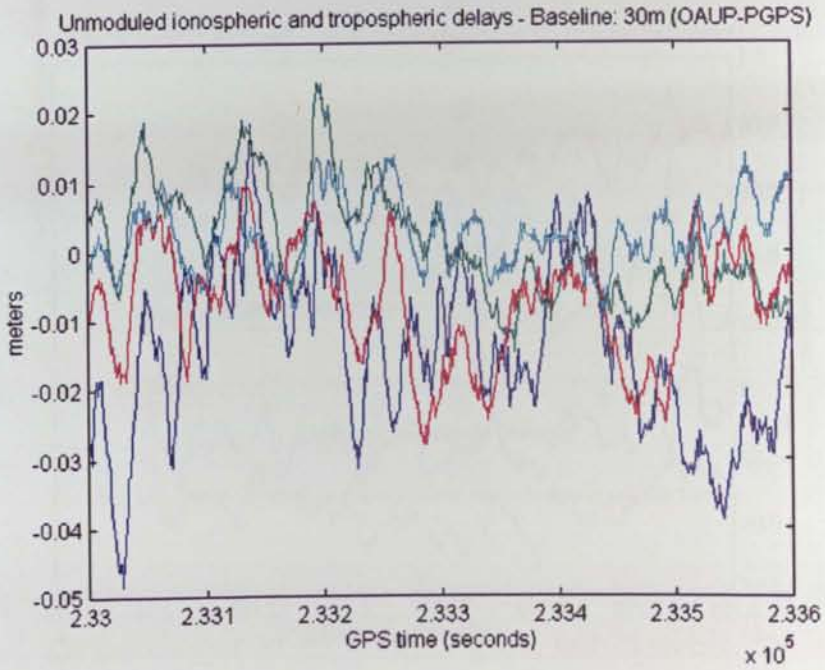


Figure 5.20 – Atmospheric residuals for a 30 m baseline.

This two reference stations' methodology can be further extended to a situation where *n* reference stations cover a certain area of interest. With these stations spread from each other creating a network of reference receivers, real-time estimates for the atmospheric influence can be obtained, through adequate modelling, in any

location within the network. Given a raw position of the rover receiver, the system that monitors the reference stations' network can estimate the atmospheric corrections that should be applied to a receiver placed in that position. Some studies on this subject can be found in [Colombo et al., 1999], [Colombo et al., 2000], [Vollath et al., 2000a], [Vollath et al., 2000b] and [Cannon et al., 2001], for example. Such implementation clearly increases the area where high precision kinematic positioning can be obtained, when compared to the solution with one only reference station. The ionospheric and tropospheric residuals get a negligible influence, as if there was a reference station very close to the rover receiver at every instant.

Another important aspect of the implementation of a real-time network of reference stations is the integrity monitoring of the GPS signals. Some particular and undesirable effects (such as high multipath) that can occur in one GPS receiver can be detected and even corrected when analysing the data of a set of ground receivers. Also, the produced corrections for a rover receiver can contain information from more than one reference station.

5.2 Relative Positioning Between Two Close Antennas

One of the main error sources of an IMU system is gyro drifting. Due to this, when processed on a stand-alone basis, the calculated IMU axes are erroneously drifting from their true directions. In order to minimise this effect, an input of one or more unbiased direction estimates would be most helpful. This can be achieved with two or more GPS antennas properly placed on the vehicle structure.

When two GPS antennas are rigidly mounted on the vehicle, the distance between them is kept constant and this fact can be used as a new constraint in the GPS processing. Another fact is that the focus is not on the absolute determination of position but in the relative position of two very close antennas, leading to an almost complete cancellation of atmospheric effects and other error sources. All these considerations led to the implementation of a processing algorithm that is completely independent of any GPS ground reference station. This is important specially for real-time navigation because, independently of any communication link, the determined direction(s) can be fed into a Kalman filter processing both IMU and GPS data, and determining the final navigation solutions, with the gyro drifting problem minimised. In this section, the referred algorithm will be explained.

5.2.1 Formulation

Considering the double difference equation (4.24), where i and j are now two moving receivers rigidly mounted in a vehicle's body in a way that their distance is kept constant, up to the desired precision, the double differentiated ionospheric and tropospheric errors can be neglected.

Choosing the stand-alone position given by one of the GPS receivers as the position estimate of both antennas with respect to which the equations are to be linearised, in the same way as shown in (4.30), equation (5.12) is reached.

$$\begin{cases} \lambda\Delta\phi_{ij}^{kl}(t,\Delta t) = \left[\widehat{u^l}(t,t-\tau^l) - \widehat{u^k}(t,t-\tau^k)\right]^T r_{ij}(t) + \lambda\Delta N_{ij}^{kl} + \varepsilon_{ij}^{kl}(t) \\ with \\ \lambda\Delta\phi_{ij}^{kl}(t,\Delta t) = \lambda\phi_{ij}^{kl}(t,\Delta t) - \lambda\widehat{N_{ij}^{kl}} - \lambda\left(D_j^l(t+\Delta t) - D_j^k(t+\Delta t)\right)\Delta t \\ r_{ij}(t) = \Delta r_i(t) - \Delta r_j(t) = r_i(t) - r_j(t) \end{cases} \quad (5.12)$$

This formulation emphasises the fact that, even considering a poor estimate of the vehicle position (around 100 meters when SA is active), a good precision on the vector between antennas is still achievable. That position error affects only the calculations of the unit vectors that are only multiplied by the short length vector r_{ij}, resulting on a negligible error.

Also, the estimate of Δt is poorer than that obtained from the knowledge of a more precise position but a precision around half microsecond is achievable in stand alone mode. Knowing that the doppler measurement is usually below 1000 meters per second, a worst case error would be around 1 millimeter.

5.2.2 METHOD

Using the phase minus code combination presented in (5.5) to estimate the wide-lane ambiguities, a set of initial candidate vectors are determined. From these ambiguity vectors, an initial test is performed in order to reduce the number of candidates. This test simply consists on checking if the antenna vector determined by each ambiguity vector has a length within a certain interval around the true distance value (which is known *a priori*). This simple strategy reduces significantly the ambiguity candidate set, increasing the efficiency of the ambiguity fixing process. Figure 5.21 shows the resulting search space reduction (on both the wide-lane and the L1 ambiguity search) after processing several consecutive data sets.

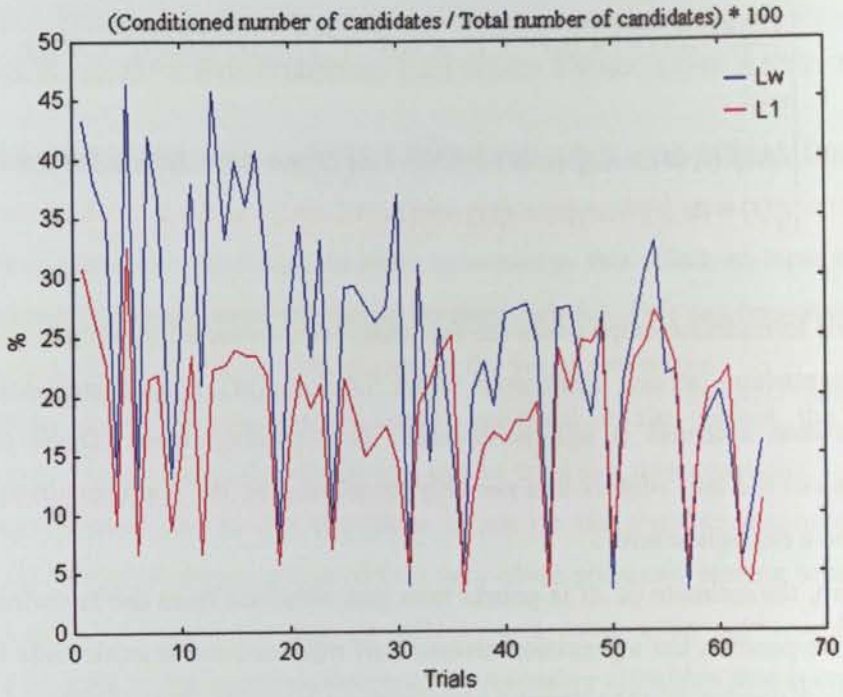


Figure 5.21 – Example of search space reduction after applying the distance condition.

With the resulting candidates, a weighting function is used to compare each ambiguity vector, based on the residuals each vector produces and also on the antenna distance error generated. After testing each candidate, the wide-lane ambiguities are fixed to the best candidate and its validation with respect to the other candidates is performed.

After fixing the wide-lane ambiguity, equation (5.8) is used to estimate the L1 carrier phase double difference ambiguities. Since the ionospheric errors are negligible due to the short distance between antennas, that term is not presented in that equation.

$$\lambda_1 \Delta\phi_{1,ij}^{kl}(t,\Delta t) - \lambda_2 \Delta\phi_{2,ij}^{kl}(t,\Delta t) \cong (\lambda_1 - \lambda_2)\Delta N_{1,ij}^{kl} + \lambda_2 \Delta N_{w,ij}^{kl} \tag{5.13}$$

Again, from applying equation (5.13), a set of possible L1 ambiguity vectors is generated. From this set are eliminated those that lead to an antenna distance which is not within a certain interval around the true distance value. Again, a significant reduction of the ambiguity set is achieved. Finally, a similar weighting function is used to select the best candidate and a validation method is performed in order to increase the certainty that the selected candidate is indeed the correct one.

After fixing the L1 ambiguity, the vector between antennas is determined for each epoch, resulting on a non-biased estimation of the vehicle attitude or, at least, of some of its angles such as yaw and pitch, depending on the number of installed antennas and their placement on the vehicle structure.

It should be mentioned that, considering for example an aircraft, the yaw angle is of more problematic determination for an IMU processing software than roll or pitch. This is due to the fact that the gravity acceleration behaves as an external input for roll and pitch, but no exterior excitation is provided related with the yaw angle. For this reason, the unbiased heading estimate provided by GPS is of great importance for the integrated navigation solution.

Figure 5.22 presents the distance error, when compared to the true antenna distance, of the determined vector between antennas – back antenna (AIRB) and front antenna (AIRF) – using the proposed method in a data set of about 2 hours, collected from an aircraft flight. The flight path is depicted in figure 5.23 together with the north, east and vertical down components of the estimated vector between antennas. As can be seen, and without requiring a ground reference station, for the whole duration of the flight, the error in distance was kept below 2 centimeters on 99.7% of the epochs. Since the real distance between antennas was 5.224 meters, a lateral error of 2 centimeters is equivalent to an angular error of about 0.22° in attitude.

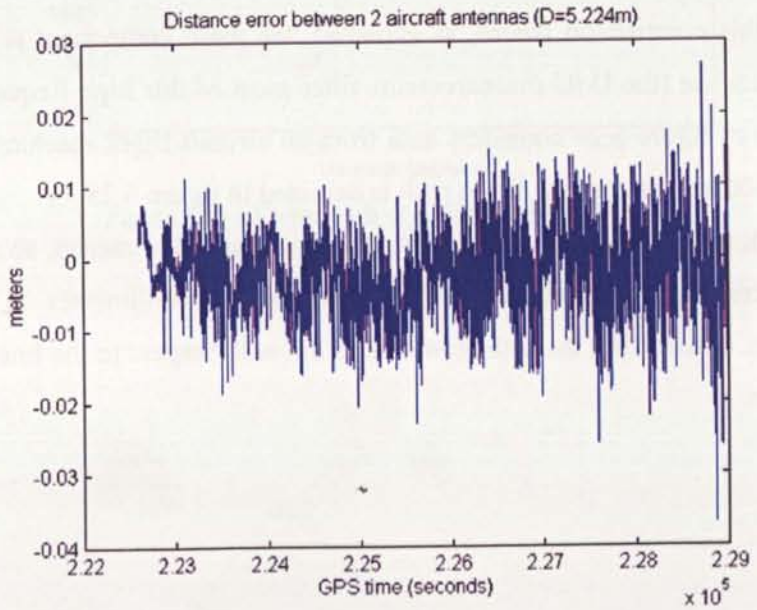


Figure 5.22 – Distance error in AIRB to AIRF vector calculation.

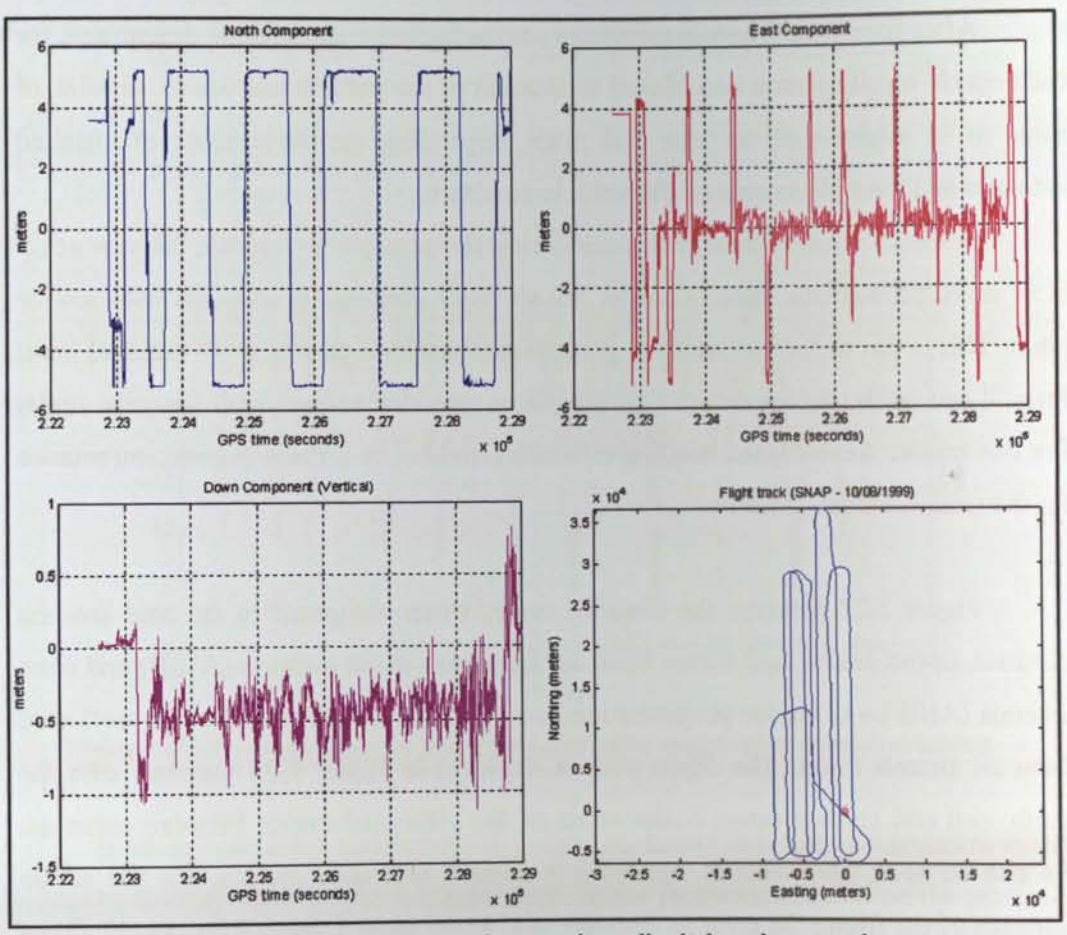


Figure 5.23 – Flight path and respective roll, pitch and yaw angles.

Another comparison to be made is between the GPS-only attitude determination and the mixed GPS/IMU attitude solution. Figure 5.24 shows an example of this comparison where, as expected, the main component is GPS phase measurement noise (the IMU measurements filter most of this high frequency noise). The example of figure 5.24 considers data from an aircraft flight reaching a baseline length over 300 km, and whose flight path is depicted in figure 5.25.

Again, the actual distance between antennas was 5.224 meters, so a yaw error of 0.1 degrees is equivalent to have an error of 9.1 millimeters in the vector determination, considering the orthogonal direction with respect to the line defined by both antennas.

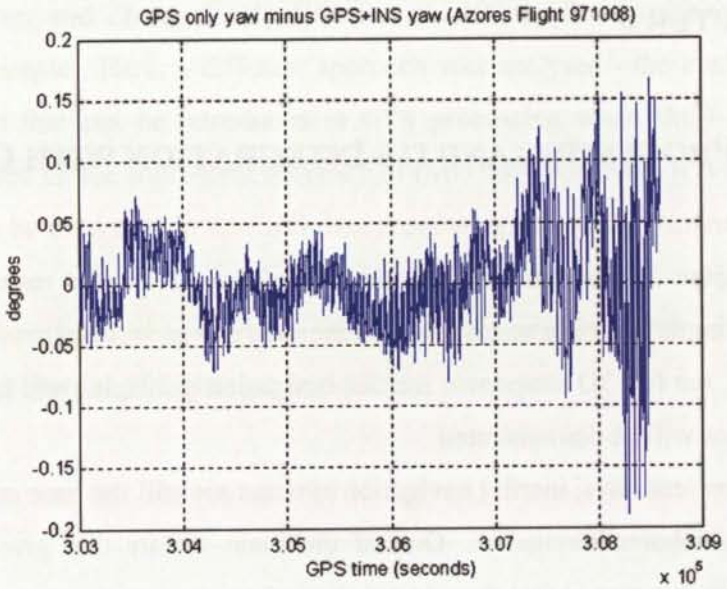


Figure 5.24 – Yaw difference between GPS-only and GPS/IMU attitude determination.

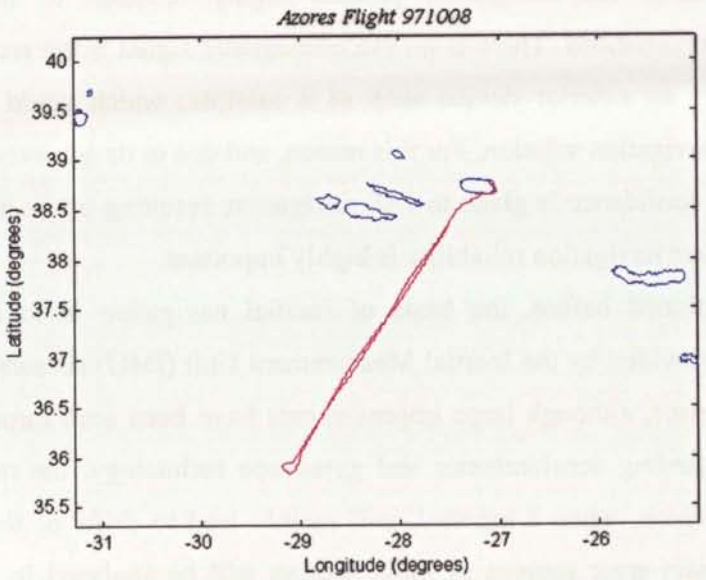


Figure 5.25 – Flown path of Azores flight 971008.

CHAPTER 6

INS PROCESSING AND ITS INTEGRATION WITH GPS

In chapter 2, an overview of the principles of inertial navigation was presented. A simple example was shown where only 2D movement was considered. In this chapter, the full 3D strapdown inertial navigation principles will be described, and its equations will be demonstrated.

In the present days, inertial navigation systems are still the base component of airborne and shipborne navigation. One of the main factors that give them such predominance in this area is that they do not depend on any exterior system or sensor, only requiring the measurements from the inertial unit installed inside the vehicle. This aspect makes this navigation process highly resistant to intentional or unintentional perturbations. There is no electromagnetic signal being received by the sensors, sent by an exterior device such as a satellite, which could be jammed, corrupting the navigation solution. For this reason, and due to its achieved precision, a good degree of confidence is given to INS navigation, resulting on its predominance in situations where navigation reliability is highly important.

As mentioned before, the basis of inertial navigation is to integrate the measurements provided by the Inertial Measurement Unit (IMU) sensors. Since there is no perfect sensor, although large improvements have been seen throughout these recent years regarding accelerometer and gyroscope technology, the measurements contain errors which, when integrated, will mainly lead to drifts of the navigation solution. The main error sources of these sensors will be analysed in this chapter, together with their influence in the navigation solution.

The final part of this chapter is dedicated to the integration of INS and GPS. The traditional perspective is to use the GPS solution to improve the INS outcome since their characteristics can be, in some way, complementary. GPS is able to provide highly accurate absolute positions but its characteristics (such as noise level) are not sufficient to make it provide vehicle attitude with high accuracy. On the other hand, the INS based absolute positions contain large offsets, but this device is able to sense attitude variations with high resolution. This integration methodology will not be described with high detail (for this purpose see [Eissfeller, 1989], [Hein and Ertel,

1993], [Schwarz and Zhang, 1994], [Wolf et al., 1996], [Bruton, 2000] and [Tomé, 2002], for example). Here, a different approach was analysed - the evaluation of the improvements that can be introduced in GPS processing when IMU data are also available. Based on the short-term accuracy of IMU only positions, it is analysed how its results can be used to help the GPS data processing, detecting/eliminating possible outliers, and even concerning carrier phase ambiguity fixing. This analysis considers only an IMU with the characteristics of the one presented in chapter 3, not being analysed the properties of higher grade devices.

6.1 Reference Frame Definition

As mentioned earlier, the choice of the reference frame is most important. The chosen frame should be the one for which, in a particular application, the resulting navigation solution would have an intuitive and immediate understanding by the users regarding the displacement of the observed vehicle. The most used frames for near-Earth 3D navigation will be now presented.

6.1.1 The Inertial Frame

The inertial frame (represented here by the index *i*) is the one relative to which the sensors (accelerometers and gyroscopes) directly measure the body movement. Its axes are considered to be static in space. For the case of near-Earth navigation, some approximations can be considered which will simplify the calculation process. For example, the acceleration imposed on a moving vehicle caused by the Earth's translation movement around the sun can be considered negligible for the most common applications. This fact enables the inertial frame to be represented with its origin in the gravitational center of the Earth. In reality, this frame's axes move with the Earth's translation movement but, to most applications, this is not significant and they are apparently seen as static axes. The direction of the three orthogonal axes are, again, defined to make the inherent calculations simple: the z axis goes from the Earth center through the North Pole, the x and the y axes are orthogonally displaced in the equatorial plane forming a right-hand reference frame. Figure 6.1 presents the inertial frame in two time instants (while the Earth has rotated between those two instants, the inertial axes remain static).

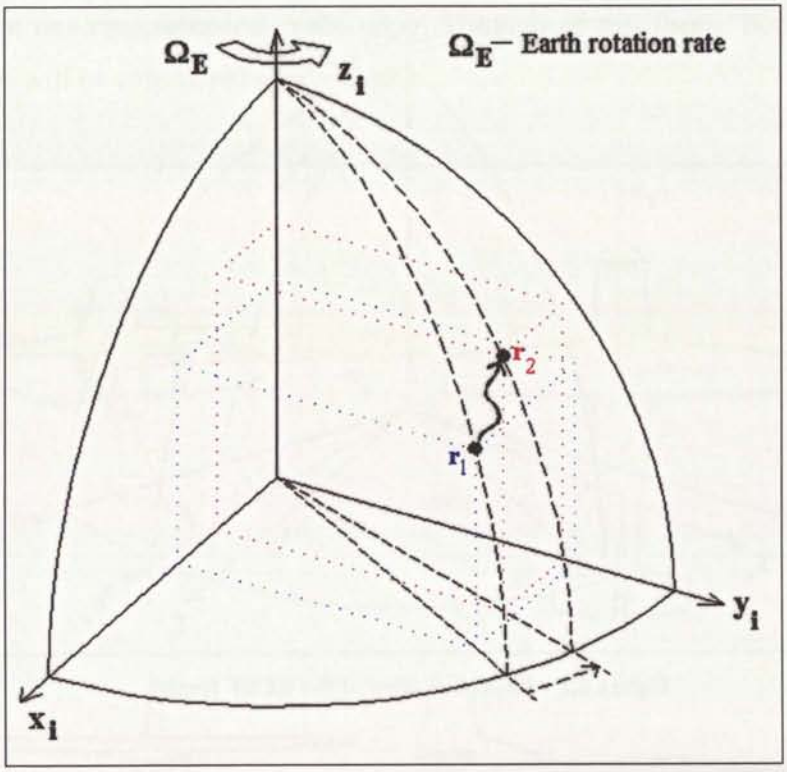


Figure 6.1 – Representation of the inertial frame.

6.1.2 The Earth-Centered, Earth-Fixed Frame (ECEF)

The Earth-Centered, Earth-Fixed (ECEF) reference frame (represented by the *e* index) is identical to the inertial frame except that the *x* and *y* axes rotate around the *z* axis at an angular velocity coincident with the Earth rotation rate. That is, the ECEF frame is fixed with the Earth, and a point not moving with respect to the Earth surface is seen as a static point when represented in this frame. For this frame, the *x* axis was defined as passing through the Greenwich meridian (at its intersection with the equator). It is with respect to this frame that the angular latitude and longitude of a point are determined. Figure 6.2 shows the representation of the ECEF frame (together with the inertial frame, for comparison).

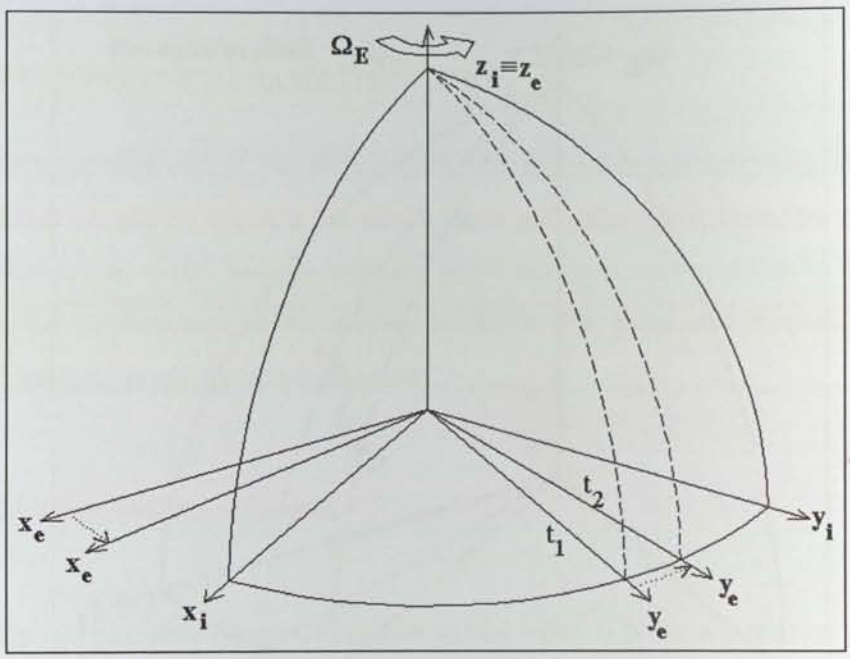


Figure 6.2 – Representation of the ECEF frame.

6.1.3 The Body Frame

The body frame (here represented by the *b* index) is an orthogonal frame rigidly coupled to the body of the vehicle (as the name indicates). For example, one possible body frame for an aircraft is one with origin on the aircraft center of mass, with the *x* axis pointing to the aircraft nose, the *y* axis through the right wing, and the *z* axis pointing down. Figure 6.3 illustrates this notation. This will be the body frame used throughout this thesis.

It should be noticed that the body frame may not coincide with the IMU frame. The IMU sensors are rigidly fixed with respect to each other, displaced in such a way that the accelerations/rotations around three orthogonally placed axes should be measured independently. Those three axes (which are the sensors' sensitive axes) constitute the IMU frame, which is defined by the IMU manufacturer. Considering only strapdown implementations, it is really difficult to mount the IMU with its frame coinciding exactly with the body frame. An origin translation and some axes rotations are usually necessary to make them match. But since their relation is kept constant through time, only some trivial mathematical transformations will be required to

change from one representation to the other. Throughout this thesis, both body and IMU frames will be considered as coincident.

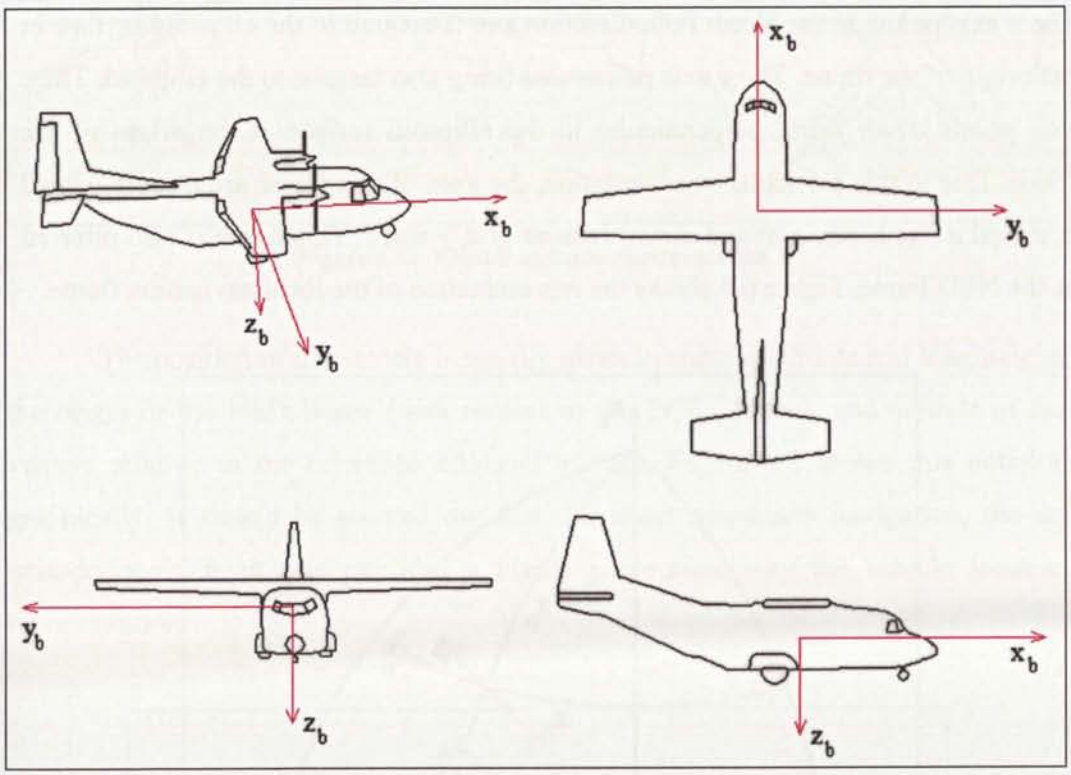


Figure 6.3 – Representation of the body frame.

6.1.4 The Local Navigation Frame

The local navigation frame (here denoted with the index *n*) is defined to give the user an immediate perception of location and attitude of a vehicle moving near the Earth surface. As explained before, in this study the shape of the Earth is considered to be represented by the World Geodetic System defined by the American Department of Defence (DoD) in 1984, usually denominated by WGS84. As mentioned in chapter 2, this model approximates the Earth to an ellipsoid with the characteristics given in table 6.1.

Table 6.1 – WGS84 ellipsoid characteristics.

Semimajor axis	a=6378137 m
Flattening	f=1/298.257223563
Earth angular velocity	We=7292115e-11 rad/s

The local navigation frame is a frame that is dependent on the vehicle's current position. Its origin is determined by the intersection of the WGS84 ellipsoid with the line passing through the vehicle position that is perpendicular to the ellipsoid surface. The *x* axis points in the North Pole direction and is tangent to the ellipsoid surface in the origin of the frame. The *y* axis points east being also tangent to the ellipsoid. The *z* axis points down being perpendicular to the ellipsoid surface at the origin of the frame. Due to this particular representation, the axes of this frame are usually named *n*, *e*, and *d* (for *n*orth, *e*ast and *d*own) instead of *x*, *y* and *z*. This frame is also referred as the NED frame. Figure 6.4 shows the representation of the local navigation frame.

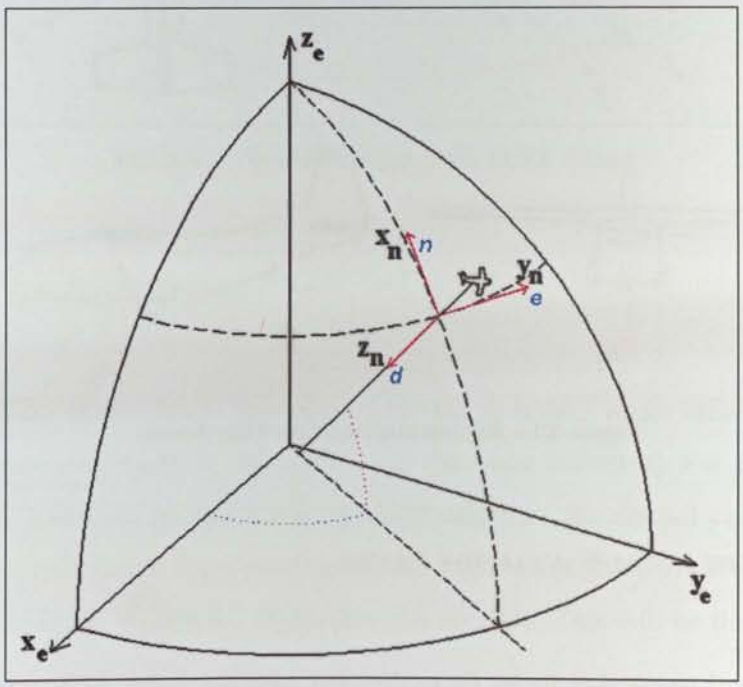


Figure 6.4 – Representation of the local navigation frame.

The angles that the body frame axes make with the axes of the NED frame are the angles that provide the vehicle attitude – roll, pitch and yaw. Similarly to figure 3.1, chapter 3, figure 6.5 illustrates this relation.

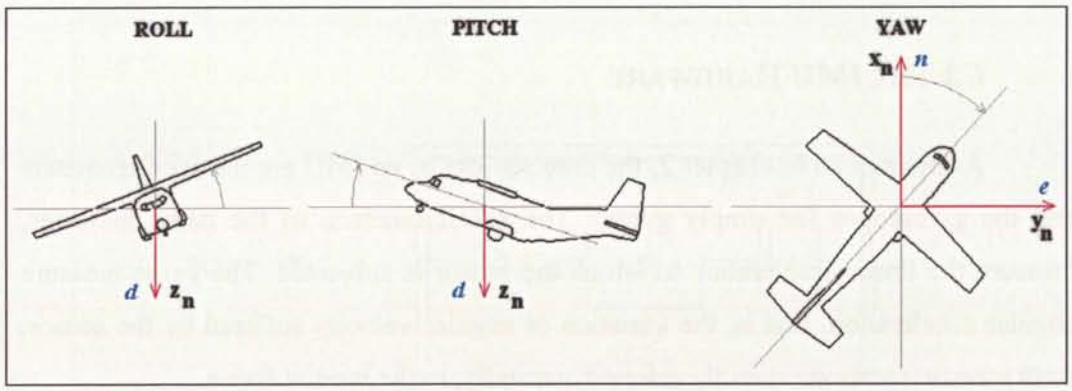


Figure 6.5 – Vehicle attitude representation.

The position of the vehicle is usually given in angular latitude and longitude of the origin of the NED frame (with respect to the ECEF frame), and altitude of the vehicle relative to the reference ellipsoid surface. Figure 6.6 shows this notation graphically. It should be pointed out that, for most near-Earth navigation, the set latitude-longitude-altitude provides a highly perceptible way for vehicle location representation.

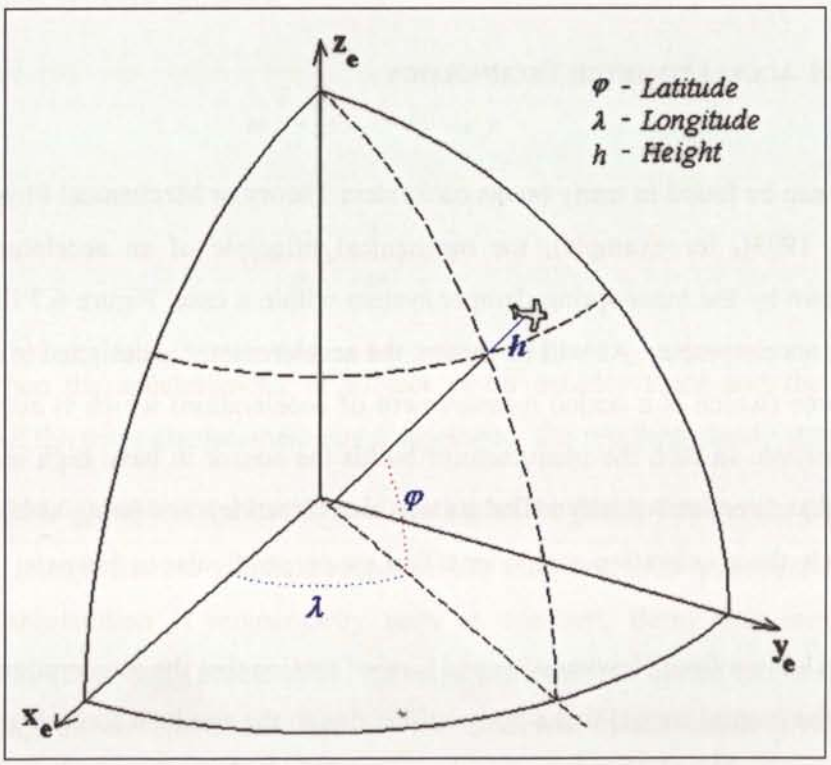


Figure 6.6 – Latitude, longitude and altitude representation of position.

6.2 THE IMU HARDWARE

As mentioned in chapter 2, the core sensors of an IMU are the accelerometers and the gyroscopes (or simply gyros). The accelerometers, as the name indicates, measure the linear acceleration to which the sensor is subjected. The gyros measure angular acceleration, that is, the variation of angular velocity suffered by the sensor. Both measurements are directly referred, naturally, to the inertial frame.

In the following paragraphs, accelerometer and gyro technology will be presented, illustrated with some examples, together with the characteristics of the most important implementations of these sensors. This description is not meant to be very detailed, it aims to give the reader the basis to connect the described processing analysis to the physical implementation aspects. More information on IMU sensor technology can be found in [Britting, 1971], [Lawrence, 1992], [Kayton and Fried, 1997], [Savage, 1996], [Siouris, 1993] and [Titterton and Weston, 1997], among others.

6.2.1 ACCELEROMETER TECHNOLOGY

As can be found in many books on System Theory or Mechanical Physics (see [Carvalho, 1993], for example), the mechanical principle of an accelerometer is simply shown by the mass-spring-damper system within a case. Figure 6.7 illustrates this simple accelerometer. As will be shown, the accelerometer is designed to measure specific force (which is a scaled measurement of acceleration) which is acting on a certain direction. In fact, the manufacturer builds the sensor to have high sensitivity regarding that direction (usually called its sensitive direction), and being as insensitive as possible to the acceleration components that are perpendicular to that axis.

It is known from Newton's Second Law of motion that the acceleration a (with respect to the inertial frame) that a body suffers due to the resultant force F applied to it can be expressed by (6.1), where m is the mass of the body.

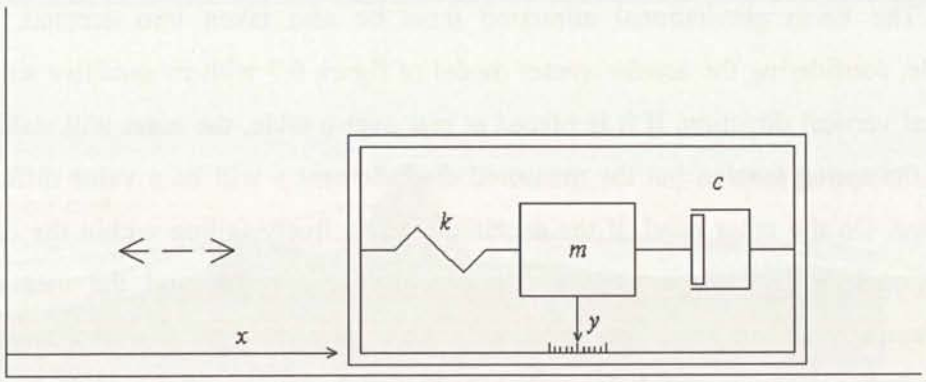


Figure 6.7 – Simple mechanical accelerometer.

$$F = ma \tag{6.1}$$

Due to the inertia of the body, a displacement will be sensed in the scale whenever a change in motion is forced in the accelerometer sensitive axis. It should be noticed that, when at rest (or with constant velocity), the resulting displacement of this ideal accelerometer is zero. Equations (6.2) and (6.3) show the mathematical model of this system's dynamics.

$$m\ddot{y} - m\ddot{x} = -ky - c\dot{y} \tag{6.2}$$

or

$$\ddot{y} + \frac{c}{m}\dot{y} + \frac{k}{m}y = \ddot{x} \tag{6.3}$$

When the accelerometer is subject to an exterior force and the transient response of the mass displacement has disappeared, the resulting steady state of the y measurement is proportional to the acceleration of the body, that is, $y \approx (m/k)\ddot{x}$. In this case, to say that the transient response has disappeared is to consider that the imposed acceleration is momentarily seen as constant. Being this measurement proportional to the body acceleration, its value can easily be scaled to the equivalent force acting on an unit mass, that is, the observed measurement given by the accelerometer is specific force. This leads to an easier insertion of these measurements in the calculations used to determine the navigation solution.

The Earth gravitational attraction must be also taken into account. For example, considering the accelerometer model of figure 6.7 with its sensitive axis in the local vertical direction, if it is placed at rest over a table, the mass will stabilise due to the spring tension but the measured displacement y will be a value different than zero. On the other hand, if the accelerometer is freely falling within the Earth gravitational field, the case and the mass will fall together and the measured displacement y will be zero. This means that the accelerometer is unable to measure the gravitational component, being only sensitive to the non-gravitational forces that are acting on it. Equation (6.4) describes the accelerometer behaviour in the local vertical direction.

$$F = ma = mf + mg \tag{6.4}$$

In this equation (6.4), f is the non-gravitational specific force and g is the gravitational acceleration. Again, and examining (6.4), if the accelerometer is freely falling, f (the measured specific force) will be null and its acceleration will be a=g. If it is static over a table, a will be null and the sensed acceleration is f=-g. This analysis demonstrates the need of having a good estimate of the local gravity acceleration. It should be mentioned that this acceleration changes from one location to the other, depending on the constitution of the Earth layers under and around the vehicle position. The surface where the value of gravitational attraction is constant, and with such a value that makes that surface fit (in a least squares sense) the global mean sea level, is denominated by Geoid (this is the geoid definition that is adopted by the National Geodetic Survey (NGS) at the National Oceanic and Atmospheric Administration (NOAA)). Figure 6.8 illustrates the differences between the geoid surface, the ellipsoid surface used to represent the Earth, and the real Earth surface.

There are several global geoid models that, based on satellite data and also on data from local surveys, provide useful gravity value estimates but they usually have a low spatial resolution, leaving undetermined higher frequency terms of the geoid. These have to be included in the navigation model as unknowns to be estimated.

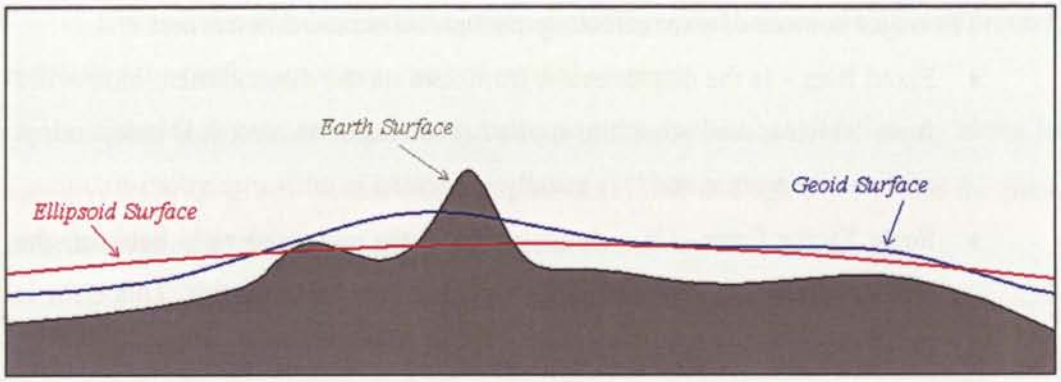


Figure 6.8 – The geoid, the ellipsoid and the Earth surface.

Regarding the construction type of the accelerometer devices, these can be divided into two categories – mechanical and solid-state. An overview of these two accelerometers types will be now presented.

6.2.1.1 Mechanical Accelerometers

Mechanical accelerometers are devices whose implementation is similar to the given example of the mass-spring-damper system of figure 6.7. Over the years, several improvements and techniques have been developed, making this type of sensor compact and reliable, providing high accuracy and a wide dynamic range. These can be divided in two different groups according to their configuration – open loop and force feedback sensors. The latter, being more precise, are capable of measuring specific force very accurately, with typical resolution of micro-g or better.

Open loop accelerometers are those whose implementation is identical to the mass-spring-damper system. When the sensor is accelerated by an exterior force, the displacement of the proof mass is observed, providing a measurement of the applied specific force. Closed loop (or force feedback) sensors try to maintain, at all times, the proof mass in the null position, measuring the necessary effort to do so. Usually, a set of coils is implemented in the sensor (replacing the spring and damper) and an electromagnetic field is controlled in order to keep the proof mass at its null position. The sensed specific force is proportional to the current necessary to stabilise the proof mass. Measuring this effort is a more accurate process than to measure a displacement on the open loop accelerometer, making the closed loop sensor the most commonly used in inertial navigation systems. Also, closed loop sensors are more stable than open loop sensors.

The major sources of error affecting mechanical accelerometers are:

- Fixed Bias – is the displacement from zero on the measurement of specific force which is read when the applied acceleration is zero. It is independent of the body motion and it is usually expressed in milli-g or micro-g;
- Scale Factor Error – is a deviation from the supposed ratio between the input acceleration and the output signal of he accelerometer. This error is usually expressed as a percentage of the measurable full scale, or simply as a ratio in parts per million (ppm);
- Cross-Coupling Error – error present in the output signal due to lack of complete insensitivity of the accelerometer to accelerations in the perpendicular directions to the sensor's sensitive axis. Due to construction imperfections, this error can exist, being often expressed as a percentage of the applied acceleration;
- Vibro-Pendulous Error – when the accelerometer is is subject to vibratory motion, dynamic cross-coupling appears owing to angular displacement of the pendulum (proof mass of a force feedback pendulous accelerometer), leading to a rectified output signal. This error is usually expressed in units of g/g^2;
- Repeatable Errors – these are errors (biases, for example) that are present each time the sensor is switched and whose value is maintained in each run, being usually predictable;
- Temperature Dependant Errors – some sensor characteristics can suffer some changes with temperature, leading to errors in the measurements. These errors can usually be calibrated and, in some cases, the sensor is mounted on a structure with a mechanism to maintain the temperature as constant as possible;
- Switch-On to Switch-On Variations – these are errors, typically random biases, that vary from one switch-on to another, but are kept constant during one run;
- In-Run Errors – during one sensor run, there are errors whose magnitude varies, being these of difficult estimation;
- Random Bias – due to instabilities within the sensor assembly.

Even with careful calibration, unpredictable residual errors are always present, restricting the performance accuracy of inertial systems.

Considering an accelerometer measuring the applied acceleration a_x along its sensitive axis, its given measurement can be described through (6.5) where the main error sources of a mechanical accelerometer are considered.

$$\widetilde{a_x} = (1+S_x)a_x + M_y a_y + M_z a_z + B_f + B_v a_x a_y + n_x \tag{6.5}$$

where:

$\widetilde{a_x}$ - the measurement quantity provided by the accelerometer;

S_x - scale factor error (it can also be expressed in polynomial form to include non-linear effects);

M_y, M_z - cross-coupling factors;

B_f - measurement bias;

B_v - vibro-pendulous error factor;

n_x - random bias.

6.2.1.2 Solid State Accelerometers

Throughout these recent years, deep studies have been conducted on new accelerometer technology in order to reduce some of the error sources affecting the mechanical accelerometers, and also to reduce its dimensions. From these researches resulted new implementations of small, rugged and reliable accelerometers with proper characteristics for strapdown applications. These accelerometers are usually called Solid State Accelerometers. Although having the same principle of the mechanical devices – reaction of a proof mass to motion – they use different technologies that, still providing a good performance, reduce the size and also the price of these devices. In the following text, only three examples of solid state accelerometers will be focused. These are the quartz-based vibrating accelerometer, the surface acoustic wave sensor, and the silicon accelerometer. These have been highly successful in this area (for details on other types of implementations see [Titterton and Weston, 1997], [Savage, 1996] and [Lawrence, 1992], for example).

Quartz Based Vibrating Accelerometer

These accelerometers are based on the vibrating properties of quartz crystal. Their principle focuses on a quartz crystal beam supporting a proof mass. At rest, the crystal beam presents its nominal vibrating pattern, vibrating at its resonant frequency. But with motion of the proof mass, in reaction to the motion accelerations, the crystal beam stretches or gets compressed, causing its vibrating frequency to change. This frequency shift is measured and a direct relation to the magnitude of the accelerations is obtained.

In order to eliminate certain error effects (such as changes in the nominal frequency of the beam due to temperature variation or ageing of the quartz crystal), these accelerometers are usually produced with two proof masses and two quartz crystal beams, in opposition to each other, as depicted in figure 6.9. This way, when one of the beams is stretched, the other is compressed and the difference in frequency between them is measured. Since this is a relative measurement, many errors cancel out with this implementation.

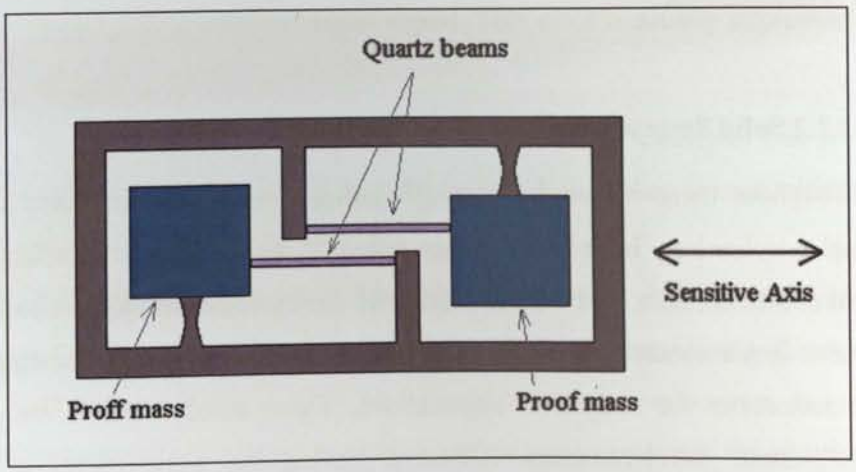


Figure 6.9 – Quartz crystal vibrating accelerometer with two beams sets in opposition.

As can be immediately retrieved from this description, this is an open loop accelerometer.

Surface Acoustic Wave Accelerometer

This is another open loop sensor. Instead of being based on the vibration characteristics of quartz crystal, it uses the properties of an acoustic wave generated

by a surface electrode that is mounted on a beam that bends in reaction to motion. Figure 6.10 shows a diagram of this sensor.

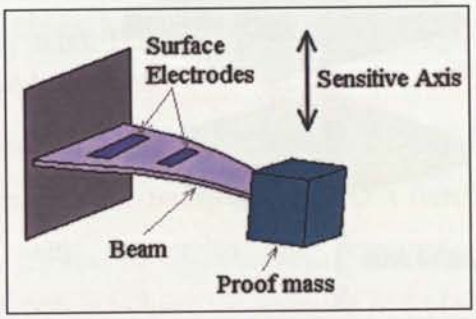


Figure 6.10 – Surface acoustic wave accelerometer.

The beam is rigidly fixed on one end and, on the other end, it holds the proof mass. When the sensor is under acceleration along its sensitive axis (which is normal to the beam surface), the beam bends causing a variation on the separation of the two metal electrode arrays. Since the wavelength of the acoustic wave is dependent on the separation of those two arrays, a comparison between the generated wave and a reference frequency (which is generated in the sensor) provides the measurement of the magnitude of the motion accelerations. Again, since the output measurement results from a comparison of two waves generated in the sensor, errors due to temperature variation get minimised.

Silicon Accelerometer

Due to the combination of the mechanical and electrical characteristics of silicon, different implementation techniques were developed with such material for acceleration sensors. There are open loop and closed loop implementations of silicon accelerometers.

In the open loop case, a beam is cut in the silicon plate where a gold layer is deposited, constituting the proof mass. On one side of the beam, a metal plate is placed in order to act as a capacitor plate. The other capacitor plate is placed on the silicon substrate, as figure 6.11 depicts. With the movement of the beam, due to the suffered accelerations, the capacitor characteristics change. These changes are measured through electrical on-chip circuits, providing this way the acceleration measurements.

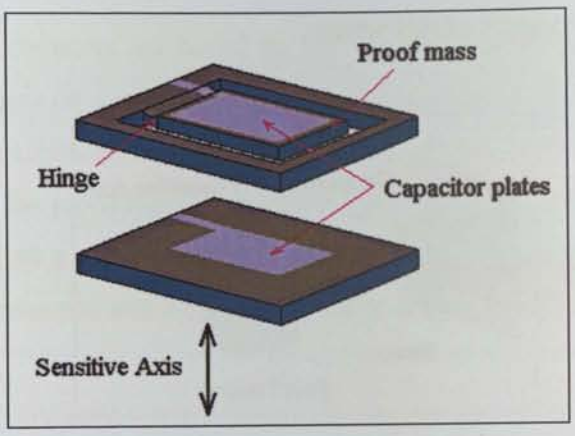


Figure 6.11 – Silicon accelerometer (open loop implementation).

In closed loop mode, two metal plates are placed under and above the beam and their function is to maintain the beam at its rest position by creating an electrostatic field. The measurement of the effort necessary to create such field is directly connected to the acceleration suffered by the sensor.

With this technology, very small and rugged accelerometers were developed, and with low pricing.

6.2.2 Gyroscope Technology

As stated earlier, the gyroscope is a device from which a measurement of angular displacement (or orientation) can be obtained. This angular displacement is, evidently, considered with respect to a certain axis – the gyro's sensitive axis. Although some sensors are capable of providing angular displacement measurements, most of the implemented gyros produce measurements of angular rate.

In the following text, some of the principal implementations of gyroscopes will be presented, being the gyro working principle given within the mechanical gyro description. Only two classes of gyros will be here considered – mechanical and optical devices – leaving out other classes such as Vibratory Gyros (that use the vibrating properties of some materials in order to detect rotation rate). More detailed information regarding gyroscope technology can be found in, for instance, [Titterton and Weston, 1997], [Lawrence, 1992] and [Savage, 1996].

6.2.2.1 Mechanical Gyroscopes

The mechanical gyro is based on the inertia of a rotating mass. If an heavy mass is spinning around a certain axis, an angular momentum vector is created (in the direction of the spinning axis). The angular momentum is equal to the product of the inertia of the spinning body by its angular velocity, as shown in equation (6.6). This angular momentum constitutes a reference direction which tends to be constant regarding the inertial frame axes. Being this direction fixed in space, it enables the detection of rotation with respect to that reference direction. One simple implementation of such gyro is to have the spinning mass (also called rotor) mounted on a pair of gimbals (which, in turn, are fixed to the gyro case). Since the reference direction tends to be kept constant (in the inertial space), case rotations will lead to rotations on the gimbals, which can be measured. Figure 6.12 shows an example of this implementation.

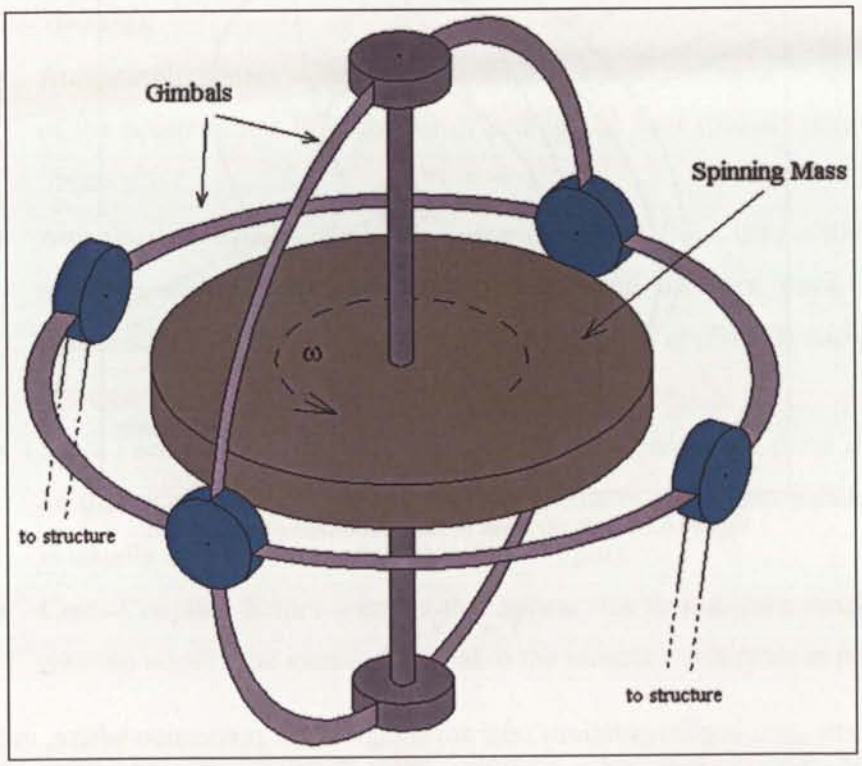


Figure 6.12 – Mechanical gyro with the rotor mounted on two gimbal sets.

$$H = I\omega \tag{6.6}$$

Another effect that must be considered in mechanical gyroscopes is the *precession*. This phenomenon consists of a reaction of a free rotating mass to an exterior torque that actuates perpendicularly to the spinning direction. That reaction, which can be verified through Newton's laws applied to rotational movement, is an angular displacement (called precession) around the axis that is normal to both the spinning and torque axes, in the sense of aligning the spinning axis with the torque axis. Figure 6.13 depicts this phenomenon and equation (6.7) shows the relation between the applied torque T, the rotation rate ω and the angular momentum H (this relation is known as the Law of Gyroscopics). The $\times$ symbol in equation (6.7) denotes the vector cross product.

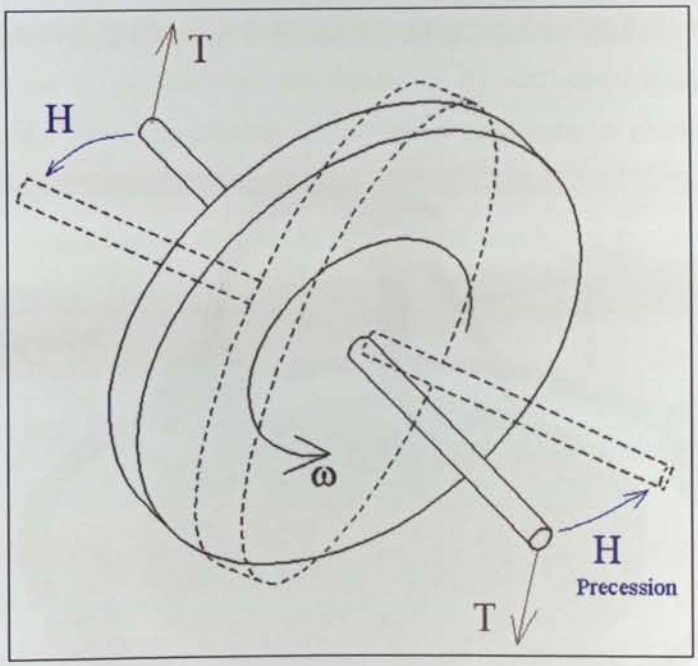


Figure 6.13 – Illustration of the precession phenomenon.

$$T = \omega \times H \tag{6.7}$$

Some gyro implementations take advantage of the precession where, instead of letting the rotor indicate a constant-in-space reference direction as in figure 6.12, it forces the rotor direction to point to a fixed reference position in the sensor's case. This is done through application of torques in the rotor's gimbal, and the magnitude of those torques provides the measurement of angular rotation (or rotation rate). These

gyros are said to be used in torque rebalance mode or in closed loop, while those similar to the one shown in figure 6.12 are said to be in open loop.

Due to non-perfect physical characteristics of the implementation of any gyro sensor, a drift on the measured angular displacement (or a bias on the measured rotating rate) is always present, being this the most significant error source of these sensors. For example, in the open loop gyro of figure 6.12, the constancy of the rotor direction is difficult to maintain due to small imperfections and non-null friction, causing the angular displacement that is read on the gimbals to drift. The following are the most significant sources of error that affect gyroscope measurements:

- Fixed Bias –explained in the above paragraph, and usually expressed in °/hour or °/second;
- Acceleration Dependant Biases – these are biases that are proportional to the accelerations that the sensor experiences (usually expressed in °/hour/g);
- Anisoelastic Biases – these are biases that are proportional to the product of the accelerations in each pair of orthogonal axes (usually expressed in °/hour/g^2);
- Anisoinertia Errors – these are biases resulting from inequalities in the spinning mass moments of inertia respecting different axes, and are proportional to the product of the angular rates applied in each pair of orthogonal axes (usually expressed in °/hour/(rad/sec)^2);
- Scale Factor Errors – as in the case of the accelerometers, these are errors on the ratio relating the output measurements and the input rotations (and is usually expressed in parts per million – ppm);
- Cross-Coupling Errors – errors that appear due to non-zero sensitivity to rotation rates in the axes orthogonal to the sensitive axis (also in ppm).

As with the accelerometers, the following error sources also affect the gyroscope measurements:

- Repeatable Errors;
- Temperature Dependant Errors;
- Switch-On to Switch-On Variations;

- In-Run Errors;
- Random Noise.

Many different implementations of mechanical gyros have been produced. Although not described in this text, a few examples are the following:

- Rate Integrating Gyro;
- Dynamically Tuned Gyro;
- Flex Gyro;
- Dual-Axis Rate Transducer (DART);
- Magneto-Hydrodynamic Gyro;

6.2.2.2 Optical Gyroscopes

Although aiming at the same purposes of mechanical gyros, the optical gyroscopes use a significantly different technique to measure angular rotation rate – they are based on the propagation properties of a beam of light (an electromagnetic radiation). They use interferometric methods to detect rotation. Two devices of this class will be addressed in the following text – Ring Laser Gyros and Fibre Optic Gyros, being these the most significant in this class.

Optical gyros are based on the path length difference that two beams of light effectively take when the beams are going through the same path but in opposite directions. Figure 6.14 illustrates this implementation aspect.

In figure 6.14, the ring is composed of a material that constrains the beam of light, disposed on a circular format of radius R. A beam splitter is placed in one point of the ring. If the ring is kept static, the travelling time that each deflected beam takes to reach once again the splitter is the same and is given by equation (6.8), where c is the speed of light in the ring material (which is considered to be constant).

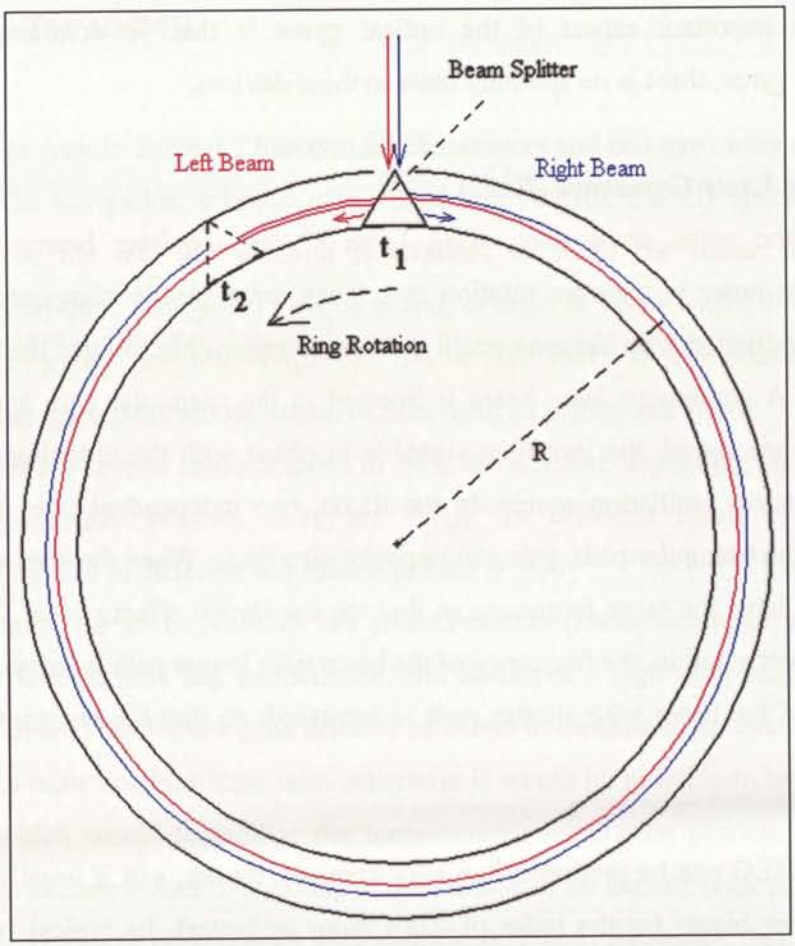


Figure 6.14 – Illustration of the principle of an optical gyro.

$$t = \frac{2\pi R}{c} \tag{6.8}$$

But if a rotation movement (around the axis that is orthogonal to the ring plane) is applied to the ring, one beam will reach the splitter sooner than the other, and the time difference between their arrival time can be approximated by equation (6.9), considering that the ring has rotated at a constant angular velocity Ω.

$$\Delta t \cong \frac{4\pi R^2 \Omega}{c^2} \tag{6.9}$$

As can be seen, the measurement of this time difference provides a direct measurement of sensor rotation rate.

One important aspect of the optical gyros is that, in contrast with the mechanical gyros, there is no spinning mass in these devices.

Ring Laser Gyroscope (RLG)

As the name emphasises, Ring Laser Gyros use laser beams and their properties in order to measure rotation rate. They are typically composed of three mirrors (constructed with extreme quality) that are responsible to form the triangular beam path. A continuous laser beam is injected in the triangular path and if, after completing one round, the incoming signal is in phase with the outgoing signals, a sustained optical oscillation occurs. In the RLGs, two independent laser beams are injected in the triangular path, going in opposite directions. When the sensor is static, both beams have the same frequency so that the oscillation effect occurs. When the sensor is under rotation, the frequency of the beam with longer path is reduced and the frequency of the beam with shorter path is increased, so that the resonant effect is maintained.

The RLG can be produced in a very compact format, and it usually presents extremely low biases (in the order of 0.001°/hour or better). Its typical beam path length is around 30 cm. Due to their construction requirements, the RLG is usually very expensive when compared to other gyros like the Fibre Optic Gyro, which will be now described.

Fibre Optic Gyroscope (FOG)

In the Fibre Optic Gyro, the light path is constrained by a fibre optic loop which can have a length of several tens of meters (100 meters, for example). The principle is identical to the shown above, where a beam of light is split in two, each going through the fibre in opposite directions, but in this case, it is the phase difference between both beams that is measured. Instead of a laser beam, a broad-band light source is used. These devices are usually less sensitive than the RLGs (the use of long fibre lengths aims at the improvement of sensitivity) and they present bias values on the order of 0.01°/hour or better. Regarding their quality range, these gyros present a relatively low cost and very compact solution.

6.2.3 THE 3D IMU

It was seen in chapter 2 that two accelerometers and one gyro were required to determine the navigation solution of a vehicle moving on the 2D space around a meridian. For the real 3D space it is required to sense the linear acceleration components on three orthogonal directions and, in order to know which directions are those, three gyros are also required. So, a 3D IMU is composed of three accelerometer-gyro pairs whose sensitive axes form an orthogonal frame.

There are several manufacturers of IMU devices and, depending on the quality of the implemented sensors, there are IMUs for different levels of accuracy, corresponding also to different acquisition prices.

Usually, the IMU provides raw measurements (linear accelerations, angular velocity variations, time tag, temperature, and others) at a high sampling frequency. Rates of 100Hz to 400Hz are quite often to be found in medium/high level IMUs. It is important to have this high data rates otherwise it would be possible to have aliasing problems which would jeopardise the measurement integration process, leading to position and attitude errors. For example, the attitude of an aircraft (especially the roll angle) can have some components with significantly high frequency that, to be well monitored, demands the IMU to have a small sampling period. This is an advantage of the IMU over the GPS receiver which usually has a maximum sampling rate from 1Hz to 10Hz. For example, with an aircraft travelling at 70 meters per second, a GPS receiver sampling at 1HZ would have a position every 70 meters, but when integrated with an IMU at 100Hz, the spatial resolution would drop down to 70 centimeters. As can be seen, just integrating the IMU measurements between two consecutive GPS positions brings a substantial benefit to the global navigation solution.

6.3 Dynamic Equations of an IMU

In this section, the relation between the dynamic equations of an IMU, in the local navigation frame, and the measurements given by its sensors (with respect to the inertial frame) will be presented. Also, those equations represented in other reference frames will be described. For that purpose, the following notation will be used:

X_a^b — X – the variable of interest (for example, the vehicle velocity vector);
a – frame in which the variable of interest is considered (for example, v_e is the velocity of the vehicle with respect to the ECEF frame);
b – frame in which the variable is expressed (for example, v_e^n is the vehicle velocity with respect to the ECEF frame but expressed in the NED frame).

Many analysis on the navigation equations associated to an IMU can be found in the literature (see, for example, [Britting, 1971], [Farrell, 1976], [Kayton and Fried, 1997], [Lawrence, 1992], [Siouris, 1993] and [Titterton and Weston, 1997]) but, in order to call the reader's attention to some intrinsic details, it was thought to be important to include such analysis in this thesis.

Starting with an analysis on the inertial frame, with respect to which the accelerometers and gyros sense their measurements, the navigation equation of a moving vehicle is described by equation (6.10).

$$\dot{v}_i^i = f_i^i + g_i^i \tag{6.10}$$

where:

v_i^i - the 3D vehicle velocity with respect to the inertial frame and expressed in the inertial frame;

f_i^i - the specific force vector measured by the 3 IMU accelerometers, but represented in the inertial frame axes;

g_i^i - representing the gravitational acceleration vector acting on the vehicle.

The integration of the left member of equation (6.10) gives the vehicle velocity (considering ideal sensors) and its double integration results on the vehicle 3D position seen from the inertial frame.

The accelerometers sense accelerations with respect to the inertial frame but their sensitive axes may not have the same orientation of the inertial frame axes. They are oriented by the body frame axes, that is, the accelerometer direct measurement is f_i^b and not f_i^i. It is necessary to convert the first specific force vector into the second and this is done through application of the direction cosine matrix C_b^i, as (6.11) illustrates.

$$f_i^i = C_b^i f_i^b \tag{6.11}$$

The direction cosine matrix C_b^i defines the angular displacement of the body frame axes with respect to the inertial frame. The IMU gyros provide the measurements indicating this angular relation. Representing the rate of this angular relation by the vector ω_{ib}^b (which is the angular variation of the body frame with respect to the inertial frame, expressed in the body frame), as shown in (6.12), the direction cosine matrix C_b^i results from the differential equation (6.13), where Ω_{ib}^b is the skew-symmetric matrix given by (6.14).

$$\omega_{ib}^b = \begin{bmatrix} a \\ b \\ c \end{bmatrix} \tag{6.12}$$

$$\dot{C}_b^i = C_b^i \Omega_{ib}^b \tag{6.13}$$

$$\Omega_{ib}^{b} = \begin{bmatrix} 0 & -c & b \\ c & 0 & -a \\ -b & a & 0 \end{bmatrix} \tag{6.14}$$

In near-Earth navigation, it is seldom the case where the navigation solution is to be used with respect to the inertial frame. Usually, it is more interesting and useful to know, for example, the vehicle velocity with respect to the Earth fixed frame (or ground speed). Let us now determine the navigation equation with the motion respecting the ECEF frame, but still expressing the variables in the inertial frame.

The Coriolis equation relates the velocity vectors with respect to the inertial and the ECEF frames. Equation (6.15) presents this relation, where the × symbol denotes the vector cross product, ω_{ie}^{i} is the turn rate of the ECEF frame with respect to the inertial frame (as shown in (6.16)), and r^{i} is the vehicle position in the inertial frame.

$$v_{i}^{i} = v_{e}^{i} + \omega_{ie}^{i} \times r^{i} \tag{6.15}$$

$$\omega_{ie}^{i} = \begin{bmatrix} 0 \\ 0 \\ \Omega \end{bmatrix}, \text{ where } \Omega = 7292115 \text{x} 10^{-11} \text{ rad/s} \tag{6.16}$$

Taking the derivative of both members of (6.15), assuming that ω_{ie}^{i} is a constant vector, and using (6.10), equation (6.17) is reached.

$$\dot{v}_{e}^{i} = f_{i}^{i} - \omega_{ie}^{i} \times v_{e}^{i} - \omega_{ie}^{i} \times \left(\omega_{ie}^{i} \times r^{i}\right) + g^{i} \tag{6.17}$$

Equation (6.17) shows the effects of representing the navigation quantities with respect to a rotating frame. In fact:

$\omega_{ie}^{i} \times v_{e}^{i}$ is the Coriolis acceleration, which is generated by the Coriolis apparent force due to system movement with respect to the rotating Earth surface;

$\omega_{ie}^{i} \times \left(\omega_{ie}^{i} \times r^{i}\right)$ is the centripetal acceleration that the system experiences due to Earth rotation.

It should be noticed that the centripetal acceleration component is not distinguishable from the gravitational acceleration acting on the system, caused by the Earth mass attraction. In fact, the sum of these two vectors is the force that an object would experience when placed on a point near the Earth surface. That resulting vector is called the Local Gravity Vector (g_l) and equation (6.18) shows its composition.

$$g_l^i = g^i - \omega_{ie}^i \times \left(\omega_{ie}^i \times r^i\right) \tag{6.18}$$

Replacing (6.18) into (6.17), and using (6.11), yields (6.19), the navigation equation with respect to the ECEF frame, expressed in the inertial frame.

$$\dot{v}_e^i = C_b^i f^b - \omega_{ie}^i \times v_e^i + g_l^i \tag{6.19}$$

A similar equation set to the one presented in the inertial frame analysis can be developed where the only differences are that the gravitational attraction vector is now the local gravity vector, and the Coriolis correction term has also to be determined.

For most near-Earth navigation situations this is still not the desired representation form since the variables are still expressed in the inertial frame. It makes more sense and it is more intuitive to have them expressed in the earth fixed frame. This next step will be now analysed.

Again, from the Coriolis equation, the variation of v_e^e (the ground speed expressed in the ECEF frame) can be related to the variation of v_e^i (the ground speed expressed in the inertial frame) through equation (6.20).

$$\dot{v}_e^e = \dot{v}_e^i - \omega_{ie}^e \times v_e^e \tag{6.20}$$

Replacing (6.19) in (6.20) and converting the measured specific force f^b into the ECEF axes, equation (6.21) is reached, which is the navigation equation of motion with respect to the ECEF frame. Also, the local gravity vector is now expressed in that frame.

$$\dot{v}_e^e = C_b^e f^b - 2\omega_{ie}^e \times v_e^e + g_l^e \tag{6.21}$$

It should be noticed that, although in (6.19) the Coriolis term $\omega_{ie}^i \times v_e^i$ was expressed in the inertial frame, its equivalent vector is now considered in (6.21) but evidently expressed in the ECEF frame.

What is new in equation (6.21) is the direction cosine matrix C_b^e. This matrix is determined from the differential equation (6.22) where Ω_{eb}^b is the skew-symmetric form of ω_{eb}^b, the body rate vector with respect to the ECEF axes.

$$\dot{C}_b^e = C_b^e \Omega_{eb}^b \tag{6.22}$$

The gyros measure ω_{ib}^b and not ω_{eb}^b, but these two vectors can be related by equation (6.23) where $C_e^b = C_b^{e^T}$, the transpose of matrix C_b^e.

$$\omega_{eb}^b = \omega_{ib}^b - C_e^b \omega_{ie}^e \tag{6.23}$$

It is apparent from (6.22) and (6.23) that the estimation of C_b^e depends on ω_{eb}^b which in turn depends on C_e^b, the transpose of C_b^e. In terms of algorithmic implementation, a new structural difference must be introduced. Now, together with the final position (r_e^e) and velocity (v_e^e), the ω_{ie}^e is also estimated, which is iteratively used in the recalculation of the direction cosine matrix C_b^e.

This representation is still not the most suitable for near-Earth navigation because the final solution is expressed in the ECEF *xyz* coordinates. It is more intuitive to express the position of the vehicle in latitude, longitude and the height over the Earth surface, that is, to express the navigation solution in the local

navigation frame (NED). Since this is the most widely used representation of position over the Earth, it makes it easier for the user to understand the navigation solution if its north, east and local vertical components are given. The following text will present the navigation equation with respect to the Earth but expressed in the local navigation frame (NED).

Once again, taking the Coriolis equation, the relation (6.24) may be written considering now that not only does the Earth rotate with respect to the inertial frame, but also does the NED axes rotate with respect to the ECEF frame since the NED axes directions change with the vehicle displacement over the Earth surface.

$$\dot{v}_e^n = \dot{v}_e^i - \left(\omega_{ie}^n + \omega_{en}^n\right) \times v_e^n \tag{6.24}$$

Replacing (6.19) in (6.24), with the quantities expressed in the NED frame, equation (6.25) is reached.

$$\dot{v}_e^n = C_b^n f_i^b - \left(2\omega_{ie}^n + \omega_{en}^n\right) \times v_e^n + g_l^n \tag{6.25}$$

As seen before, the accelerometer specific force measurement has now been converted from the body frame to the NED frame through application of the direction cosine matrix C_b^n, once again obtained from the gyro measurements and also from the vehicle position estimate. That matrix C_b^n results from the solution of the differential equation (6.26).

$$\dot{C}_b^n = C_b^n \Omega_{nb}^b \tag{6.26}$$

Now, Ω_{nb}^b is the skew-symmetric matrix respecting the ω_{nb}^b vector which represents the rotation rate of the body axes with respect to the NED frame. Since the gyros only measure ω_{ib}^b, its relation to ω_{nb}^b has to be established. With an estimate of the vehicle position and velocity, it is possible to determine an estimate of the turn rate of the NED axes with respect to the Earth, expressed in the NED frame (that is,

ω_{en}^{n}). It is also possible to express the turn rate of the ECEF axes, with respect to the inertial frame, in the estimated NED frame (ω_{ie}^{n}). The sum of these two turn rates, expressed in this estimated NED frame, is an estimate of the turn rate of the NED frame with respect to the inertial space (still expressed in the NED frame). Following this analysis, equation (6.27) is reached.

$$\omega_{nb}^{b} = \omega_{ib}^{b} - C_{n}^{b}\left(\omega_{ie}^{n} + \omega_{en}^{n}\right) \tag{6.27}$$

As in (6.23), with (6.26) and (6.27) there is the need to iteratively use the quantities ω_{nb}^{b} and C_{n}^{b} since they both depend on each other (and ω_{ie}^{n} and ω_{en}^{n} depend on the navigation solution – position and velocity in the NED frame).

Let us now study with more detail the navigation equation in the NED frame. Starting with the velocity vector v_{e}^{n} with respect to the Earth, it can be written through its north, east and local vertical components.

$$v_{e}^{n} = \begin{bmatrix} v_{N} \\ v_{E} \\ v_{D} \end{bmatrix} \tag{6.28}$$

Taking now the specific force measurements from the accelerometers, expressed in the NED frame, (6.29) is used.

$$f_{i}^{n} = C_{b}^{n} f_{i}^{b} = \begin{bmatrix} f_{N} \\ f_{E} \\ f_{D} \end{bmatrix} \tag{6.29}$$

The vehicle position r^{n} is determined by latitude (φ), longitude (λ) and height (h) over the Earth surface.

$$r^n = \begin{bmatrix} \varphi \\ \lambda \\ h \end{bmatrix} \tag{6.30}$$

The Earth rotation rate regarding the inertial frame and expressed in the local navigation frame is determined through (6.31).

$$\omega_{ie}^n = \begin{bmatrix} \Omega\cos(\varphi) \\ 0 \\ -\Omega\sin(\varphi) \end{bmatrix} \quad \text{with } \Omega = 7292115\text{x}10^{-11} \text{ rad/s} \tag{6.31}$$

The turn rate of the NED axes with respect to the ECEF frame (also known as the transport rate) can be expressed through (6.32).

$$\omega_{en}^n = \begin{bmatrix} \dot{\lambda}\cos(\varphi) \\ -\dot{\varphi} \\ -\dot{\lambda}\sin(\varphi) \end{bmatrix} \tag{6.32}$$

Till now, through this analysis, the Earth has been considered to be a sphere of radius R_o. Continuing with this approach, the latitude and longitude derivatives can be expressed through equations (6.33).

$$\dot{\varphi} = \frac{v_N}{R_o + h} \qquad \dot{\lambda} = \frac{v_E}{(R_o + h)\cos(\varphi)} \tag{6.33}$$

So, ω_{en}^n can be rewritten substituting (6.33) into (6.32).

$$\omega_{en}^{n} = \begin{bmatrix} \dfrac{v_E}{R_o + h} \\ -\dfrac{v_N}{R_o + h} \\ -\dfrac{v_E \tan(\varphi)}{R_o + h} \end{bmatrix} \tag{6.34}$$

It should be noticed that the third component of ω_{en}^{n} looses significance as the vehicle approaches the Earth poles. This has only to do with the selected mathematical representation. Through some mathematical manipulation, this problem is easily eliminated (see, for example, the wander azimuth mechanisation in [Titterton and Weston, 1997], [Farrell, 1976] or [Siouris, 1993]). This problem will not be considered here in this thesis (the data available for processing was obtained in the Portuguese territory, at mid latitude values).

The local gravity vector, as described earlier, is the sum of the Earth gravitational attraction (g) and the centripetal acceleration caused by the Earth rotation ($\omega_{ie}^{n} \times \omega_{ie}^{n} \times r$). The latter can be decomposed into (6.35).

$$\omega_{ie}^{n} \times \omega_{ie}^{n} \times r = \frac{\Omega^2 (R_o + h)}{2} \begin{bmatrix} \sin(2\varphi) \\ 0 \\ 1 + \cos(2\varphi) \end{bmatrix} \tag{6.35}$$

With all this considerations, the navigation equation in the NED frame can be written in terms of three equations ((6.36) to (6.38)) reflection the dynamics on each of the local navigation axes.

$$\dot{v}_N = f_N - 2\Omega v_E \sin(\varphi) + \frac{v_N v_D - v_E^2 \tan(\varphi)}{R_o + h} + \xi_g \tag{6.36}$$

$$\dot{v}_E = f_E + 2\Omega \left(v_N \sin(\varphi) + v_D \cos(\varphi) \right) + \frac{v_E}{R_o + h} \left(v_D + v_N \tan(\varphi) \right) + \zeta_g \tag{6.37}$$

$$\dot{v}_D = f_D - 2\Omega v_E \cos(\varphi) - \frac{v_E^2 + v_N^2}{R_o + h} + g \tag{6.38}$$

In (6.38), the g value is obtained from models of the gravity field which relate the vehicle position with a certain value of the gravity acceleration. As seen in equations (6.36) to (6.38), the main part of the gravity effect is in the local vertical axis but, due to gravity anomalies which exist all around the Earth (due to inhomogeneous mass distribution), there may be some minor gravity components in the local horizontal axes, being these here represented by ξ_g and ζ_g. For more details on gravity field representations see [Britting, 1971], for example.

The assumption of the spherical Earth representation causes some errors which can be considered high enough to compromise the navigation solution accuracy for several applications. It is well known that the shape of the Earth is better approximated by an ellipsoid rather than a sphere. The following paragraphs will introduce the reader to the changes in (6.36) to (6.38) so that the ellipsoid model of the Earth can be considered. With this model, a better accuracy is achieved in the final navigation solution. Since the GPS system uses the WGS84 ellipsoid as a model of the shape of the Earth, that same ellipsoid will be considered in this analysis, although it is also appliable to any other ellipsoid modelling the Earth.

For a certain position in the ellipsoid, instead of considering only one radius (R_o), two radii are now considered – the meridian radius of curvature (R_N) and the transverse radius of curvature (R_E), which are defined by (6.39) and (6.40). Notice that R_o can be considered as the mean radius of curvature, being given by $R_o = \sqrt{R_N R_E}$.

$$R_N = \frac{R(1-e^2)}{\sqrt{1-e^2\sin^2(\varphi)}^3} \tag{6.39}$$

$$R_E = \frac{R}{\sqrt{1-e^2\sin^2(\varphi)}} \tag{6.40}$$

R is the ellipsoid semimajor axis and e is the eccentricity of the ellipsoid.

Now, the variation of latitude and longitude are given through (6.41).

$$\dot{\varphi} = \frac{v_N}{R_N + h} \qquad \dot{\lambda} = \frac{v_E}{(R_E + h)\cos(\varphi)} \tag{6.41}$$

Finally, the transport rate is written with these new radii.

$$\omega_{en}^{n} = \begin{bmatrix} \dfrac{v_E}{R_E + h} \\ \dfrac{-v_N}{R_N + h} \\ \dfrac{-v_E \tan(\varphi)}{R_N + h} \end{bmatrix} \tag{6.42}$$

6.4 Representations of Vehicle Attitude

As has been clear from the presented notation, the axis set considered as the vehicle (body) frame constitutes an orthogonal right-handed frame. It is said to be right-handed since positive rotation around one of its axis is considered when the rotation is made clockwise when observed from the frame origin and looking through the axis positive direction.

There are several ways to mathematically represent the attitude of a vehicle with respect to a reference frame. Three of those representations will be mentioned in the following text.

6.4.1 Direction Cosine Matrix

This has been the method used in the above description of IMU system mechanisation. It is based on a 3x3 matrix whose columns are the unit vectors of the body frame projected along the considered reference frame axes.

6.4.2 Euler Angles

It is known that the transformation of one orthogonal frame into another can be carried out through three (properly ordered) successive rotations, one around each of the three axes. This is usually the most intuitive approach regarding frame transformation and attitude representation. The result is a 3x3 matrix resulting from the multiplication of three 3x3 matrices, each representing the rotation over one of the axes. Attention must be taken regarding the order those rotations are performed.

6.4.3 Quaternions

This representation is based on the idea that to transform one coordinate frame into another it is only required to perform one rotation around a certain μ vector

defined with respect to the considered reference frame. The quaternion q is a 4x1 vector defined by (6.43).

$$q = \begin{bmatrix} \cos(|\mu|/2) \\ (\mu_x/|\mu|)\sin(|\mu|/2) \\ (\mu_y/|\mu|)\sin(|\mu|/2) \\ (\mu_z/|\mu|)\sin(|\mu|/2) \end{bmatrix} \tag{6.43}$$

μ_x, μ_y and μ_z are the components of the 3x1 vector μ, and $|\mu|$ is its module. The module of μ is set so that a rotation of an angle of $|\mu|$ around the vector μ is sufficient to transform the first frame into the second. See, for instance, [Titterton and Weston, 1997] for more detailed information on quaternions.

6.5 INTEGRATION OF IMU AND GPS DATA

As mentioned in the beginning of this chapter, the main focus of the work here presented will not be the advantages that the IMU processing could obtain from the GPS measurements, but the usefulness that the IMU data would have in GPS data processing. Although a brief description of the former analysis will follow, the latter is focused with more emphasis since the former was addressed with high detail in [Tomé, 2002].

6.5.1 IMU PROCESSING INTEGRATING GPS DATA

As can be seen in the formulation presented throughout this chapter, the IMU is a typical dead-reckoning device, whose measurements have to pass through an integration process in order to obtain vehicle position, velocity and attitude. Since the IMU does not have any position reference input, it relies on the accuracy and stability of its accelerometers and gyros to determine the subsequent navigation solutions, through integration. A navigation system based only on an IMU device typically would start from a known location, with known velocity and orientation. From then on, the navigation solutions would be determined through processing the measurements of the accelerometers and gyros. Even though these sensors can be, nowadays, produced with high quality, the smallest bias on the measurements is accumulated though time leading to drifts on the navigation solution. One of the predominant error sources is gyro drifting, making the absolute position errors significant after some seconds (for applications aiming sub-meter accuracy). To improve this navigation solution, the main sensor biases can be estimated and, after this estimation, they can be compensated (usually, the IMU manufacturer provides these parameters), but there are always some minor terms that remain undetermined, causing the solution to drift.

As mentioned in the first part of this chapter, these biases are not constant, changing with time and with other factors such as temperature (although many IMUs have internal temperature compensation/stabilisation). An on-line estimation of these errors would be desired but this would have to be achieved with external precise

position updates (and possibly with other information such as external attitude estimate). This is where GPS comes into consideration. With the methodologies presented in chapter 5, absolute positioning together with aircraft attitude can be estimated with GPS measurements from more than one receiver. This way, the two systems can be integrated by means of a Kalman filter, leading to a navigation solution providing high accuracy position and attitude, at a high sampling rate. For more information on filtering techniques see, for instance, [Anderson and Moore, 1979], [Brown and Hwang, 1992], [Gelb, 1974], [Grewal and Andrews, 1993], [Maybeck, 1979/82] and [Meditch, 1969].

The set of IMU navigation equations, together with the estimated parameters modelling the sensor errors, can be used to predict the navigation solution for the next epoch where a GPS solution is available. The obtained error between both solutions can be the variable of interest in this analysis, over which a Kalman filter can be implemented. This scheme, where a Kalman filter is based on the deviations regarding a reference trajectory (a trajectory in the wide sense, that is, an initial approximation to the real solution), is usually denominated by Extended Kalman Filter.

Having an initial estimate of the parameters modelling the errors of the sensors, the epoch-to-epoch deviation of those parameters can be also considered as variables of interest, making the Kalman filter state vector a set of deviations from earlier determined parameters (the navigation solution plus sensor error parameters). The deviation from the vertical gravity estimate can also be added to the state vector. Figure 6.15 presents a diagram illustrating the mechanisation of this process.

A state vector for a Kalman filter applied to the navigation system presented in chapter 3 could be composed of 3 variables for position deviation (latitude, longitude and altitude, for example), 3 variables for velocity deviation, 3 for attitude deviation (roll, pitch and yaw), 3 for accelerometer bias deviation (one variable for each accelerometer), 3 for gyro bias deviation, one for each gyro (note that a bias in angular variation is equivalent to a drift of the angular values), and finally 1 variable for vertical gravity deviation. This would lead to a Kalman filter of dimension 16. In the scope of the SNAP project, a Kalman filter performing this integration was implemented, being the main focus of the work presented in [Tomé, 2002].

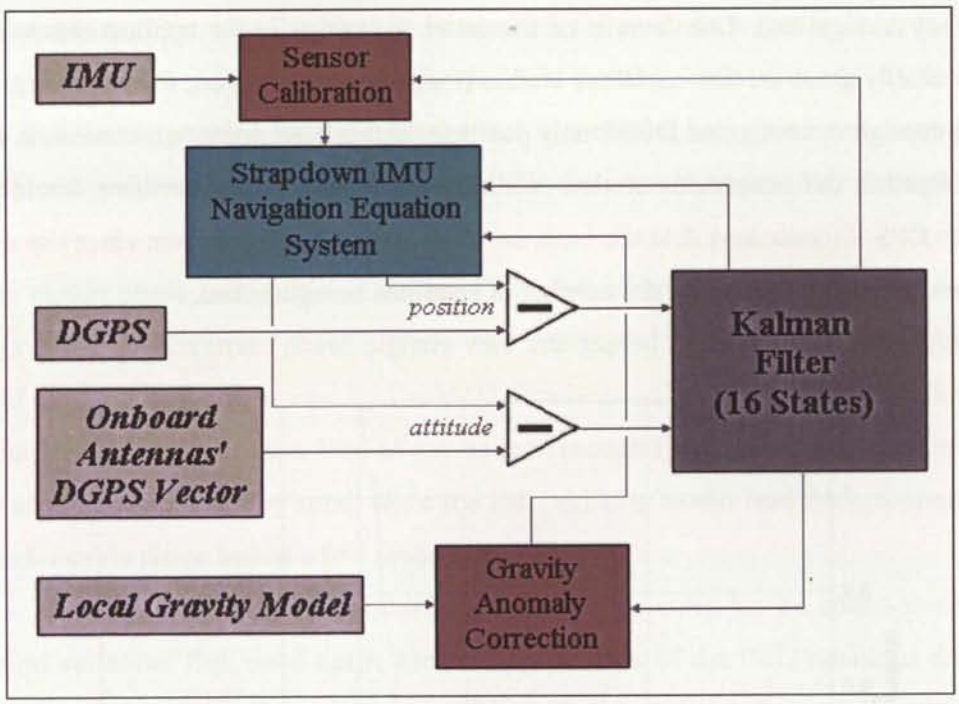


Figure 6.15 – Mechanisation scheme of the GPS/IMU integration process.

In order to illustrate the importance of the GPS position/attitude update in the Kalman filter, in figure 6.16 a situation where the effect of momentary absence of that input is presented. In this case, 60 seconds after the (here considered) initial time instant, the GPS results were disabled as input to the Kalman filter, which remained on its own for 60 seconds, being then reapplied the GPS input. As can be seen, with the navigation solution being computed only by the IMU introduced in chapter 3, a drifting is evident after a few seconds of GPS data absence.

After the Kalman filter estimation process is performed, in post-processing mode, the final solutions can be further improved through a smoothing process. This is based on applying the estimated parameters obtained by the Kalman filter to all the data epochs (including past epochs).

It should be referred that the integration of GPS related data with IMU data can be performed considering the GPS results after DGPS processing (being considered in the integration the absolute DGPS position of one of the antennas, and the vector between two or more onboard antennas), or considering the GPS measurement equations (with the carrier phase ambiguities previously solved, for high

accuracy navigation). One benefit of the latter technique is for applications where momentarily there are few satellites visible (for ground navigation, for example), not being enough to compute a DGPS only position. In this case, some information is still considered in the integrated solution (while in the former technique there would not be any GPS information). But the latter is more complex to implement since the state vector dimension varies with the number of satellites being tracked.

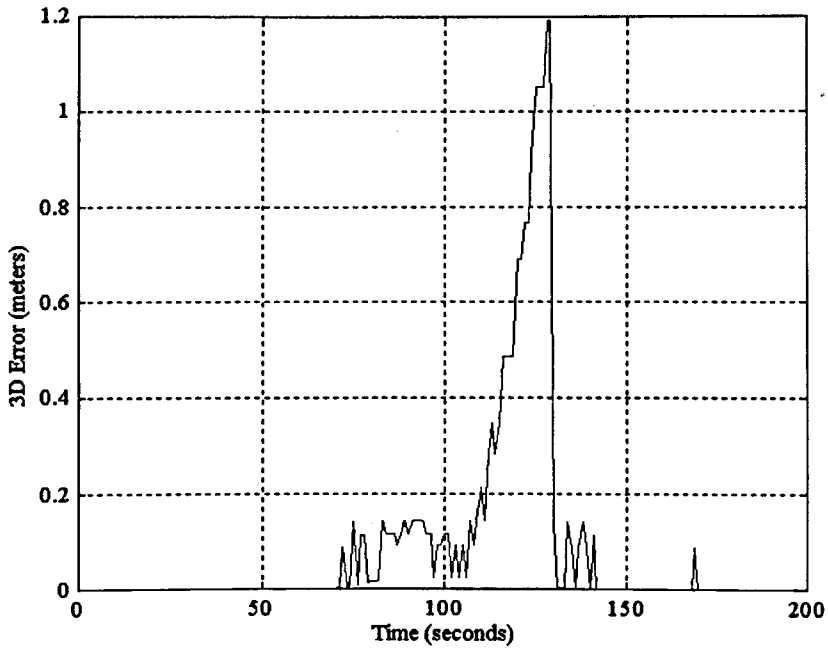


Figure 6.16 – Effect on position of a momentary absence of GPS results in the Kalman filter.

6.5.2 GPS PROCESSING INTEGRATING IMU DATA

Another perspective to this integration process is how to use the IMU data to improve GPS processing. Since the IMU data is available throughout the survey, its use was analysed with the scope on helping DGPS carrier phase ambiguity fixing, and also on improving the robustness of the GPS results.

There are several ways to include the IMU only results into the ambiguity fixing process. One evident way is to use the IMU computation to predict the position for the next GPS epoch, being that position used as an initial estimate for the computation/validation of GPS ambiguities. If the time elapsed between two consecutive epochs is short, this is an highly accurate estimate, which can be used to

decrease the number of ambiguity candidates. But the problem is that in order to have an highly accurate position estimate for the next epoch, obtained though IMU data only, an accurate position for the current epoch is required, being assumed that (all or some) ambiguities have already been fixed for the current epoch. So, through this perspective, the usefulness of the IMU only results is limited regarding the process of fixing carrier phase ambiguities. Only on a situation where, suddenly, the tracking of all (or almost all) carrier phase signals was interrupted and soon after reacquired, would the positions determined by the IMU data help on a rapid re-determination of the carrier phase ambiguities. But, as can be seen though figure 6.16, the reacquisition time would have to be very small since the IMU drifting would lead the positions out of the L1 cycle range in just a few seconds.

Another perspective to explore IMU data is to consider its epoch-to-epoch position variation. But, once again, the drifting patterns of the IMU positions do not allow the elimination of ambiguity candidates just based on their epoch-to-epoch position variation.

One point that should be considered is the comparison between the epoch-to-epoch position variation obtained with the IMU system and the same variation obtained with the GPS data. Being a dead reckoning system, the IMU is only able to determine the current position with respect to the previously determined position. With the GPS data, a similar procedure can also be adopted using the triple difference measurements. The triple difference measurements are obtained by subtraction of the double differences of two consecutive epochs. This way, no ambiguities have to be determined (assuming that the carrier tracking was not interrupted between epochs) since they cancel out. On the other hand, only the position variation between epochs can be determined through this process. Based on equation (4.30), equation (6.44) shows the basic equation for the triple difference measurement.

$$\begin{aligned}
&\lambda\phi_{ij}^{kl}(t,\Delta t)-\lambda\phi_{ij}^{kl}(t_{-1},\Delta t_{-1})-\widehat{\rho_{ij}^{kl}}(t,\Delta t)+\widehat{\rho_{ij}^{kl}}(t_{-1},\Delta t_{-1})+\widehat{I_{ij}^{kl}}(t)-\widehat{I_{ij}^{kl}}(t_{-1})-\widehat{T_{ij}^{kl}}(t)+\widehat{T_{ij}^{kl}}(t_{-1})= \\
&=\lambda\Delta\phi_{ij}^{kl}(t,\Delta t,t_{-1},\Delta t_{-1})\cong\left(\widehat{u_i^l}(t,t-\tau_i^l)-\widehat{u_i^k}(t,t-\tau_i^k)\right)^T\cdot\left(\Delta r_i(t)-\Delta r_i(t_{-1})\right)- \\
&\qquad -\Delta I_{ij}^{kl}(t)+\Delta I_{ij}^{kl}(t_{-1})+\Delta T_{ij}^{kl}(t)-\Delta T_{ij}^{kl}(t_{-1})+\varepsilon_{ij}^{kl}(t)
\end{aligned} \tag{6.44}$$

The subscript $_{-1}$ indicates that the respective value refers to the previous epoch. The relation between the true positions, the estimated positions and the position residuals is given though equation (6.45).

$$r_i(t) - r_i(t_{-1}) = \hat{r}_i(t) - \hat{r}_i(t_{-1}) + \Delta r_i(t) - \Delta r_i(t_{-1}) \tag{6.45}$$

In equation (6.44), since the epoch-to-epoch variation of the ionospheric terms is very small, a further approximation consists on the elimination of such terms. Also, with the tropospheric delay, the residuals of the difference of the values given by the tropospheric model can be neglected.

Given these considerations, the implementation of these equations produced results that, when compared with the L1 positions (with ambiguity fixing), an estimate of the drifting effect of the triple difference measurements can be obtained. Figure 6.17 presents such a comparison, where the data of one test flight was processed with triple differences (considering one initial position for the aircraft antenna) and with L1 carrier phase double differences (absolute positions with ambiguity fixing). Presented is the difference between both solutions whose predominant term is the drift on the triple difference solution, which appears from the integration of the determined epoch-to-epoch position variations (the small errors, such as measurement noise, also get integrated causing a drift effect).

After analysing several data sets, the drifting behaviour did not differ significantly from the one presented in figure 6.17. As can be immediately noticed, the procedure of the triple difference measurements leads to a dead reckoning form with a much lower drift than the one obtained with the IMU system being used in this study (presuming that at least four satellites have been continuously tracked in every epoch-to-epoch interval). This analysis shows that it is preferable to use the triple difference measurements when considering the position variation of the rover antenna in a somewhat short interval, rather than the IMU only results.

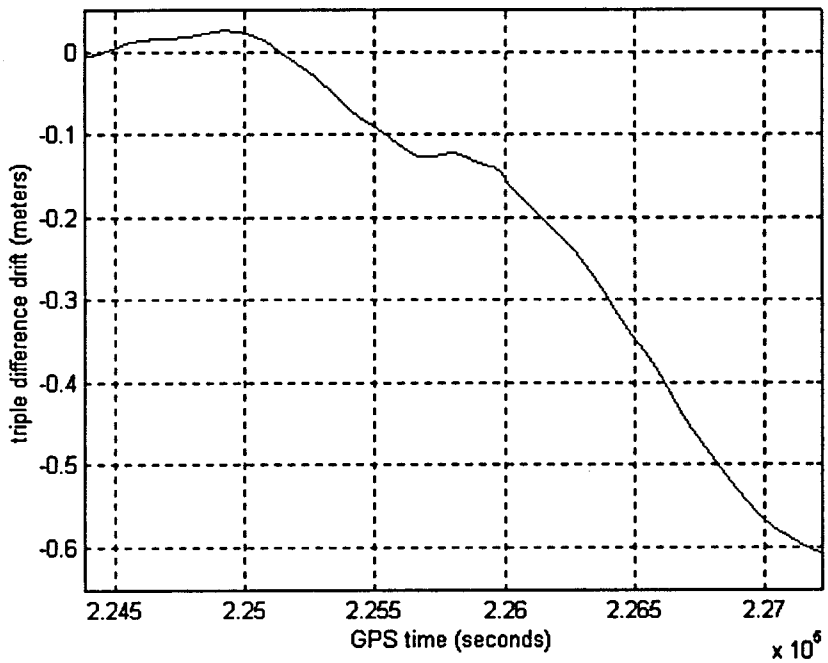


Figure 6.17 – Drift example of the triple difference solution (data from a test flight).

From this analysis it is concluded that the use of this particular IMU data to help fixing the L1 carrier phase ambiguities is not very rewarding. But it should be noticed that the IMU is able to provide a position variation between epochs which is independent of the GPS measurements (although some parameters of the algorithm that deals with the IMU data were estimated also with base on GPS measurements/solutions). This way, and since the precision of the IMU position for the following epoch (one second) is within the L1 cycle range, it is very useful for quality control of the GPS solutions, contributing to an increase of system's robustness. Since the short-term characteristics of the IMU data present a smooth pattern in the variation of its determined positions, the GPS cycle-slip algorithms can be aided by the IMU position estimate since an undetected cycle-slip would lead to a position jump. Through this matching with the next epoch's expected position (given by the IMU solution), it becomes even more difficult to leave undetected a possible cycle-slip or other sort of abnormal offset, resulting on a more robust navigation system.

As seen above, when all (or almost all) the satellite signals get their tracking continuity interrupted for a short period (a few seconds), the IMU solution is still useful for the reduction of the ambiguity search space, permitting a rapid recovery of the L1 precision positioning. The IMU-only positions and their uncertainty allow an

early elimination of possible ambiguity candidates when the satellite signals are reacquired. But from the characteristics of the IMU introduced in chapter 3, the blockage of the satellite signals would have to take a short period of time because the uncertainty of the IMU-only position rapidly increases and the valid ambiguity search space also increases. For higher grade IMUs (with ring laser gyros, for example), the drifting phenomenon is more stable and, after a sudden blockage of the GPS signals, the estimate of the IMU biases produces IMU-only solutions with smaller errors for longer periods. In this case, the usage of these solutions for delimiting the ambiguity search space is more useful. Even in the case of loss of lock of only some of the GPS signals, and further reacquisition, the short-term positioning accuracy of these high grade IMU solutions (possibly aided by the remaining GPS measurements) will probably bring benefits to the determination of the carrier phase ambiguities of the reacquired signals.

CHAPTER 7

IMPLEMENTATION, CAMPAIGNS AND RESULTS

This chapter starts by describing the implementation aspects of the algorithms presented in the previous chapters. These GPS processing methods were coded in C++ language, forming the core module of a software application developed specifically for testing each step of this work. From data collection, interpretation, matching and processing, this application allows an easy integration of new algorithms and new file formats, without having to recompile the whole code. A general description of this application is presented in the following section.

The second subject of this chapter is the description of the airborne campaigns that were performed with the objective of testing the GPS/IMU system presented in chapter 3. Since the GPS processing algorithms, both for absolute positioning and for attitude estimation, are also part of this navigation system, these campaigns were very important for the definition and tuning of the methods. From the experience of these real applications, certain feelings are acquired which probably would not be considered when analysing data in the office. Both real-time and post-processing modes were tested with the data gathered from these campaigns. The first airborne campaign took place in October 1997 in the Azores archipelago (Portugal). The purpose of this campaign was to collect data from diverse onboard equipment for *a posteriori* estimation of the gravity anomalies on the Azores region. The navigation system presented in chapter 3 was installed on the aircraft and its data stored. Also, the communication link between aircraft and ground reference station was tested. The second campaign was performed in the Portuguese region of Estremadura, in August 1999, and its objective was to test the GPS/IMU navigation system performance in real-time. The pilots were supplied with the predefined trajectory through a graphical interface showing the instantaneous error between the current and desirable trajectory. Also installed on the aircraft was a photogrammetric camera, rigidly attached to its structure, that took several photos during the flights. The idea was to use photogrammetry processing techniques to estimate the aircraft attitude and position, comparing those to the GPS/IMU solutions.

Some important results from these campaigns are shown in this chapter.

7.1 SOFTWARE IMPLEMENTATION

The operating system selected for the industrial PC used in the navigation system was Microsoft Windows NT4.0. The applications were developed in C++, using the Borland C++ 5.0 compiler.

Basically, the GPS software implementation consisted on a main application that was organised in several modules. The structure of this application was previously defined so that some objectives were verified, such as:

- Possibility of developing several processing algorithms without having to change much of the program code (like the data acquisition modules); this way it would be possible to test new ideas for processing GPS data with the smallest effort, saving time;
- Possibility of processing data from several types of GPS receivers without having to change much of the program code (like the processing modules);
- Possibility of using the same processing modules in both real-time mode and post-processing mode;
- Possibility to use the basic and common processing routines (ephemeris handling, data matching, epoch matching, clock offset estimation, etc.) in all processing modules.

Based on these requirements, the structure represented in figure 7.1 was implemented. As can be seen, a modular implementation was used. With it, an internal data specification was defined. Every data acquisition module converts the data retrieved from each GPS receiver into that common data format, with which the processing algorithms work. This allows an easy implementation of new algorithms without having to change anything regarding the data acquisition. Also, for the application to handle a new GPS receiver, all that is necessary is to introduce the respective data acquisition module, converting its format to the internal format. This implementation approach turned out to be time efficient regarding the number of experimented processing algorithms and also the number of receiver types that were used. It also made possible to use the same code to process data real-time and post-processing modes. As shown before, the developed algorithms aimed at real-time

processing, but it was also intended that they could be used in post-processing mode for testing and tuning purposes.

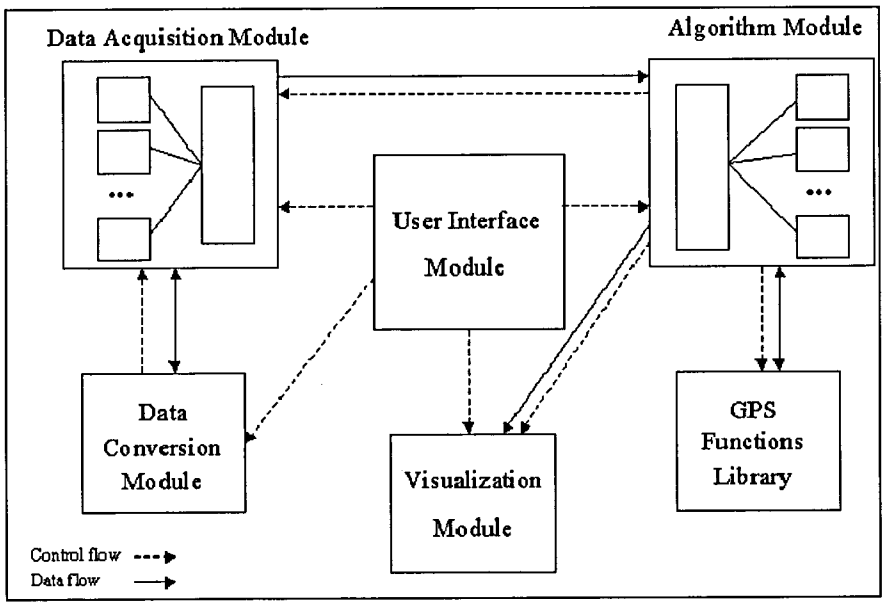


Figure 7.1 – Basic structure of the GPS processing application.

The data acquisition module can be decomposed into two distinct blocks – the real-time and post-processing acquisition blocks. The post-processing block uses library functions to automatically determine the type of a data file that the user selects. According to that type, the respective data-decoding sub-block is activated and is used to fetch the data for the next epoch, commanded by the processing module. When that data is retrieved from the file, the sub-block decodes it into the internal data format and signals the processing module. The data acquisition module allows an easy integration of new sub-blocks, permitting the integration of new data file types (from new GPS receivers). Up to the moment this thesis was written, 9 sub-block were implemented for post-processing, including the RINEX V2 file type.

In order to permit other applications to process the same raw data used with this application, a data conversion module was implemented. It allows saving the data from one of the implemented file types into another of those types.

The real-time block of the data acquisition module is similar to the post-processing block, except that these handle serial port communication instead of file access routines. Also, they have a data storage buffer where each epoch's data is gathered and when the processing module asks for the next data epoch, it is fetched

from the buffer. This mechanism prevents data loss when CPU time becomes scarce, for some reason. Another feature of these sub-blocks is to store the collected data on the PC hard disk.

The processing module (or algorithms' module) is responsible for processing the acquired GPS data using the method selected by the user. This module commands the data acquisition module. This way, the matching between the data from both receivers becomes independent of the acquisition module. The processing module consists of a set of distinct methods for GPS data processing. The method selected by the user is activated and uses the common command interface to control the data fetching. Each method is implemented independently from each other, but since there are many functions that are common to all (or most), a library of basic GPS functions was created.

When the active processing method determines a solution, it is passed to the visualisation module which depicts it in its graphical interface.

The user interface module is built from a set of buttons and dialog boxed through which the user commands and sets-up the other application modules. This module is also closely connected to the visualisation module.

The visualisation module is used to feedback to the user the information describing the current behaviour of the processing algorithms. This module consists of a set of graphical interfaces where the data resulting from the processing mechanisms is plot. Different graphical objects can be implemented in this interface, independently of the rest of the application modules. Figure 7.2 shows one of the graphical interfaces that were implemented.

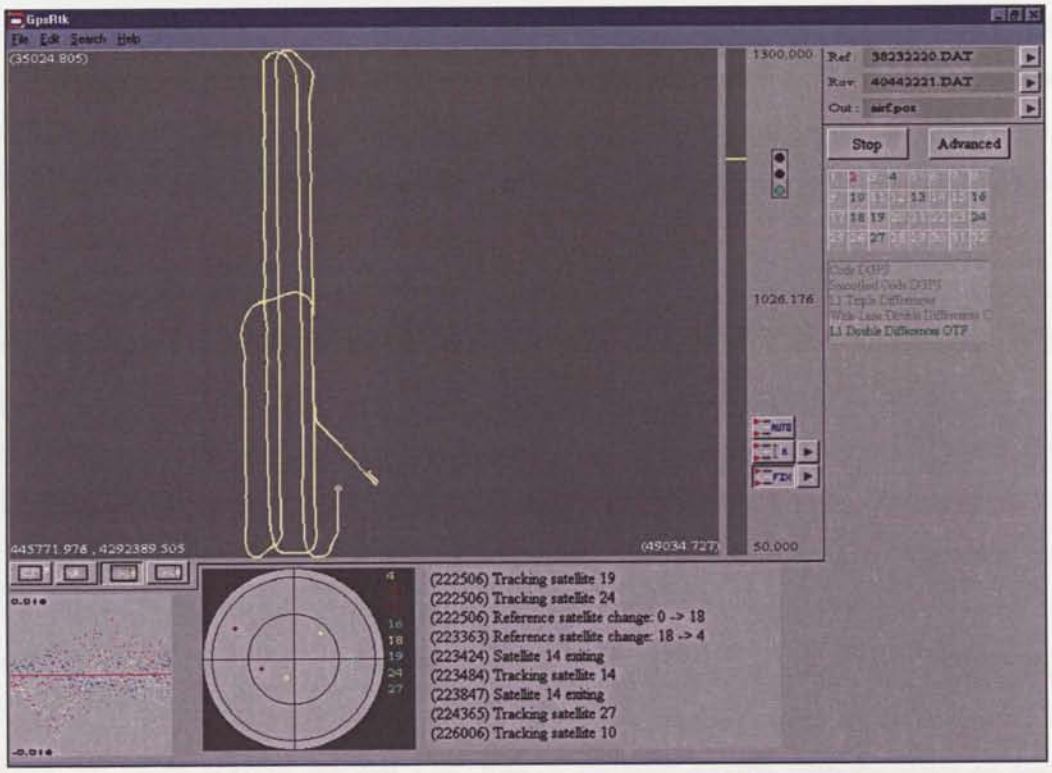


Figure 7.2 – Graphical interface for the GPS processing application.

The interface shown in figure 7.2 is built from a collection of independent graphical C++ objects, each compiled as a Dynamic Link Library (DLL). Moreover, each module of the GPS processing application whose functionality could be well defined and isolated was developed as a DLL. The main application then groups a set of DLLs, making calls to their functions. This architecture allows debugging of these modules independently of the rest of the application. Also, these objects can be changed without even having to recompile the whole applications, all that is required is to replace the old DLL file corresponding to that object with the new one.

Following is a description of the graphical objects in the interface shown in figure 7.2.

Taking most of the screen space, the horizontal position plot shows the positions determined every epoch by the algorithms. The positions are always determined in WGS84 coordinates (the GPS processing algorithms always work over the *xyz* WGS84 coordinates) and, for plotting purposes, they are converted to planar coordinates. In the lower left corner, the absolute coordinates of the corner are presented. The width and the height of the area represented by the whole rectangle in

shown in brackets, in the lower right and upper left corners, respectively. The behaviour of this plot can be controlled through the selection of one of four modes:

 The represented area is kept fixed;

 The width and height are kept fixed but the area moves keeping the current position at the center of the plot;

 The width and height automatically change when the current position falls outside the plotting area, maintaining the aspect ratio;

 The width and height automatically change when the current position falls outside the plotting area, not regarding the aspect ratio;

Zoom in and zoom out features were implemented in this object, being active before, after and during processing of new positions.

In the right side of this plot window, the altitude plot object is shown. The yellow horizontal line shows the current altitude in a definable scale, and the current altitude numeric value is shown in grey, in the middle. A dimmed trail is left for the past 10 epochs to give an idea of performed vertical displacements. Three plotting modes are selectable:



Automatic mode where the scale limits expand with the determined altitude values;



Follow mode where the current altitude is always represented on the center of the scale, being the scale limits shifted (the scale amplitude can be defined);



Fixed scale mode, where the used specified the scale limits.

The small traffic sign presented in the interface is used to provide information on the status of the processing algorithms. For example, in the case of the L1 ambiguity fixing algorithms, the red light indicates that only a code DGPS solutions (with carrier aiding) is being determined; the yellow light indicates that wide-lane ambiguity fixing was achieved and the current positions are being determined by the Lw phase measurement; and the green light indicates that the L1 ambiguities were fixed, being the current solution based on L1 phase measurements.

In the lower left corner of the interface, a graphic with the current residual values is plotted. The residuals from the measurements equation system are shown in this sliding window which depicts values of the last 120 epochs. Implemented with an auto-scaling feature, this interface is important to analyse the quality of the current solution, and to detect possible outliers.

Next to the residuals' graphic is the current sky plot, that is, the position on the sky of the visible satellites, as seen by the reference receiver. This is the typical polar plot of elevation versus azimuth. Every satellite is represented by a distinct colour, and the same colour table is used in the residuals' graphic, so it is easy to check the location of a satellite whose residuals show an unexpected behaviour, for example.

Following the sky plot object is an information interface that displays messages resulting from the occurrence of certain events, like satellites entering or exiting the set considered in the calculations, or a change of reference satellite. When a sudden undesired effect appears, for example, reflected on the residuals, this interface helps correlating that fact with a possible events that occurred in that moment.

In the upper right corner of the interface of figure 7.2 is the file management tool. Through this, the rover and references receiver settings are introduced, and the file that stores the resulting solutions is specified. This interface allows the selection of the processing mode, either real-time of post-processing. In post-processing mode, the data files stored on the PC hard disk are specified for each receiver, together with the ephemeris file. In this mode, the receiver type is automatically detected from the files specified. In real-time mode, instead of the data files, the serial COM ports are specified and their settings selected. Also, the receiver type for each port is specified. In both processing modes, the coordinates of the reference station antenna are specified. Figure 7.3 displays two examples of configuration of the reference receiver settings, in both processing modes.

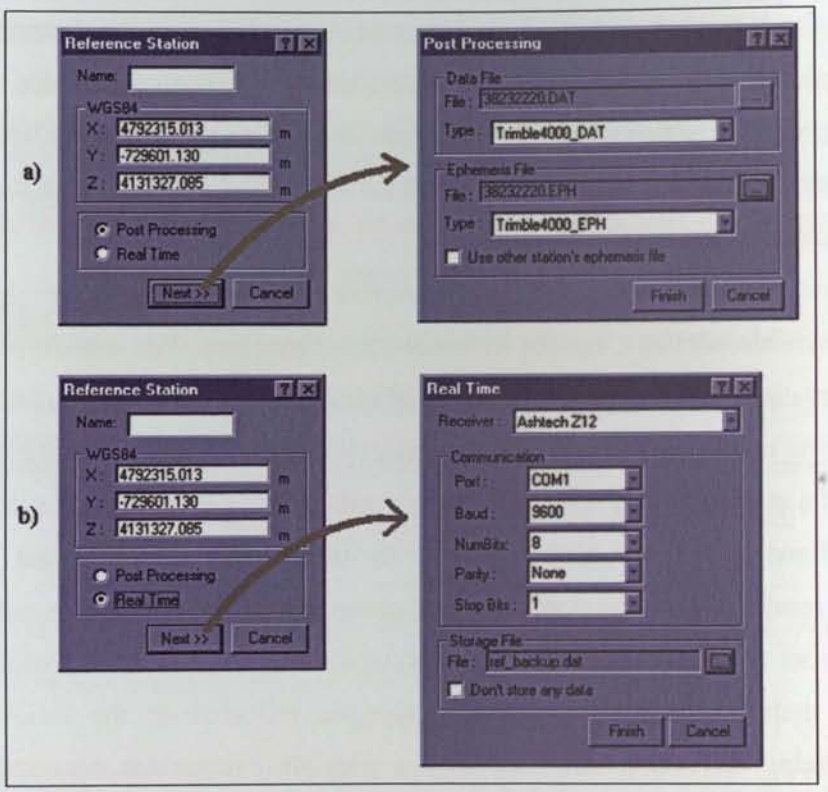


Figure 7.3 – Reference receiver settings - a) post-processing mode; b) real-time mode.

Right below the file management tool, the *Start/Stop* button and the *Advanced* button appear. The former starts of stops the processing modules. The latter launches a dialog box where some processing parameters can be specified, depending on the selected processing algorithm. Figure 7.4 displays the dialog that appears for the L1 carrier phase processing method. It should be noticed that the user can change these parameters even while the algorithms are running.

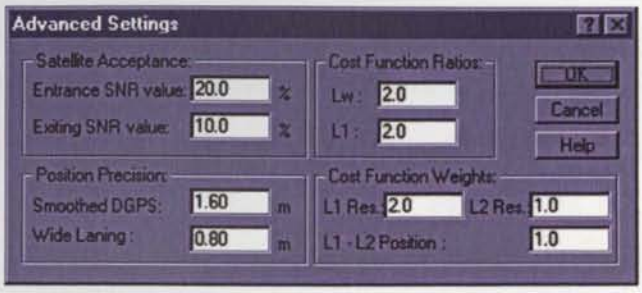


Figure 7.4 – Advanced settings dialog for the L1 carrier phase processing method.

Figure 7.5 shows the used satellites interface. Though this, the user can see which satellites are being considered in the calculations – these are the ones whose

PRN are depicted in green. If the user clicks over one PRN, that satellite is automatically excluded from the calculations and its PRN becomes red. If that PRN is clicked again, it becomes available for processing again. The dimmed PRNs represent satellites that are not being tracked simultaneously by both receivers, or whose data quality is low enough for them to be rejected. The user can select/deselect the satellites even while the algorithms are processing the data.



Figure 7.5 – Used satellites interface.

Finally, below the used satellites object is the processing method selection box. By clicking in the desired method, the user selects which algorithm will be used for processing the data. Again, it is possible to change between algorithms in the middle of processing.

As shown, though this application interface, the user can visualise the determined DGPS solutions and their quality. But there can be other applications that would require to have access to those solutions. In post-processing mode this would be simply performed by opening the GPS output file. But in real-time mode, this is not that simple. For example, in the navigation system shown in chapter 3, the IMU data processing application requires the GPS solutions as input into the Extended Kalman filter (see [Tomé, 2002]). To avoid mixing the code of both applications (GPS and IMU), these were developed independently and a data link was established between them using *pipes*. In order to allow other applications to have access to the GPS solutions, a real-time output module was developed. This module enables connections though *pipes*, TCP/IP and serial ports, used to send on the real-time navigation solutions as soon as they were available. With these communication channels, even remote applications can access the determined positions.

7.2 CAMPAIGNS

7.2.1 AZORES 1997

In October 1997, under the European project AGMASCO (Airborne Geoid MApping System for Coastal Oceanography – project funded by the MAS3-CT95-0014 from the European Commission), an airborne gravimetric and altimetric campaign was organised, taking place at the Portuguese archipelago of Azores. The main purpose of this project was to prove the efficiency of airborne methods, being much cheaper and efficient than terrestrial and shipborne methods to determine the geoid undulations. An accuracy identical to that obtained with marine methods can be achieved, with a spatial resolution higher than that provided by satellite-based gravimetry. Just for enlightening purposes, a brief description of what was to be determined is subsequently presented. Some more details on the Azores survey of project AGMASCO can be found in [Bastos et al., 1998], [Bastos et al., 1999], [Bastos et al., 2000a], [Bastos et al., 2000b] and [Cunha et al., 1998].

As explained before, the geoid is an imaginary surface with constant gravitational potential. For most of the applications considering altitude, it is usually used the geoid as reference for those altitudes. The geoid has the gravitational potential value that leads to a surface most coincident with the mean sea surface. Due to its importance, the determination of this reference surface is a central goal of many researches (see, for instance, [Forsberg et al., 1996a] and [Forsberg et al., 2000]), where many methods have been developed for that purpose. One of those methods is airborne gravimetry.

The principle of airborne gravimetry is presented in figure 7.6. After processing the gravimeter data, together with the aircraft's navigation solution (including the motion related accelerations), the local gravity acceleration value is determined. From processing the altimeter data, the altitude of the aircraft over the sea level is also determined. Combining these results leads to the determination of the geoid altitude with respect to the reference ellipsoid, which was the primary objective of the project.

In the Azores triple junction region, where the African, European and American tectonic plates meet, the detailed knowledge of the geoid can be very useful for understanding the complex system faults crossing the region.

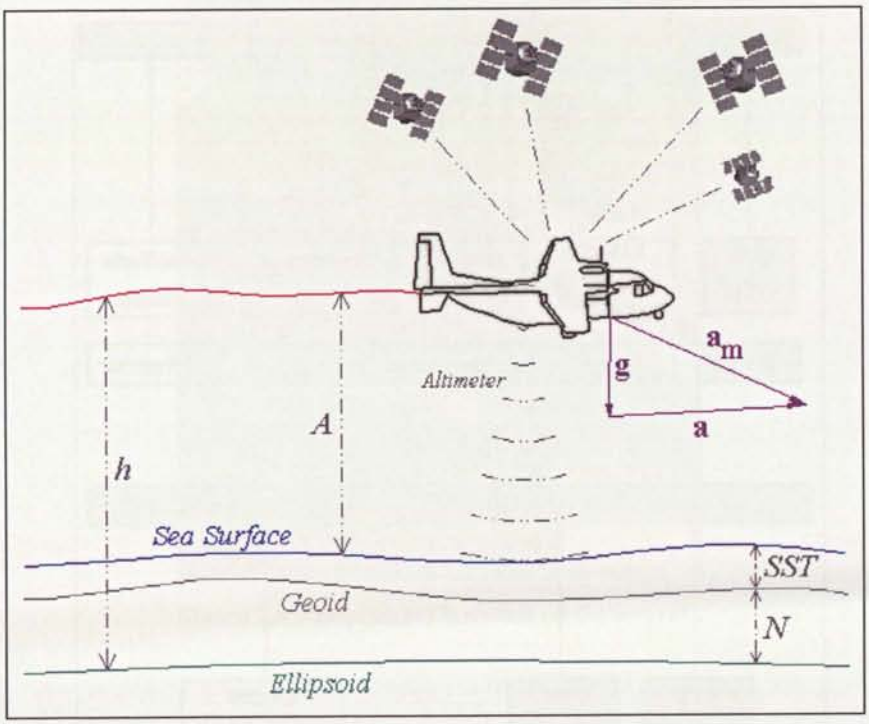


Figure 7.6 – Principle of airborne gravimetry.

The air segment of this campaign consisted of a Portuguese Air Force aircraft (CASA212) equipped with a gravimeter (with its stabilising platform), a radar altimeter, a laser altimeter, together with other sensors such as two prototypes of IMU systems specially developed for vertical acceleration measurements. Since the information of these devices is useless unless the aircraft position and attitude (and also its velocity and acceleration) are determined, the developed navigation system, as described in chapter 3, was also installed on the aircraft.

A communication link using DGR-115HWW radios from Freewave Technologies was established in order to test its efficiency and performance in a real situation. The data collected during the campaign was essential for the following development of the real-time navigation algorithms and software.

Figure 7.7 presents a scheme of the configuration implemented on the aircraft for the AGMASCO campaign. Figure 7.8 shows a picture of some of the equipment installed onboard. Before proceeding with any flight, the position of every equipment

was determined with respect to the aircraft referential (defined by a metal strip along the aircraft floor structure, and its orthogonal axes – vertical and towards the right wing). This was done using two total stations while the aircraft was inside the hangar.

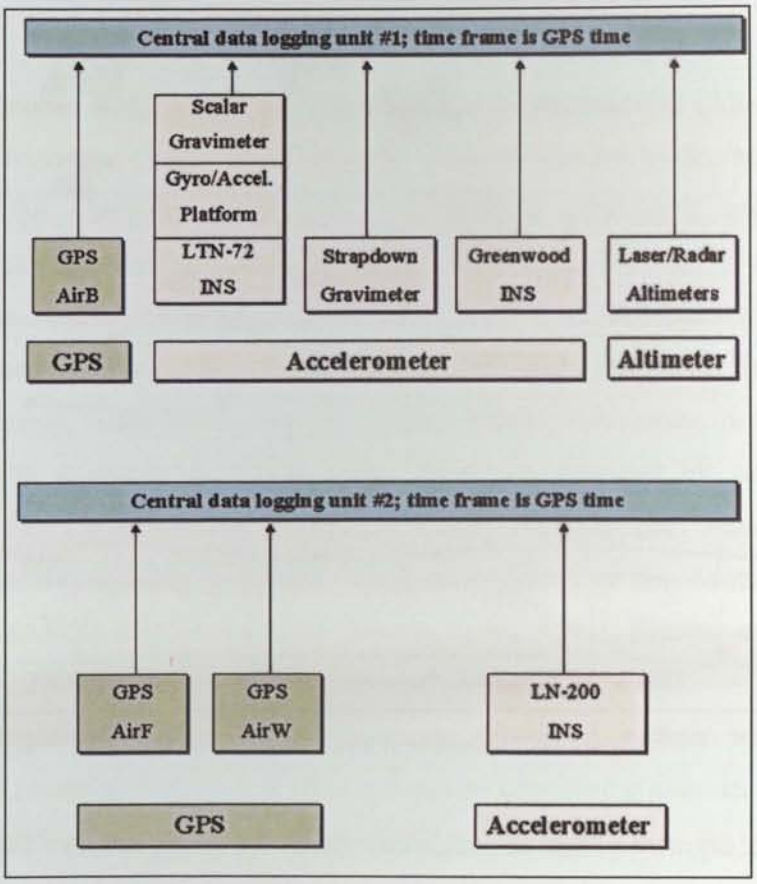


Figure 7.7 – Scheme of the onboard equipment configuration.

The ground segment consisted of a set of reference stations spread along the Azores islands. In one of the reference stations, a radio unit was installed in order to allow the communication tests. GPS differential corrections were sent to the aircraft. Figure 7.9 shows the placement of the reference stations.

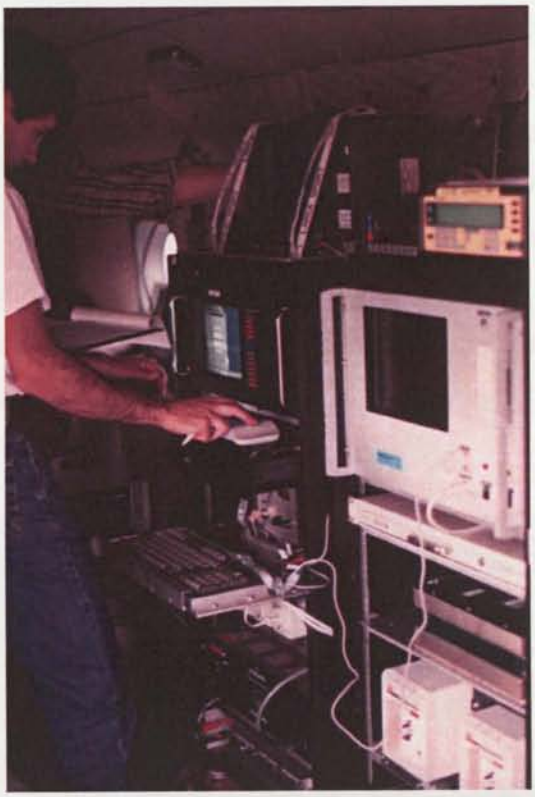


Figure 7.8 – Equipment installed on the aircraft.

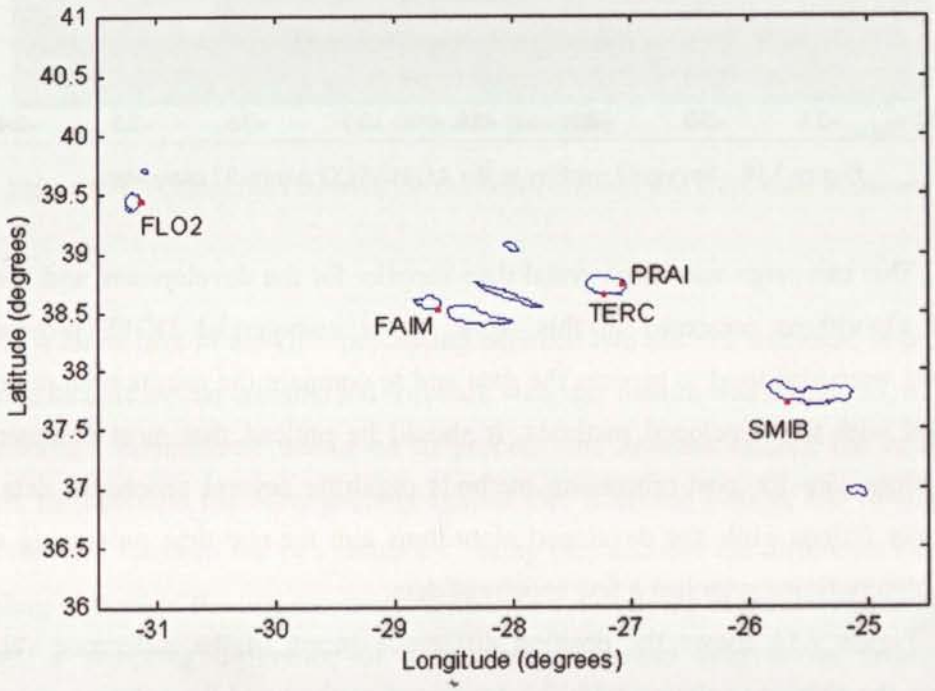


Figure 7.9 – AGMASCO reference stations in the Azores islands.

A total of 14 flights were flown, always keeping the aircraft at a low altitude (about 250 and later 150 meters over the sea). The flown profiles were previously determined in order to cover the area of interest and also to have some profiles coincident with the ground tracks of the Topex/Poseidon and ERS satellites, for later comparison of the results. The oceanographic vessel R/V Håkon Mossby from the University of Bergen (Norway) was used to cover a few of the flown tracks allowing a third comparison of the obtained results, in this case with the traditional gravimetric marine survey method. Figure 7.10 shows the set of flown profiles.

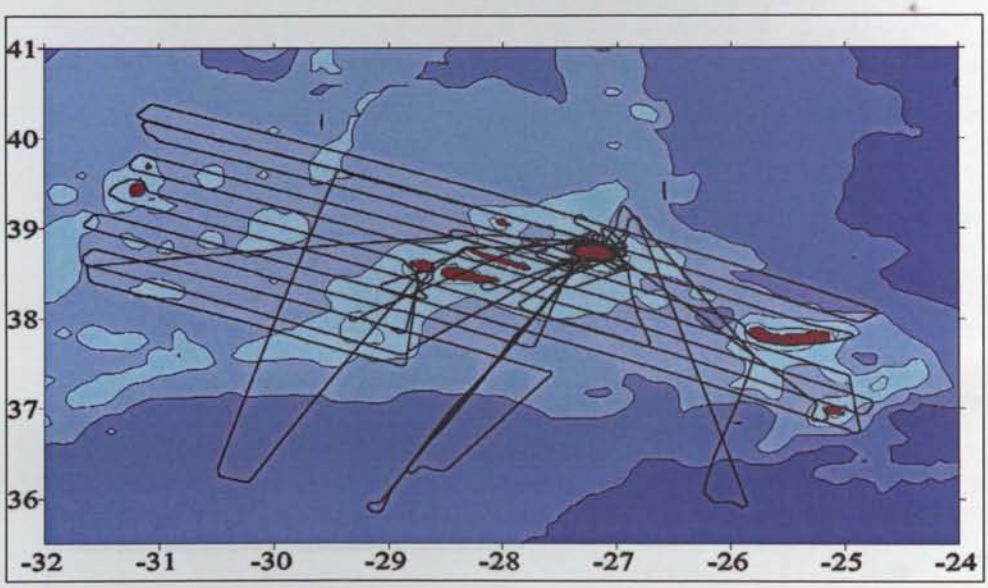


Figure 7.10 – Surveyed profiles in the AGMASCO Azores97 campaign.

This campaign was an essential data supplier for the development and testing of the algorithms presented in this work. Other commercial DGPS processing software were also used to process the data and to compare the results with the ones obtained with the developed methods. It should be noticed that most commercial applications aim for post-processing methods requiring several epochs of data for ambiguity fixing, while the developed algorithms aim for real-time processing with L1 ambiguity fixing with just a few epochs of data.

Figure 7.11 shows the position difference (norm of the difference vector) between the obtained solution with the developed method and the solution given by the commercial software GeoGenius from Spectra Precision Terrasat GmbH (Germany), for the flight taken in the 4th October 1997. The flight profile is presented in the upper right corner of figure 7.11. As can be seen, there is a difference that

reaches a few decimeters, which clearly increases with baseline length. This can reflect, for example, the use of different treatments of ionospheric or tropospheric errors. In this case, the baseline length reaches the value of 124 km. It also should be mentioned that the satellite availability and geometry was not very good for a long section of this flight.

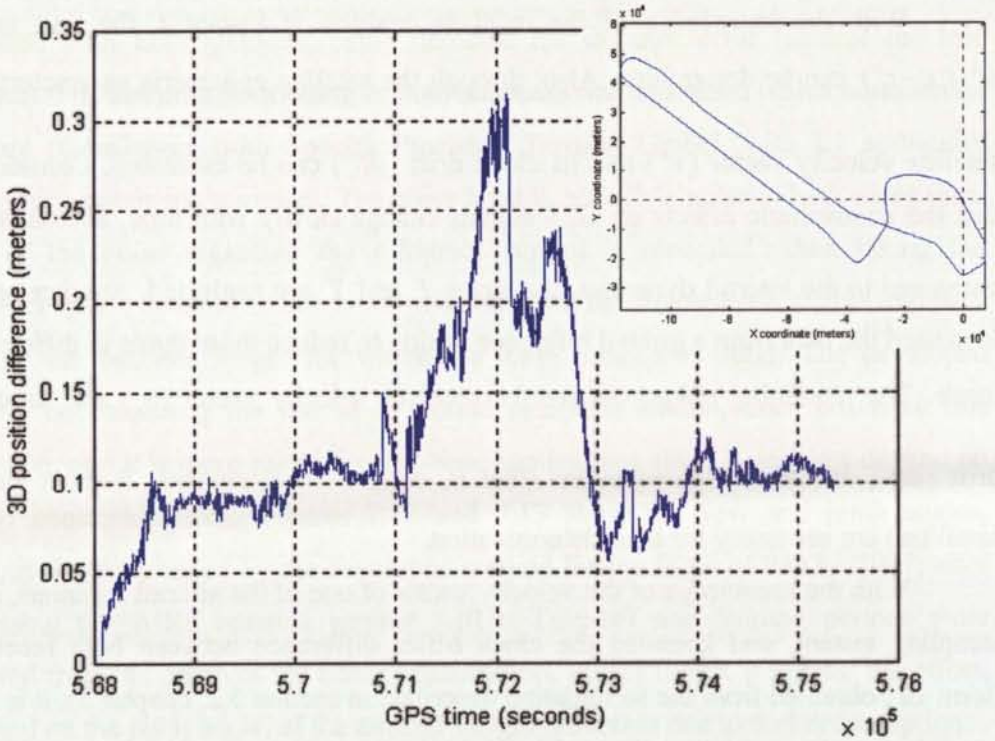


Figure 7.11 – Comparison between the developed software and GeoGenius solutions.

With respect to the GPS processing between two aircraft antennas, in order to estimate its attitude, no commercial software with this feature was found. So, the way to perform a comparison would be to process one antenna against the reference station, then process the other antenna against that reference station, and finally take the difference between the two solutions, taking into account the difference between sampling instants of the two receivers. With the aircraft flying at around 70 meters per second, a sampling difference of 1 millisecond would lead to an error of 7 centimeters, so the aircraft velocity is also required. As seen in equation (4.10), chapter 4, the doppler measurement is the instantaneous derivative of the carrier phase measurement. Considering that $v^k(t-\tau_i^k)$ is the velocity vector of the satellite k, at

instant $t-\tau_i^k$,and that $v_i(t)$ is the velocity vector of the receiver i, at instant t, equation (4.10) can be rewritten in the form of equation (7.1).

$$\lambda D_i^k(t) = u_i^k(t,t-\tau_i^k)^T \cdot \left(v^k(t-\tau_i^k) - v_i(t)\right) + (\dot{dt}_i - \dot{dt}^k)\cdot c - \dot{I}_i^k + \dot{T}_i^k + \dot{\varepsilon}_i^k(t) \qquad (7.1)$$

With the knowledge of the receiver position at instant t, the unit vector $u_i^k(t,t-\tau_i^k)$ can be determined. Also, through the satellite ephemeris parameters, the satellite velocity vector (v^k) and its clock drift ($\dot{dt}^k$) can be estimated. Considering that the atmospheric effects on GPS signals change slowly with time, at least when compared to the aircraft dynamics, the terms $\dot{I}$ and $\dot{T}$ are neglected. Another option is to used the data from a ground reference station to reduce those terms in differential mode. The remaining unknowns are the receiver velocity vector (v_i) and its clock drift ($\dot{dt}_i$), and at least 4 equations (that is, doppler measurements from at least 4 satellites) are necessary for their determination.

With the knowledge of the velocity vector of one of the aircraft antennas, at its sampling instant, and knowing the clock offset difference between both receivers (term Δt, obtained from the formulation described in section 5.2, chapter 5), it is then possible to estimate the position of both receivers at the same time instant. This is performed through a simple linear extrapolation as shown in equation (7.2). Since Δt is always below 1 millisecond, the error introduced by this extrapolation is negligible.

$$r_i(t+\Delta t) \simeq r_i(t) + v_i(t)\cdot\Delta t \qquad (7.2)$$

It is then possible to determine the vector between two aircraft antennas based on the prior determination of the their absolute positions, as shown in equation (7.3). A comparison between this method and the one presented in section 5.2, chapter 5, can be now performed. It should be mentioned that, for a correct comparison, the selection of the sampling instant, to which both receiver positions are to be determined, must be the one used in the method of section 5.2.

$$r_{ij}(t+\Delta t) = r_i(t+\Delta t) - r_j(t+\Delta t) \tag{7.3}$$

The developed method, without requiring the reference station, determines the vector between antennas with the same level of precision as the difference of the absolute positions of both antennas. Figure 7.14 shown an example where the data from AIRB and AIRF antennas, collected on the flight shown in figure 7.12, was processed with both methods, being depicted the distance error (against the true distance). The absolute positioning of both antennas was processed with a commercial software (GeoGenius from Spectra Precision Terrasat GmbH, with L1 ambiguity fixing) for comparison purposes. The noise level is actually similar in both cases since most of the noise regarding the reference station is cancelled when taking the difference of the determined antennas' positions. But the atmospheric effects impose a limit on the baseline length for which the latter method is valid. The developed method, not requiring the use of a ground reference station, does not have this restriction, and it is more suited for real-time applications since it does not depend on ground communications. Figures 7.12 and 7.13 show the yaw and pitch angles, respectively, determined by the developed method for the flight of 08/Oct/1997, after processing the AIRF antenna against AIRB. Take-off and landing periods were removed from the graphics for better visualisation. In this figure, it is clear the effect, reflected on the pitch angle, of the aircraft weight reduction due to fuel consumption.

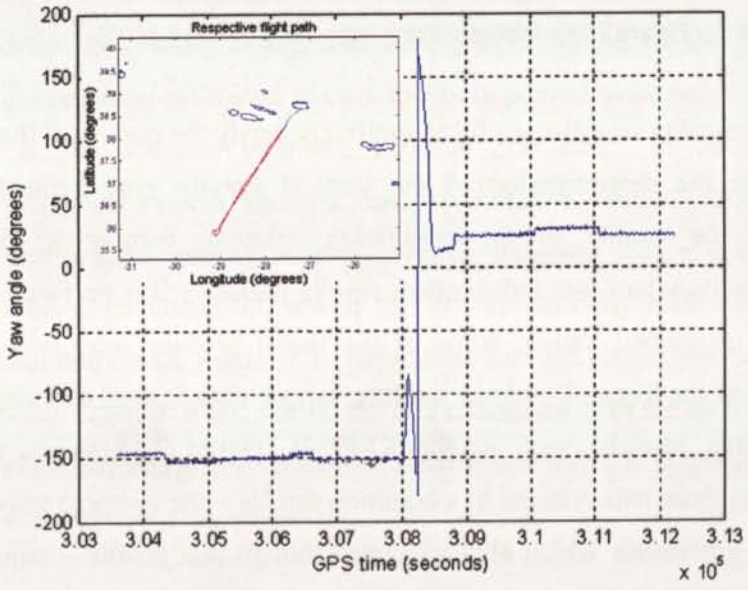


Figure 7.12 – Yaw angle for flight of day 08/Oct/1997, determined by the developed method.

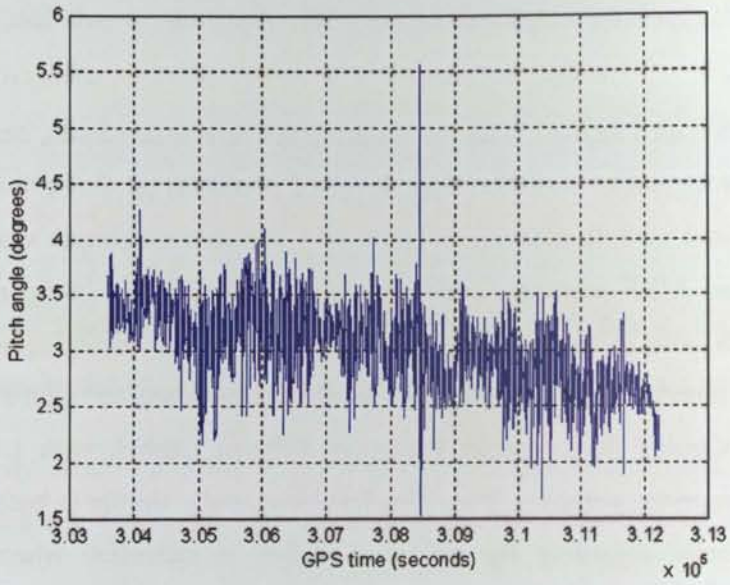


Figure 7.13 – Pitch angle for flight of day 08/Oct/1997, determined by the developed method.

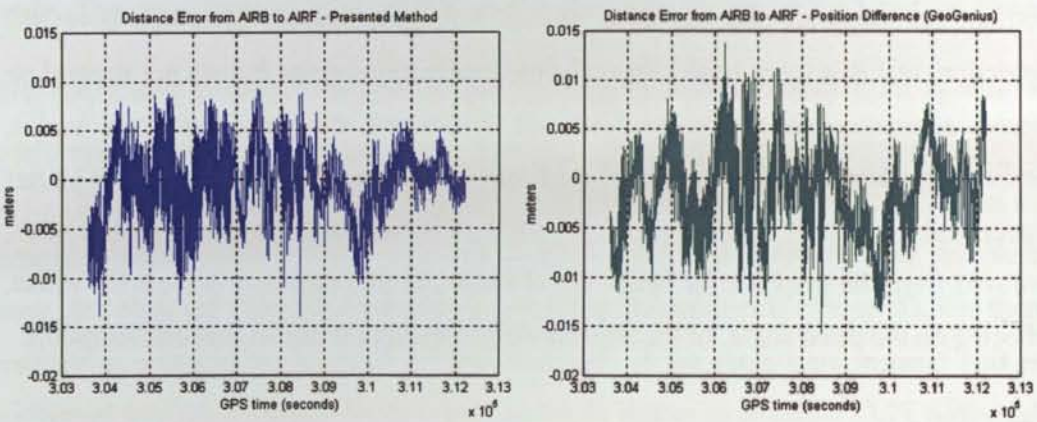


Figure 7.14 – Distance error between AIRB and AIRF.

This campaign was also useful to indirectly verify the quality of the navigation solution. Since the determination of the vertical gravity measurement is highly dependent of the quality of the navigation solution, comparing the airborne gravimetric results with other independent results indicates if it performed or not as expected. As mentioned earlier, some of the flown profiles were coincident with ground tracks of the Topex/Poseidon satellite, whose data is used to compute global scale gravimetric models (such as the KMS99). Figure 7.15 shows the gravity anomaly results from two systems in a common profile – the airborne gravimeter and the shipborne gravimeter which also navigated though that profile – adjusted to the

KMS99 model (more information regarding this comparison can be found in [Bastos el al, 2000b]). As can be seen, a high correlation exists between them.

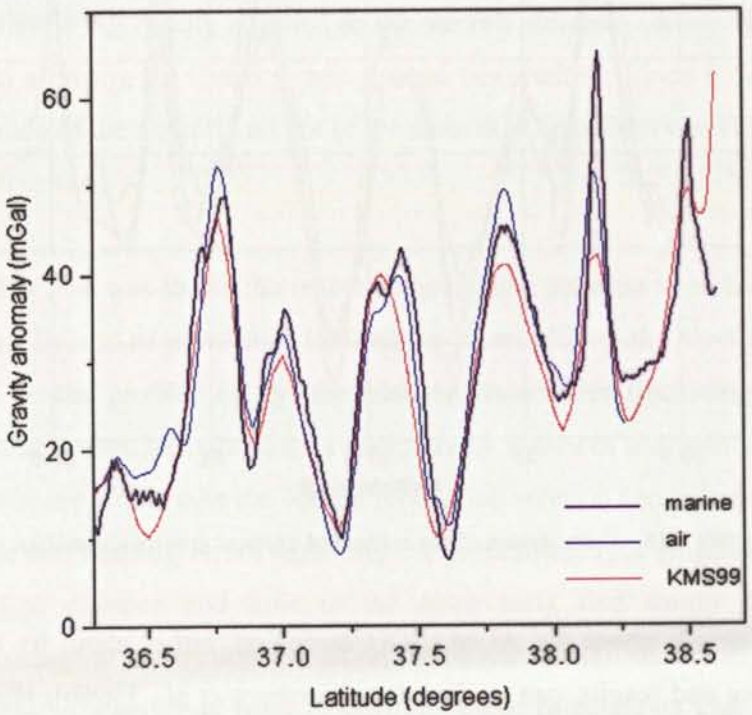


Figure 7.15 – Gravimetric results obtained in a common area with three different methods.

As mentioned in chapter 6, the vertical gravity anomaly is also a state of the Kalman filter that processes the IMU data together with the GPS results. This state is also estimated with the equipment used in this navigation system, as can be found with more detail in [Tomé, 2002], and after proper tuning of the Kalman filter parameters, the resulting estimated gravity anomaly proved to be accurate enough up to face the results obtained with the airborne gravimeter. In other words, the developed navigation system showed that, by itself, it could determine a good estimate of the vertical gravity anomaly, which indicates that a good navigation solution was being produced, otherwise the gravity anomaly estimate would most probably reflect that effect. Figure 7.16 depicts the vertical gravity anomaly estimated by the navigation Kalman filter, versus the one calculated with the airborne Lacost & Romberg gravimeter, and also with the one determined with the shipborne gravimeter (also a Lacost & Romberg equipment).

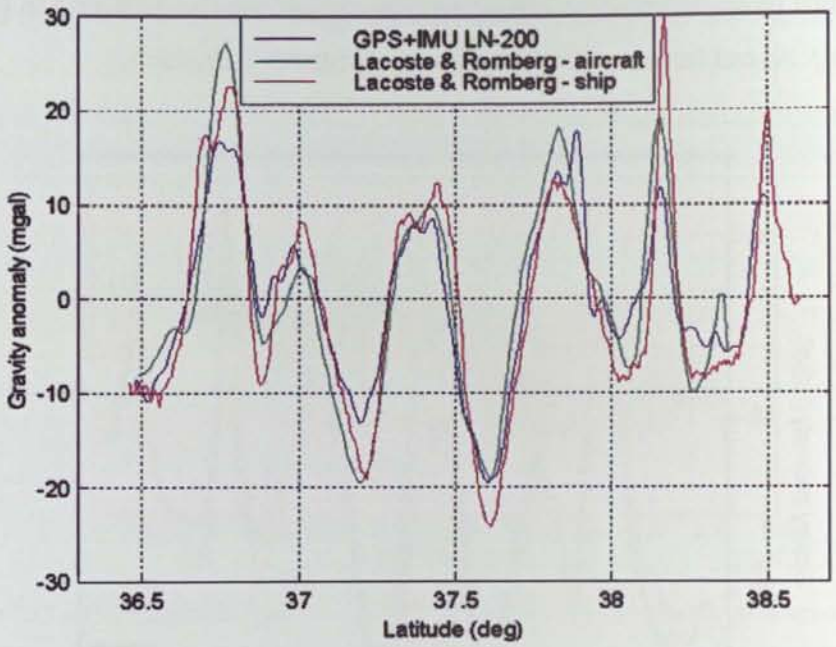


Figure 7.16 – Comparison of the estimated vertical gravity anomalies.

More details about the AGMASCO campaign, either about its installation, data processing and results, can be found in [Forsberg et al., 1996b], [Bastos et al., 1997], [Bastos et al., 1998], [Bastos et al., 1999] and [Bastos et al., 2000a], among others.

7.2.2 SINTRA 1999

The second airborne campaign took place in August 1999, in the region of Estremadura, with the center of operations at the Portuguese Air Force Base near Sintra. The objective of this campaign was to test the system working in real-time and to have an assessment of its accuracy. At first, the idea was to mount in the aircraft, together with the described navigation system, another navigation system based on a high grade Inertial Navigation System (INS). This system, being much more expensive than the developed system, was supposed to be lent by a foreign institution but, due to an incompatible time schedule, it turned out to be impossible to have such system for the flights. An alternative way to get an independent source for checking the system's accuracy was to install onboard the aircraft a photogrammetric camera

and use its photos to determine the aircraft position and attitude. This was the implemented solution, and a Leica RC-10 photogrammetric camera was installed.

In traditional photogrammetry, the camera stands on a more-or-less stabilised platform, which is not rigidly attached to the aircraft structure (dumping the aircraft vibration and allowing its levelling and ground orientation). Since it was meant to have the attitude of the aircraft and not of the camera, its platform was rigidly fixed to the aircraft structure.

Another idea was to use the real-time navigation solution to indicate the pilots the way to go. Instead of previously indicate the pilots, during the pre-flight briefing, what would be the profiles to fly, the planned trajectories (including curves and landing approach) were introduced on a computer by means of waypoints. A specially developed software would take the current navigation solution and calculate the cross-track, altitude and heading errors regarding the predefined track (together with other parameters like distance and time to the track end), and would display them graphically using a Horizontal Situation Indicator (HSI) interface. A detailed description of the algorithms used to perform these calculations can be found in [Sérgio, 2001]. It was selected the HSI interface since it is an interface the pilots are used to work with.

A laptop computer was used to handle these calculations, having the waypoints stored in a file and receiving through a TCP/IP connection the real-time navigation solution from the system. It graphically simulated the HSI interface and from it, after converting the VGA signal to a TV signal, that same graphical interface was shown in the aircraft cockpit through a mini TV set, properly installed. This way, a control loop was established through the pilots of the aircraft.

Another laptop was used to display the current aircraft position on a map of the region being flown.

Figure 7.17 shows a scheme of the onboard installed equipment for this campaign. Figures 7.18 and 7.19 present some photos of the mounted equipment, and in figure 7.20 the HSI interface is displayed.

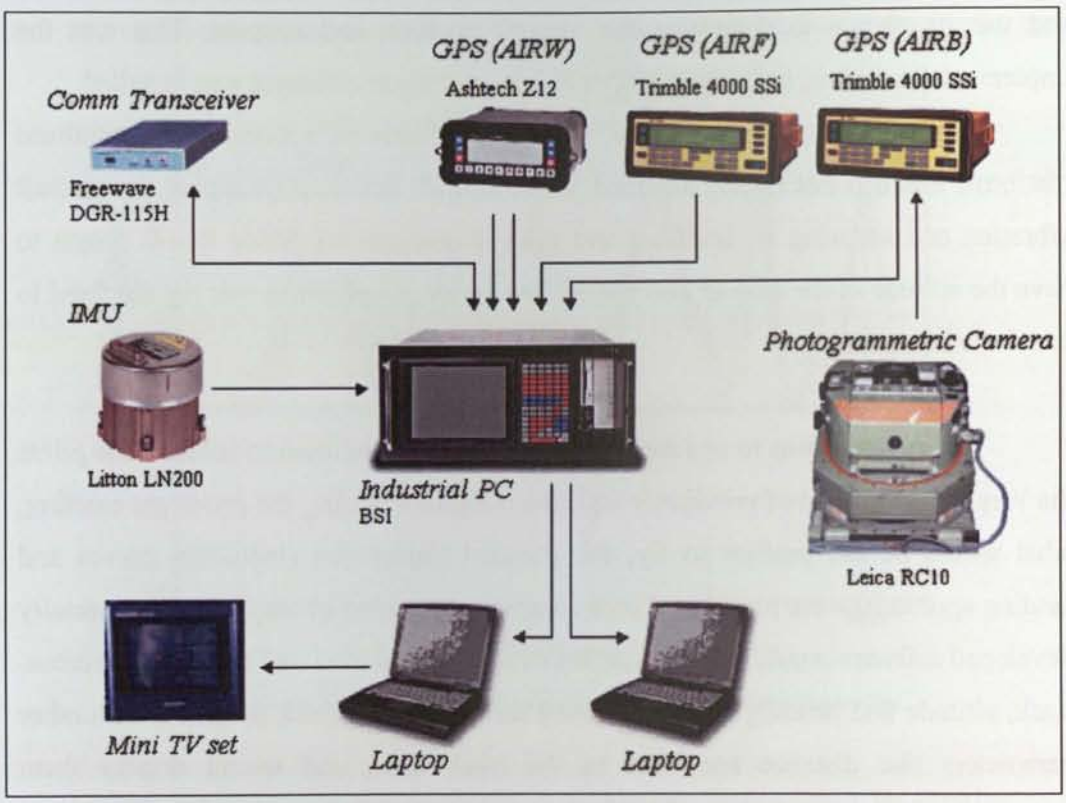


Figure 7.17 – Scheme of the onboard equipment for the Sintra99 campaign.

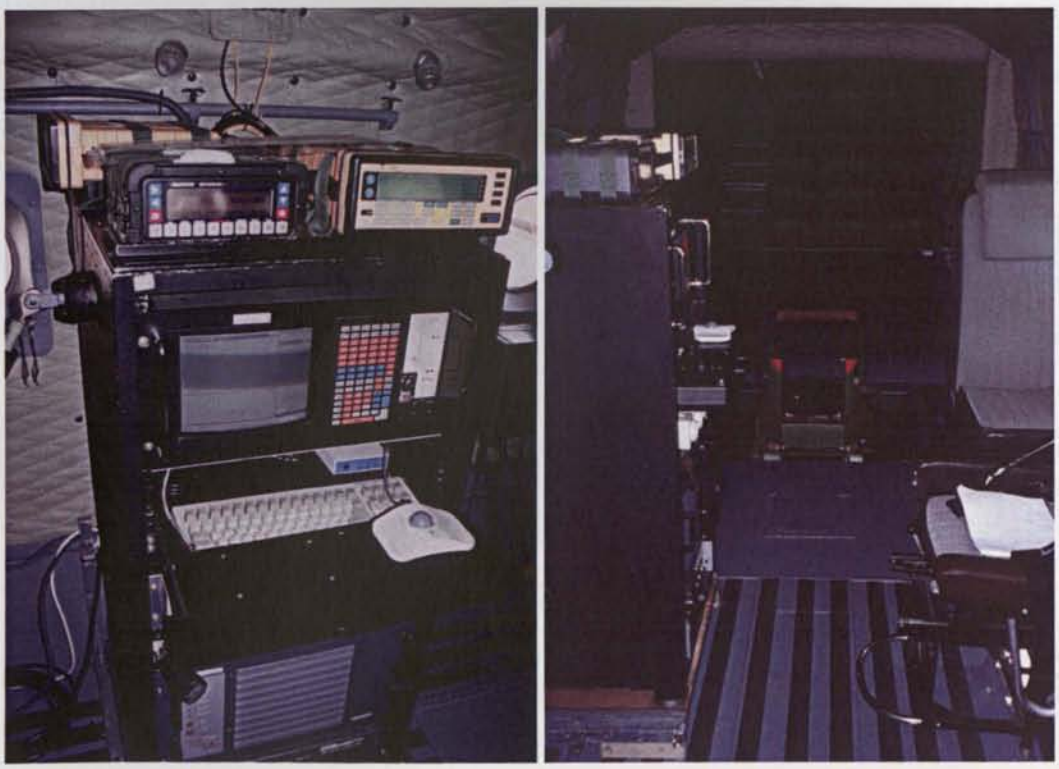


Figure 7.18 – Photos of the mounted equipment.



Figure 7.19 – Photos of the mounted equipment.



Figure 7.20 – The HSI graphical interface.

On the ground, two GPS reference stations were mounted. One of them was used to send its compressed data to the aircraft in order to enable differential GPS processing. Since the communication was bi-directional, the onboard computed solution was sent back to the main reference station that plotted the aircraft position on a map, and also a replica of the HSI interface was generated.

The communication system consisted of five radio transceivers DGR-115HWW from Freewave Technologies. These devices were configured to work as a network with one client and one server (the aircraft and the reference station), and the

other three, working as repeaters, were spread in high places along the flight path, covering the largest possible area where the aircraft was supposed to pass.

After one brief test flight, two flights were performed, most of it at 800 meters over ground, and with some parts at half of that altitude (the 800 meters altitude was the recommended altitude for the photogrammetric camera parameters, and the 400 meters altitude was considered to increase image resolution of the photos). Figure 7.21 shows the flown tracks, together with the reference stations' positions. In figure 7.22 the locations where photos were taken are indicated. The trajectories were projected to pass through places where control points on the ground could be easily identified. Also, in some areas, sequences of photos were considered with 30% superposition so that a stereoscopic analysis could be performed. These sequences were also taken to allow boresight calibration of the camera. A total of around 400 photos were taken, being digitalised 76 of them.

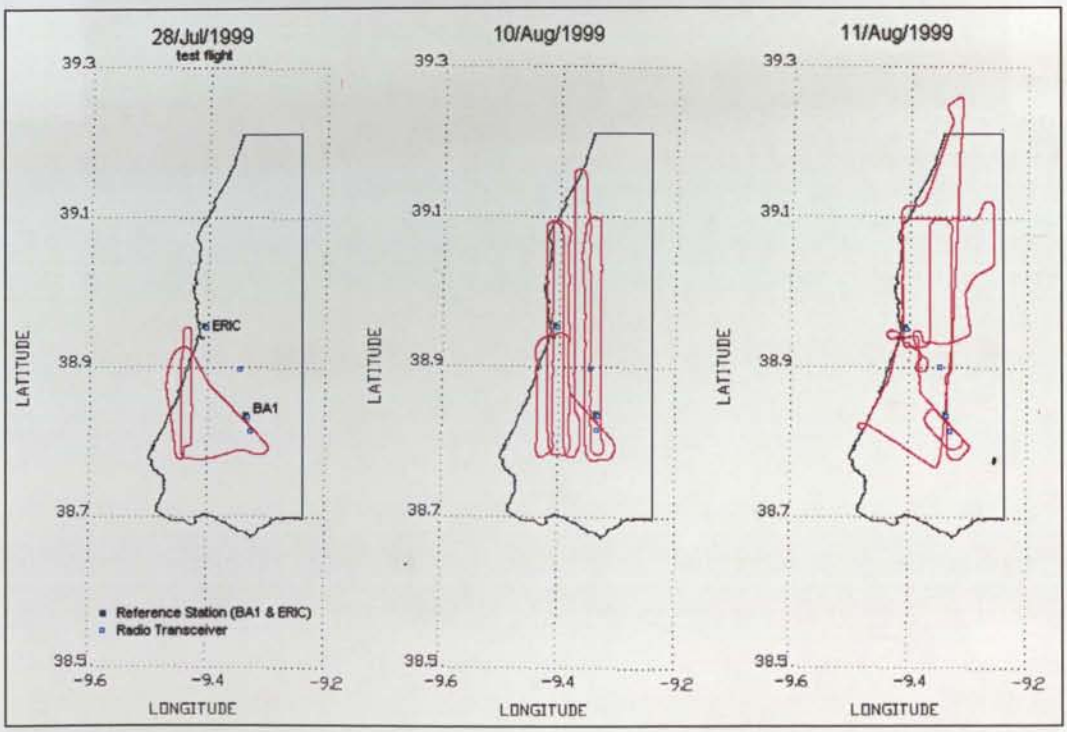


Figure 7.21 – Flight profiles of the Sintra99 campaign.

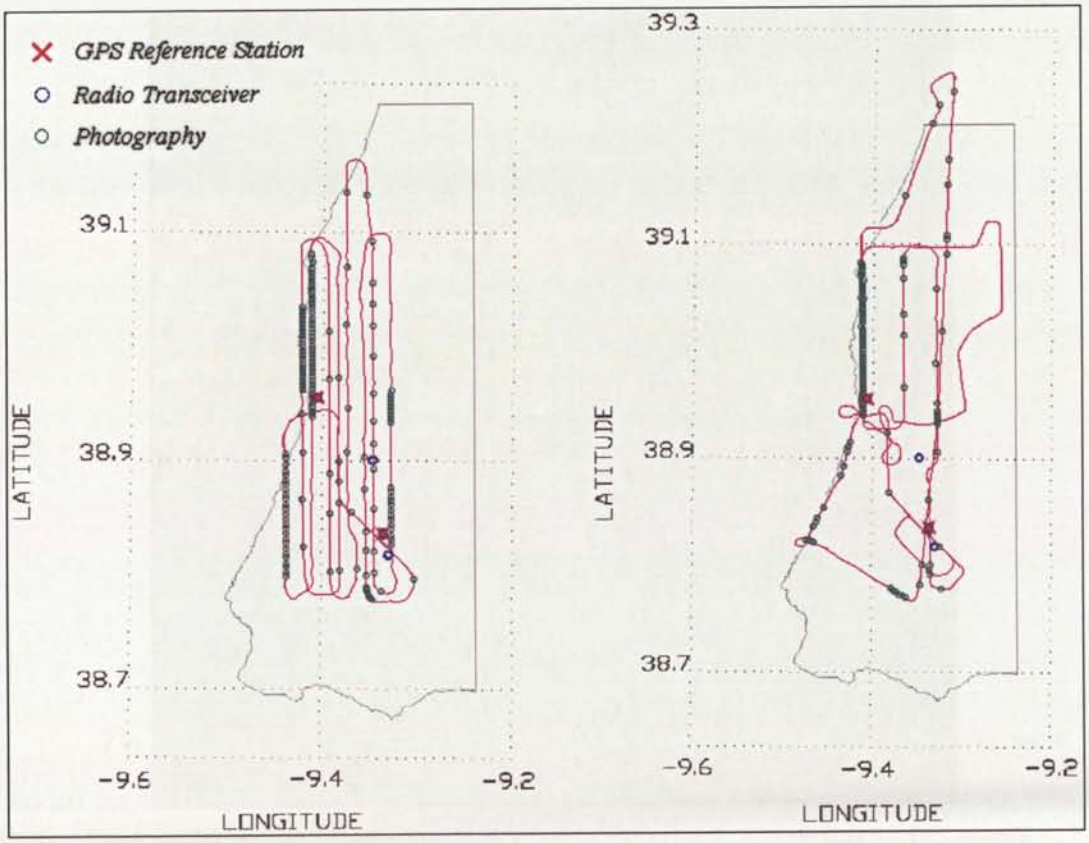


Figure 7.22 – Photos taken with the photogrammetric camera.

Another test that was considered, while programming the flight trajectories was to pass through the same profile more than once (and take photos) to check the repeatability of the navigation solution. Figure 7.23 presents an example of a taken photo.

As mentioned above, the pilots were closing the feedback loop minimising the difference between the current position aircraft position and the predefined on-track position. The sensitivity of the pilots, the maneuverability of the aircraft and the flight conditions (wind speed and wind variation) impose the lower limit on the achievable navigation error regarding the predefined tracks. As an illustration, figures 7.24 and 7.25 show the total and the vertical flight trajectory errors observed on a 10 km section of one of the flown profiles. The oscillatory characteristics of these errors agree with the observed effort from the pilots to constantly reduce the off-track indications.



Figure 7.23 – Example of a photo taken with the photogrammetric camera (photo 8602).

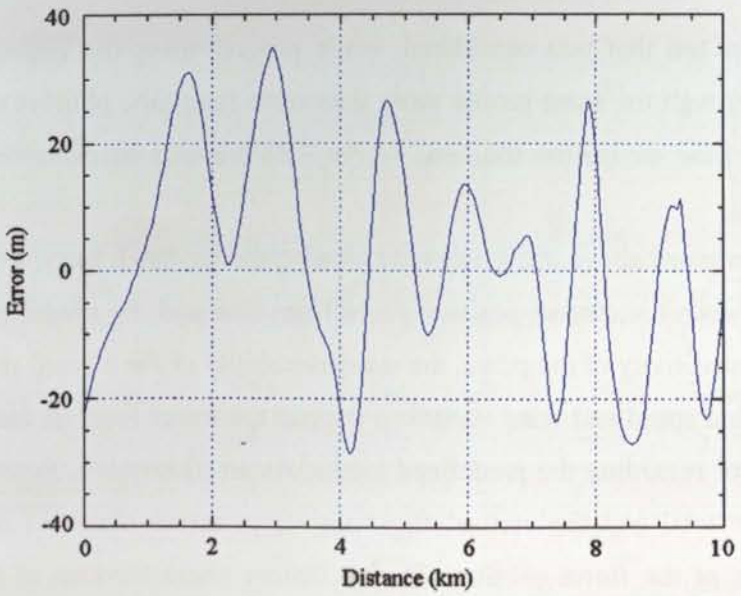


Figure 7.24 –Total off -track error on a section of a profile.

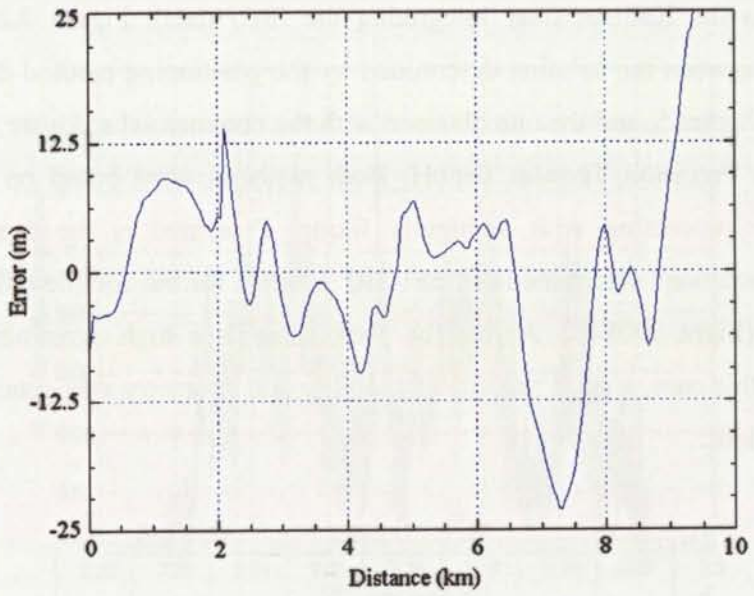


Figure 7.25 – Vertical off-track error on a section of a profile.

On the flight on the 11th August (flight 990811), extra predefined tracks were added for landing approach. With careful control from the pilots, this trajectory was followed and the resulting achieved vertical error is depicted in figure 7.26. As can be seen, the pilots actually performed a touch-and-go maneuver.

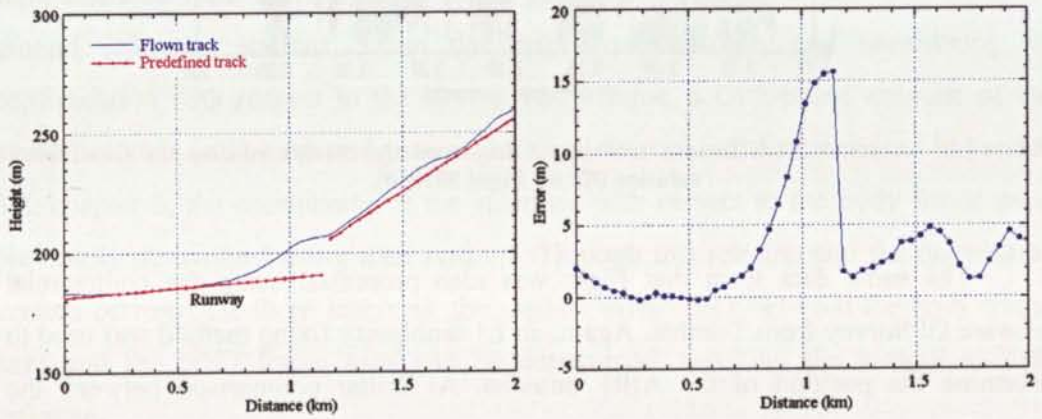


Figure 7.26 – Vertical off-track error during landing approach.

The data retrieved from these flights was analysed, and processed by the algorithms presented in this thesis, either in real-time (on the aircraft) and in post-processing mode. Both methods, for high accuracy absolute DGPS positioning and for determination of the vector between two aircraft antennas, were used (and their results

were fed into the Kalman filter integrating the IMU data). Figure 7.27 shows a comparison between the solution determined by the positioning method described in section 5.1, chapter 5, and the one obtained with the commercial software GeoGenius from Spectra Precision Terrasat GmbH. Both methods were based on DGPS L1 carrier phase processing with ambiguity fixing. Presented is the distance error between the solutions determined for the AIRF antenna for the complete flight on the 10th August (flight 990810). As can be seen, there is a high agreement on both solutions. In this case, a good satellite availability and geometry was obtained during most of the flight.

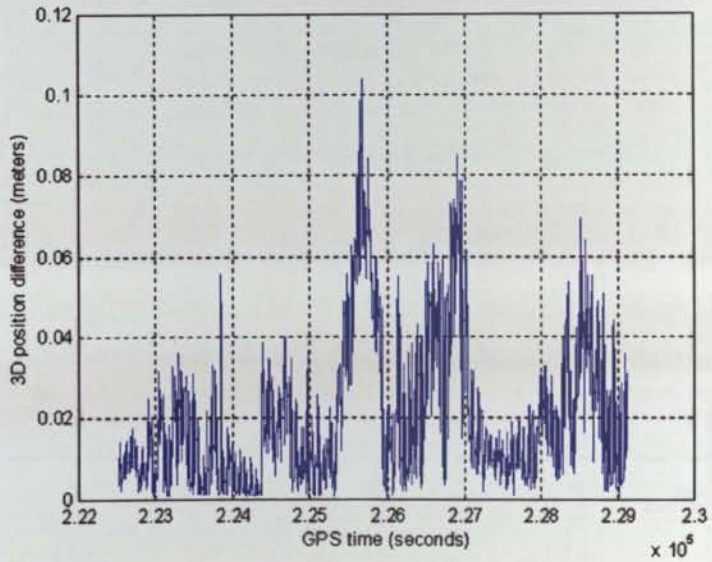


Figure 7.27 - Absolute 3D difference between the developed algorithm's solution and GeoGenius solution (SNAP flight 990810).

The same data from that flight was also processed using the commercial software GPSurvey from Trimble. Again, an L1 ambiguity fixing method was used to determine the position of the AIRF antenna. A similar comparison between the GPSurvey solution and the one obtained with the developed algorithm is shown in figure 7.28. As can be seen, the observed difference is again very small, although a better agreement was achieved with the GeoGenius solution. The use of different tropospheric model parameters could be a possible explanation for this fact since it appears to be a correlation between the aircraft altitude and the obtained difference (both ends of the plot of figure 7.28 reflect the periods where the aircraft was at the airport).

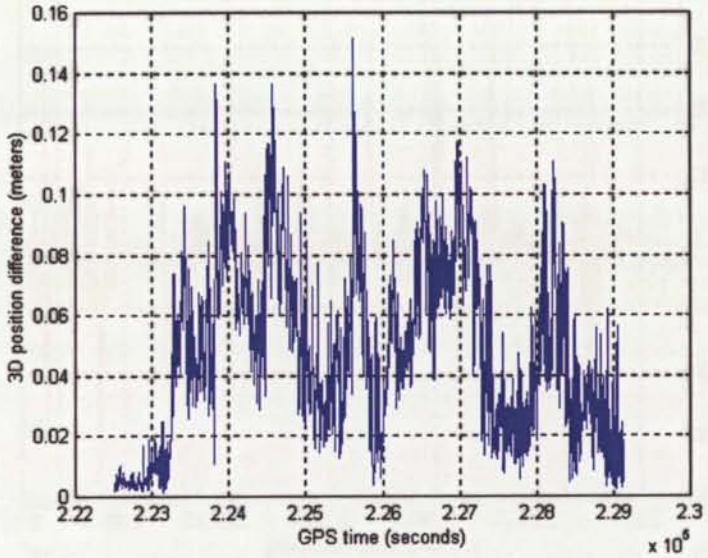


Figure 7.28 – Absolute 3D difference between the developed algorithm's solution and GPSurvey solution (SNAP flight 990810).

The vectors between AIRB and AIRF and between AIRB and AIRW were determined using the method presented in section 5.2, chapter 5. Again, these vectors were obtained from the L1 carrier phase measurements without any data from the ground reference stations. From the determined triangle, and considering its configuration with respect to the aircraft body frame, a GPS-based estimate of the aircraft attitude (roll, pitch and yaw angles) was determined. As mentioned in section 3.2, chapter 3, the coordinates of the antennas with respect to the body frame were previously determined using total stations. Through this relation and the determined vectors between the three antennas, the angular differences between the body frame axes and the NED frame axes can be determined, resulting the aircraft attitude estimate.

Figures 7.29 to 7.31 show the obtained attitude angles for flight 990810. Since almost all of the profiles of this flight are in the South-North direction, it is easy to associate the depicted attitude angles with the flight trajectory.

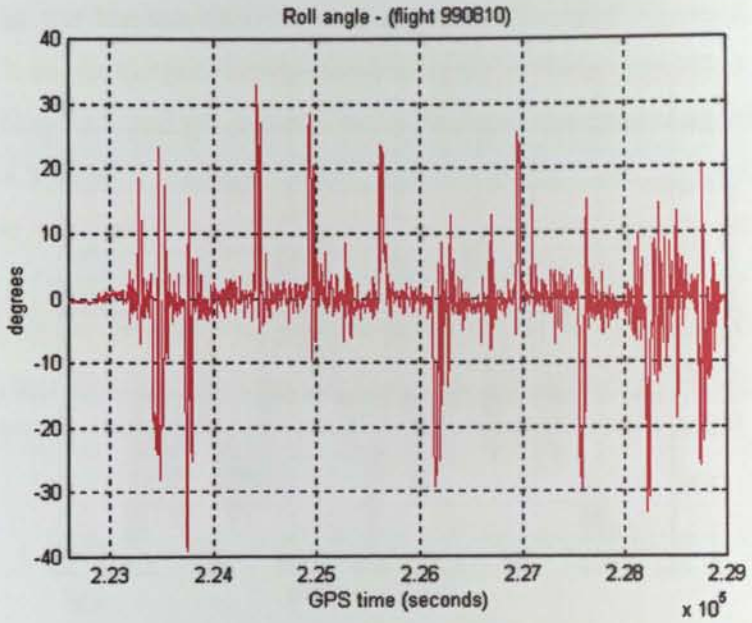


Figure 7.29 – GPS-based roll angle estimate for flight 990810.

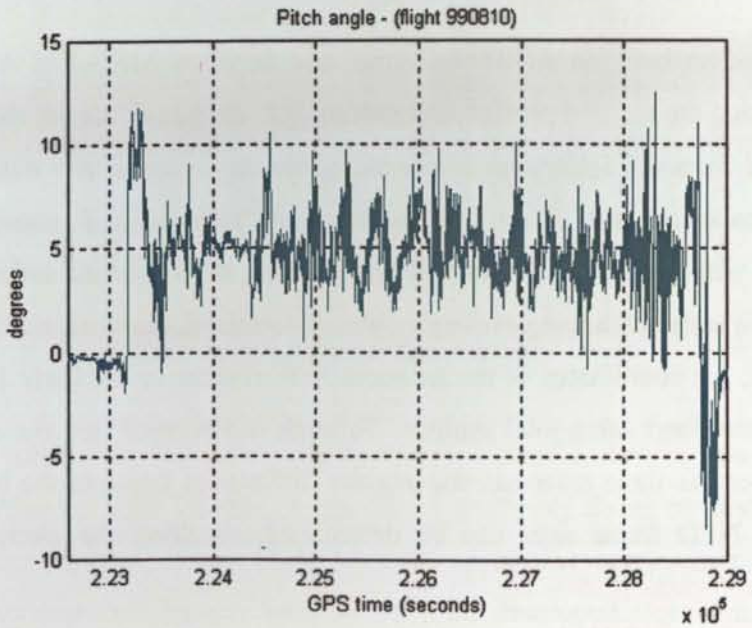


Figure 7.30 - GPS-based pitch angle estimate for flight 990810.

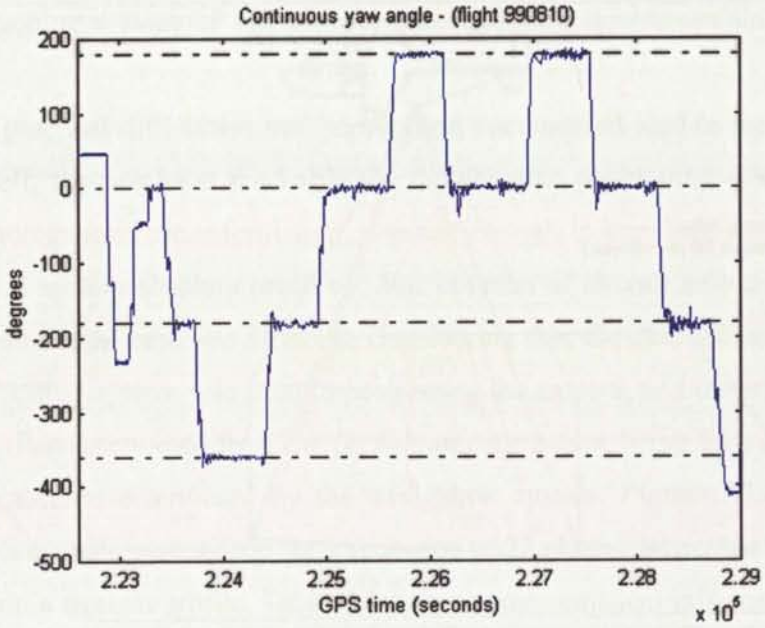


Figure 7.31 - GPS-based yaw angle estimate for flight 990810.

After revelling and digitalising the photos, some areas of interest were selected and about 80 ground control points were surveyed with GPS receivers. These points were chosen from the photos in a way that there would be around 6 well spread coordinated points per photo. The ground control points enable the photogrammetric processing, together with the camera properties. Two different software packages were used - OrthoEngine from PCI Geomatics and a modified version of a package developed at the Astronomical Observatory of the University of Porto [Gonçalves, 1993]. Figure 7.32 depicts the principle used to determine the aircraft position and attitude based on photogrammetric processing.

The digitalisation of the photos was made at two resolutions – most of them at 21 micron and some at 16 micron. That is, being the scale of the photos of f/H, where H is the flown altitude over the ground and f the camera focal distance (which, for the considered camera, was 150mm), for H = 800 m a pixel of the photo corresponds to $21e^{-6} \cdot 800/0.150 = 0.112$ m on the ground.

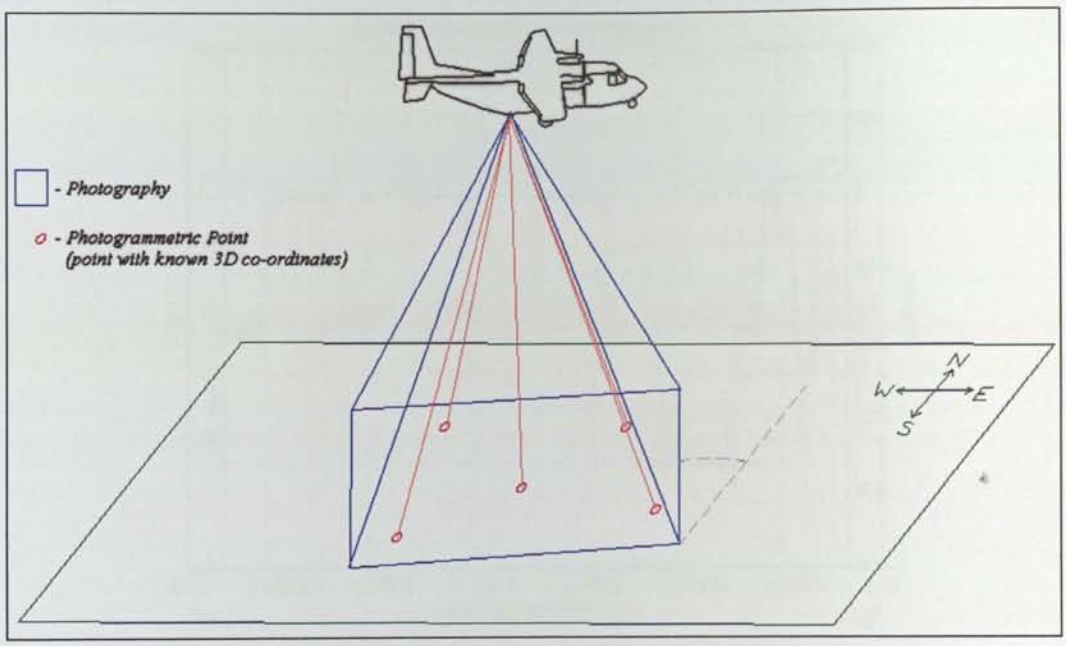


Figure 7.32 – Aircraft position and attitude determination using photogrammetry.

Initially, the traditional aerial triangulation bundle adjustment (see [Wolf, 1983]) was performed with the OrthoEngine program from PCI Geomatics. The results obtained with this method were not very satisfactory, most probably because one of the four fiducial marks of the camera was not visible in de photos, and because, in some cases, the number of effective ground control points per photo, or their geometric distribution, was not ideal due to terrain constraints. The method described in figure 7.32 was then used through an application developed at the Astronomical Observatory of the University of Porto, after some modifications.

When processing the photos, with a photo resolution of 11 cm per pixel, the matching of the ground control points on the photo wasn't always strait-forward. But the main difficulties encountered were related with the camera. First of all, there was obviously a misalignment between the camera and the aircraft, which had to be estimated. The sequences of photos were used for this estimation. Secondly, there was the need to know the exact instant when each photo was taken. After studying the camera electronic specifications, a simple electronic circuit was developed to connect a point where a pulse is generated at shooting instant, to the event marker input of one of the GPS receivers. Although not specified, a delay was verified to exist between the real shooting instant and the registered one, and this was another parameter to

estimate (reaching a value of 127 milliseconds, but some doubts remained about its constancy).

The practical difficulties and imprecision encountered lead to the conclusion that, for itself, the precision reachable for the absolute positioning of the aircraft, based on photogrammetric information, was not enough to conclude anything about the navigation system absolute precision. But in terms of aircraft attitude, especially for the yaw angle, the case was different. Considering this, the absolute position given by the DGPS/IMU system was used to positioning the camera, and the attitude of the camera was then determined from the photogrammetric data, being then compared to the aircraft attitude determined by the navigation system. Figure 7.33 shows the results of this attitude comparison for a sequence of 22 photos, where the aircraft was flying thought a straight profile. Table 7.1 shows some statistical information for this analysis.

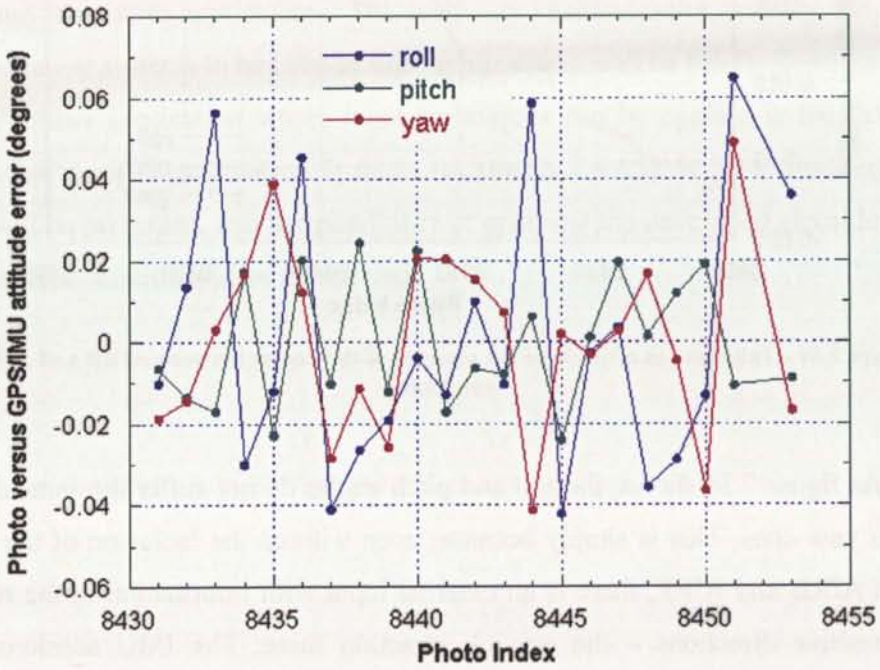


Figure 7.33 – Comparison between GPS/IMU attitude and photogrammetric derived attitude.

Table 7.1 – Attitude comparison between navigation system and photogrammetric solutions.

(degrees)	Roll	Pitch	Yaw
Mean	-0.000002	-0.000620	0.000148
Std	0.0328	0.0157	0.0231

One interesting fact appears when the Kalman filter integrating the GPS and IMU data is processed without the input of the GPS vector between back and front antennas. When comparing the attitude results with the ones produced with the photogrammetric data, the yaw drift is evident (due to gyro drifting), thus revealing the importance of that vector in the final solution. Figure 7.34 illustrates this fact, presenting the difference between the comparison of the GPS/IMU attitude (not considering the AIRB-AIRF vector input) with the photogrammetric derived attitude.

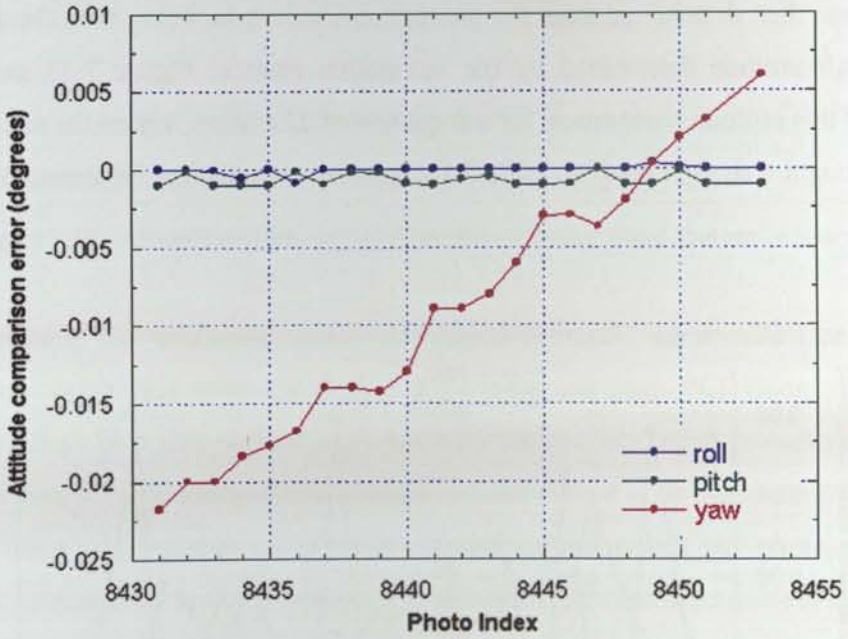


Figure 7.34 – Influence in attitude of the absence of the vector between AIRB and AIRF antennas.

As figure 7.34 shows, the roll and pitch angles do not suffer the same drifting effect as yaw does. This is simply because, even without the inclusion of the vector between AIRB and AIRF, there is an external input with information in the roll and pitch sensitive directions – the gravity attraction force. The IMU accelerometers (especially the vertical accelerometer) sense the gravity attraction effect (more correctly, the force the aircraft floor imposes on the IMU to fight gravitational acceleration) and this information is used by the Kalman filter, reducing the roll and pitch angles' drifting.

CHAPTER 8

OTHER APPLICATION AREAS

In this chapter, other areas where the presented methodologies can (and, in some cases, were) applied will be described. It can be noticed that throughout this thesis, the main application area that was focused was airborne navigation where the absence of obstacles blocking the GPS signals is predominant. This chapter will start by describing other navigation scenarios such as terrestrial navigation, and will show the principal modifications that are necessary to consider in order to apply the presented methods in such environments. Also, the integration with other sensors will be focused which, compensating the performance reduction of GPS, will produce an overall solution with enough accuracy and reliability, meeting the requirements of many land kinematic applications. The hardware characteristics, namely the proper communication systems to be used in such applications, will be briefly described.

Another application where these techniques can be applied is the generally called Local Area Augmentation Systems (or simply LAAS). A brief introduction to LAAS will be presented, and the possibility of applying the developed algorithms in a LAAS implementation will be mentioned.

8.1 Terrestrial Navigation

Up to this moment, most of the presented issues have considered the aircraft as the vehicle whose navigation solution is to be determined. Although the exposed methodology is independent of the navigation environment and type of vehicle being considered, in the case of the aircraft there are some phenomena that are usually not significant, but in other environments such has terrestrial navigation they must be equationed.

When a land vehicle, like a car, is moving in an urban environment with a GPS antenna on its roof, the signals being received from the GPS satellites are frequently blocked by the buildings and trees on the neighbourwood of the vehicle. When considering an aircraft, these situations only occur when it makes high roll or pitch maneuvers. In the case of the land vehicle, this phenomenon usually makes the satellite geometry to be weak most of the time, with few satellites distributed along the street direction.

Another problem is the reflection of the GPS signals in the buildings near the vehicle – multipath. These reflections create offsets in the measurements that are of difficult estimation, especially in the case of a moving antenna. With the aircraft, multipath can also occur when the signals reflect on some parts of the aircraft structure before being captured by the GPS receiver. Also, when the aircraft is banking over the sea, some reflected components on the sea surface can induce multipath errors. Figure 8.1 shows an example of the influence of multipath on a vehicle's position while going through Porto streets (in this case, multipath occurred while the car was stopped in a traffic light, in an area with considerable tall buildings). Only code positioning (DGPS) was considered in this example, and multipath's influence on those measurements caused the presented position errors.

L1 ambiguity resolution for moving vehicles in urban environments is difficult to achieve. Since the signal tracking continuity is being broken very frequently, ambiguities have to be determined in many occasions during a survey. For that determination it is desirable to have at least five visible satellites with good signal tracking (and with good geometry) for a certain number of consecutive epochs. These requirements are not easily verified in this environment.

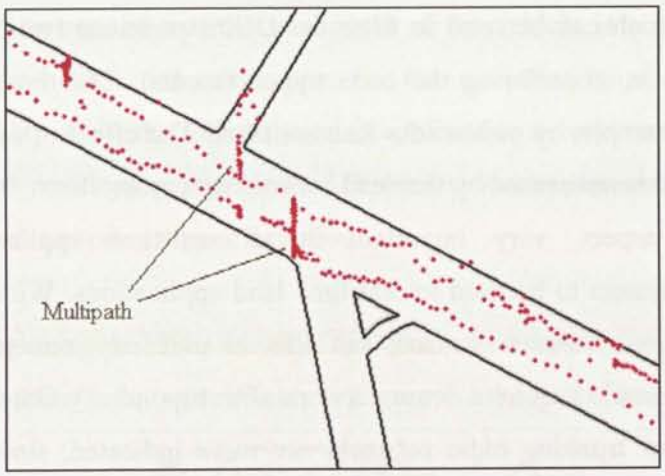


Figure 8.1 – Example of multipath effect in an urban environment.

Fortunately, most applications for moving land vehicles do not require centimeter or decimeter level accuracy. Actually, an accuracy of a few meters is usually enough for most real-time kinematic applications in urban environments. Some applications like wide area fleet management are fully satisfied with the stand-alone position that is determined by the onboard GPS receiver. Some other applications such as bus or taxi fleet management can be satisfied with differential code positioning (sometimes with carrier smoothing), obtaining positions with an overall accuracy around 2 to 5 meters.

There are applications that, although requiring meter level accuracy, they require robust positioning and with high availability of navigation solutions, that is, the maximum time period with no position update has to be very reduced. Examples of such applications are real-time vehicle tracking for security reasons (for example, when a vehicle is stolen), public transportation vehicle tracking for providing the users with time of arrival estimates, and real-time police vehicle tracking to control field operations.

For applications such as this, it is usual to complement the DGPS positioning with other sensors, usually dead-reckoning sensors. Most common sensors used in integration with GPS on moving land vehicles are the odometer, the compass, the accelerometer, and the gyroscope, among others. Being able to provide relative movement (linear or angular) every epoch, these sensors' measurements can (up to a limit) compensate the lack of availability of DGPS positions (for example, when going through tunnels, or under foliage, whenever the number of visible satellites is insufficient). Another characteristic of such sensors is the smooth pattern of their

measurements which can be used to filter the DGPS positions (which have a high level random noise, considering the code measurements). This integration can be performed, for example, by means of a Kalman filter. The effect of multipath can be attenuated since it is not sensed by the dead-reckoning sensors.

Another aspect, very important in all real-time applications, is the communication system to be used in real-time land applications. With the aircraft, a line-of-sight radio system was used, but this is evidently not suited for land environments (it would require a dense network of transponders). Other systems such as GSM/UMTS or trunking radio networks are more indicated, since they already provide the coverage and their communication delays are usually within the acceptable range.

The following sections show some examples of land applications where the presented methodology was, or can be, used.

8.1.1 Mobile Mapping Application

So far, the focus has been on real-time kinematic applications. But there are kinematic land applications where the real-time component is not an issue, but still the position accuracy and its high availability are under concern. An example of these applications is mobile mapping. In mobile mapping the objective is to gather information about several elements (like traffic signs, bus-stops, streets, and so on, making an inventory of city roads and infra-structures), being their coordinates one of the attributes. This can be performed using a navigation system in a moving platform, together with an information storage system. As described in section 3.3, chapter 3, the GPS/IMU system that was developed within the SNAP project for aircraft navigation was also implemented in a land vehicle, as shown in figure 3.10, chapter 3. The GPS/IMU system implementation was much identical to the aircraft implementation. The slight differences were that only two GPS antennas were installed, no real-time processing was performed (it was not necessary), GPS algorithms were set to consider only code differential processing, and the covariance parameters of the IMU Kalman filter with respect to the GPS solutions were re-tuned.

It should be noticed that the yaw angle of the vehicle is coincident with its moving direction, which did not happen in the aircraft (figure 3.9, chapter 3, illustrates this fact). Also, the roll variation is confined to a very narrow range. This, and the required positioning precision of 2 meters, made unnecessary the 3 GPS antenna triangle as attitude estimate supplier.

In the beginning of 1999, a total of 1300 km of road were surveyed in the area of Vila Nova de Famalicão (with 180 km^2). Figure 8.2 shows the resulting road map.

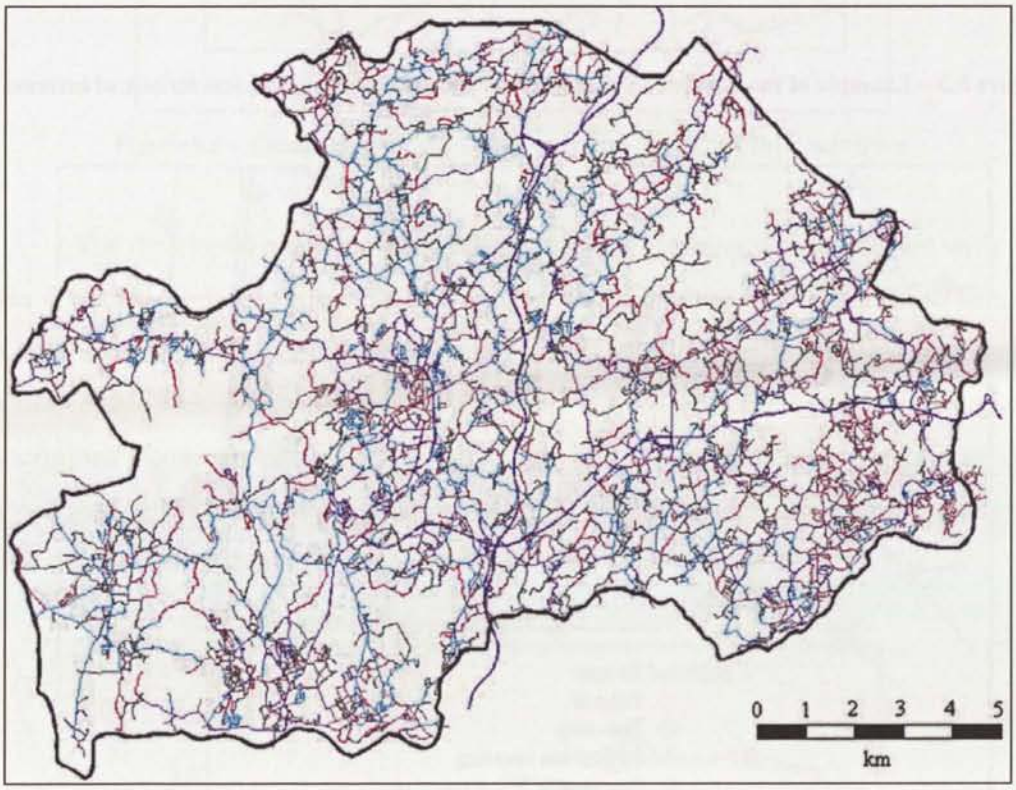


Figure 8.2 – Surveyed roads in the Vila Nova de Famalição campaign.

After collecting all the data, it was processed and the final results were treated and presented in CAD digital format. Different elements and different attributes were stored in different layers, with different colours, so the end user would easily interpret the results. Figure 8.3 shows an example of a few roads with different pavements (distinguishable by their colours) and figure 8.4 gives an example of some collected elements.

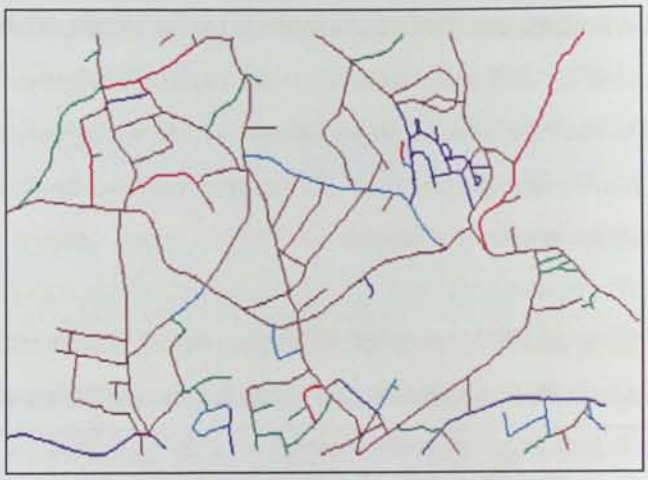


Figure 8.3 – Example of roads viewed using their pavement material as characteristic of interest.

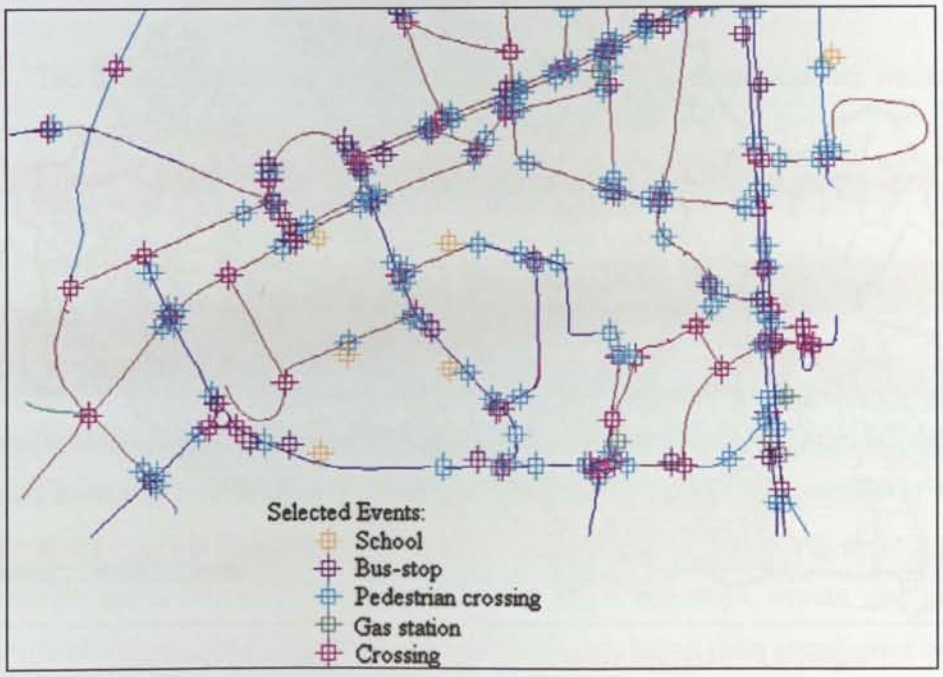


Figure 8.4 – Example of collected road elements.

With the GPS/IMU integration, the availability of navigation solutions was very near to 100%, and the obtained positioning precision was within the 2 meters range (some verification tests were performed afterwards with GPS receivers in static mode).

For comparison purposes, figure 8.5 presents the comparison of the DGPS only and the DGPS/IMU solutions for an area of the surveyed region.

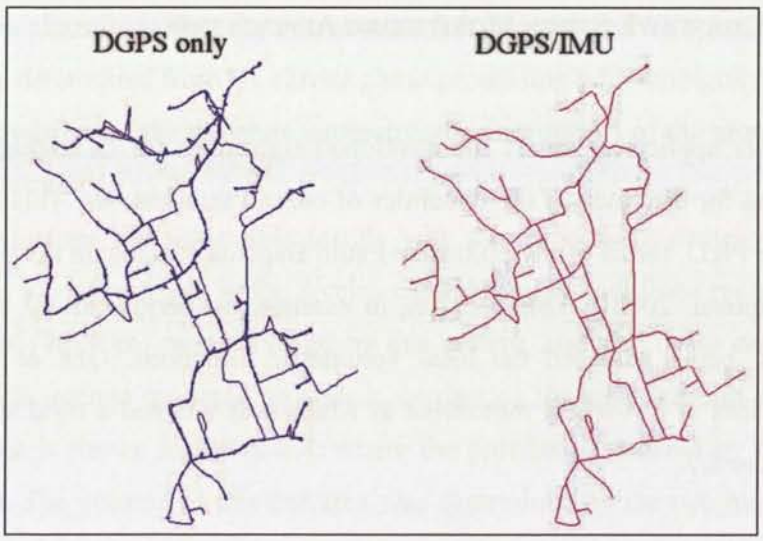


Figure 8.5 – Comparison of the DGPS only and the DGPS/IMU solutions.

The developed algorithms for carrier phase processing were also used with the data collected from this survey. The purpose was to analyse how they would behave in such environment, with frequent loss of carrier lock and with a limited number of available satellites. An example is given in figure 8.6 where in blue is represented the determined positions using code DGPS, and in red are the positions successfully determined with carrier phase processing. Only 39% of the presented track was able to be determined with higher precision.

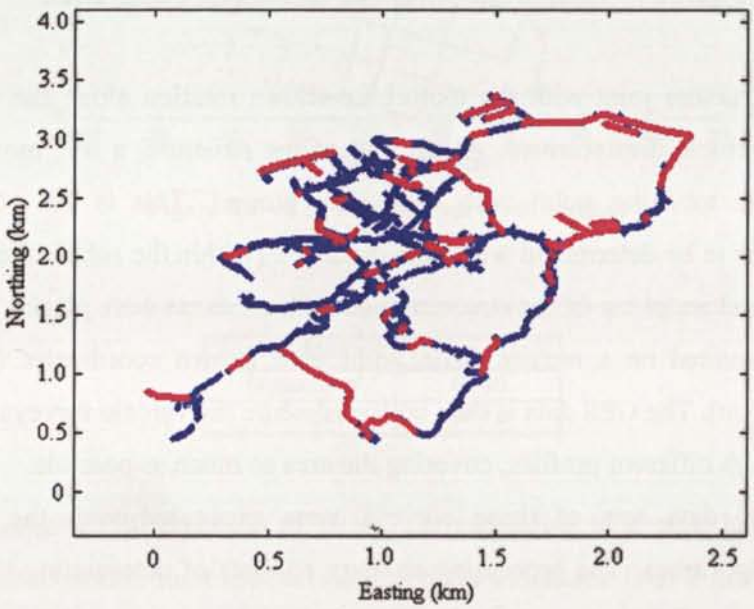


Figure 8.6 – Example of positioning with carrier phase processing in an urban environment.

8.1.2 Coastal Erosion Monitoring Application

Another application where the developed algorithms for L1 ambiguity fixing were used was for the study of the dynamics of coastal sand masses. This is the main subject of the Ph.D. thesis of my colleague Paulo Baptista (details on his work can be found in [Baptista, 2002]). This consists, in essence, on periodical 3D mapping of coastal areas, being analysed the local volumetric variations. One of the survey methods consists of a 4-wheel motorbike to which was adapted a rigid structure, as shown in figure 8.7.

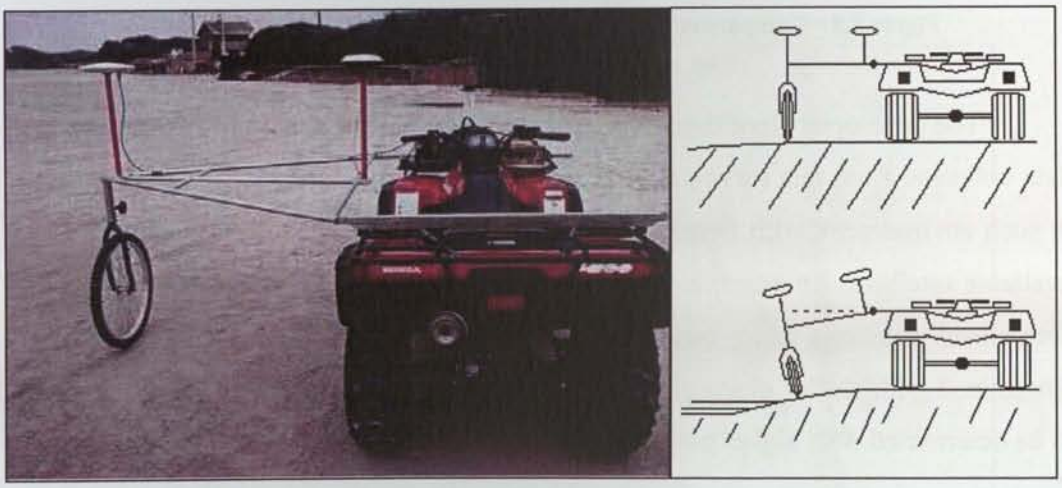


Figure 8.7 – Implemented mechanism for mapping coastal areas.

The structure joint with the motorbike allows rotation along the axis of the direction of vehicle displacement. At the end of the structure, a free moving wheel establishes the touching point with the sandy ground. This is the point whose coordinates are to be determined with high precision (within the sub-decimeter level). In the horizontal metal bar of the structure, two GPS antennas were placed, and a third antenna is mounted on a nearby static point with known coordinates (this is the reference station). The GPS data is then collected while the vehicle surveys the area of interest, through different profiles, covering the area as much as possible.

Several data sets of these surveys were processed with the developed positioning algorithms. The processing strategy consists of determining the absolute position of one of the antennas (using the methodology presented in section 5.1, chapter 5), and then the 3D vector between the two rover antennas is determined (by

means of the algorithms described in section 5.2, chapter 5). With these two values (which were determined from L1 carrier phase processing with ambiguity fixing), and with the knowledge of the structure geometry, the coordinates of the ground touching point are determined.

To illustrate the achievable results with this processing strategy, a test was conducted in a confined area in the Aveiro coastal region. A defined rectangular area, with 3500 m^2 (70x50m), was surveyed by this system, and also by an on-foot survey with one GPS antenna mounted on a stick, contacting the sand through a wheel. The surveyed area is shown in figure 8.8, where the profiles considered by both surveys are depicted. The volume of this test area was determined by the two methods, being the results presented in table 8.1.

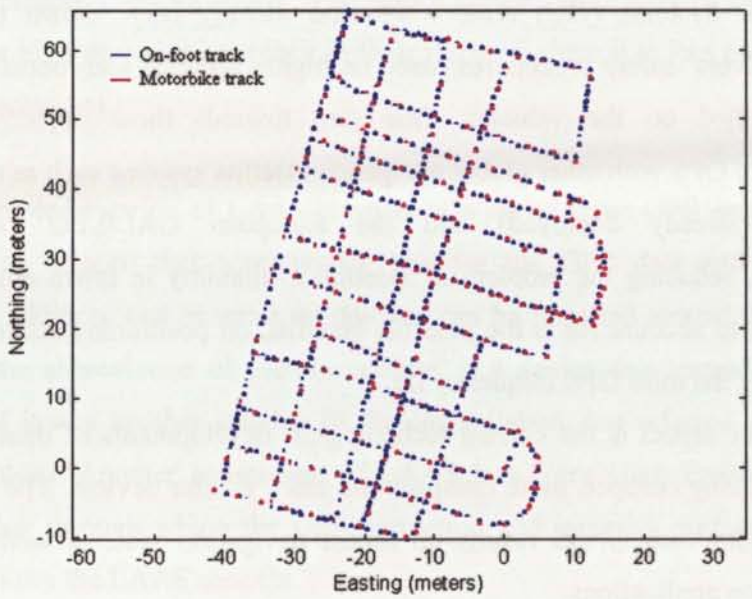


Figure 8.8 – Test area and surveyed tracks.

Table 8.1 – Volumetric results in the test area using two survey methods.

Survey Method	Volume (m3)
Motorbike	9416
On-foot	9370

The obtained difference is of 46 m^3, corresponding to a mean height offset of 1.3 cm, which is within the expected precision for kinematic DGPS positioning with L1 carrier phase ambiguity fixing.

The most significant advantage of the presented method, over the on-foot method (and also over the traditional approach with total station profiles), is that is can cover wider areas in less time, maintaining the same level of precision.

8.1.3 VEHICLE TRACKING

As described, terrestrial navigation is an area that includes many interesting applications and, depending on the specific characteristics of each application, a wide range of approaches can be considered. It is a challenging area with important reflexes on society. These emerging applications are demanding a constant increase of the quality and availability of navigation solutions. One example is in the Intelligent Transportation Systems (ITS) area, where has already been shown the will to implement drivers' safety procedures based on highly accurate and robust navigation systems installed on the vehicles. One step towards these objectives is the combination of GPS with other global navigation satellite systems such as the Russian GLONASS (already deployed) and the European GALILEO (still under development), reducing the problem of satellite availability in urban environments. Another issue to account for is the possible benefits, on positioning accuracy, of the introduction of the third GPS frequency L5.

Another aspect is the current technological developments of dead-reckoning sensors, producing cheaper, more compact and more precise devices. The integration of these sensors with GNSS results on robust navigation systems well suited for vehicle location applications.

8.2 Local Area Augmentation Systems (LAAS)

The concept of Local Area Augmentation Systems (LAAS) is especially oriented for aircraft approach and landing procedures. Nevertheless, this concept can also be applied to some other applications. LAAS is a system constituted by different devices whose objective is to provide a highly accurate and highly available signal, with high integrity, that allows the positioning of a moving vehicle (in the case, of an aircraft) with high accuracy and high reliability, being GPS signals the base for this positioning process. One feature of LAAS is to provide this positioning capability for all-weather precision approach and landing. The requirements' level of a LAAS implementation must be high enough in order to comply with the CAT I, II and III precision approaches specifications. With such a system, more airports can have these standards for high precision approach in their runways since it is less expensive than ILS implementations.

An implementation of LAAS consists of a set of static GPS antennas, in the vicinity of an airport, that continuously monitor the GPS data and check their integrity. In addition, one or more pseudolites can be installed around the airport (a pseudolite, the abbreviation of pseudo-satellite, is a device that transmits GPS like signals, as if it was another satellite in the constellation, but referred to its known ground position). Another component of LAAS is a Very High Frequency (VHF) radio data link through which the GPS correction and integrity messages are sent. Figure 8.9 shows the LAAS concept.

The algorithms that were developed within the work being presented can be adapted to be incorporated in a LAAS implementation, for position determination and also for monitoring the quality/integrity of the GPS signals being received in the set of reference stations. With a few modifications to the algorithms, the real-time GPS corrections can be determined using the set of ground receivers instead of only one GPS receiver.

BIBLIOTECA F.E. PORTO

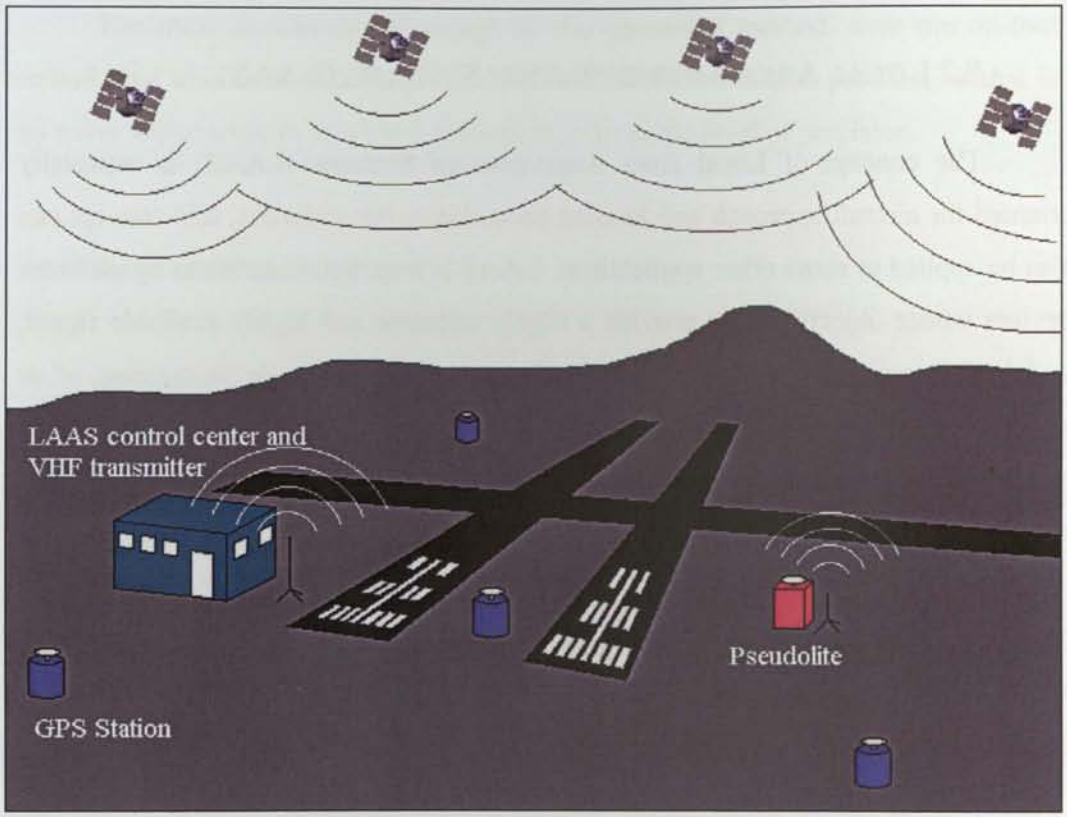


Figure 8.9 – Representation of a Local Area Augmentation System (LAAS).

CHAPTER 9

CONCLUSIONS AND FINAL REMARKS

9.1 CONCLUSIONS

Navigation has been, from centuries, a discipline of major importance and with great and direct impact on society. As with every area, the technology developments of this era made their appearance in navigation, bringing new and more accurate sensors, and making possible the existence of global navigation systems based on artificial satellites which are revolutionising the field of navigation. Being able to provide, in an affordable way, to any user anywhere in the world, the capability of knowing the 3D position within a few meters (or even better), Global Navigation Satellite Systems (GNSS) make feasible a new and diverse group of applications which are totally or partially based on navigation.

At the time this work has been elaborated, the Global Positioning System (GPS) was the deployed GNSS that presented the most suitable characteristics for the main application supporting this work – real-time high-accuracy aircraft positioning and attitude determination. With an achievable accuracy within the decimeter level (or even sub-decimeter), GPS was the system that received the main focus in this work.

In this thesis, a methodology for processing differential GPS data has been presented, being this analysis oriented for real-time kinematic applications where highly accurate absolute positioning is demanded. The main incidence of the presented analysis is on rapid L1 ambiguity fixing, where an innovative method is presented in detail. Taking advantage of the characteristics of such kind of applications, such as a sampling rate of 1 Hz or higher, the presented algorithms make some specific considerations when processing the GPS data which allow L1 ambiguity determination with just a few seconds of data (usually under 10 seconds), and with a considerably high reliability.

This GPS processing methodology was presented with every step included, from cycle-slip detection and fixing, to L1 ambiguity determination technique, passing through smoothed code DGPS positioning and wide-lane ambiguity fixing.

Several tests have been performed, for every step of the algorithm, and the most significant were here presented. The results of such tests indicate that the developed method for high accuracy absolute positioning is effective and efficient, providing sub-decimeter level positions with a few epochs of data. Also the robustness of the method was tested, with very satisfactory results, as illustrated in chapter 5.

Besides the aircraft absolute positioning, attitude determination was also considered. Since the true goal is to reference the instruments carried onboard an aircraft (photogrammetric cameras, altimeters, and others), the attitude of those instruments must be determined so that their measurements can be processed into something useful. A methodology for attitude estimation based on GPS measurements from two or three antennas has been presented in this thesis. Although irrelevant to the method itself, in order to have a correlation between the determined vectors and the vehicle attitude, it is required for the GPS antennas to be placed in strategic spots of the aircraft – for example, one in the front, one in the back and the other in one of the wings. Evidently, the longer the sides of the formed triangle are, the more accurate becomes the attitude estimation. The developed method considers the high accuracy determination of the 3D vector between a pair of aircraft antennas, not requiring precise absolute positions of the antennas. This way, there is no need for a ground reference station in what regards the attitude determination, being this estimate available independently of any communication link with the ground station for real-time applications. Again, within only a few seconds of data, the L1 ambiguities are determined and the vector between antennas is obtained with an accuracy around 2 centimeters (which is equivalent to an angular accuracy of 0.23° with a distance of 5 meters between antennas). It should be noticed that the atmospheric effects do not influence this procedure since the two antennas are very close to each other. Not including a possible occurrence of multipath, carrier phase noise is the predominant error in this approach. The efficiency and robustness of this method are further improved when the condition of the known distance between antennas is introduced. In chapter 5, results obtained with this method are presented, illustrating its good performance.

Another aspect that was studied in this work was the combination of the measurements of the Inertial Measurement Unit (IMU) with the GPS data. The analysis of the usefulness of the IMU data on the GPS processing was emphasised.

Regarding the absolute positioning of one of the aircraft antennas, it was concluded that, with the IMU that was used in the tests, only an increase on the robustness of the overall positioning could be obtained. The characteristics of the IMU data, especially those predominant in a short time span, make possible the determination of the position for the next GPS epoch (only with IMU dead-reckoning) with a negligible loss of position accuracy. This is used for checking the integrity of the GPS data for that next epoch since the next GPS position should be within a short vicinity of the IMU based position. With this strategy, some spurious effects on GPS measurements, which could have passed the GPS filtering algorithms, get a high probability of being detected (and eliminated).

Also, in this thesis it was shown the importance that the attitude estimate based on GPS processing has on the final GPS/IMU attitude. In fact, since the IMU major error source is gyro drift, it is very difficult to keep the aircraft attitude from drifting with respect to its true attitude, when processing IMU data only. This appears especially in the yaw angle since the pitch and roll angles still have the gravitational acceleration that, being sensed by the accelerometers, imposes a limit on the drifting of these two angles. Even more, in an aircraft the flight track can be distinct from the yaw direction due to the wind, making the yaw angle difficult to be maintained within a certain value (the true value). This is where the benefits of including the GPS attitude estimate in the Kalman filter that is processing the IMU data are obtained. This procedure improves the estimation of the drift parameters of the IMU gyros, improving the quality of the overall GPS/IMU navigation solution.

Several tests were performed with the implemented GPS/IMU system, some of which included external sensors that were used to evaluate the precision of the navigation solutions provided by the developed navigation system. From the presented tests, two are enlightened – the gravity anomaly determination (and comparison with other sensors values) in the AGMASCO/SNAP campaign in the Azores region (1997), and photogrammetry data comparison in the SNAP campaign in the Estremadura region (1999). In the former, the gravity anomaly that was determined by the GPS/IMU Kalman filter (which was one of the state vector variables) was compared with the anomalies determined by an airborne gravimeter (mounted on a stabilised platform), by a shipborne gravimeter, and by the Topex/Poseidon satellite. The successful matching of these results led to the

conclusion that the navigation parameters were being satisfactorily estimated in the GPS/IMU system. Again, the same conclusion was verified when the photogrammetric triangulation was compared with the aircraft attitude. After surveying the ground control points, the attitude of the photogrammetric camera was determined and compared with that of the aircraft (the camera was rigidly fixed to the aircraft structure), being the obtained coincidence within the range of the expected errors for this test.

Other tests were made to evaluate the accuracy of the absolute positioning results. These included surveying points in the ground with known coordinates, with different baseline lengths. Within the area where the level of the atmospheric effects in the GPS measurements were still bearable to this method, the expected accuracy was verified, with successful fixing of the L1 ambiguities. That area was estimated to be such where the baseline length is 30 km or less. It should be noticed that these tests were performed in an epoch near a maximum of solar activity, which greatly increases the ionosopheric effects on the GPS measurements. In epochs out of this solar maximum, L1 ambiguity fixing is expected to be obtainable for wider baselines. Nevertheless, a strategy with more than one ground reference stations has been analysed in chapter 5, with the objective of increasing the baseline length where L1 ambiguity fixing would still be possible with this method. With properly spread reference stations, it is possible to obtain some modelling of the atmospheric influences in the area comprised by those stations. This way, a significant reduction of the atmospheric residuals is obtained, permitting a successful L1 ambiguity fixing with the proposed methodology. A test has been described where only two reference stations, about 100 km apart, were used, with a rover receiver surveying several points in the line between both stations. The results of such test revealed that, using both reference stations, all the positions in between were successfully determined, which did not happened when only one reference station was considered at each time (in this case, only baselines below 30 km were fixed).

One of the goals of this work was the implementation of an airborne navigation system that, being significantly cheaper than a traditional highly expensive high grade Inertial Navigation System (INS), would achieve in real-time the same degree of accuracy or, at least, the same applicability and usefulness as the latter

system. From the presented methodology, and from the results of the real flight tests that were performed, it is concluded that this objective was fulfilled.

Other applications of the exposed methods were also presented, with particular focus on the implementation of the developed techniques on land vehicles. In this environment, multipath and the frequent satellite signal blocking become very significant, and the need for integrating GPS with different sensors becomes evident (especially, dead-reckoning sensors). With this in mind, the GPS/IMU system that has been developed for aircraft navigation was implemented in a land vehicle, with just some minor modifications. With this system, the full region of Vila Nova de Famalicão was surveyed and its roads were mapped in digital format as a result of this survey. Also, the location and characterisation of several city items (like crossings, schools, bus stops, pavement material and status, and others) were also gathered. After proceeding with quality control tests, with static point surveys with GPS receivers, it was concluded that the obtained accuracy with this system was around 2 meters, simply using code DGPS processing techniques (and further integration with the IMU data).

Another application of the presented L1 ambiguity fixing algorithms was on a project for studying the dynamics of sand masses in coastal areas (see [Baganha, 2002]). Using a 4-wheel motorbike, with a special structure mounted on it with 2 GPS antennas, those areas are periodically surveyed and a 3D mapping is obtained after determining the absolute position of the point that structure touches the sandy floor. This is achieved by determining the absolute position of one of the antennas using the developed methods, and also the calculation of the vector between both antennas is required (which is, again, calculated by the presented algorithms). Both of these results are obtained with L1 ambiguity fixing, resulting on a high precision 3D mapping of the area. This allows the analysis of the seasonal local volumetric variations, qualifying and quantifying the nature of the soil dynamics of such areas.

9.2 Future Developments and Perspectives

As mentioned before, navigation development is expanding rapidly. And the next years are truly promising, especially regarding the GNSS sector. In March 2002, a positive decision was reached by the European Community for going ahead with the development and implementation of the GALILEO system. This system is expected to be operational in the year 2008. This will provide a new constellation with 27 satellites emitting navigation signals to the Earth (and also other signals for the implementation of services that GALILEO is meant to provide). Besides the timing and positioning accuracy that GALILEO will be supposed to offer, further enhancements, especially on the land navigation area, will be achieved with the combination of the existing GNSS. For example, if a receiver will be able to capture simultaneously the GPS and GALILEO signals, satellite availability will be greatly improved for a land vehicle moving through urban canyons.

In addition, the intention of implementing a third frequency signal on the GPS system has been announced by the American Government. This will improve the positioning capabilities of the GPS system and high accuracy positioning is expected to become more accessible to the users. Regarding the GLONASS system, it is expected that the maintenance that the system requires ends up to be fulfilled, re-establishing the full operation and usefulness of this system.

The navigation power that is foreseeable with two, or even three, available GNSS is very promising. The obtainable positions are expected to have higher accuracy and also to be more robust since they are based in independent navigation systems (and, also, integrity monitoring mechanisms are expected to be implemented). The improvement on satellite availability will be very significant. Many applications that were more demanding regarding positioning will become feasible, and several new applications will appear given the availability and robustness of the achievable positioning. Another contribution is the technology advances that are constantly appearing in dead-reckoning sensors, which are becoming smaller, more accurate and cheaper, making integrated navigation solutions more accessible to the diverse users spread all around the world.

Regarding the possible developments that could be performed over the methodologies presented in this thesis, in the sense of improving them, one area to be explored is the modelling of the atmospheric effects over a certain area based on a network of ground reference stations. With this estimation process, the robustness and efficiency of the presented L1 ambiguity fixing algorithms should be greatly improved for baseline lengths higher that 30 km. This results from the sensitivity that the developed methods show to the differential atmospheric residuals. Several studies have already been published on the estimation of model parameters for the ionospheric delay, using GPS networks (see, for example, [Colombo et al., 1999], [Colombo et al., 2000], [Vollath et al., 2000a] and [Vollath et al., 2000b]). The application of such studies to the proposed positioning algorithms, and the subsequent performance analysis, would be an interesting subject.

In what concerns the IMU data integration for improving the GPS processing, a possible interesting analysis would be to study the data from different IMU units, of different grades, and to determine the benefits obtained for each class of IMU. Also, the integration of GPS with other dead-reckoning sensors for land applications such as vehicle positioning is an interesting subject especially in the sense of achieving highly robust solutions, with the maximum accuracy possible, and keeping a continuous availability of navigation solutions.

BIBLIOTECA F.E. PORTO

REFERENCES

- Anderson, B.O. and J.B. Moore (1979) *Optimal Filtering*, Prentice-Hall, Inc.
- ARINC Research Corporation (1991) *NAVSTAR GPS Interface Control Document* (document ICD-GPS-200), Government of the United States of America.
- Baptista, P., L.C. Bastos, C. Bernardes, and A. Dias (2002) 'A GPS Based System for Monitoring Sand Movements – The Aveiro Coastline Case', Proceedings of the 6th International Symposium LITTORAL 2002, The Changing Coast, EUROCOAST/EUCC, Porto, Portugal, pp. 347-351.
- Bastos, L., S. Cunha, R. Forsberg, A. Olesen, A. Gidskehaug, U. Meyer, T. Boebel, L. Timmen, M. Nesemann, and K. Hehl (1997) 'An Airborne Geoid Mapping System for Regional Sea-Surface Topography', Geodesy on the Move, IAG Proceedings Series 119, Springer Verlag, pp. 30-36.
- Bastos, L. and H. Landau (1998) 'Fixing Cycle Slips in Dual-Frequency Kinematic GPS Applications Using Kalman Filtering', Manuscripta Geodaetica, vol. 13, nº 4, pp. 249-256.
- Bastos, L., S. Cunha, P. Tomé, T. Cunha, R. Forsberg, A. Gidskehaug, K. Hehl, T. Boebel, U. Meyer., M. Nesemann, A. Olesen, L. Timmen, and G. Xu (1998) 'Airborne Gravity and Altimetry System: Application to Coastal and Islands Areas', Proceedings of the 9th General Assembly of the WEGENER Project, Krokkleiva, Norway.
- Bastos, L., S. Cunha, R. Forsberg, A. Gidskehaug, L. Timmen, and U. Meyer (1999) 'The Role of Airborne Gravimetry in Gravity Field Modelling: Experiences from the AGMASCO Project', Solicited paper at the XXIV Meeting of the European Geophysical Society, The Hague, Holland. Published in Physics and Chemistry of the Earth, vol. 25, nº 1, pp. 1-7.
- Bastos, L, S. Cunha, R. Forsberg, A. Olesen, A. Gidskehaug, L. Timmen, and U.Meyer (2000a). 'On the Use of Airborne Gravimetry in Gravity Field Modeling: Experiences from the AGMASCO Project'. Physics and Chemistry of the Earth, vol. 25, No.1, Elsevier Science Ltd.
- Bastos, L., P. Tomé, T. Cunha, M.J. Fernandes, and S. Cunha (2000b) 'Gravity Anomalies from Airborne Measurements - Experiments Using a Low Cost IMU Device', The International Association of Geodesy Symposia Series, vol. 123, Springer-Verlag, Inc., pp. 253-258.
- Benedicto, J. (2001) 'GALILEO Space and Ground Segment Architecture', Proceedings of the VGNSS International Symposium (GNSS 2001), Seville, Spain.
- Benedicto, J. and D. Ludwig (2001) 'GALILEO System Architecture and Services', Proceedings of the Conference 7th International Workshop on Digital Signal Processing Techniques for Space Communications (DSP 2001), Lisbon, Portugal.
- Bishop, G.J., J.A. Klobuchar, and P.H. Doherty (1985) 'Multipath Effects on the Determination of Absolute Ionospheric Time Delay from GPS Signals', Radio Science, vol. 20, nº 3, pp. 388-396.
- Black, H.D. (1978) 'An Easily Implemented Algorithm for the Tropospheric Range Correction', Journal of Geophysical Research, vol. 83.
- Black, H.D. and A. Eisner (1984) 'Correcting Satellite Doppler Data for Tropospheric Effects', Journal of Geophysical Research, vol. 89, nº D2, pp. 2616-2626.

- Boon, F.G., P.J. de Jonge, C.M. Tiberius (1997) 'Precise Aircraft Positioning by Fast Ambiguity Resolution Using Improved Troposphere Modelling', Proceedings og the Conference ION-GPS-97, pp. 1877-1884.
- Bradley, P.A. (1989) 'Propagation of Radiowaves in the Ionosphere', In Radiowaves Propagation, Peter Peregrinus, Ltd.
- Britting, K.R. (1971) *Inertial Navigation Systems Analysis*, John Wiley & Sons, Inc.
- Brown, R.G. and P.C. Hwang (1992) *Introduction to Random Signals and Applied Kalman Filtering, 2nd Edition*, John Wiley & Sons, Inc.
- Brunner, F.K. (1988) *Atmospheric Effects on Geodetic Space Measurements*, University of New South Wales, Australia.
- Brunner, F.K. and M. Gu (1991) 'An Improved Model for the Dual Frequency Ionospheric Correction of GPS Observations', Manuscripta Geodaetica, vol. 16, pp. 205-214.
- Brunner, F.K. and W.M. Welsch (1993) 'Effect of the Troposphere on GPS Measurements', GPS World, vol. 4, n° 1, pp. 42-51.
- Bruton, A.M. (2000) *Improving the Accuracy and Resolution of SINS/DGPS Airborne Gravimetry*, Ph.D. thesis, University of Calgary, Report n° 20145.
- Cannon, M.E., G. Lachapelle, L.P. Fortes, P. Alves, and B. Townsend (2001) 'The Use of Multiple Reference Station VRS for Precise Kinematic Positioning', Proceedings of the Japan Institute of Navigation, GPS Symposium 2001, Tokyo, Japan, pp. 29-37.
- Carvalho, J.M. (1993) *Dynamical Systems and Automatic Control*, Prentice-Hall, Inc.
- Colombo, O.L. (1986) 'Ephemeris Errors of GPS Satellites', Bulletin Geodesique, vol. 60, n° 1, pp. 64-84.
- Colombo, O.L., M. Hernandez-Pajares, J.M. Juan, J. Sanz, and J. Talaya (1999) 'Resolving Carrier-Phase Ambiguities On-The-Fly, at More Than 100 km From Nearest Site, With the Help of Ionospheric Tomography', Proceedings of the ION-GPS-99, Nashville, Tennessee.
- Colombo, O.L., M. Hernandez-Pajares, J.M. Juan, and J. Sanz (2000) 'Ionospheric Tomography Helps Resolve GPS Ambiguities On-The-Fly at Distances of Hundreds of Kilometers During Increased Geomagnetic Activity', Proceedings of the IEEE PLANS 2000, San Diego, California.
- Coordination Scientific Information Center (1998) *GLONASS Interface Control Document* (GLONASS-ICD), Russian Federation Ministry of Defence.
- Counselman, C.C. and S.A. Gourevitch (1981) 'Miniature Interferometer Terminal for Earth Surveying: Ambiguity and Multipath with Global Positioning System', IEEE Transactions on Geoscience and Remote Sensing, vol. GE-19, n° 4, pp. 244-252.
- Cunha, S., P. Tomé., T. Cunha, and L. Bastos (1998) 'On the INS and GPS Data Processing for Airborne Gravity Applications', Presentation in the Workshop 'Airborne Gravity and the Polar Gravity Field', Kangerlussuaq, Greenland.
- Cunha, S. (2001) 'Programação Semidefinida em Controlo Impulsional, Aplicação em Navegação Aérea', Ph.D.. Thesis, Faculty of Engineering of the University of Porto, Portugal.

- Davis, J.L., T.A. Herring, I.I. Shapiro, A.E. Rogers, and G. Elgered (1985) 'Geodesy by Radio Interferometry: Effects of Atmospheric Modelling Errors on Estimates of Baseline Length', Radio Science, vol. 20, n° 6, pp.1593-1607.
- Dellago, R., F. Luongo, M. Marinelli, J. Hahn, and R. Lucas (2001) 'GALILEOSAT: System Architecture and Design Status', Proceedings of the Conference GNSS-2001, Seville, Spain.
- de Munck, J.C. and T.A. Spoelstra (1992) *Proceedings of the Symposium on Refraction of Transatmospheric Signals in Geodesy*, Netherlands Geodetic Commission.
- Eissfeller, B. (1989) 'Analysis of a Geodetic Space-Stabilised Inertial Platform and Integration with GPS [Global Positioning System]', University of the Bundeswehr, Munich, Germany.
- Euler, H.J. and H. Landau (1992) 'Fast Ambiguity Resolution On-The-Fly for Real-Time Applications', Proceedings of the 6th International Geodetic Symposium on Satellite Positioning, Columbus, Ohio, pp. 650-729.
- Evans, A.G. and B.R. Hermann (1990) 'A Comparison of Several Techniques to Reduce Signal Multipath from the Global Positioning System', The International Association of Geodesy Symposia Series, vol. 102, Springer-Verlag, Inc., pp. 74-81.
- Farrell, J.L. (1976) *Integrated Aircraft Navigation*, Academic Press, Inc.
- Feess, W.A. and S.G. Stephens (1986) 'Evaluation of GPS Ionospheric Time Delay Algorithm for Single-Frequency Users', Proceedings of the PLANS-86 conference, Las Vegas, Nevada.
- Forsberg, R., J. Kaminskis, and D. Solheim (1996a), 'Geoid of the Nordic and Baltic Region From Gravimetry and Satellite Altimetry', Proceedings of the International Symposium on Gravity, Geoid and Marine Geodesy, Tokyo, Japan.
- Forsberg, R., K. Hehl, L. Bastos, A. Gidskehaug, and U. Meyer (1996b) 'Development of an Airborne Geoid Mapping System for Coastal Oceanography (AGMASCO)', in Gravity, Geoid and Marine Geodesy, IAG Symposium Series 117, Springer Verlag, pp. 163-170.
- Forsberg, R., A. Olesen, L. Bastos, A. Gidskehaug, U. Meyer, and L. Timmen (2000) 'Airborne Geoid Determination', Earth Planets Space, n° 52, pp. 863-866.
- Frei, E. and G. Beutler (1990) 'Rapid Static Positioning Based on the Fast Ambiguity Resolution Approach FARA: Theory and First Results', Manuscripta Geodaetica, vol. 15, n° 6.
- Gelb, A. (1974) *Applied Optimal Estimation*, The Analytic Sciences Corporation (The M.I.T. Press).
- Georgiadou, Y. and A, Kleusberg (1988) 'On the Effect of Ionospheric Delay on Geodetic Relative GPS Positioning', Manuscripta Geodaetica, vol. 13, pp. 1-8.
- Goad, C.C. and L. Goodman (1974) 'A Modified Hopfield Tropospheric Correction Model', Presentad at the American Geophysical Union Fall Annual Meeting, San Francisco, California.
- Goad, C. (1986) 'Precise Positioning with the Global Positioning System', Proceedings of the 3rd International Symposium on Inertial Technology for Surveying and Geodesy, Banff, Canada, pp. 745-756.
- Gonçalves, J. (1993) *Development of a Mono-Plotting System within ArcInfo. Application in Forestry*, M.Sc. Thesis, University of London.

References

- Grewal, M.S. and A.P. Andrews (1993) *Kalman Filtering – Theory and Practice*, Prentice-Hall, Inc.
- Hatch, R. (1990) 'Instantaneous Ambiguity Resolution', Proceeding s of IAG International Symposium on Kinematic Systems in Geodesy, Surveying and Remote Sensing, Springer-Verlag, Inc. pp. 299-308.
- Hein, G.W. and M.M. Ertel (1993) 'High Precision Aircraft Navigation System Using DGPS/INS Integration', Proceedings of the 2nd International Symposium on Differential Satellite Navigation, Amsterdam, The Netherlands.
- Hein, G.W., J. Godet, J.L. Issler, J.C. Martin, and T. Pratt (2001) 'The GALILEO Frequency Structure and Signal Design', Proceedings of the Conference ION-GPS-2001, Salt Lake City, Utah.
- Herring, T.A. (1992) 'Modelling Atmospheric Delays in the Analysis of Space Geodetic Data', Proceedings of the Symposium on Refraction of Transatmospheric Signals in Geodesy, Delft, The Netherlands, n° 36, pp. 157-164.
- Hofmann-Wellenhof, B., H. Lichtenegger and J. Collins (1998) *Global Positioning System – Theory and Practice, 4th Edition*, Springer-Verlag, Inc.
- Hopfield, H.S. (1969) 'Two-Quartic Tropospheric Refractivity Profile for Correcting Satellite Data', Journal of Geophysical Research, vol. 74, n° 18, pp. 4487-4499.
- Kayton, M. and W.R. Fried (1997) *Avionics Navigation Systems, 2nd Edition*, John Wiley & Sons, Inc.
- Klobuchar, J.A. (1986) 'Design and Characteristics of the GPS Ionospheric Time Delay Algorithm for Single Frequency Users', Proceedings of the PLANS-86 conference, Las Vegas, Nevada, pp. 280-286.
- Klobuchar, J.A. (1991) 'Ionospheric Effects on GPS', GPS World, vol. 2, n° 4, pp. 48-51.
- Lawrence, A. (1992) *Modern Inertial Technology – Navigation, Guidance and Control, 2nd Edition*, Springer-Verlag, Inc.
- Leick, A. (1995) *GPS Satellite Surveying, 2nd Edition*, John Wiley & Sons, Inc.
- Lu, G., M.E. Cannon, and G. Lachapelle (1995) 'Improving the Reliability of OTF Ambiguity Resolution with Dual Frequency GPS Observations', Proceedings of the Conference ION-GPS-95, Palm Springs, California, pp. 1111-1116.
- Lutgens, F.K. and E.J. Tarbuck (1989) *The Atmosphere: An Introduction to Meteorology, 4th Edition*, Prentice-Hall, Inc.
- Mader, G.L. (1990) 'Ambiguity Function Techniques for GPS Phase Initialization and Kinematic Solutions', Proceedings of the 2nd International Symposium on Precise Positioning with the Global Positioning System, The Canadian Institute of Surveying and Mapping, pp. 87-111.
- Martin, E.H. (1978) 'GPS User Equipment Error Models', Navigation, Journal of the Institute of Navigation, vol. 25, n° 2, pp. 201-210.
- Maybeck, P.S. (1979/82) *Stochastic Models, Estimation and Control*, Academic Press, Inc.
- Meditch, J.S. (1969) *Stochastic Optimal Linear Estimation and Control*, McGraw-Hill, Inc.

- Ober, P.B. (1993) 'Split-Second Ambiguity Resolution for GPS Using the Basis-Reduction Method', Report n° A-565, Faculty of Electrical Engineering, Delft University of Technology, The Netherlands.
- Parkinson, B.W. and J.J. Spilker Jr. (1996) *Global Positioning System: Theory and Applications (vol. I & II)*, American Institute of Aeronautics and Astronautics, Inc.
- Remondi, B.W. (1984) 'Using the Global Positioning System (GPS) Phase Observable for Relative Geodesy: Modelling, Processing and Results', Ph.D. dissertation, National Geodetic Information Center, NOAA.
- Remondi, B.W. (1986) 'Performing Centimeter-Level Surveys in Seconds with GPS Carrier Phase: Initial Results', Journal of Navigation, vol. 3, pp. 194-208.
- Remondi, B.W (1991) 'Pseudo-Kinematic GPS Results Using the Ambiguity Function Method', Journal of Navigation, vol. 38, n° 1, pp. 17-36.
- Saastamoinen, J. (1973) 'Contributions to the Theory of Atmospheric Refraction', Bulletin Geosdésique, n° 105, pp. 279-298; n° 106, pp. 383-397; n° 107, pp. 13-34.
- Savage, P.G. (1996) *Introduction to Strapdown Inertial Navigation Systems*, Strapdown Associates.
- Schwarz, K.P. and G. Zhang (1994) 'Development and Testing of a Low Cost Integrated GPS/INS', Proceedings of the ION-GPS-1994 conference, Salt Lake City, Utah.
- Seeber, G. (1993) *Satellite Geodesy: Foundations, Methods and Applications*, Walter de Gruyter.
- Siouris, G.M. (1993) *Aerospace Avionics Systems – A Modern Synthesis*, Academic Press, Inc.
- Smith, E.K. and S. Weintraub (1953) 'The Constants in the Equation of Atmospheric Refractive Index at Radio Frequencies', Proceedings of the Institute of Radio Engineers, vol. 41, n° 8, pp. 1035-1037.
- Teunissen, P.G (1993) 'Least-Squares Estimation of the Integer GPS Ambiguities', Invited Lecture at the IAG General Meeting, Beijing, Republic of China.
- Teunissen, P.G. (1994) 'On the GPS Double-Differences Ambiguities and their Partial Search Spaces', Proceedings of the Hotine-Marussi Symposium on Mathematical Geodesy, L'Aquila, Italy.
- Teunissen, P.G. and C.M. Tiberius (1994) 'Integer Least-Squares Estimation of the GPS Phase Ambiguities', Proceedings of the International Symposium on Kinematic Systems in Geodesy, Geomatics and Navigation (KIS-94), Banff, Canada, pp. 221-231.
- Thayer, G.D. (1974) 'An Improved Equation for the Radio Refractive Index of Air', Radio Science, vol. 9, n° 10, pp. 803-807.
- Titterton, D.H. and J.L. Weston (1997) *Strapdown Inertial Navigation Technology*, Peter Peregrinus, Inc.
- Tomé, P. (2002) 'Integration of Inertial and Satellite Navigation Systems for Aircraft Attitude Determination', Ph.D.. Thesis, Faculty of Science of the University of Porto, Portugal.
- Vollath, U., S. Birnbach, H. Landau, J.M. Fraile-Ordonez, and M. Martin-Neira (1998) 'Analysis of the Three Carrier Ambiguity Resolution (TCAR) Technique for Precise Relative Positioning in GNSS-2', Proceedings of the ION-GPS-98, pp. 417-426.

References

- Vollath, U., A. Buerchl, H. Landau, C. Pagels, and B. Wagner (2000a) 'Multi-Base RTK Positioning Using Virtual Reference Stations', Proceedings of the ION-GPS-2000, 13th International Technical Meeting of the Satellite Division of the Institute of Navigation, Salt Lake City, Utah.
- Vollath, U., A. Buerchl, H. Landau, C. Pagels, and B. Wagner (2000b) 'Long-Range RTK Positioning Using Virtual Reference Stations', Proceedings of the ION-GPS-2000, 13th International Technical Meeting of the Satellite Division of the Institute of Navigation, Salt Lake City, Utah.
- Webster, I. and A. Kleusberg (1992) 'Regional Modelling of the Ionosphere for Single Frequency Users of the Global Positioning System', Proceedings of the 6th International Geodetic Symposium on Satellite Positioning, Columbus, Ohio, pp. 230-239.
- Wild, U., G. Beutler, W. Gurtner, and M. Rothacher (1989) 'Estimating the Ionosphere Using One or More Dual Frequency GPS Receivers', Proceedings of the 5th International Geodetic Symposium on Satellite Positioning, Las Cruces, New Mexico, pp. 724-736.
- Wolf, P. R. (1983) *Elements of Photogrametry, 2nd Edition*, McGraw-Hill, New York.
- Wolf, R., G.W. Hein, B. Eissfeller, and E. Leohnert (1996) 'An Integrated Low Cost GPS/INS Attitude Determination and Position Location System', Proceedings of the Conference ION-GPS-96, Kansas City, Missouri..
- Wübbena, G. (1991) 'Zur Modellierung von GPS-Beobachtungen für die Hochgenaue positionsbestimmung', Ph.D. dissertation, University of Hannover, Germany.
- Yunck, T.P. (1993) 'Coping with the Atmosphere and Ionosphere in Precise Satellite and Ground Positioning', Geophysical Monograph, n° 73, pp. 1-16, American Geophysical Union.



FACULDADE DE ENGENHARIA
UNIVERSIDADE DO PORTO
BIBLIOTECA
0000065415